Universitat Politècnica de València

Instituto de Tecnología Química

INSTITUTO DE TECNOLOGÍA QUÍMICA   CSIC   UNIVERSITAT POLITÈCNICA DE VALÈNCIA

Clusters and single atoms of Pd and Pt: Synthesis and applications in catalysis and as antitumoral agents.

Doctoral Thesis

Presented by:

Rossella Greco

Supervised by:

Dr. Antonio Leyva Pérez

Valencia, June 2021

Antonio Leyva Pérez, Distinguised Researcher at the Instituto Universitario Mixto de Tecnología Química (UPV-CSIC), hereby

CERTIFY: That the thesis entitled "**Clusters and single atoms of Pd and Pt: Synthesis and applications in catalysis and as antitumoral agents**" has been carried out under my supervision by Mrs. Rossella Greco at the Instituto Universitario Mixto de Tecnología Química

Dr. Antonio Leyva Pérez

Abstract

The synthesis and application of metal clusters (MCs) and single atoms catalysts (SACs) of Pd and Pt is explored in this *Thesis*. Both clusters and single atoms were synthesized by following novel ligand-free procedures in solution, or by supporting them on Metal-Organic Frameworks (MOFs) or on polymers. After their synthesis, these entities were deeply characterized by techniques, such as Ultraviolet-Visible (UV-Vis), emission, X-ray Absorption (XAS) spectroscopies, Induced Coupled Plasma-Atomic Emission Spectroscopy (ICP-AES), X-ray Diffraction and microscopy, among others. Finally, MCs or SACs were used as catalyst in homo- or cross-coupling reactions, in alcohol oxidation reactions, and as antitumoral agents. Especially, the supporting of Pd^{II} dimers inside a MOF network allowed the following formation of Supramolecular Coordination Complexes (SCCs) within the MOF channels (SCCs@MOF). In the SCCs, the Pd^{II} dimers represent the pivotal centers and different pyridyl ligands, fluorinated and non-fluorinated, embody the linkers between the bimetallic units. After being characterized, the SCCs@MOF were used as catalysts in homocoupling reactions of boronic acids and alkynes, in cross-coupling reactions of alkynes and in alkyl alcohols oxidation. These catalysts were compared with its homogeneous counterparts, i.e., a pre-synthesized Pd metallacycle or the system Pd(OAc)$_2$/ligands. Overall, we show some examples of C-C coupling and oxidation reactions catalyzed by SCCs.

Moreover, benzyl alcohols oxidation reaction catalyzed by palladium single

atoms is described. The small metal species were prepared *in situ*, leading to one of the first example of ligand-free single atoms in solution. Afterward, in order to verify the real activity of single atoms and to stabilize them, they were supported inside a cysteine-based MOF and used in the same oxidation process.

Finally, the application of Pt clusters (MCs) in antitumoral treatments is portrayed. The clusters were synthesized in solution by using a polymer as reductant and in a similar procedure they were supported on the same polymer, which acted as a reducing agent, but also as a support. The Pt MCs gave also positive results in usually Pt-resistant cell lines.

Resumen

En esta *Tesis* se han estudiado la síntesis y aplicación de clústeres y átomos metálicos aislados de Pd y Pt. Clústeres y átomos aislados han sido sintetizados siguiendo nuevas metodologías en disolución, sin utilizar ligandos orgánicos, y soportándolos en materiales metal-orgánico estructurados (MOFs) o polímeros. Después de la síntesis, las pequeñas especies metálicas se han caracterizado con diferentes técnicas, como espectroscopias ultravioleta-visible, de emisión, de absorción de rayos X, análisis atómico de emisión por plasma de inducción acoplado, difracción de rayos X y microscopía. Los clústeres y los átomos aislados se han utilizado como catalizadores en reacciones de acoplamiento C-C, de oxidación de alcoholes y como agentes antitumorales.

La síntesis de dímeros de Pd^{II} soportados dentro de las cavidades del MOF ha dado lugar a la formación de complejos supramoleculares de coordinación en los canales del MOF (SCCs@MOF). En los SCCs, los dímeros de Pd^{II} representan los centros de coordinación, y ligandos de piridina fluorados y no-fluorados son los conectores entre las unidades bimetálicas. Después de la caracterización, los SCCs@MOF se han empleado como catalizadores en reacciones de acoplamiento C-C de ácidos borónicos y/o alquinos y de oxidación de alcoholes alquílicos. Estos catalizadores se comparan con los respectivos homogéneos, como un complejo cíclico de paladio, previamente sintetizado, o el sistema $Pd(OAc)_2$/ligandos. Además, se mostrarán algunos de los pocos ejemplos de reacciones de acoplamiento C-C y de oxidación

catalizadas por SCCs.

También se ha llevado a cabo la reacción de oxidación de alcohol bencílicos catalizada por átomos aislados de paladio. Estas pequeñas especies fueron preparadas *in situ*, dando lugar a uno de los primeros ejemplos de átomos aislados en disolución en ausencia de ligandos. Para averiguar la actividad real de los átomos aislados y poder estabilizarlos, se han soportado en un MOF basado en cisteína y se han utilizado en el mismo proceso de oxidación. Por último, se ha desarrollado también la aplicación de los clústeres de Pt en tratamientos antitumorales. Los clústeres se han sintetizado en disolución utilizando un polímero como agente de reducción y una metodología similar ha permitido soportarlos en el mismo polímero. Estos clústeres han presentado resultados positivos en líneas celulares usualmente resistentes al platino.

Resum

En la present *Tesi* doctoral s'ha realitzat un estudi de la síntesi i aplicació de clústers metàl·lics i àtoms aïllats de Pd i Pt com a catalitzadors.

Ambdós s'han sintetitzat seguint noves metodologies en dissolució, sense la utilització de lligams i suportant-los en materials metal-orgànic estructurats (MOFs) o polímers. Una vegada sintetitzats, s'ha dut a terme una caracterització minuciosa amb diferents tècniques, com espectroscòpia Ultraviolat-Visible (UV-Vis), d'emissió, d'absorció de raigs X (XAS), d'emissió atòmica per plasma d'acoblament inductiu (ICP-AES), difracció de raigs X i microscòpia. Aquests clústers i àtoms aïllats s'han utilitzat com a catalitzadors en reaccions d'acoblament C-C, en oxidacions d'alcohols i en tractaments antitumorals.

Concretament, la síntesi dels dímers de Pd^{II} suportats dins de les cavitats del MOF ha donat lloc a la formació de complexos de coordinació supramoleculars dins dels canals del MOF (SCCs@MOF). En els SCCs, els dímers de Pd^{II} representen els centres de coordinació, i les diferents unitats bimetàl·liques estan connectades per lligams de piridina fluorats i no fluorats. Després de la seua caracterització, els SCCs@MOF s'han utilitzat com a catalitzadors de reaccions d'acoblament C-C d'àcids borònics i/o alquins i en reaccions d'oxidació d'alcohols alquílics. També s'ha dut a terme la comparació entre els corresponents catalitzadors homogenis, per exemple un complex cíclic de pal·ladi o del sistema Pd(OAc)^2/lligams. D'altra banda, mostrem un dels pocs exemples de reaccions d'acoblament C-C i de reaccions

d'oxidació catalitzades per SCCs.

A més, també es descriu la reacció d'oxidació d'alcohol benzílic catalitzada per àtoms aïllats de Pd. Aquestes espècies menudes es preparen *in situ*, donant lloc a un dels primers exemples d'àtoms aïllats en dissolució sense lligams. A més a més, per a poder verificar la seua activitat i estabilitzar-los, s'han suportat en MOFs basats amb cisteïna, utilitzant-se en el mateix procés d'oxidació.

Finalment, s'ha desenvolupat l'aplicació de clústers de Pt (MCs) en tractaments antitumorals. Aquests clústers s'han preparat en dissolució utilitzant un polímer com agent reductor, i de forma similar s'han suportat en el mateix polímer. Els Pt MCs han donat resultats molt positius en línies cel·lulars que normalment són resistents al Pt.

Abbreviations

acac	acetyl acetonate
AC HAADF-STEM	Aberration Corrected High-angle Annular Dark-field Scanning Transmission Electron Microscopy
AES	Absorption Emission Spectroscopy
AFM	Atomic Force Microscopy
AnnV	annexin V
BE	Binding Energy
BET	Brunauer−Emmett−Teller
BF	Bright–field
bmim	4-butyl-1-methylimidazolium
btc	1,3,5-benzenetricarboxylic acid
COF	Covalent Organic Framework
DABCO	1,4-diazabicyclo[2.2.2]octane
dba	tris(dibenzilideneacetone)
DFT	Density-functional Theory
DMF	*N,N*-dimethylformamide
DMSO	dimethyl sulfoxide
DNA	deoxyribonucleic acid
DR	Diffuse-Reflectance
EDX	Energy Dispersive X–ray
en	ethylenediamine
ESI	Electrospray Ionization

EVOH	ethylene vinyl alcohol
EWG	Electron Withdrawing Group
EXAFS	Extended X-ray Absorption Fine Structure
FITC	fluorescein isothiocyanate
FT-IR	Fourier Transform Infrared
GC	Gas Chromatography
GC-MS	Gas Chromatography-Mass Spectrometry
HMRS	High Resolution Mass Spectrometry
HOMO	Highest Occupied Molecular Orbital
HPLC	High Pressure Liquid Chromatography
HRTEM	High Resolution Transmission Electron Microscopy
ICP	Inductively Coupled Plasma
IR	Infrared
KIE	Kinetic Isotopic Effect
LDH	lactate dehydrogenase
L-SG	L-glutathione
LUMO	Lowest Unoccupied Molecular Orbital
MALDI-TOF	Matrix-Assisted Laser Desorption/Ionization-Time Of Flight
MAS	Magic Angle Spinning
MC	Metal Cluster
MCPBA	*m*-chloroperbenzoic acid
Mecysmox	bis[S-methylcysteine]oxalyl diamide
Me₃mpba	2,4,6-trimethyl-1,3-phenylenebis(oxamate)
MIL	Matériaux de l'Institut Lavoisier
MOF	Metal-organic Framework

MS	Mass Spectrometry
MSA	mercaptosuccinic acid
MTG	Methanol to Gasoline
MTT	3-[4,5-dimethylthiazole-2-yl]-2,5-diphenyltetrazolium bromide
NMR	Nuclear Magnetic Resonance
NP	Nanoparticle
NU	Northwestern University
PAMAM	poly(amidoamine)
PBS	Phosphate Buffer Solution
PEG	polyethylene glycol
PET	polyethylene terephthalate
PGM	Platinum Group Metal
PI	propidium iodide
PMAA	poly(methacrylic acid)
PVP	polyvinylpyrrolidone
SA	Single Atom
SAC	Single Atoms Catalyst
SBU	Secondary Building Unity
SCC	Supramolecular Coordination Complex
SCXRD	Single Crystal X-ray Diffraction
SD	Standard Deviation
SEM	Scanning Electron Microscopy
SG	glutathione
SMC	Supramolecular Metallacyclic Complex
STEM	Scanning Transmission Electron Microscopy

TBAN	tetrabutylammonium nitrate
TEM	Transmission Electron Microscopy
TEMPO	2,2,6,6-tetramethylpiperidine 1-oxyl
TGA	Thermogravimetric Analyses
THF	tetrahydrofuran
TLC	Thin-Layer Chromatography
TOF	Turnover Frequency
TON	Turnover Number
TPR	Temperature-Programmed Reduction
UiO	Universitetet i Oslo
UV-Vis	Ultraviolet-Visible
WGSR	Water Gas-Shift Reaction
XANES	X-ray Absorption Near Edge Structure
XAS	X-ray Absorption Spectroscopy
XPS	X-Ray Photoelectron Spectroscopy
XRD	X-Ray Diffraction
ZIF	Zeolitic Imidazolate Frameworks
ZMOF	Zeolite-like Metal Organic Framework
ZSM	Zeolite Socony Mobil

Index

Chapter 1

General Introduction

1 General Introduction

1.1 Catalysis

Ostwald, who was awarded with the Nobel Prize in 1909 "*in recognition of his work on catalysis and for his investigations into the fundamental principles governing chemical equilibria and rates of reaction*", described a catalyst as "*any substance which alters the velocity of a chemical reaction without appearing in the end products*". Indeed, he believed that catalysis is a general phenomenon that could be used to make faster often very slow reactions, without influencing the equilibrium [1].

As a matter of fact, catalysis concerns modifications on the path to equilibrium, i.e., it deals with kinetics, not thermodynamics. Considering the example of a walk on the mountain (Figure 1.1), it starts at point A, and after hours it is possible to get to point B. We can relate the reaction thermodynamics to the difference of altitude between the starting point and the end. At the contrary, the chosen pathway represents the reaction kinetics. In addition, the catalyst is not exhausted during the process, so that each molecule of it can be used in following cycles and only a small amount of catalyst relative to the substrate is necessary. The substrate/catalyst ratio indicates the catalyst performance, which is measured as turnover number or turnover frequency (see *Paragraph 1.1.4*).
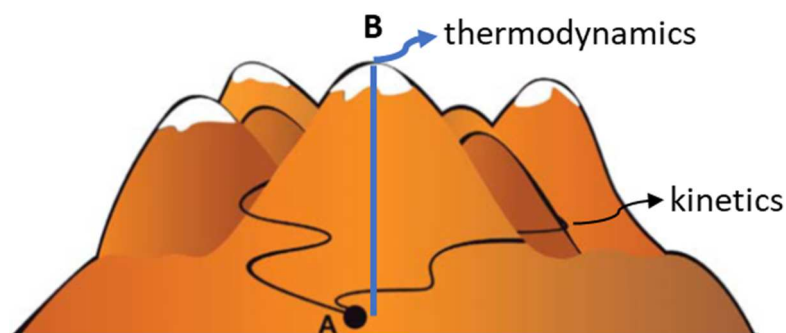
Figure 1.1 Differences between kinetics and thermodynamics [2].

Catalysts vary from the proton, H^+, through Lewis acids, organometallic complexes, organic and inorganic polymers, to enzymes. For the sake of simplification, catalysts are usually classified into three categories: homogeneous catalysis, heterogeneous catalysis and biocatalysis [2].

1.1.1 Homogeneous catalysis

Since World War II, as consequence of the development of many industrial catalytic processes, e.g., the carboxylation of olefins or the synthesis of nylon 66, the use of homogeneous catalysts has grown dramatically [1].

In homogeneous catalysis, catalyst, reactants, also called substrates, and products are in the same phase. Many homogeneous catalysts are composed by a (transition) metal atom, usually stabilized by ligands (Figure 1.2), which typically are organic molecules bearing a specific atom with the capability of binding the metal. In addition, by changing the ligand, it is possible to change the catalyst properties: activity, selectivity, and stability [2].

Generally, it is possible to obtain very high selectivity in homogeneous catalytic reactions and, consequently, these catalysts are used in the synthesis of some industrial relevant molecules (Figure 1.3).
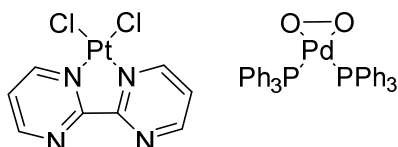
Figure 1.2 Examples of complexes of platinum and palladium.

| L-Dopa | L-Menthol | Intermediate for prosulfuron | Ibuprofen | (S)-Metolachlor |
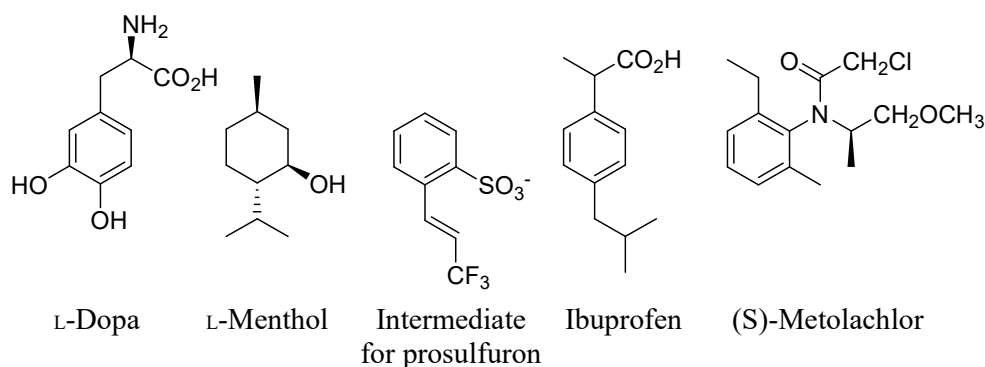
Figure 1.3 Examples of molecules obtained by homogeneous catalysis.

One of the biggest advantages of homogeneous catalysts is that the behavior of the catalyst can be studied at molecular level, due to the simple identification of the active species by common techniques, e.g., spectroscopic techniques, such as Infrared (IR) and Nuclear Magnetic Resonance (NMR). Therefore, the performance of a homogeneous catalyst can be perfectly adjusted selecting the proper metal, ligand, or process conditions, on the basis of mechanistic studied, which are easy to reach by using the techniques mentioned above.

The main drawback of homogeneous catalysts is their arduous recovery after reaction, which is the reason why the industry often tries to replace homogeneous by heterogeneous catalysts [3].

1.1.2   Heterogeneous catalysis

Heterogeneous catalysis covers the cases where the catalyst and the substrate are in different phase. However, when chemists use the definition of heterogeneous catalysis, they commonly mean a system where the catalyst is solid, and the substrates are gases or liquids. One important benefit of heterogeneous catalysis is the ease of catalyst recuperation by separation from the substrates or products. Indeed, in gas/solid systems the catalyst is effortlessly separated and washed, and in liquid/solid systems, it can be just filtered [2].

To understand the significance of heterogenous catalysis, it is worth to mention that more than 90% of the chemical processes use heterogeneous catalysts: manufacture of food and medicines, production of fabrics, building materials, and almost all the fuels for our transport systems.

Certainly, one of the best examples of heterogenous catalyst is the automobile catalytic converter, which is composed by platinum-rhodium bimetallic particles. The latter are effective catalysts in the conversion of unwanted species like carbon monoxide (CO), nitric oxide (NO) and hydrocarbons into innocuous products like carbon dioxide, nitrogen and water.

Moreover, the process to synthesize petrol (gasoline) starting from CH_3OH, also known as Methanol To Gasoline (MTG) process (Figure 1.4), is performed with another heterogeneous catalyst, the zeolite ZSM-5, used as well as in the xylene isomerization, to boost the production of *p*-xylene, and

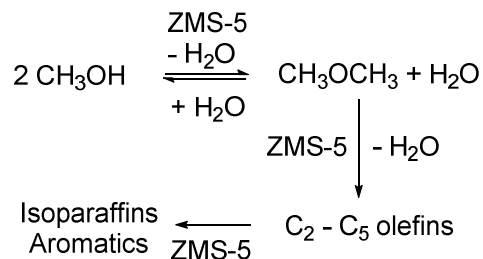in a large amount of other significant industrial processes [4].

$$2\,CH_3OH \; \underset{+\,H_2O}{\overset{\substack{ZMS-5\\-\,H_2O}}{\rightleftharpoons}} \; CH_3OCH_3 + H_2O$$

$$ZMS-5 \;\Big|\; -\,H_2O$$

$$\text{Isoparaffins}\;\underset{ZMS-5}{\longleftarrow}\; C_2 - C_5 \text{ olefins}$$
$$\text{Aromatics}$$

Figure 1.4 ZSM-5 catalyzed Methanol To Gasoline (MTG) process [5].

1.1.3   Biocatalysis

Biocatalysis can be considered as a bridge between homogeneous and heterogeneous catalysis. The biocatalyst is mainly an enzyme, which is an elaborate protein and can catalyze reactions in biological systems, e.g., living cells. Usually, enzymes can finalize 1000 catalytic cycles in one second, being remarkably productive compared to homogeneous or heterogeneous catalysts, which can complete between 100 and 10000 cycles per hour. In addition, the high activity of enzymes is also a consequence of their specificity in the conversion of a certain substrate. Not only does this phenomenon represent a great advantage, but also a drawback, considering the unfeasibility to use a wide range of substrates.

Moreover, biocatalytic reactions are often carried out at mild conditions and in H_2O, because of the enzymes´ vulnerability in harsh reaction conditions.

In spite of the fact that these catalysts are still more expensive than homogeneous and heterogeneous, they are already applied in some industrial processes (Figure 1.5), because of their enormous activity [2].
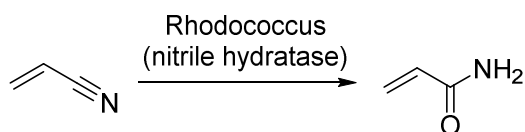
Figure 1.5 Biocatalytic synthesis of acrylamide from acrylonitrile, performed in Japan on a scale of 10000 tons per year [2].

1.1.4 TON and TOF

The catalyst turnover number (TON) and the turnover frequency (TOF) are two significant quantities used for comparing catalysts efficiency. However, their definitions differ minimally among the three catalysis fields.

In homogeneous catalysis, as shown in the Eq. 1.1a, the TON represents the number of cycles that the catalyst can carry out before deactivation, i.e., the number of A molecules that can be converted into B molecules by one molecule of catalyst. The TOF is just TON/time, i.e., the number of A molecules that can be converted into B molecules by one molecule of catalyst in one second, minute, or hour.

In heterogeneous catalysis, TON and TOF are mainly considered per active site of catalyst (Eq. 1.1b), owing to the impossibility to know exactly the amount of catalyst molecules on the surface.

In biocatalysis, as described in Eq. 1.1c, the TON and TOF are defined by the ratio between the rate measured when all the enzyme molecules are bound with a reactant molecule and the total enzyme concentration [2].

$$TON = \frac{N_{cycles}}{mol_{catalyst}} \qquad\qquad a)$$

$$TON = \frac{mol_{product}}{N_{active\ sites}} \qquad\qquad b)$$

$$TON = \frac{\nu_{max}}{[enzyme]} \qquad\qquad c)$$

Equation 1.1 Definition of TON in homogeneous catalysis (a), heterogeneous catalysis (b) and biocatalysis (c) [6-8].

1.2 Platinum Group Metals (PGMs)

Certainly, some of the most relevant catalysts in industrial processes are based on PGMs, i.e., ruthenium, rhodium, palladium, osmium, iridium, and platinum. Indeed, the catalysis performed with these metals has a long story and the PGM-based catalysts variate from complexes, prepared especially using phosphines or other electron-donor ligands, to very small species, e.g., supported cluster or single atoms, to bigger agglomerates, such as nanoparticles or directly bulk material. All the metals of this group are especially active in hydrogenation and dehydrogenation, olefin metathesis, hydroformylation (complexes of Rh) and cross-coupling reactions (Pd and Pt) [9, 10].

1.2.1   Sources of PGMs

As long as we know, one of the first proof of the use of platinum by humans is given by a gold etui covered with hieroglyphic inscriptions, from the 7th century B.C. Nowadays, we have much more information about this useful

and relevant metal. Indeed, platinum is present in its native form with small quantities of iridium, osmium, palladium, ruthenium, and rhodium, which are all components of the same group of metals. Despite knowing the platinum since many centuries, the accompanying metals were discovered only around 1800. Indeed, W. H. Wollaston (1766–1828) discovered palladium (at beginning also called "new silver") and rhodium; S. Tennant (1761–1815) discovered iridium and osmium and C. Claus (1796–1864) discovered ruthenium in 1844.

Today, the main deposits of PGMs are in the Ural Mountains, Columbia, Canada, and South Africa. Workable ore deposits are composed mainly by sperrylite ($PtAs_2$), cooperite (PtS), stibiopalladinite (Pd_3Sb), laurite (RuS_2), ferroplatinum (Fe-Pt), polyxene (Fe-Pt-other platinum metals), osmiridium (Os-Ir), and iridium-platinum (Ir–Pt) [10, 11]. The current prices of these metals are indicated in the Table 1.1 [12]. As it can be seen, the prices of Pd, Ir, Rh and Ru have been continuously increasing during the last five years, while Pt is becoming cheaper.

Table 1.1 Prices of the PGMs, expressed in dollars per troy ounce (1 troy ounce = 31.1 g).

	2015	**2016**	**2017**	**2018**	**2019**
Palladium	694.99	617.39	874.30	1,036.43	1,500.00
Platinum	1,056.09	989.52	951.23	882.66	850.00
Iridium	544.19	586.90	908.35	1,293.27	1,500.00
Rhodium	954.90	696.84	1,112.59	2,225.30	3,300.00
Ruthenium	47.63	42.00	76.86	244.41	270.00

1.2.2 Physicochemical characteristics of PGMs

However, to understand the chemistry of this group, it is important to know their intrinsic properties, such as electronic configurations or atomic sizes. The electronic configurations of platinum group metals start from the inert gas structures of krypton and xenon (Table 1.2).

All of them have two valence orbitals: an *s* and an inner *d* shell. Due to the small energy gap between the valence shells, one or two electrons from the outer 5*s* or 6*s* shells can be taken up by the 4*d* or 5*d* shells in some of these elements, bringing these metals to different oxidation states (Table 1.3).

Table 1.2 Electronic configurations of PGMs.

Ru	[Kr] $4d^7 5s^1$	**Rh**	[Kr] $4d^8 5s^1$	**Pd**	[Kr] $4d^{10}$
Os	[Xe] $4f^{14} 5d^6 6s^2$	**Ir**	[Xe] $4f^{14} 5d^7 6s^2$	**Pt**	[Xe] $4f^{14} 5d^9 6s^1$

Table 1.3 Oxidation states of PGMs, in bold the principal ones.

Ru	-2		0		+2	**+3**	**+4**	+5	+6	+7	+8
Rh		-1	0	+1	+2	**+3**	+4	+5	+6		
Pd			0		+2	+3	+4				
Os	-2		0	+1	+2	+3	**+4**	+5	+6		+8
Ir		-1	0	+1	+2	+3	**+4**	+5	+6		
Pt			0		**+2**		**+4**	+5			

The slight differences in the atomic sizes of the elements of the second and the third row are consequences of the full occupation of the $4f^{14}$ electron orbitals in the "heavy" elements (Os, Ir, and Pt), phenomenon known as

lanthanide contraction. Therefore, these elements show, compared to the "light" platinum group elements (Ru, Rh, and Pd), differences in their catalytic activities, owing to the splitting of p and d orbitals to other energy levels. As a matter of fact, in the case of "heavy" elements it is relevant to cite the relativistic effect, which is common for the platinum. Indeed, for "lighter" elements non-relativistic quantum mechanics give good approximation of the physical properties, due to the very high speed of the few core electrons. In contrast, "heavy" atoms present discrepancies between the theoretical properties and the observed ones when the relativity is not taken into account, because of the high number of electrons [13, 14]. For instance, this phenomenon leads to a high affinity of platinum, bringing to a more stable Pt-Pt bond compared to the Pd-Pd bond [15]. Moreover, relativistic effects are very important during the design of platinum complexes [16].

The platinum group metals have shared characteristics in physical and chemical properties, i.e., high melting point, low vapor pressure, high temperature coefficient of electrical resistivity, and low coefficient of thermal expansion (Table 1.4). Overall, the remarkable physical properties of the platinum group metals are of great relevance for their industrial use.

Indeed, platinum, which is a silvery-white metal in its pure form, presents high malleability, and ductility, all relevant properties for metals. In addition, another significant property of this metal is its resistance to oxidation in air, even at high temperatures, although it can be corroded by halogens, cyanides, sulfur, and alkalis. It cannot be solubilized in hydrochloric and nitric acid, but when these acids are mixed as aqua regia, it forms chloroplatinic acid (H_2PtCl_6), a key compound for the synthesis of many platinum-based

compounds.

Finally, palladium does not oxidize in air, and it has the lowest density and melting point of the platinum group of metals. On the contrary of platinum, it is soft and ductile, when annealed, and it can be attacked by nitric and sulfuric acid.

Table 1.4 Atomic and physical properties of PGMs.

	Ru	**Rh**	**Pd**	**Os**	**Ir**	**Pt**
Atomic number	44	45	46	76	77	78
Relative atomic mass	101.07	102.905	106.42	190.2	192.22	195.08
Naturally occuring isotopes	7	1	6	7	2	6
Melting point (°C)	2310	1966	1554	3045	2410	1772
Boiling point (°C)	3900	3700	2970	5000	4130	3827
Density (g/cm^3)	12.45	12.41	12.02	22.59	22.56	21.45

1.2.3   Applications of Pt and Pd

Platinum has a plethora of uses, e.g., in the assembly of electrical contacts and corrosion-resistant apparatus. It is utilized in jewelry, in dentistry, in the fabrication of wires and vessels for laboratory and industrial use [11, 17]. Platinum is recognized to be an excellent catalyst in many processes. Indeed, the possibility of its adsorption of large volumes of hydrogen leads to its well-known applicability in hydrogenation reactions [18, 19]. Moreover, it is also applied in the cracking of petroleum products [20] and, surely, one of the most notorious uses is its application in antipollution devices for vehicles [21].

Moreover, platinum compounds are also worldly recognized for their anticancer activity, in fact since the '70s platinum has been almost the only source of anticancer drugs [22]. Cisplatin was the first complex of platinum applied in many anticancer therapies and, starting from this, many other platinum-based anticancer drugs have been developed during the last decades, such as oxaliplatin, carboplatin and nedaplatin. Usually, these drugs are platinum complexes, which can enter in the cell using either transporters or by passive diffusion. Once in the cell, an adduct of platinum covalently bonded to purine DNA bases induces the apoptosis of the cancer cells, due to the inhibition of DNA synthesis [23-25].

Concerning palladium applications, it is also used in jewelry trades, in dentistry, watchmaking, and in the creation of surgical instruments and electrical contacts, when alloyed. As platinum, palladium has the incredible property of adsorbing up to 900 times its volume of hydrogen at room temperature, bringing to its high viability in hydrogenation and dehydrogenation reactions [26].

Recently, palladium has substituted the higher priced platinum in catalytic converters because it is more susceptible to be poisoned by sulfur and lead. This has caused a large raise in the price of palladium, whereas, in 2002, the cost of the two metals was about the same [10, 17].

During the last decades, palladium has been one of the most investigated and used metal in many research fields since well-defined palladium-catalyzed cross-coupling reactions were first developed in the 1970s. These processes have transformed the organic chemists' approach towards the formation of new bonds in complex molecules and the extensive effect of this procedure was recognized awarding the Nobel Prize in Chemistry in 2010. The fast

success of palladium-catalyzed cross-coupling is due to wide and well-structured investigations on reaction mechanisms. Mechanistic studies have disclosed that almost all of these processes include catalysis by palladium in the 0 or +2 oxidation states, also known as 'low-valent' palladium. Subsequently, the feasibility of the characterization of Pd^0 and Pd^{2+} catalytic intermediates and the study of steric and electronic influence of supporting ligands has been crucial in the development of new catalysts structures and innovative transformations [27, 28].

1.3   Size matters: from nanoparticles to single atoms

Back in the 1925, after Langmuir developed his theory about the adsorption of species onto simple surfaces, Taylor firmly affirmed that "(catalyst) *activation consists in increasing the amount of the surface atoms which are in a state of unsaturation relative to the main body of the catalyst material*" [29].

Following this statement, in the '70s, the importance of the catalyst size started to be pointed out, considering in particular the number of metal atoms composing the active sites [30]. Indeed, size reduction of metal particles can improve the performance of catalysts in many ways, in particular bringing to a low-coordination environment of the metal centers, due to unsaturated metal atoms more exposed on the small-sized particles, and to quantum size effects, where confinement of electrons leads to a discrete energy level distribution and a distinctive HOMO-LUMO gap (see Figure 1.6) [31, 32].

Since researchers have put effort in downsizing the particles of the catalysts, firstly, they reached a variety of synthesis and applications of nanoparticles (NPs), commonly considered between 1-100 nm [33].

Going forward, metal clusters (MCs) were the next species to generate interest. They are defined as monodispersed particles less than 10 nm in diameter with properties between bulk materials and single atoms [34]. However, which is the most effective way to have all the atoms exposed? Single atoms (SAs) are considered in this view the best active sites because they are totally unsaturated and then completely exposed to the reaction environment [31]. One of the aims of this thesis will be to analyze clusters and single atoms activity in catalysis and in antitumoral treatments.
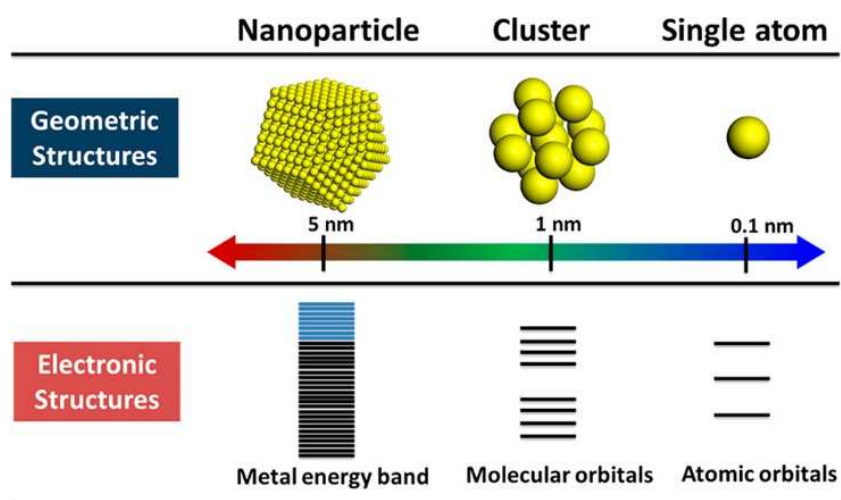

Figure 1.6 Influence of the geometric structures of the particles on the electronic distributions [32].

1.3.1 Metal clusters: synthesis and characterization

Metal clusters (MCs) are isolable metal particles, between 1-10 nm, classically considered to be formed from three up to a dozen or more atoms [35, 36]. The very first example of MC was given in the late 50´s by the case of the Chini complex. Chini was a pioneer in the study of cobalt carbonyl

species, $Co_2(CO)_8$ and $Co_4(CO)_{12}$ (Figure 1.7), as catalysts for the hydroformylation of olefins [37].

By the end of the last century, the breakthrough of new technologies and then new techniques of characterization [38] made possible the efficient development of novel synthesis of *nano*catalysts, among them MCs [39]. Considering their thermodynamically instability, these small metallic entities tend to aggregate, consequently the synthesis and their following storage must avoid this undesired process.
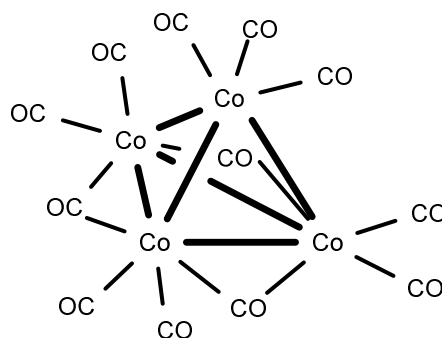

Figure 1.7 Molecular structure of $Co_4(CO)_{12}$ [40].

The synthetic approaches can be divided in two categories: "bottom up" and "top down" methods. Among them, the techniques widely applied until now are "bottom up" methodologies. In this case, metal salts undergo reduction, nucleation and following growth of the desired particles (see Table 1.5).

In the other case, the nanosized metal particles result from the mechanical downsizing of bulk metals or nanoparticles and subsequent stabilization by the addition of protecting agents, as shown in Table 1.6 [36].

Table 1.5 Different "bottom up" routes for the synthesis of MCs [39, 41].

Method	Description	Examples
direct-synthesis method	• synthesis of thiol protected MCs • $NaBH_4$ common reducing agent • polydispersed MCs are obtained	$Au_{25}(SC_6H_{13})_{18}$ [42], $Au_{55}(SC_{18})_{32}$ [43]
size-focusing method	after the direct-synthesis, the solutions of particles are purified to extract the smallest MCs	$Au_{38}(SC_{12}H_{25})_{24}$ [44], $Au_{38}(PET)_{24}$ [45]
photoreduction		Ag@PAMAM [46]
microwave assisted	radiations can form radicals that can help the nucleation and growth of the MCs	Ag@L-SG [47]
radiolytic approach		Ag_3^{2+} [48], Ag_4^{2+} [49]
microemulsion technique	• formation of nanodroplets of water with surfactants and/or amphiphilic block copolymers • nanodroplets used as nanoreactors to obtain MCs with well-defined sizes [50]	Ag_n [50]

Method	Description	Examples
sonochemical synthesis	ultrasounds improve the formation of radicals that are involved in the nucleation and growth of the MCs	Ag@PMAA [51]
electrochemical synthesis	• metal cations are reduced at the cathode • the reduced metal aggregates and is stabilized by the surfactants in solution	Cu@TBAN [52]
template mediated	• surfactant micelles enclose metal ions to form amphiphilic microreactor • examples of templates: thiols, polymers, proteins, DNA, dendrimer [36]	Au_8@PAMAM [53], Pt_2@MOF [54], Pd_5@EVOH [55], Pd_4@MOF [56],
solid state route	• mixture of metal salts, stabilizers and reducing agents in the solid state • the absence of protic solvents removes the uncontrolled growth of the particles [57]	Ag_9 [58], Pt_{11} [59]

Table 1.6 Different "top down" routes for the synthesis of MCs [36].

Method	Description	Examples
alloying	• starting from monometallic NPs • the presence of different metal makes the MCs stable due to the changes in the electronic structure [60]	$Au_{24}Pd(SR)_{18}$ [61], $Au_{24}Pt(SR)_{18}$ [62], $Ag_7Au_6(H_2MSA)_{10}$ [63]
etching	• starting from monometallic NPs • ligand induced, temperature induced, etc.	$Au_{25}(SG)_{18}$ [64], Ag@MSA [65], $Au_7@CeO_2$ [66]
ligand exchange	introduction of functional groups in presynthesized MCs to improve their stability and reactivity [67]	$Au_{11}(SR)_{11-18}$ [68]

Moreover, the structural information is very important to know the applications of these particles. The characterization of these species is then a very important tool, which has been helped by the recent growing of wide-ranging advanced techniques.

1. Ultraviolet-Visible (UV-Vis) absorption spectroscopy makes possible to know the electronic structure of the MCs and their optical properties. Indeed, MCs have discrete electronic levels, as molecules

and not as NPs or bulk metals, and from the UV-Vis peak wavelengths the electronic energy gaps are known [39].

2. <u>Fluorescence emission spectroscopy,</u> combined with the previous technique, gives a mean to understand the electronic structure of the MCs and their optical properties. From the emission wavelength, and using the jellium model, is possible to know the approximate number of atoms present in the MCs [69].

3. <u>EXAFS</u> (Extended X-ray Absorption Fine Structure) is an X-ray based technique, which gives information about the electronic transitions from core levels. In this way, distances between atoms and coordination numbers can be calculated, in order to understand the chemical environment of the atoms composing the clusters [70].

4. <u>XANES</u> (X-ray Absorption Near Edge Structure) is another X-ray based technique, which gives knowledge about the oxidation states of the atoms in the MCs and about their geometries [39].

5. <u>Mass spectrometry</u> is a reliable way to have information about the mass and the composition of the MCs. The best ionization method appears to be electrospray ionization (ESI), which avoids the extensive fragmentation into low-mass ions, that is typical of other approaches [71].

6. <u>ICP analysis</u> (Inductively Coupled Plasma) is a technique that can analyze the concentration of metals. It has to be followed by a spectrometer, e.g., atomic emission or mass spectrometry, to recognize the metals from the emission bands or from the m/z value [72].

7. <u>Microimaging</u> provides not only atomic-resolution lattice images but also, in some cases, chemical information at a spatial resolution of <1 nm, allowing direct identification of a single particle. It includes TEM (Transmission Electron Microscopy), HRTEM (High Resolution TEM, including aberration-corrected instrumentation), STEM (Scanning TEM) or AFM (Atomic Force Microscopy) [72-74].

1.3.2   Metal clusters: catalytic applications

Considering the optical and structural properties of MCs, it appears obvious that these species have a plethora of applications. Firstly, they are widely known to be used in chemical sensors because of their optical properties. Moreover, they have been used in other areas of interest, e.g., biomedicine, biological labeling, electronics, and catalysis [75].

From a catalytic point of view, MCs are interesting because of the high number of exposed unsaturated metal centers, inclined to being involved in the reaction. Besides, the metal atoms in the MC can cooperate during the catalysis. Notice that we consider here ligand-free MCs, since MCs stabilized by ligands are poorly effective in catalysis due to the fatal destabilization exerted by reactant coordination and subsequent ligand displacement.

One of the first noteworthy examples of catalysis performed with MCs is the CO oxidation reaction. Au MCs between 8 and 20 atoms were demonstrated to be active in this process [76]. Furthermore, a study on Pt MCs confirmed the importance of the catalyst size. Indeed, Figure 1.8 shows that the reactivity has a non-linear relation with the number of atoms composing the MCs, i.e., the reaction is highly catalyzed by specific metal aggregates composed by 8 up to 15 atoms [77]. The processes mentioned above were of

inspiration for the following studies regarding CO oxidation. Actually, the work of Hutchings can be seen as an additional example, where Au MCs supported on FeO_x, were demonstrated to be highly active in the same reaction [78].
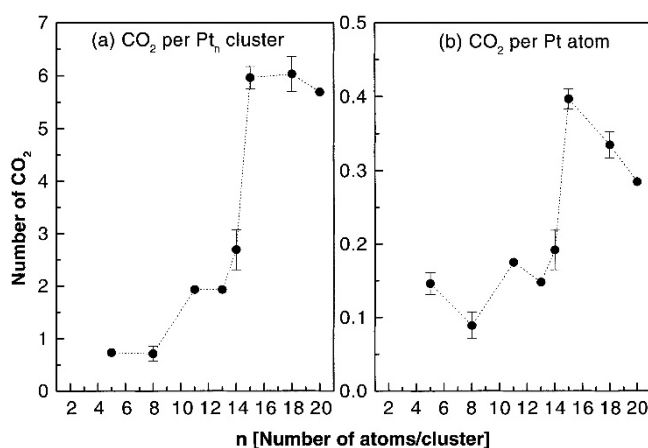

Figure 1.8 CO oxidation catalyzed by Pt MCs [77].

Further relevant examples of the catalytical applicability of MCs are oxidation, hydrogenation, dehydrogenation, and photocatalytic and electrocatalytic reactions.

A good exemplification is the very desired oxidation of CH_4 to CH_3OH catalyzed by Cu/ZMS-5. Here, mechanistic studies, performed with various zeolites, point out to Cu_2 as active species in the methanol conversion [79].

The hydrogenation reaction is another industrial key process, which has also been explored with the use of MCs, such as Pt_{13} in ethylene hydrogenation. Figure 1.9 shows MCs TPR (Temperature-programmed Reduction) spectra compared with one measured for Pt(111) surface. The desorption temperature for the MCs is $\sim 100\,K$ below the temperature measured for the extended

Pt(111) surface, indicating activation energies for MCs significantly lower than the ones obtained for the reaction catalyzed by Pt(111) [80].
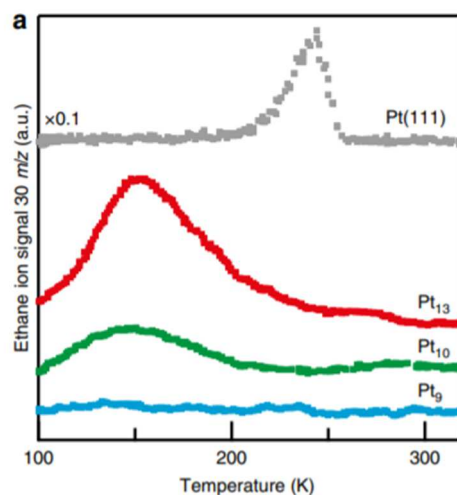

Figure 1.9 TPR spectra of ethylene hydrogenation on different Pt clusters and on Pt(111) [80].

Another interesting process catalyzed by MCs is the dehydrogenation reaction. For instance, the reaction of production of propene starting from propane has been catalyzed by Pt MCs due to their high affinity with small molecules such as propane, as demonstrated by DFT (Density-functional Theory) calculations shown in Figure 1.10 [81].
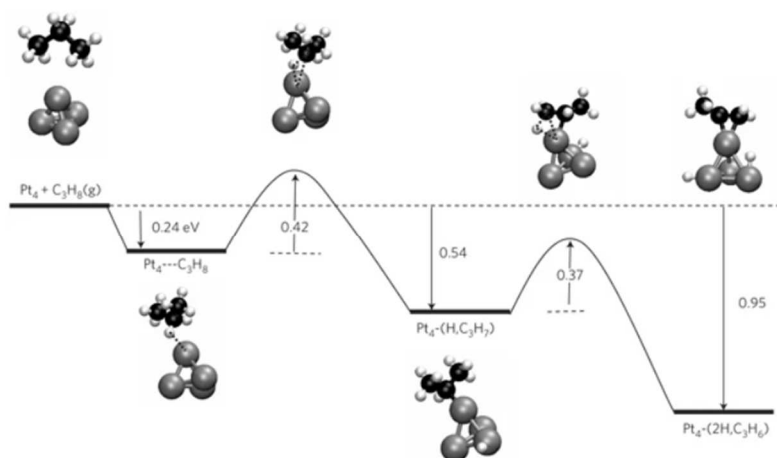
Figure 1.10 Energy barriers calculated by DFT calculations for the π (a) and σ (b) bonded ethylene on Pt_{10}/MgO, in presence of dissociated H_2 [81].

The reactions reported up to now make quite clear that MCs have a wide range of applicability and, probably for this reason, we are moving to study species even smaller, i.e., single atoms. Indeed, as demonstrated until now, the size matters.

1.3.3 Single atoms: synthesis and characterization

Going forward in time, during the 90's, it was not common yet to speak about Single Atoms Catalysts (SACs). Considering the techniques available in those times, the detection of these species would have been rather difficult. "Single-site heterogeneous catalysts" was the more frequent definition, where the isolated active sites (single-site in this case) consisted in one or more atoms [82]. Only in the 2000´s, a single atom of palladium, supported on MgO, was finally identified, and firmly declared to be catalytically active in the trimerization reaction of acetylene to benzene [83].

As in the case of MCs, it is particularly crucial to avoid further agglomeration of SACs to bigger agglomerates, such as NPs and MCs, thus the synthetic approaches have as main object to keep these tiny entities well isolated and stable. Tables 1.7 and 1.8 describe some of the synthetic methodologies, which variate and range from impregnation to other ingenious techniques, such as ionic-liquid assisted or ball-milling methods [84]. As it occurs for MCs, "bottom up" and "top down" synthetic approaches have been developed.

Table 1.7 Synthetic "bottom up" procedures for the preparation of SACs [84].

Method	Description	Examples
impregnation and coprecipitation	• control of the metal loading • importance of suitable supports	Pt_1/FeO_X [85]
spatial confinement	• in zeolites, MOFs, or COFs • the porosity and the functional groups stabilize SAs by confining them	Pt_1/Y zeolite [86] Pt_1^{1+}/NiMOF [87]
coordination site construction	• by polymers, MOFs, modified carbon-based materials • functional groups stabilize single atoms by coordination	Ir_1/amino pyridine polymer [88] Fe/graphene [89]

Method	Description	Examples
defect design	• on oxides or hydroxides, on graphene • anchoring of metals atoms onto surface vacancies	Pt_1/CeO_2 [90] Cu_1/graphene [91]
photochemical reduction	• adsorption of photons and formation of excited electronic states	Pd_1/TiO_2 [92]
atomic layer deposition	• importance of suitable supports • M-O bonds with the support	Pt_1/C [93]
freezing-assisted	• to avoid agglomeration by diffusion • usually cooperates with one of the methods mentioned above	Pt_1/C [94]
microwave-assisted	• time-saving approach • few secondary reactions	Co_1/graphene [95]
ionic-liquid-assisted	• electrostatic interactions stabilize the SAs	Pt_1 in [bmim][BF_4] [96]

Table 1.8 Synthetic "top down" approaches for the preparation of SACs [84].

Method	Description	Examples
downsizing NPs	• breaking metal-metal bonds by mechanical or electrochemical methods, such as etching or alloying	Pt_1/SiO_2 [97]
downsizing bulk metal	• creating new bonds between the single atom and a proper support	Cu_1/C [98]

1.3.4   Single atoms: catalytic applications

Over the last ten years, the meaning of single-atom catalysis began to be more popular and less extravagant. For instance, Figure 1.11 illustrates the catalytic oxidation reaction of CO to CO_2 in presence of Pt_1/FeO_x, being one of the first published reactions to be explicitly catalyzed by SACs. A short explanation of the mechanism of this reaction was given by DFT calculations and confirmed that the adsorption of the CO molecule over one platinum atom has a binding energy (1.27 eV in step iii) much lower than platinum MCs, clarifying the catalytic findings [85].

Subsequently and up to now, single atoms catalysis experienced a significant growth and the applications of these small species moved towards quite interesting reactions.
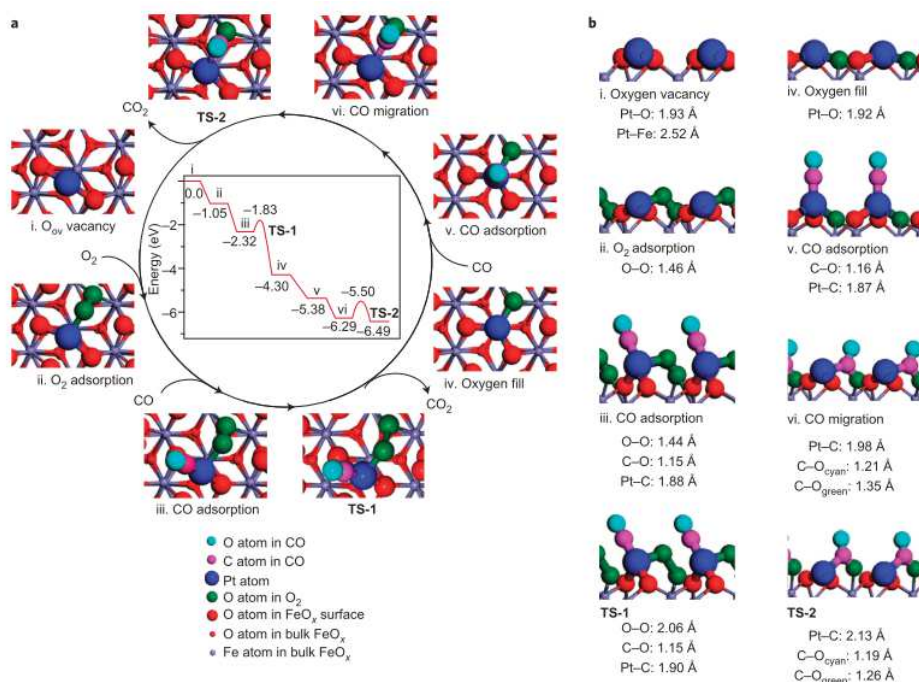
Figure 1.11 Mechanism proposed for CO oxidation reaction on Pt_1/FeO_x. Top view (a) and side view (b) [85].

Most of the uses of SACs are dedicated to the activation of carbon-free small molecules such as O_2, H_2 or H_2O, frequently in electrochemical and photochemical processes. For instance, two of the more explored reactions have been the CO oxidation and the Water Gas-shift Reaction (WGSR). Indeed, Au_1/FeO_X was demonstrated to be active in the CO oxidation reaction. Figure 1.12 shows the increase of CO conversion with the decrease of the Au loading on the catalyst [99]. In addition, Figure 1.9 shows the results obtained with Pt_1/FeO_X compared with the commercial Au/FeO_X: the TOF increases with the decrease of Pt loading [85].
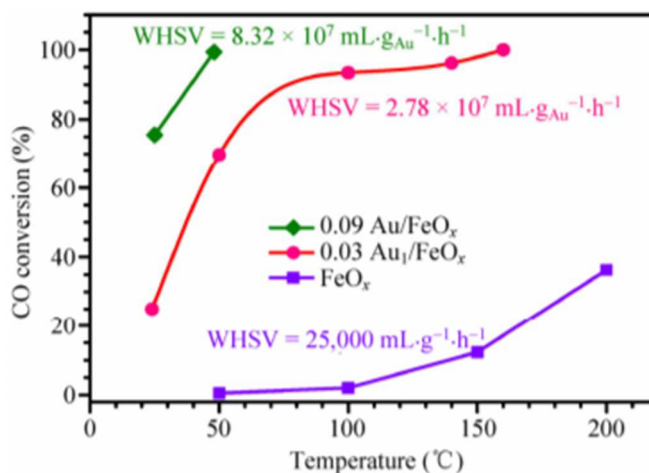
Figure 1.12 CO conversion during the CO oxidation with different Au/FeO$_x$ catalysts [99].

Table 1.9 TOF of the CO oxidation with the catalyst Pt$_1$/FeO$_X$ [85].

Entry	Catalyst	Metal loading (wt%)	Specific rate × 10² (mol$_{CO}$·h^{-1}·g$_{metal}$$^{-1}$)	TOF × 10² (s^{-1})
1	Pt$_1$/FeO$_x$	0.17	43.5	13.6
2		2.5	17.7	8.01
3	Au/Fe$_2$O$_3$ (commercial)	4.4	21.7	4.76

Figure 1.13 (top) shows the results of DFT calculations on Pt$_1$/TiO$_2$ for the WGSR, where the activity of SAs is higher than NPs at low temperature, due to their chemical environment. Indeed, one molecule of CO, one atom of H and the support act as ligands for the Pt single atom, making the second molecule of CO more reactive and more willing to react with O$_2$ [100]. As

shown in Figure 1.13 (bottom), the different activation energies (E_a) in presence of Pt NPs and Pt SAs can highlight the significance of isolated and low-coordinated metallic species. Actually, E_a raises with the platinum loading on FeO_x, providing the lowest value for the more diluted sample, which is principally constituted by isolated SACs, as confirmed by HAADF-STEM measurements [101].
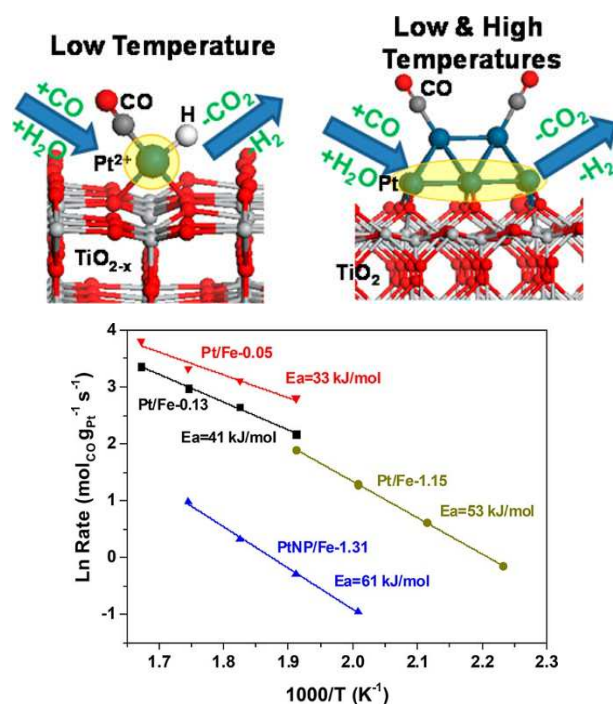

Figure 1.13 DFT calculations with SACs and NPs of Pt/TiO_2 for the WGSR (top) [100] and experimental activation energies for the WGSR in presence of Pt/FeO_X at different metal loadings (bottom) [101].

In 2007, Pd SACs supported on mesoporous alumina were claimed to be active in the selective oxidation of allylic alcohols. As shown in Figure 1.14,

the smaller the Pd species, the higher the TOF value, up to reaching the maximum with Pd SAs, preserving high selectivity too [102].
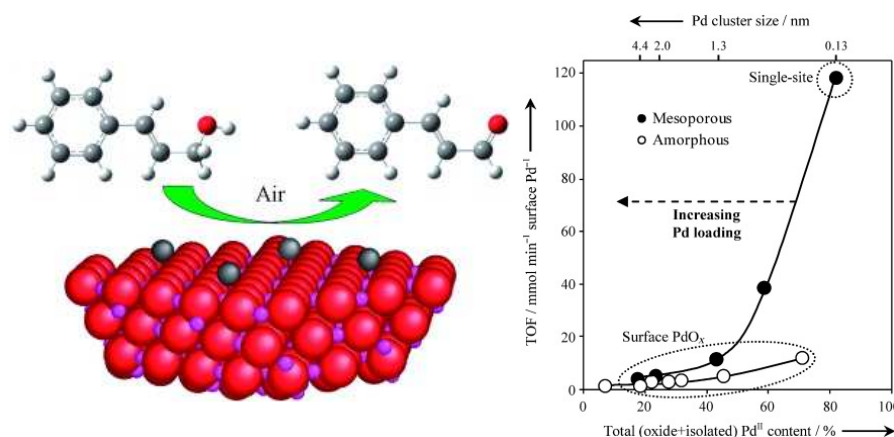

Figure 1.14 Pd/Al$_2$O$_3$ activity, expressed in TOF, in the oxidation of crotyl alcohol [102].

Moreover, another relevant example is the hydrogenation reaction. In this case, an example is given by Ni and Ru SACs supported on carbon nanotubes and TiO$_2$. These catalysts expressed high activity in the CO$_2$ hydrogenation reaction, with high selectivity for CO and CH$_4$, for Ni and Ru, respectively [103].

During the last few years, the catalysis of SAs has seen a rather big development and it has explored many reactions, such as dehydrogenation, hydroformylation, photocatalysis, electrocatalysis and even cross-coupling reactions [32]. However, there is still a lot to discover and probably it would be relevant to look at well-known important NPs applications with a new perspective: single atoms.

1.4 Supramolecular Coordination Complexes (SCCs)

During the last decades, the coordination chemistry has gone forward, almost at the same speed of downsizing the size of the catalytic site. In the following *Chapters*, especially in *Chapter 4*, the application of self-assembled SCCs to catalysis will be highlighted but, first of all, it is interesting to move throughout the history of these complexes of high complexity, which were discovered just by a fortunate coincidence in 1988 [104].

Indeed, the coordination chemistry has its roots in nature, which is the master in the design of self-assembled constructs, e.g., the formation of the cell membrane [105]. Mimicking the nature, the principles of self-assembly were initially applied for the synthesis of simply helicates [106, 107] (Figure 1.15), molecular grids [108, 109] and metallamacrocyclic complexes [110], reaching more intricate structures like cages [111, 112] (Figure 1.16) or catenates [113, 114].

All the constructs mentioned above are generated by a self-assembly procedure where labile metal ions are mixed with polydentate organic ligands, resulting in the formation of non-covalent bonds. Certainly, the self-assembly process leads to a plethora of combinations that somehow are not predictable, but up to now we have been unconscious witnesses of an enormous amount of these complex structures where the exchange of metal or ligands brings to different geometries with different applications [111, 115, 116].
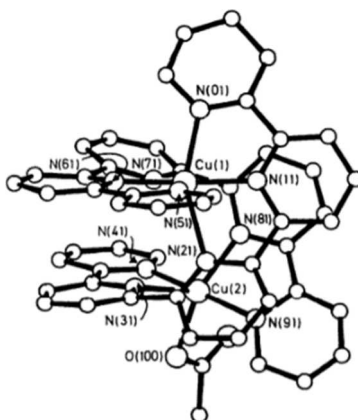
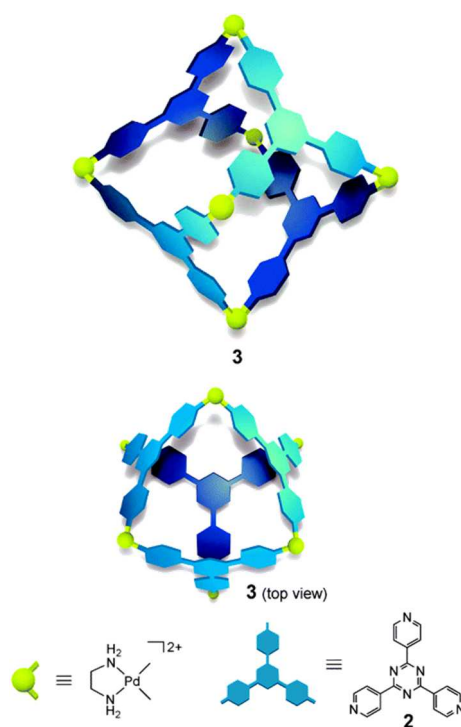**Figure 1.15** Example of helicate based on copper and quinquepyridine ligands.

Figure 1.16 Example of cage based on palladium and a tridentate triangular ligand to form an M_6L_4 geometry [112].

1.4.1 Synthesis of SCCs

The synthetic approach to prepare these species involves a self-assembly procedure, but the most important is the previous design. Indeed, in order to obtain a specific geometry or symmetry, it is extremely relevant to choose the appropriate pivotal metals and the ligands, which will be the linkers between them. Certainly, the coordination geometry of the metal chosen will define the final structure, while the polydentate ligands will offer different geometries depending on the number of anchoring groups that they dispose and on the stoichiometry respect to the metal [117]. The use of a bidentate ligand will result in planar geometries, e.g., metallamacrocyclic complexes [110, 117], whereas the use of polydentate ligands will bring to 3D geometries, such as cages [111, 112]. Depending upon the types of ligands, these constructs can be synthesized following different strategies: edge- or face-directed self-assembly, symmetry interaction, weak link and dimetallic building block. As shown in Figure 1.17a, the edge- directed self-assembly is characterized by the use of linkers or nodes (metal centers) which will lie on the edges of the final geometry and the angles of the precursors will define the angles of the structure. This is the more classical procedure to generate less complex geometries, such as two-dimensional or M_4L_6 tetrahedral or M_8L_8 cubic [118-120]. On the other hand, the face-directed self-assembly approach (Figure 1.17b) is accomplished using ligands which occupy the faces of the final structure, leading to more complex three-dimensional symmetries and/or geometries, e.g., truncated tetrahedron or cuboctahedron [121-123]. The symmetry interaction approach makes possible the preparation of high symmetry coordination cluster, shown in Figure 1.18, where the chosen ligands belong to specific symmetry groups in order to

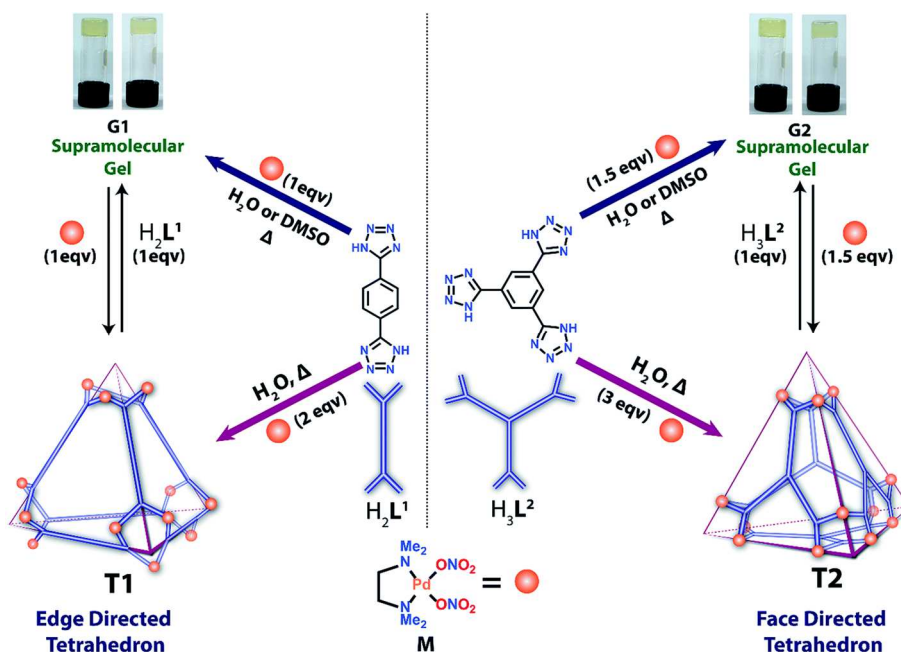obtain SCCs with precise symmetries [124, 125].

Figure 1.17 Edge- (a) and face-directed (b) self-assembly strategy for the synthesis of 3D coordination assemblies [120].
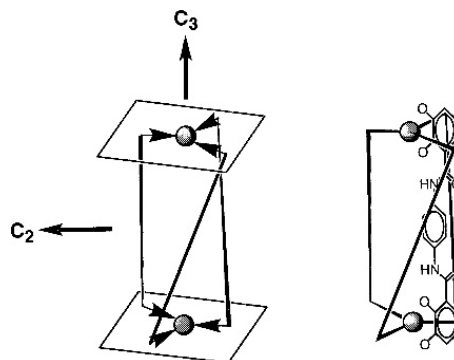

Figure 1.18 Example of high symmetry coordination cluster correlated with his symmetry axes and planes [124].

The synthetic approaches described up to now are driven by thermodynamic principles, whereas the weak link and dimetallic building block methodology are led by the kinetics of the complex formation. The weak link method involves the use of hemilabile ligands, which have strong and weak coordination groups. This feature of the ligands makes possible the interchange between different geometries of the complex, e.g., adding small ions or molecules or influencing the kinetic of formation [126]. Finally, the bimetallic building block approach implies the use of bimetallic entities as pivotal metallic centers, instead of metal ions, leading to paddlewheel-like structures where a plethora of metals can be used and where the structure is kept more stable by the formation of neutral geometries [127].

Certainly, in the synthesis of these species, both 2- and 3-D, the conditions are particularly crucial. The choice of the solvent, the pH, the stoichiometric ratio between ligands and metal precursor and the metal source itself and its counter anion will determine the final symmetry and geometry [115].

The SCCs are fully recognized by a complete characterization, including NMR and IR spectroscopy, elemental analysis, X-ray crystallography and mass spectrometry [128-130].

1.4.2   Applications of SCCs

One of the main characteristics of these complexes is the presence of a cavity which made these species perfect candidates for host-guest chemistry. Indeed, this element opens the door for a wide number of applications, such as chemical transportation [131-134], molecular recognition [135-137], or guest stabilization [138-140], which can find an interesting use in biomedical systems [141].

In this thesis we will focus more on a less explored application of SCCs: catalysis. The cavity plays a key role also in this case, due to its similarity with the active site of enzymes [142]. Indeed, these complexes show specificity to bind specific substrates, as in the case of enzymes, and this characteristic makes SCCs quite interesting in catalytic processes, where the complex acts as a catalyst but as well as a reaction vessel [143]. Naturally, SCCs can have different sites where the catalysis can be performed: the cavity or active species encapsulated in the structure [144]. One of the most studied reaction is the Diels-Alder [145-147], where the catalytic and host-guest properties of the SCCs are perfectly combined. Undeniably, as shown in Figure 1.19, the lack of catalytic activity of the metal precursor of the complex demonstrated the relevance of the hydrophobic pocket, which made possible the preorganization of the reagents [144, 147]. The cavity can also have the role of stabilizing the intermediate [144], such as in the aza-Cope reaction [148-150], the Kemp elimination [151], the Knoevenagel condensation [152], hydrolysis [153, 154], cyclization [155-157], cascade reactions [158, 159], and photocatalytic processes [160, 161].

As mentioned above, the catalyst can be incorporated within the structure of the complex and is usually held inside by the presence of quite sophisticated ligands present on the structure of the SCCs by covalent or non-covalent bonds. In this particular case, the cavity only acts as a reaction vessel, resulting in high regio- and stereo-selectivity of the products [143]. Certainly, the catalyst alone shows a lower activity from the catalyst embedded in the cage and one of the first examples was given by the hydroformylation of 1-octene performed by a rhodium catalyst within a metalloporphyrin-based box [162] and by the olefin epoxidation catalyzed by the same family of catalysts

[163]. These new compounds cleared the way for the encapsulation of transition metal catalysts in proper cages. This is the case of iridium or rhodium complexes in Ga_4L_6 assemblies for the C-H activation of aldehydes [164] and for allylic alcohol isomerization, respectively [165]. Moreover, the encapsulation of a gold complex within a resorcin[4]arene hexameric entities favored the hydration of 4-phenylbutyne [166] and the hydroalkoxylation of an allene when the gold complex was inserted in a Ga_4L_6 assembly [167], as shown in Figure 1.20.
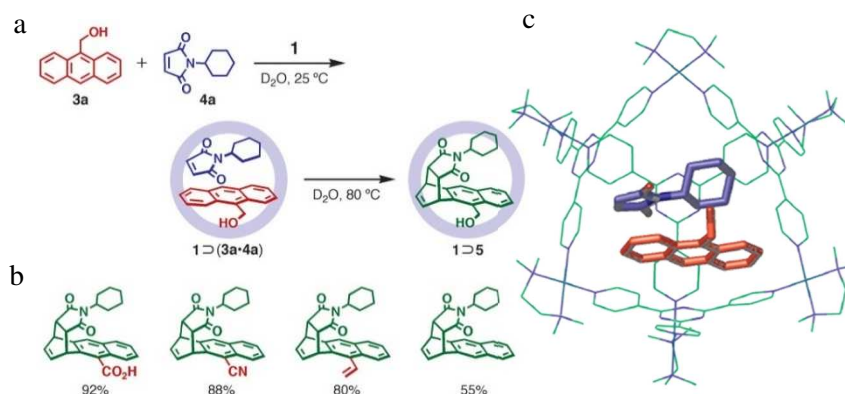

Figure 1.19 Example of Diels-Alder reaction (a) and the syn-1,4-regioselective products (b) obtained within the cavity of a cage (c) [147].
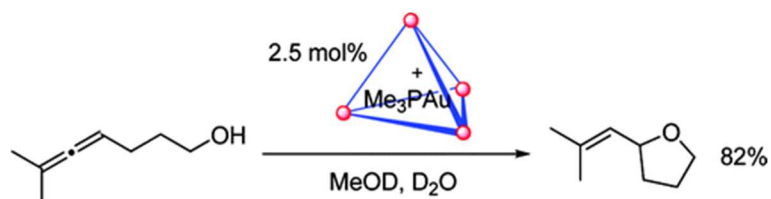

Figure 1.20 Hydroalkoxylation reaction performed by a gold complex within a Ga_4L_6 assembly [167].

1.5 Metal-Organic Frameworks (MOFs)

Over the past few decades, together with the SCCs mentioned above, the chemistry of coordination developed a large class of coordination polymers, which are crystalline materials with top stability and tunable characteristics, such as organic functionalities, and porosity [168].

Typically, in these materials metal ions are connected by organic linkers (Figure 1.21), resulting in porous polymeric structures, known as Metal-organic Frameworks (MOFs), opposite to supramolecular coordination complexes which are discrete entities [169]. The synthesis of MOFs can be defined as the process of directing rigid molecular building blocks into well-ordered networks, held by strong bonds. A relevant feature of this synthesis is that the building blocks are kept unaltered during the construction, from the point of view of the structural integrity and rigidity.

It is difficult to predict which structures are going to be synthesized simply knowing the metal ions and the linkers, due to the lack of directionality of the ions and then flexibility around them. Consequently, a multiplicity of structures is possible and there is quite a broad deficit of control [170]. In order to know the topology of the materials before the synthesis, a good approach can be the prediction of the Secondary Building Unit (SBU). The latter represents a cluster of the metal ions and the organic linkers and, indeed, MOFs can be considered the extension of these unities in the space (Figure 1.22) [171].
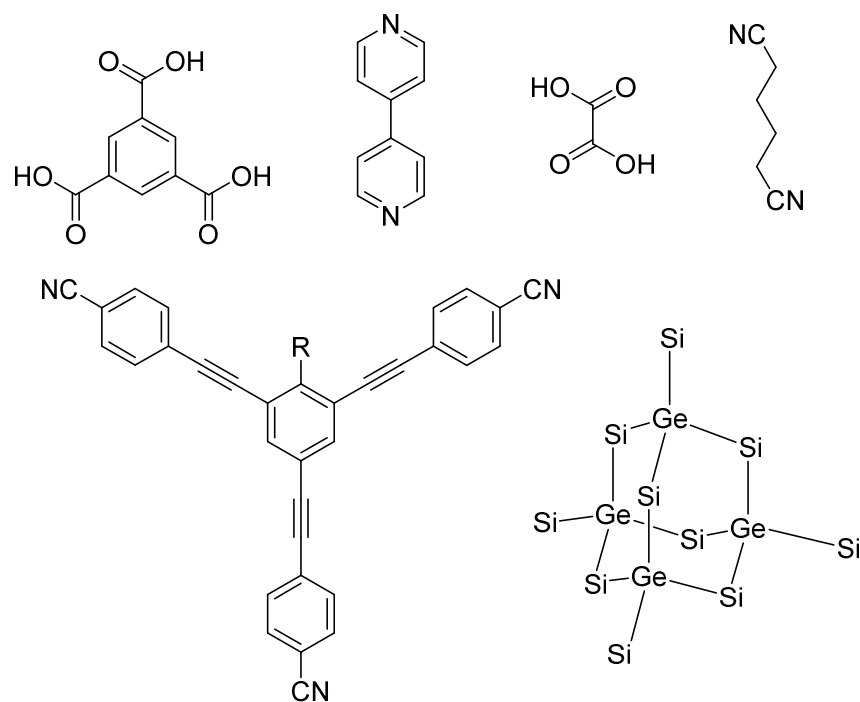
Figure 1.21 Examples of organic linkers implied in the synthesis of MOFs.
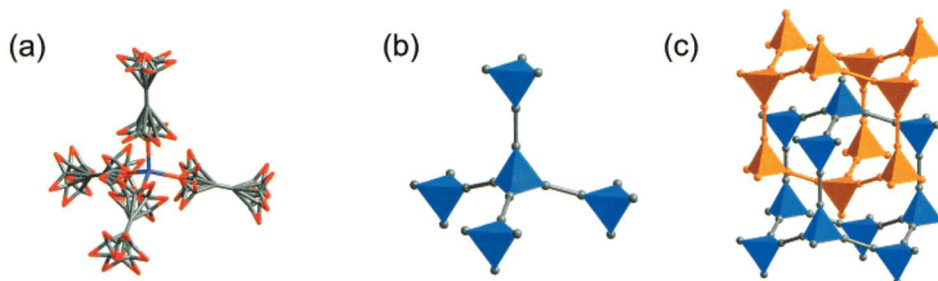

Figure 1.22 MOF-31 showing tetrahedral zinc (blue) centers with disordered carboxylates with acetylene links (a), tetrahedral secondary building unities (SBUs) formed by carboxylate carbon atoms (gray spheres) connected by acetylene bonds (gray rods) (b) to produce two interpenetrating diamond frameworks (c) [171].

1.5.1   Synthesis of MOFs

Not only is the information of possible SBUs helpful in guiding the synthesis efforts, but also the knowledge of typical metal coordination environments or the preparation conditions of conventional inorganic building blocks are extremely crucial. Therefore, one of the main goals is to perform the synthesis circumventing any structural change of the organic linkers. At the same time, the synthesis ought to be carried out keeping in mind the kinetics of crystallization, that have to allow nucleation and growth of the desired phase. There are various synthetic approaches, due to the genesis of MOFs from different fields, including coordination chemistry and zeolites chemistry.

In conventional synthesis, the temperature is the main factor and two temperature ranges, solvothermal and non-solvothermal, make a distinction between two different reaction configurations. The first one refers to conditions where the temperature is above the boiling point of the solvent, making the synthesis to occur under autogenous pressure. On the other side, the non-solvothermal synthesis is performed at temperatures below the boiling point of the solvent, including room-temperature procedures. Common solvents are alcohols, dialkyl formamides and pyridine [168, 172].

During the last few years, high-throughput methods have been developed in order to enhance the efficiency of solvothermal synthesis. This innovative automated technique implies four major steps: design of experiment, synthesis, characterization, and data evaluation which are combined in a workflow to achieve a maximum of productivity and innovation [173].

At the same time, other techniques have been developed and applied in the design of MOFs, e.g., microwave-assisted synthesis, electrochemical synthesis, mechanochemical synthesis and sonochemical synthesis.

The solid nature of MOFs makes them perfect candidate for powder and single crystal X-ray crystallography, solid NMR and IR spectroscopies, which allow to characterize their structure, merged with the use of other characterization techniques useful to know their composition, such as elemental analysis or ICP-MS and ICP-AES [169, 174].

1.5.2 Applications of MOFs

Since the origin, MOFs have shown a plethora of applications. The first use studied was the gas storage/separation, followed by nonlinear optics, ferroelectricity, conductivity/semiconductivity, magnetism, luminescence, chemical sensing, biomedical imaging, drug delivery, solar energy harvesting and finally catalysis [175]. In this *Thesis* we will focus mainly on their application in catalysis.

Taking advantage of their high porosity, MOFs can be used as supports for homogeneous catalysts, size selective catalysts, agents to encapsulate catalysts within their pores, or catalysts by themselves [176]. These materials have three different components where the catalysis can occur: the metal, the organic linker, and the space within the pores [177].

Two examples of catalysis performed by the metal are the cyclization of citronellal and the isomerization of α-pinene oxide using the building block $[Cu_3(btc)_2]$, that behaves as Lewis acid [178]. Then the same MOF was proved to be active in the cyclopropanation of alkenes with diazoacetates [179]. Other cases where the metal centers act as active sites are the application of MIL-101 in the addition of trimethylsilylcyanide to benzaldehyde, as shown in Figure 1.23, and Pd@MIL-101 in the hydrogenation of styrene [180]. Moreover, the oxidation of CO to CO_2 was

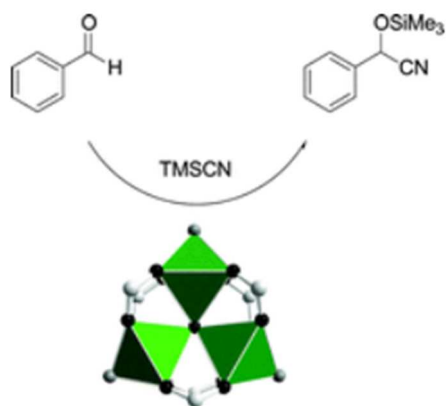performed using a MOF based on alkali metals [181].

Figure 1.23 Addition of trimethylsilylcyanide to benzaldehyde catalyzed by MIL-101 [180].

Speaking about the activity directly related to the organic linkers, we should consider that the structure must have at least one free functional group on the organic linkers, willing to take part in the catalysis. Indeed, it was confirmed that secondary chiral dihydroxy groups, inserted in a Cd-based MOF, allowed the addition of diethylzinc to aromatic aldehydes to afford chiral secondary alcohols, as illustrated in Figure 1.24 [182]. As well as, the combination of a symmetrical urea tetracarboxylate linker and $Zn(NO_3)_2 \cdot 6H_2O$ provided a new microporous MOF (NU-601), effective hydrogen-bond-donor catalyst for Friedel-Crafts reactions between pyrroles and nitroalkenes [183].

In the third case, an active specie is encapsulated into the pores of the MOF, which plays the role of support in this occasion. Figure 1.25 shows the catalytic activity toward the oxidation of cyclohexane of metal-porphyrin encapsulated in rho-ZMOF [184].
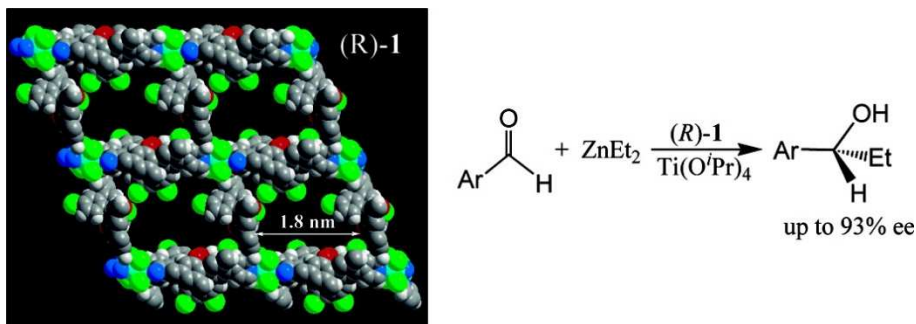
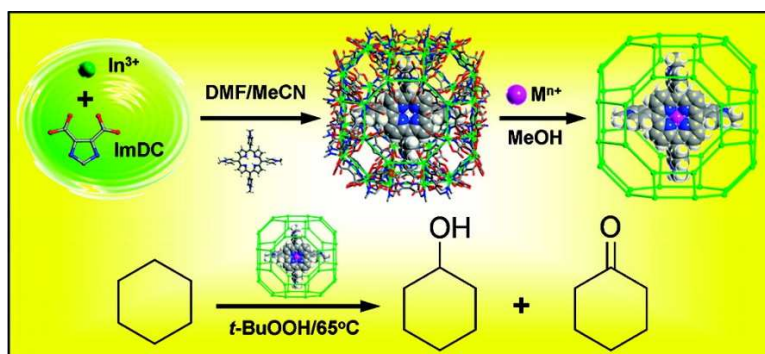**Figure 1.24** Synthesis of chiral secondary alcohols, using a Cd-based MOF [182].

Figure 1.25 Scheme of the synthesis of metal-porphyrin within rho-ZMOF and the following oxidation reaction of cyclohexane [184].

1.5.2.1 MOFs as supports in catalysis

As mentioned above, taking into account the well-defined and isolated sites for the anchoring of catalytic species, another important feature of the MOFs is the possibility to work as support for entities that therefore would undergo sintering or would not be characterizable. At first, MOFs were applied as support of NPs [185], having the first example in Pd NPs@MOF-5 [186], but in these pages we will focus more on their use as support for MCs and SAs

[57, 187].

In 2009, the support of Au MCs on ZIF-8 made these species very active in the CO oxidation, avoiding the undesired agglomeration of the MCs [188]. Later, Au-Pd MCs with size between 8-11 nm were successfully immobilized in MIL-101, using a wet impregnation method, and showed high activity towards the reaction of dehydrogenation of formic acid [189]. Certainly, these works were followed by an increasing number of similar materials, e.g., Pt MCs@UiO-66-NH$_2$ for cinnamaldehyde hydrogenation [190], the ethylene hydrogenation in presence of Pt MCs@NU-1000 [191], or the Pd$_4$@Cu-based MOF (Figure 1.26) active in carbene-transfer reactions [57].
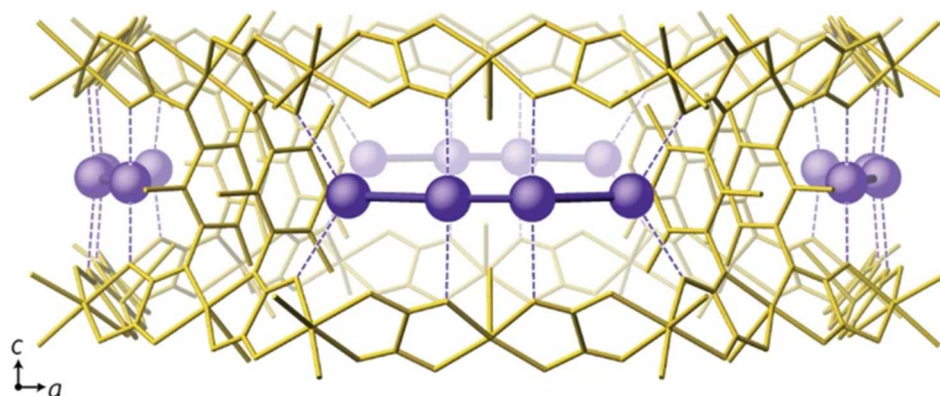

Figure 1.26 View along the *b* crystallographic axis of the crystal structure of Pd$_4$@Cu-based MOF. The gold sticks represent the MOF structure, meanwhile Pd atoms are the purple spheres [57].

Moving towards smaller species, it is necessary to underline the relevance of MOFs as support for SAs. Indeed, the use of a support is of vital importance for the existence of SAs which otherwise would not exist, except in special conditions. For instance, Ni SAs were isolated on NU-1000 and showed high

resistance towards agglomeration and, furthermore, high activity in the hydrogenation of ethylene [192], also quite selective when catalyzed by Fe^{III}/Fe^{III}_2 supported on a Cu-based MOF [193]. Moreover, the isolation of Mg atoms on a Zr-MOF was a noteworthy case where the segregation could make the catalyst more stable and active in reactions which would not have been catalyze by the bulk catalyst [194]. The catalyst Cu_1@UiO-66 was tested in the CO oxidation showing very high activity with 100% of conversion of CO [195]. Another work to mention is the case of SA-based vanadium oxide supported on Hf-MOF-808 and Zr-NU-1000, which showed high activity towards the oxidation of benzyl alcohols [196], as well as when catalyzed by Pd_1@Cu-based MOF [197]. Moreover, Pt_1^{1+} and Pt_2^0 supported on MOFs could catalyze industrial relevant processes, i.e., the water gas shift reaction and the synthesis of HCN, respectively [54, 87].

As a matter of fact, the improvement of characterization techniques has helped and still helps with the development of these extraordinary catalysts, which represent probably the future for a better use of our primary resources.

1.6 References

1. Smith, J. K., History of catalysis, in *Encyclopedia of catalysis*, Horváth, I., Editor. **2010**, John Wiley & Sons, Inc.

2. Rothenberg, G., *Catalysis: concepts and green applications*, Rothenberg, G., Editor. **2008** Wiley-VCH Verlag GmbH & Co. KGaA.

3. Bhaduri., S.; Mukesh., D., Chemical industry and homogeneous catalysis, in *Homogeneous catalysis,* Bhaduri., S.; Mukesh., D., Editors. **2000**, John Wiley & Sons, Inc.

4. Thomas, J. M.; Thomas, W. J., Heterogeneous catalysis: Examples, case histories and current trends, in *Principles and practice of heterogeneous catalysis*, Thomas, J. M.; Thomas, W. J., Editors. **2015**, Wiley-VCH Verlag GmbH & Co. KGaA.

5. Olsbye, U.; Svelle, S.; Lillerud, K. P.; Wei, Z. H.; Chen, Y. Y.; Li, J. F.; Wang, J. G.; Fan, W. B., The formation and degradation of active species during methanol conversion over protonated zeotype catalysts. *Chem. Soc. Rev.* **2015**, *44* (20), 7155-7176.

6. Thomas, J. M.; Thomas, W. J., Setting the scene, in *Principles and practice of heterogeneous catalysis*, Thomas, J. M.; Thomas, W. J., Editors. **2015**, Wiley-VCH Verlag GmbH & Co. KGaA.

7. Roskoski, R., Michaelis-Menten kinetics, in *Reference module in biomedical sciences*. **2015**, Elsevier.

8. Kozuch, S.; Martin, J. M. L., "Turning over" definitions in catalytic cycles. *ACS Catal.* **2012**, *2* (12), 2787-2794.

9. Kettler, P. B., Platinum group metals in catalysis: Fabrication of catalysts and catalyst precursors. *Org. Process Res. Dev.* **2003**, *7* (3), 342-354.

10. Renner, H.; Schlamp, G.; Kleinwächter, I.; Drost, E.; Lüschow, H. M.;

Tews, P.; Panster, P.; Diehl, M.; Lang, J.; Kreuzer, T.; Knödler, A.; Starz, K. A.; Dermann, K.; Rothaut, J.; Drieselmann, R.; Peter, C.; Schiele, R.; Coombes, J.; Hosford, M.; Lupton, D. F., Platinum group metals and compounds, in *Ullmann's encyclopedia of industrial chemistry.* **2018**, Wiley-VCH Verlag GmbH & Co. KGaA.

11. Greenwood, N. N.; Earnshaw, A., Nickel, palladium and platinum, in *Chemistry of the elements*, Greenwood, N. N.; Earnshaw, A., Editors. **1984**, Butterworth-Heinemann.

12. Survey, U. S. G., Mineral commodity survey. **2020**.

13. Pyykkö, P., Relativistic effects in chemistry: More common than you thought. *Annu. Rev. Phys. Chem.* **2012**, *63* (1), 45-64.

14. Swirles, B.; Hartree, D. R., The relativistic self-consistent field. *Proc. R. Soc. A* **1935**, *152* (877), 625-649.

15. Jansen, M., Effects of relativistic motion of electrons on the chemistry of gold and platinum. *Solid State Sci.* **2005**, *7* (12), 1464-1474.

16. Creutzberg, J.; Hedegård, E. D., Investigating the influence of relativistic effects on absorption spectra for platinum complexes with light-activated activity against cancer cells. *Phys. Chem. Chem. Phys.* **2020**, *22* (46), 27013-27023.

17. Hammond, C. R., The Elements, in *Handbook of chemistry and physics*, Lide, D. R., Editor. **2004**, CRC Press.

18. Bratlie, K. M.; Lee, H.; Komvopoulos, K.; Yang, P.; Somorjai, G. A., Platinum nanoparticle shape effects on benzene hydrogenation selectivity. *Nano Lett.* **2007**, *7* (10), 3097-3101.

19. Zhao, M.; Crooks, R. M., Homogeneous hydrogenation catalysis with monodisperse, dendrimer-encapsulated Pd and Pt nanoparticles. *Angew.*

Chem. Int. Ed. **1999**, *38* (3), 364-366.

20. Yoo, J. S.; Jaecker, J. A., Catalyst for conversion of hydrocarbons. *U.S. 484,085* **1984**.

21. Wiseman, C. L. S.; Zereini, F., Airborne particulate matter, platinum group elements and human health: A review of recent evidence. *Sci. Total Environ.* **2009**, *407* (8), 2493-2500.

22. Rosenberg, B., Platinum complexes for the treatment of cancer. *Interdiscipl. Sci. Rev.* **1978**, *3* (2), 134-147.

23. Kelland, L., The resurgence of platinum-based cancer chemotherapy. *Nat. Rev. Cancer* **2007**, *7* (8), 573-584.

24. Ghosh, S., Cisplatin: The first metal based anticancer drug. *Bioorg. Chem.* **2019**, *88*, 102925.

25. Desoize, B.; Madoulet, C., Particular aspects of platinum compounds used at present in cancer treatment. *Crit. Rev. Oncol. Hematol.* **2002**, *42* (3), 317-325.

26. Teschner, D.; Revay, Z.; Borsodi, J.; Haevecker, M.; Knop-Gericke, A.; Schloegl, R.; Milroy, D.; Jackson, S. D.; Torres, D.; Sautet, P., Understanding palladium hydrogenation catalysts: When the nature of the reactive molecule controls the nature of the catalyst active phase. *Angew. Chem. Int. Ed.* **2008**, *47* (48), 9274-9278.

27. Hickman, A.; Sanford, M., High-valent organometallic copper and palladium in catalysis. *Nature* **2012**, *484*, 177–185.

28. Johansson Seechurn, C. C. C.; Kitching, M. O.; Colacot, T. J.; Snieckus, V., Palladium-catalyzed cross-coupling: A historical contextual perspective to the 2010 Nobel Prize. *Angew. Chem. Int. Ed.* **2012**, *51*, 5062-5085.

29. Taylor, H. S., A theory of the catalytic surface. *Proc. R. Soc. A* **1925**, *108* (745), 105-111.

30. Ozin, G. A., Metal atom matrix chemistry. Correlation of bonding with chemisorbed molecules. *Acc. Chem. Res.* **1977**, *10* (1), 21-26.

31. Yang, X. F.; Wang, A.; Qiao, B.; Li, J.; Liu, J.; Zhang, T., Single-atom catalysts: A new frontier in heterogeneous catalysis. *Acc. Chem. Res.* **2013**, *46* (8), 1740-1748.

32. Liu, L.; Corma, A., Metal catalysts for heterogeneous catalysis: From single atoms to nanoclusters and nanoparticles. *Chem. Rev.* **2018**, *118* (10), 4981–5079.

33. Burda, C.; Chen, X.; Narayanan, R.; El-Sayed, M. A., Chemistry and properties of nanocrystals of different shapes. *Chem. Rev.* **2005**, *105* (4), 1025–1102.

34. Aiken, J. D.; Finke, R. G., A review of modern transition-metal nanoclusters: Their synthesis, characterization, and applications in catalysis. *J. Mol. Catal. A Chem.* **1999**, *145* (1-2), 1-44.

35. Schmid, G., General features of metal nanoparticles physics and chemistry, in *Metal nanoclusters in catalysis and material science: the issue of size control*, Corain, B., Schmid, G., Toshima, N., Editors. **2008**, Elsevier.

36. Bönnemann, H.; Nagabhushana, K. S., Metal nanoclusters: Synthesis and strategies for their size control, in *Metal nanoclusters in catalysis and material science: the issue of size control*, Corain, B.; Schmid, G.; Toshima, N., Editors. **2008**, Elsevier.

37. Ercoli, R.; Chini, P.; Massi-Mauri, M., Sintesi del tetracobalto dodecacarbonile, per riduzione del cobalto cationico con idrogeno e

dicobalto ottacarbonile. *Chim. Ind.* **1959**, *41*, 132-135.

38. Li, X.; Yang, X.; Zhang, J.; Huang, Y.; Liu, B., In situ/operando techniques for characterization of single-atom catalysts. *ACS Catal.* **2019**, *9* (3), 2521–2531.

39. Du, Y.; Sheng, H.; Astruc, D.; Zhu, M., Atomically precise noble metal nanoclusters as efficient catalysts: A bridge between structure and properties. *Chem. Rev.* **2020**, *120* (2), 526–622.

40. Chini, P., The closed metal carbonyl clusters. *Inorg. Chim. Acta Rev.* **1968**, *2*, 31-51.

41. Chakraborty, I.; Pradeep, T., Atomically precise clusters of noble metals: Emerging link between atoms and nanoparticles. *Chem. Rev.* **2017**, *117* (12), 8208–8271.

42. Tsunoyama, R.; Tsunoyama, H.; Pannopard, P.; Limtrakul, J.; Tsukuda, T., MALDI mass analysis of 11 kDa gold clusters protected by octadecanethiolate ligands. *J. Phys. Chem. C* **2010**, *114* (38), 16004-16009.

43. Devadas, M. S.; Kwak, K.; Park, J.-W.; Choi, J.-H.; Jun, C.-H.; Sinn, E.; Ramakrishna, G.; Lee, D., Directional electron transfer in chromophore-labeled quantum-sized Au_{25} clusters: Au_{25} as an electron donor. *J. Phys. Chem. Lett.* **2010**, *1* (9), 1497-1503.

44. Gaur, S.; Miller, J. T.; Stellwagen, D.; Sanampudi, A.; Kumar, C. S. S. R.; Spivey, J. J., Synthesis, characterization, and testing of supported Au catalysts prepared from atomically-tailored $Au_{38}(SC_{12}H_{25})_{24}$ clusters. *Phys. Chem. Chem. Phys.* **2012**, *14* (5), 1627-1634.

45. Qian, H.; Eckenhoff, W. T.; Zhu, Y.; Pintauer, T.; Jin, R., Total structure determination of thiolate-protected Au_{38} nanoparticles. *J. Am. Chem. Soc.*

2010, *132* (24), 8280-8281.

46. Zheng, J.; Dickson, R. M., Individual water-soluble dendrimer-encapsulated silver nanodot fluorescence. *J. Am. Chem. Soc.* **2002**, *124* (47), 13982-13983.

47. Liu, T.; Su, Y.; Song, H.; Lv, Y., Microwave-assisted green synthesis of ultrasmall fluorescent water-soluble silver nanoclusters and its application in chiral recognition of amino acids. *Analyst* **2013**, *138* (21), 6558-6564.

48. Ershov, B. G.; Henglein, A., Reduction of Ag^+ on polyacrylate chains in aqueous solution. *J. Phys. Chem. B* **1998**, *102* (52), 10663-10666.

49. Linnert, T.; Mulvaney, P.; Henglein, A.; Weller, H., Long-lived nonmetallic silver clusters in aqueous solution: Preparation and photolysis. *J. Am. Chem. Soc.* **1990**, *112* (12), 4657-4664.

50. Ledo-Suárez, A.; Rivas, J.; Rodríguez-Abreu, C. F.; Rodríguez, M. J.; Pastor, E.; A., H. C.; Oseroff, S. B.; López-Quintela, M. A., Facile synthesis of stable subnanosized silver clusters in microemulsions. *Angew. Chem. Int. Ed.* **2007**, 46, 8823-8827.

51. Xu, H.; Suslick, K. S., Sonochemical synthesis of highly fluorescent Ag nanoclusters. *ACS Nano* **2010**, *4* (6), 3209-3214.

52. Vilar-Vidal, N.; Blanco, M. C.; López-Quintela, M. A.; Rivas, J.; Serra, C., Electrochemical synthesis of very stable photoluminescent copper clusters. *J. Phys. Chem. C* **2010**, *114* (38), 15924-15930.

53. Oliver-Meseguer, J.; Cabrero-Antonino, J. R.; Domínguez, I.; Leyva-Pérez, A.; Corma, A., Small gold clusters formed in solution give reaction turnover numbers of 10^7 at room temperature. *Science* **2012**, *338* (6113), 1452-1455.

54. Mon, M.; Rivero-Crespo, M. A.; Ferrando-Soria, J.; Vidal-Moya, A.; Boronat, M.; Leyva-Pérez, A.; Corma, A.; Hernández-Garrido, J. C.; López-Haro, M.; Calvino, J. J.; Ragazzon, G.; Credi, A.; Armentano, D.; Pardo, E., Synthesis of densely packaged, ultrasmall Pt^0_2 clusters within a thioether-functionalized MOF: Catalytic activity in industrial reactions at low temperature. *Angew. Chem. Int. Ed.* **2018**, *57* (21), 6186-6191.

56. Fernández, E.; Rivero-Crespo, M. A.; Domínguez, I.; Rubio-Marqués, P.; Oliver-Meseguer, J.; Liu, L.; Cabrero-Antonino, M.; Gavara, R.; Hernández-Garrido, J. C.; Boronat, M.; Leyva-Pérez, A.; Corma, A., Base-controlled Heck, Suzuki, and Sonogashira reactions catalyzed by ligand-free platinum or palladium single atom and sub-nanometer clusters. *J. Am. Chem. Soc.* **2019**, *141* (5), 1928-1940.

57. Fortea-Pérez, F. R.; Mon, M.; Ferrando-Soria, J.; Boronat, M.; Leyva-Pérez, A.; Corma, A.; Herrera, J. M.; Osadchii, D.; Gascon, J.; Armentano, D.; Pardo, E., The MOF-driven synthesis of supported palladium clusters with catalytic activity for carbene-mediated chemistry. *Nat. Mater.* **2017**, *16*, 760-766.

58. Rao, T. U. B.; Nataraju, B.; Pradeep, T., Ag_9 quantum cluster through a solid-state route. *J. Am. Chem. Soc.* **2012**, *132* (46), 16304-16307.

59. Chakraborty, I.; Govindarajan, A.; Erusappan, J.; Ghosh, A.; Pradeep, T.; Yoon, B.; Whetten, R. L.; Landman, U., The superstable 25 kDa monolayer protected silver nanoparticle: Measurements and interpretation as an icosahedral $Ag_{152}(SCH_2CH_2Ph)_{60}$ cluster. *Nano Lett.* **2012**, *12* (11), 5861-5866.

60. Chakraborty, I.; Bhuin, R. G.; Bhat, S.; Pradeep, T., Blue emitting undecaplatinum clusters. *Nanoscale* **2014**, *6* (15), 8561-8564.

61. Hossain, S.; Niihori, Y.; Nair, L. V.; Kumar, B.; W., K.; Negishi, Y., Alloy clusters: Precise synthesis and mixing effects. *Acc. Chem. Res.* **2018**, *51* (12), 3114–3124.

62. Negishi, Y.; Kurashige, W.; Niihori, Y.; Iwasa, T.; Nobusada, K., Isolation, structure, and stability of a dodecanethiolate-protected Pd_1Au_{24} cluster. *Phys. Chem. Chem. Phys*. **2010**, *12* (23), 6219-6225.

63. Qian, H.; Jiang, D. E.; Li, G.; Gayathri, C.; Das, A.; Gil, R. R.; Jin, R., Monoplatinum doping of gold nanoclusters and catalytic application. *J. Am. Chem. Soc.* **2012**, *134* (39), 16159-62.

64. Udayabhaskararao, T.; Sun, Y.; Goswami, N.; Pal, S. K.; Balasubramanian, K.; Pradeep, T., Ag_7Au_6: A 13-atom alloy quantum cluster. *Angew. Chem. Int. Ed.* **2012**, *51* (9), 2155-2159.

65. Shichibu, Y.; Negishi, Y.; Tsunoyama, H.; Kanehara, M.; Teranishi, T.; Tsukuda, T., Extremely high stability of glutathionate-protected Au_{25} clusters against core etching. *Small* **2007**, *3* (5), 835-9.

66. Dhanalakshmi, L.; Udayabhaskararao, T.; Pradeep, T., Conversion of double layer charge-stabilized Ag@citrate colloids to thiol passivated luminescent quantum clusters. *Chem. Commun.* **2012**, *48* (6), 859-61.

67. Oliver-Meseguer, J.; Dominguez, I.; Gavara, R.; Doménech-Carbó, A.; González-Calbet, J. M.; Leyva-Pérez, A.; Corma, A., The wet synthesis and quantification of ligand-free sub-nanometric Au clusters in solid matrices. *Chem. Commun.* **2017**, *53* (6), 1116-1119.

68. Woehrle, G. H.; Hutchison, J. E., Thiol-functionalized undecagold clusters by ligand exchange: Synthesis, mechanism, and properties. *Inorg. Chem.* **2005**, *44* (18), 6149-6158.

69. Niihori, Y.; Matsuzaki, M.; Pradeep, T.; Negishi, Y., Separation of precise

compositions of noble metal clusters protected with mixed ligands. *J. Am. Chem. Soc.* **2013**, *135* (13), 4946-4949.

70. Zheng, J.; Nicovich, P. R.; Dickson, R. M., Highly fluorescent noble-metal quantum dots. *Annu. Rev. Phys. Chem.* **2007**, *58*, 409-431.

71. Toshima, N.; Harada, M.; Yonezawa, T.; Kushihashi, K.; Asakura, K., Structural analysis of polymer-protected Pd/Pt bimetallic clusters as disperse catalysts by using extended X-ray absorption fine structure spectroscopy. *J. Phys. Chem.* **1991**, *95* (19), 7448–7453.

72. Negishi, Y.; Takasugi, Y.; Sato, S.; Yao, H.; Kimura, K.; Tsukuda, T., Magic-numbered Au_n clusters protected by glutathione monolayers (n = 18, 21, 25, 28, 32, 39): Isolation and spectroscopic characterization. *J. Am. Chem. Soc.* **2004**, *126* (21), 6518–6519.

73. Toshima, N.; Yan, H.; Shiraishi, Y., Recent progress in bimetallic nanoparticles: their preparation, structures and functions, in *Metal nanoclusters in catalysis and material science: the issue of size control*, Corain, B., Schmid, G., Toshima, N., Editors. **2008**, Elsevier.

74. Wilcoxon, J. P.; Provencio, P. P., Heterogeneous growth of metal clusters from solutions of seed nanoparticles. *J. Am. Chem. Soc.* **2004**, *126* (20), 6402–6408.

75. Lu, Y.; Chen, W., Sub-nanometre sized metal clusters: From synthetic challenges to the unique property discoveries. *Chem. Soc. Rev.* **2012**, *41*, 3594-3623

76. Sanchez, A.; Abbet, S.; Heiz, U.; Schneider, W.-D.; Häkkinen, H.; Barnett, R. N.; Landman, U., When gold is not noble: Nanoscale gold catalysts. *J. Phys. Chem. A* **1999**, *103* (48), 9573–9578.

77. Heiz, U.; Sanchez, A.; Abbet, S.; Schneider, W.-D., Catalytic oxidation

of carbon monoxide on monodispersed platinum clusters: Each atom counts. *J. Am. Chem. Soc.* **1999**, *121* (13), 3214–3217.

78. Herzing, A. A.; Kiely, C. J.; Carley, A. F.; Landon, P.; Hutchings, G. J., Identification of active gold nanoclusters on iron oxide supports for co oxidation. *Science* **2008**, *321* (5894), 1331–1335.

79. Tomkins, P.; Ranocchiari, M.; van Bokhoven, J. A., Direct conversion of methane to methanol under mild conditions over Cu-zeolites and beyond. *Acc. Chem. Res.* **2017**, *50* (2), 418–425.

80. Crampton, A. S.; Rötzer, M. D.; Ridge, C. J.; Schweinberger, F. F.; Heiz, U.; Yoon, B.; Landman, U., Structure sensitivity in the nonscalable regime explored via catalysed ethylene hydrogenation on supported platinum nanoclusters. *Nat. Commun.* **2016**, *7*, 10389.

81. Vajda, S.; Pellin, M. J.; Greeley, J. P.; Marshall, C. L.; Curtiss, L. A.; Ballentine, G. A.; Elam, J. W.; Catillon-Mucherie, S.; Redfern, P. C.; Mehmood, F.; Zapol, P., Subnanometre platinum clusters as highly active and selective catalysts for the oxidative dehydrogenation of propane. *Nat. Mater.* **2009**, *8*, 213-216.

82. Thomas, J. M.; Raja, R.; Lewis, D. W., Single-site heterogeneous catalysts. *Angew. Chem. Int. Ed.* **2005**, *44* (40), 6456-6482.

83. Abbet, S.; Sanchez, A.; Heiz, U.; Schneider, W.-D.; Ferrari, A. M.; Pacchioni, G.; Rösch, N., Acetylene cyclotrimerization on supported size-selected Pd_n clusters ($1 \leq n \leq 30$): One atom is enough! *J. Am. Chem. Soc.* **2000**, *122* (14), 3453–3457.

84. Ji, S.; Chen, Y.; Wang, X.; Zhang, Z.; Wang, D.; Li, Y., Chemical synthesis of single atomic site catalysts. *Chem. Rev.* **2020**, *120* (21), 11900-11955.

85. Qiao, B.; Wang, A.; Yang, X.; Allard, L. F.; Jiang, Z.; Cui, Y.; Liu, J.; Li, J.; Zhang, T., Single-atom catalysis of CO oxidation using Pt_1/FeO_x. *Nat. Chem.* **2011**, *3* (8), 634-641.

86. Liu, Y.; Li, Z.; Yu, Q.; Chen, Y.; Chai, Z.; Zhao, G.; Liu, S.; Cheong, W.-C.; Pan, Y.; Zhang, Q.; Gu, L.; Zheng, L.; Lu, Y.; Wang, D.; Chen, C.; Peng, Q.; Liu, L.; Chen, J.; Li, Y., A general strategy for fabricating isolated single metal atomic site catalysts in Y zeolite. *J. Am. Chem. Soc.* **2019**, *141* (23), 9305–9311.

87. Rivero-Crespo, M. A.; Mon, M.; Ferrando-Soria, J.; Lopes, C. W.; Boronat, M.; Leyva-Pérez, A.; Corma, A.; Hernández-Garrido, J. C.; López-Haro, M.; Calvino, J. J.; Ramos-Fernandez, E. V.; Armentano, D.; Pardo, E., Confined Pt_1^{1+} water clusters in a MOF catalyze the low-temperature water-gas shift reaction with both CO_2 oxygen atoms coming from water. *Angew. Chem. Int. Ed.* **2018**, *57* (52), 17094-17099.

88. Shao, X.; Yang, X.; Xu, J.; Liu, S.; Miao, S.; Liu, X.; Su, X.; Duan, H.; Huang, Y.; Zhang, T., Iridium single-atom catalyst performing a quasi-homogeneous hydrogenation transformation of CO_2 to formate. *Chem* **2019**, *5* (3), 693-705.

89. Fei, H.; Dong, J.; Feng, Y.; Allen, C. S.; Wan, C.; Volosskiy, B.; Li, M.; Zhao, Z.; Wang, Y.; Sun, H.; Chen, W.; Guo, Z.; Lee, C.; Chen, D.; Shakir, I.; Liu, M.; Hu, T.; Li, Y.; Kirkland, A. I.; Duan, X.; Huang, Y., General synthesis and definitive structural identification of MN_4C_4 single-atom catalysts with tunable electrocatalytic activities. *Nat. Catal.* **2018**, *1*, 63-72.

90. Dvořák, F.; Farnesi Camellone, M.; Tovt, A.; Tran, N.-D.; Negreiros, F. R.; Vorokhta, M.; Skála, T.; Matolínová, I.; Mysliveček, J.; Matolín, V.;

Fabris, S., Creating single-atom Pt-ceria catalysts by surface step decoration. *Nat. Commun.* **2016**, *7*, 10801.

91. Huang, F.; Deng, Y.; Chen, Y.; Cai, X.; Peng, M.; Jia, Z.; Xie, J.; Xiao, D.; Wen, X.; Wang, N.; Jiang, Z.; Liu, H.; Ma, D., Anchoring Cu_1 species over nanodiamond-graphene for semi-hydrogenation of acetylene. *Nat. Commun.* **2019**, *10*, 4431.

92. Ge, X.; Zhou, P.; Zhang, Q.; Xia, Z.; Chen, S.; Gao, P.; Zhang, Z.; Gu, L.; Guo, S., Palladium single atoms on TiO_2 as a photocatalytic sensing platform for analyzing the organophosphorus pesticide chlorpyrifos. *Angew. Chem. Int. Ed.* **2019**, *132* (1), 238-242.

93. Cheng, N.; Stambula, S.; Wang, D.; Banis, M. N.; Liu, J.; Riese, A.; Xiao, B.; Li, R.; Sham, Y.-K.; Liu, L.-M.; Botton, G. A.; Sun, X., Platinum single-atom and cluster catalysis of the hydrogen evolution reaction. *Nat. Commun.* **2016**, *7*, 13638.

94. Wei, H.; Huang, K.; Wang, D.; Zhang, R.; Ge, B.; Ma, J.; Wen, B.; Zhang, S.; Li, Q.; Lei, M.; Zhang, C.; Irawan, J.; Liu, L.-M.; Wu, H., Iced photochemical reduction to synthesize atomically dispersed metals by suppressing nanocrystal growth. *Nat. Commun.* **2017**, *8*, 1490.

95. Fei, H.; Dong, J.; Wan, C.; Zhao, Z.; Xu, X.; Lin, Z.; Wang, Y.; Liu, H.; Zang, K.; Luo, J.; Zhao, S.; Hu, W.; Yan, W.; Shakir, I.; Huang, Y.; Duan, X., Microwave-assisted rapid synthesis. *Adv. Mater.* **2018**, *30*, 1802146.

96. Ding, S.; Guo, Y.; Hülsey, M. J.; Zhang, B.; Asakura, H.; Liu, L.; Han, Y.; Gao, M.; Hasegawa, J.-Y.; Qiao, B.; Zhang, T.; Yan, N., Electrostatic stabilization of single-atom catalysts by ionic liquids. *Chem* **2019**, *5* (12), 3207-3219.

97. Moliner, M.; Gabay, J. E.; Kliewer, C. E.; Carr, R. T.; Guzman, J.; Casty,

G. L.; Serna, P.; Corma, A., Reversible transformation of Pt nanoparticles into single atoms inside high-silica chabazite zeolite. *J. Am. Chem. Soc.* **2016**, *138* (48), 15743-15750.

98. Qu, Y.; Li, Z.; Chen, W.; Lin, Y.; Yuan, T.; Yang, Z.; Zhao, C.; Wang, J.; Zhao, C.; Wang, X.; Zhou, F.; Zhuang, Z.; Wu, Y.; Li, Y., Direct transformation of bulk copper into copper single sites via emitting and trapping of atoms. *Nat. Catal.* **2018**, *1*, 781-786.

99. Qiao, B.; Liang, J.-X.; Wang, A.; Xu, C.-Q.; Li, J.; Zhang, T.; Liu, J. J., Ultrastable single-atom gold catalysts with strong covalent metal-support interaction (CMSI). *Nano Res.* **2015**, *8*, 2913-2924.

100. Ammal, S. C.; Heyden, A., Water-gas shift activity of atomically dispersed cationic platinum versus metallic platinum clusters on titania supports. *ACS Catal.* **2017**, *7* (1), 301-309.

101. Chen, Y.; Lin, J.; Li, L.; Qiao, B.; Liu, J.; Su, Y.; Wang, X., Identifying size effects of Pt as single atoms and nanoparticles supported on FeO_x for the water-gas shift reaction. *ACS Catal.* **2018**, *8* (2), 859-868.

102. Hackett, S. F. J.; Brydson, R. M.; Gass, M. H.; Harvey, I.; Newman, A. D.; Wilson, K.; Lee, A. F., High-activity, single-site mesoporous Pd/Al_2O_3 catalysts for selective aerobic oxidation of allylic alcohols. *Angew. Chem. Int. Ed.* **2007**, *46* (45), 8593-8596.

103. Rivera-Cárcamo, C.; Scarfiello, C.; García, A. B.; Tison, Y.; Martinez, H.; Baaziz, W.; Ersen, O.; Le Berre, C.; Serp, P., Stabilization of metal single atoms on carbon and TiO_2 supports for CO_2 hydrogenation: The importance of regulating charge transfer. *Adv. Mater. Interfaces* **2020**, 2001777.

104. Saalfrank, R. W.; Stark, A.; Peters, K.; von Schnering, H. G., The first

"adamantoid" alkaline earth metal chelate complex: Synthesis, structure, and reactivity. *Angew. Chem. Int. Ed.* **1988**, *27* (6), 851-853.

105. Cooper, J. A., Self-assembly of actin filaments, in *Self-assembling architecture*, Varner, J. E., Editor. **1988**, Wiley-Liss.

106. Lehn, J. M.; Rigault, A.; Siegel, J.; Harrowfield, J.; Chevrier, B.; Moras, D., Spontaneous assembly of double-stranded helicates from oligobipyridine ligands and copper(I) cations: Structure of an inorganic double helix. *Proc. Natl. Acad. Sci. U.S.A.* **1987**, *84* (9), 2565-2569.

107. Barley, M.; Constable, E. C.; Corr, S. A.; McQueen, R. C. S.; Nutkins, J. C.; Ward, M. D.; Drew, M. G. B., Molecular helicity in inorganic complexes: Double helical binuclear complexes of $2,2' : 6',2'' : 6'',2''' : 6''',2''''$-quinquepyridine (L): Crystal structures of $[Cu_2L_2(O_2CMe)][PF_6]_3 \cdot H_2O$ and $[Cu_2L_2][PF_6]_3 \cdot 2MeCN$. *J. Chem. Soc. Dalton Trans.* **1988**, *10*, 2655-2662.

108. Baxter, P. N. W.; Lehn, J.-M.; Fischer, J.; Youinou, M.-T., Self-assembly and structure of a 3×3 inorganic grid from nine silver ions and six ligand components. *Angew. Chem. Int. Ed.* **1994**, *33* (22), 2284-2287.

109. Youinou, M.-T.; Rahmouni, N.; Fischer, J.; Osborn, J. A., Self-assembly of a Cu_4 complex with coplanar copper(I) ions: synthesis, structure, and electrochemical properties. *Angew. Chem. Int. Ed.* **1992**, *31* (6), 733-735.

110. Fujita, M.; Yazaki, J.; Ogura, K., Preparation of a macrocyclic polynuclear complex, $[(en)Pd(4,4'-bpy)]_4(NO_3)_8$ (en = ethylenediamine, bpy = bipyridine), which recognizes an organic molecule in aqueous media. *J. Am. Chem. Soc.* **1990**, *112* (14), 5645-5647.

111. Seidel, S. R.; Stang, P. J., High-symmetry coordination cages via self-assembly. *Acc. Chem. Res.* **2002**, *35* (11), 972-983.

112. Fujita, M.; Tominaga, M.; Hori, A.; Therrien, B., Coordination assemblies from a Pd(II)-cornered square complex. *Acc. Chem. Res.* **2005**, *38* (4), 369-378.

113. Sauvage, J.-P., Transition metal-containing rotaxanes and catenanes in motion: toward molecular machines and motors. *Acc. Chem. Res.* **1998**, *31* (10), 611-619.

114. Fuller, A.-M. L.; Leigh, D. A.; Lusby, P. J.; Slawin, A. M. Z.; Walker, D. B., Selecting topology and connectivity through metal-directed macrocyclization reactions: A square planar palladium [2]catenate and two noninterlocked isomers. *J. Am. Chem. Soc.* **2005**, *127* (36), 12612-12619.

115. Han, M.; Engelhard, D. M.; Clever, G. H., Self-assembled coordination cages based on banana-shaped ligands. *Chem. Soc. Rev.* **2014**, *43* (6), 1848-1860.

116. Ward, M. D., Polynuclear coordination cages. *Chem. Commun.* **2009**, *2009* (30), 4487-4499.

117. Stang, P. J.; Olenyuk, B., Self-assembly, symmetry, and molecular architecture: Coordination as the motif in the rational design of supramolecular metallacyclic polygons and polyhedra. *Acc. Chem. Res.* **1997**, *30* (12), 502-518.

118. Jaya Prakash, M.; Oh, M.; Liu, X.; Han, K. N.; Seong, G. H.; Lah, M. S., Edge-directed [(M$_2$)$_2$L$_4$] tetragonal metal-organic polyhedra decorated using a square paddle-wheel secondary building unit. *Chem. Commun.* **2010**, *46* (12), 2049-2051.

119. Tian, D.; Liu, S.-J.; Chang, Z.; Zhang, Y.-H.; Zhao, J.-P.; Bu, X.-H., Edge-directed assembly of a 3D 2p-3d heterometallic metal-organic

framework based on a cubic $Co_8(TzDC)_{12}$ cage. *CrystEngComm* **2013**, *15* (45), 9344-9347.

120. Howlader, P.; Mukherjee, P. S., Face and edge directed self-assembly of Pd_{12} tetrahedral nano-cages and their self-sorting. *Chem. Sci.* **2016**, *7* (9), 5893-5899.

121. Leininger, S.; Fan, J.; Schmitz, M.; Stang, P. J., Archimedean solids: transition metal mediated rational self-assembly of supramolecular-truncated tetrahedra. *Proc. Natl. Acad. Sci. U. S. A.* **2000**, *97* (4), 1380-1384.

122. Mitchell, S. G.; Streb, C.; Miras, H. N.; Boyd, T.; Long, D.-L.; Cronin, L., Face-directed self-assembly of an electronically active Archimedean polyoxometalate architecture. *Nat. Chem.* **2010**, *2* (4), 308-312.

123. Caskey, D. C.; Yamamoto, T.; Addicott, C.; Shoemaker, R. K.; Vacek, J.; Hawkridge, A. M.; Muddiman, D. C.; Kottas, G. S.; Michl, J.; Stang, P. J., Coordination-driven face-directed self-assembly of trigonal prisms. face-based conformational chirality. *J. Am. Chem. Soc.* **2008**, *130* (24), 7620-7628.

124. Caulder, D. L.; Raymond, K. N., Supermolecules by design. *Acc. Chem. Res.* **1999**, *32* (11), 975-982.

125. Caulder, D. L.; Brückner, C.; Powers, R. E.; König, S.; Parac, T. N.; Leary, J. A.; Raymond, K. N., Design, formation and properties of tetrahedral M_4L_4 and M_4L_6 supramolecular clusters. *J. Am. Chem. Soc.* **2001**, *123* (37), 8923-8938.

126. Gianneschi, N. C.; Masar, M. S.; Mirkin, C. A., Development of a coordination chemistry-based approach for functional supramolecular structures. *Acc. Chem. Res.* **2005**, *38* (11), 825-837.

127. Cotton, F. A.; Lin, C.; Murillo, C. A., Supramolecular arrays based on dimetal building units. *Acc. Chem. Res.* **2001**, *34* (10), 759-771.

128. Schmidt, A.; Casini, A.; Kuehn, F. E., Self-assembled M_2L_4 coordination cages: Synthesis and potential applications. *Coord. Chem. Rev.* **2014**, *275*, 19-36.

129. Yu, W.; Qiu, F.-Y.; Luo, S.-T.; Shi, H.-T.; Yuan, G.; Wei, X.-W., Coordination assembly and host-guest chemistry of a triply interlocked [2]catenane. *Inorg. Chem. Front.* **2021**, Ahead of Print.

130. Zhang, Y.-W.; Bai, S.; Wang, Y.-Y.; Han, Y.-F., A strategy for the construction of triply interlocked organometallic cages by rational design of poly-NHC precursors. *J. Am. Chem. Soc.* **2020**, *142* (31), 13614-13621.

131. Park, C.; Yang, B. J.; Jeong, K. B.; Kim, C. B.; Lee, S.; Ku, B.-C., Signal-induced release of guests from a photolatent metal-phenolic supramolecular cage and its hybrid assemblies. *Angew. Chem. Int. Ed.* **2017**, *56* (20), 5485-5489.

132. Goeb, S.; Salle, M., Electron-rich coordination receptors based on tetrathiafulvalene derivatives: Controlling the host-guest binding. *Acc. Chem. Res.* **2021**, *54* (4), 1043-1055.

133. Yang, D.; Zhao, J.; Yu, L.; Lin, X.; Zhang, W.; Ma, H.; Gogoll, A.; Zhang, Z.; Wang, Y.; Yang, X.-J.; Wu, B., Air- and light-stable P_4 and As_4 within an anion-coordination-based tetrahedral cage. *J. Am. Chem. Soc.* **2017**, *139* (16), 5946-5951.

134. Lorzing, G. R.; Gosselin, A. J.; Trump, B. A.; York, A. H. P.; Sturluson, A.; Rowland, C. A.; Yap, G. P. A.; Brown, C. M.; Simon, C. M.; Bloch, E. D., Understanding gas storage in cuboctahedral porous coordination

cages. *J. Am. Chem. Soc.* **2019**, *141* (30), 12128-12138.

135. Tashiro, S.; Tominaga, M.; Kawano, M.; Therrien, B.; Ozeki, T.; Fujita, M., Sequence-selective recognition of peptides within the single binding pocket of a self-assembled coordination cage. *J. Am. Chem. Soc.* **2005**, *127* (13), 4546-4547.

136. Custelcean, R., Anion encapsulation and dynamics in self-assembled coordination cages. *Chem. Soc. Rev.* **2014**, *43* (6), 1813-1824.

137. Ogata, D.; Yuasa, J., Dynamic open coordination cage from nonsymmetrical imidazole-pyridine ditopic ligands for turn-on/off anion binding. *Angew. Chem. Int. Ed.* **2019**, *58* (51), 18717.

138. Takezawa, H.; Tabuchi, R.; Sunohara, H.; Fujita, M., Confinement of water-soluble cationic substrates in a cationic molecular cage by capping the portals with tripodal anions. *J. Am. Chem. Soc.* **2020**, *142* (42), 17919-17922.

139. Canton, M.; Grommet, A. B.; Pesce, L.; Gemen, J.; Li, S.; Diskin-Posner, Y.; Credi, A.; Pavan, G. M.; Andreasson, J.; Klajn, R., Improving fatigue resistance of dihydropyrene by encapsulation within a coordination cage. *J. Am. Chem. Soc.* **2020**, *142* (34), 14557-14565.

140. Gemen, J.; Ahrens, J.; Shimon, L. J. W.; Klajn, R., Modulating the optical properties of BODIPY dyes by noncovalent dimerization within a flexible coordination cage. *J. Am. Chem. Soc.* **2020**, *142* (41), 17721-17729.

141. Casini, A.; Woods, B.; Wenzel, M., The promise of self-assembled 3D supramolecular coordination complexes for biomedical applications. *Inorg. Chem.* **2017**, *56* (24), 14715-14729.

142. Bhattacharyya, S.; Ali, S. R.; Venkateswarulu, M.; Howlader, P.;

Zangrando, E.; De, M.; Mukherjee, P. S., Self-assembled Pd$_{12}$ coordination cage as photoregulated oxidase-like nanozyme. *J. Am. Chem. Soc.* **2020**, *142* (44), 18981-18989.

143. Brown, C. J.; Toste, F. D.; Bergman, R. G.; Raymond, K. N., Supramolecular catalysis in metal-ligand cluster hosts. *Chem. Rev.* **2015**, *115* (9), 3012-3035.

144. Fang, Y.; Powell, J. A.; Li, E.; Wang, Q.; Perry, Z.; Kirchon, A.; Yang, X.; Xiao, Z.; Zhu, C.; Zhang, L.; Huang, F.; Zhou, H.-C., Catalytic reactions within the cavity of coordination cages. *Chem. Soc. Rev.* **2019**, *48* (17), 4707-4730.

145. Fujita, M.; Yoshizawa, M. New properties and reactions in self-assembled M$_6$L$_4$ coordination cages, in *Modern supramolecular chemistry: strategies for macrocycle synthesis*, Diederich, F.; Stang, P. J.; Tykwinski, R.R., Editors. **2008**, Wiley-VCH Verlag GmbH & Co. KGaA.

146. McGuirk, C. M.; Stern, C. L.; Mirkin, C. A., Small molecule regulation of self-association and catalytic activity in a supramolecular coordination complex. *J. Am. Chem. Soc.* **2014**, *136* (12), 4689-4696.

147. Yoshizawa, M.; Tamura, M.; Fujita, M., Diels-Alder in aqueous molecular hosts: unusual regioselectivity and efficient catalysis. *Science* **2006**, *312* (5771), 251-254.

148. Brown, C. J.; Bergman, R. G.; Raymond, K. N., Enantioselective catalysis of the aza-Cope rearrangement by a chiral supramolecular assembly. *J. Am. Chem. Soc.* **2009**, *131* (48), 17530-17531.

149. Hastings, C. J.; Fiedler, D.; Bergman, R. G.; Raymond, K. N., Aza Cope rearrangement of propargyl enammonium cations catalyzed by a self-assembled "nanozyme". *J. Am. Chem. Soc.* **2008**, *130* (33), 10977-10983.

150. Fiedler, D.; Bergman, R. G.; Raymond, K. N., Supramolecular catalysis of a unimolecular transformation: Aza-Cope rearrangement within a self-assembled host. *Angew. Chem. Int. Ed.* **2004**, *43* (48), 6748-6751.

151. Cullen, W.; Misuraca, M. C.; Hunter, C. A.; Williams, N. H.; Ward, M. D., Highly efficient catalysis of the Kemp elimination in the cavity of a cubic coordination cage. *Nat. Chem.* **2016**, *8* (3), 231-236.

152. Murase, T.; Nishijima, Y.; Fujita, M., Cage-catalyzed Knoevenagel condensation under neutral conditions in water. *J. Am. Chem. Soc.* **2012**, *134* (1), 162-164.

153. Taylor, C. G. P.; Metherell, A. J.; Argent, S. P.; Ashour, F. M.; Williams, N. H.; Ward, M. D., Coordination-cage-catalyzed hydrolysis of organophosphates: Cavity- or surface-based? *Chem. Eur. J.* **2020**, *26* (14), 3065-3073.

154. Zou, Y.-Q.; Jahovic, I.; Nitschke, J. R., Hydrolysis of twisted amides inside a self-assembled coordination cage. *Chem* **2020**, *6* (6), 1217-1218.

155. Hart-Cooper, W. M.; Zhao, C.; Triano, R. M.; Yaghoubi, P.; Ozores, H. L.; Burford, K. N.; Toste, F. D.; Bergman, R. G.; Raymond, K. N., The effect of host structure on the selectivity and mechanism of supramolecular catalysis of Prins cyclizations. *Chem. Sci.* **2015**, *6* (2), 1383-1393.

156. Kaphan, D. M.; Toste, F. D.; Bergman, R. G.; Raymond, K. N., Enabling new modes of reactivity via constrictive binding in a supramolecular-assembly-catalyzed aza-Prins cyclization. *J. Am. Chem. Soc.* **2015**, *137* (29), 9202-9205.

157. Hart-Cooper, W. M.; Clary, K. N.; Toste, F. D.; Bergman, R. G.; Raymond, K. N., Selective monoterpene-like cyclization reactions

achieved by water exclusion from reactive intermediates in a supramolecular catalyst. *J. Am. Chem. Soc.* **2012**, *134* (43), 17873-17876.

158. Salles, A. G.; Zarra, S.; Turner, R. M.; Nitschke, J. R., A Self-organizing chemical assembly line. *J. Am. Chem. Soc.* **2013**, *135* (51), 19143-19146.

159. Jiao, J.; Li, Z.; Qiao, Z.; Li, X.; Liu, Y.; Dong, J.; Jiang, J.; Cui, Y., Design and self-assembly of hexahedral coordination cages for cascade reactions. *Nat. Commun.* **2018**, *9* (1), 4423.

160. Yoshizawa, M.; Miyagi, S.; Kawano, M.; Ishiguro, K.; Fujita, M., Alkane oxidation via photochemical excitation of a self-assembled molecular cage. *J. Am. Chem. Soc.* **2004**, *126* (30), 9172-9173.

161. Yoshizawa, M.; Takeyama, Y.; Okano, T.; Fujita, M., Cavity-directed synthesis within a self-assembled coordination cage: Highly selective [2 + 2] cross-photodimerization of olefins. *J. Am. Chem. Soc.* **2003**, *125* (11), 3243-3247.

162. Slagt, V. F.; Reek, J. N. H.; Kamer, P. C. J.; van Leeuwen, P. W. N. M., Assembly of encapsulated transition metal catalysts. *Angew. Chem. Int. Ed.* **2001**, *40* (22), 4271-4274.

163. Merlau, M. L.; Grande, W. J.; Nguyen, S. T.; Hupp, J. T., Enhanced activity of manganese(III) porphyrin epoxidation catalysts through supramolecular complexation. *J. Mol. Catal. A Chem.* **2000**, *156* (1), 79-84.

164. Leung, D. H.; Fiedler, D.; Bergman, R. G.; Raymond, K. N., Selective C-H bond activation by a supramolecular host-guest assembly. *Angew. Chem. Int. Ed.* **2004**, *43* (8), 963-966.

165. Leung, D. H.; Bergman, R. G.; Raymond, K. N., Highly selective

supramolecular catalyzed allylic alcohol isomerization. *J. Am. Chem. Soc.* **2007**, *129* (10), 2746-2747.

166. Cavarzan, A.; Scarso, A.; Sgarbossa, P.; Strukul, G.; Reek, J. N. H., Supramolecular control on chemo- and regioselectivity via encapsulation of (NHC)-Au catalyst within a hexameric self-assembled host. *J. Am. Chem. Soc.* **2011**, *133* (9), 2848-2851.

167. Wang, Z. J.; Brown, C. J.; Bergman, R. G.; Raymond, K. N.; Toste, F. D., Hydroalkoxylation catalyzed by a gold(I) complex encapsulated in a supramolecular host. *J. Am. Chem. Soc.* **2011**, *133* (19), 7358-7360.

168. Yaghi, O. M.; O'Keeffe, M. O.; Ockwig, N. W.; Chae, H. K.; Eddaoudi, M.; Kim, J., Reticular synthesis and the design of new materials. *Nature* **2003**, *423*, 705-714.

169. Cook, T. R.; Zheng, Y.-R.; Stang, P. J., Metal-organic frameworks and self-assembled supramolecular coordination complexes: Comparing and contrasting the design, synthesis, and functionality of metal–organic materials. *Chem. Rev.* **2013**, *113* (1), 734-777.

170. Tranchemontagne, J. D.; Mendoza-Cortés, J. L.; O'Keeffe, M., Secondary building units, nets and bonding in the chemistry of metal-organic frameworks. *Chem. Soc. Rev.* **2009**, *38* (5), 1257-1283.

171. Kim, J.; Chen, B.; Reineke, T. M.; Li, H.; Eddaoudi, M.; Moler, D. B.; O'Keeffe, M.; Yaghi, O. M., Assembly of metal-organic frameworks from large organic and inorganic secondary building units: New examples and simplifying principles for complex structures. 2001. 123.

172. Stock, N.; Biswas, S., Synthesis of metal-organic frameworks (MOFs): routes to various MOF topologies, morphologies, and composites. *J. Am. Chem. Soc.* **2001**, *123* (34), 8239–8247.

173. Ferey, G., Hybrid porous solids: past, present, future. *Chem. Soc. Rev.* **2008**, *37* (1), 191-214.

174. Lucier, B. E. G.; Chen, S.; Huang, Y., Characterization of metal-organic frameworks: Unlocking the potential of solid-state NMR. *Acc. Chem. Res.* **2018**, *51* (2), 319-330.

175. Cheng, W.; Demin, L.; Wenbin, L., Metal-organic frameworks as a tunable platform for designing functional molecular materials. *J. Am. Chem. Soc.* **2013**, *135* (36), 13222–13234.

176. Furukawa, H.; Cordova, K. E.; O'Keeffe, M.; Yaghi, O. M., The chemistry and applications of metal-organic frameworks. *Science* **2013**, *341* (6149), 1230444.

177. Gascon, J.; Corma, A.; Kapteijn, F.; Llabrés i Xamena, F. X., Metal organic framework catalysis: Quo vadis? *ACS Catal.* **2014**, *4* (2), 361–378.

178. Alaerts, L.; Séguin, E.; Poelman, H.; Thibault-Starzyk, F.; Jacobs, P. A.; De Vos, D. E., Probing the Lewis acidity and catalytic activity of the metal–organic framework $[Cu_3(btc)_2]$ (btc=benzene-1,3,5-tricarboxylate). *Chem. Eur. J.* **2006**, *12* (28), 7353-7363.

179. Corma, A.; Iglesias, M.; Llabrés i Xamena, F. X.; Sanchez, F., Cu and Au metal-organic frameworks bridge the gap between homogeneous and heterogeneous catalysts for alkene cyclopropanation reactions. *Chem. Eur. J.* **2010**, *16* (32), 9789-9795.

180. Henschel, A.; Gedrich, K.; Kraehnertb, R.; Kaskel, S., Catalytic properties of MIL-101. *Chem. Commun.* **2008**, *2008* (35), 4192-4194.

181. Zou, R. Q.; Sakurai, H.; Xu, Q., Preparation, adsorption properties, and catalytic activity of 3D porous metal-organic frameworks composed of

cubic building blocks and alkali-metal ions. *Angew. Chem. Int. Ed.* **2006**, *45* (16), 2542-2546.

182. Wu, C. D.; Hu, A.; Zhang, L.; Lin, W., A homochiral porous metal-organic framework for highly enantioselective heterogeneous asymmetric catalysis. *J. Am. Chem. Soc.* **2005**, *127* (25), 8940–8941.

183. Roberts, J. M.; Fini, B. M.; Sarjeant, A. A.; Farha, O. K.; Hupp, J. T.; A., S. K., Urea metal-organic frameworks as effective and size-selective hydrogen-bond catalysts. *J. Am. Chem. Soc.* **2012**, *134* (7), 3334–3337.

184. Alkordi, M. H.; Liu, Y.; Larsen, R. W.; Eubank, J. F.; Eddaoudi, M., Zeolite-like metal-organic frameworks as platforms for applications: On metalloporphyrin-based catalysts. *J. Am. Chem. Soc.* **2008**, *130* (38), 12639–12641.

185. Dhakshinamoorthy, A.; Garcia, H., Catalysis by metal nanoparticles embedded on metal-organic frameworks. *Chem. Soc. Rev.* **2012**, *41* (15), 5262-5284.

186. Hermes, S.; Schröter, M.-K.; Schmid, R.; Khodeir, L.; Muhler, M.; Tissler, A.; Fischer, R. W.; Fischer, R. A., Metal@MOF: Loading of highly porous coordination polymers host lattices by metal organic chemical vapor deposition. *Angew. Chem. Int. Ed.* **2005**, *44* (38), 6237-6241.

187. Canivet, J.; Aguado, S.; Schuurman, Y.; Farrusseng, D., MOF-supported selective ethylene dimerization single-site catalysts through one-pot postsynthetic modification. *J. Am. Chem. Soc.* **2013**, *135* (11), 4195–4198.

188. Jiang, H.-L.; Liu, B.; Akita, T.; Haruta, M.; Sakurai, H.; Xu, Q., Au@ZIF-8: CO oxidation over gold nanoparticles deposited to

metal−organic framework. *J. Am. Chem. Soc.* **2009**, *131* (32), 11302-11303.

189. Gu, X.; Lu, Z.-H.; Jiang, H.-L.; Akita, T.; Xu, Q., Synergistic catalysis of metal-organic framework-immobilized Au-Pd nanoparticles in dehydrogenation of formic acid for chemical hydrogen storage. *J. Am. Chem. Soc.* **2011**, *133* (31), 11822-11825.

190. Guo, Z.; Xiao, C.; Maligal-Ganesh, R. V.; Zhou, L.; Goh, T. W.; Li, X.; Tesfagaber, D.; Thiel, A.; Huang, W., Pt nanoclusters confined within metal-organic framework cavities for chemoselective cinnamaldehyde hydrogenation. *ACS Catal.* **2014**, *4* (5), 1340-1348.

191. Kim, I. S.; Li, Z.; Zheng, J.; Platero-Prats, A. E.; Mavrandonakis, A.; Pellizzeri, S.; Ferrandon, M.; Vjunov, A.; Gallington, L. C.; Webber, T. E.; Vermeulen, N. A.; Penn, R. L.; Getman, R. B.; Cramer, C. J.; Chapman, K. W.; Camaioni, D. M.; Fulton, J. L.; Lercher, J. A.; Farha, O. K.; Hupp, J. T.; Martinson, A. B. F., Sinter-resistant platinum catalyst supported by metal-organic framework. *Angew. Chem. Int. Ed.* **2018**, *57* (4), 909-913.

192. Li, Z.; Schweitzer, N. M.; League, A. B.; Bernales, V.; Peters, A. W.; Getsoian, A. B.; Wang, T. C.; Miller, J. T.; Vjunov, A.; Fulton, J. L.; Lercher, J. A.; Cramer, C. J.; Gagliardi, L.; Hupp, J. T.; Farha, O. K., Sintering-resistant single-site nickel catalyst supported by metal-organic framework. *J. Am. Chem. Soc.* **2016**, *138* (6), 1977-1982.

193. Tejeda-Serrano, M.; Mon, M.; Ross, B.; Gonell, F.; Ferrando-Soria, J.; Corma, A.; Leyva-Pérez, A.; Armentano, D.; Pardo, E., Isolated Fe(III)-O sites catalyze the hydrogenation of acetylene in ethylene flows under front-end industrial conditions. *J. Am. Chem. Soc.* **2018**, *140* (28), 8827-

8832.

194. Manna, K.; Ji, P.; Greene, F. X.; Lin, W., Metal-organic framework nodes support single-site magnesium-alkyl catalysts for hydroboration and hydroamination reactions. *J. Am. Chem. Soc.* **2016**, *138* (24), 7488-7491.

195. Abdel-Mageed, A. M.; Behm, R. J.; Rungtaweevoranit, B.; Pei, X.; Yaghi, O. M.; Rungtaweevoranit, B.; Pei, X.; Yaghi, O. M.; Parlinska-Wojtan, M., Highly active and stable single-atom Cu catalysts supported by a metal-organic framework. *J. Am. Chem. Soc.* **2019**, *141* (13), 5201-5210.

196. Otake, K.-I.; Cui, Y.; Buru, C. T.; Li, Z.; Hupp, J. T.; Farha, O. K.; Farha, O. K., Single-atom-based vanadium oxide catalysts supported on metal-organic frameworks: Selective alcohol oxidation and structure-activity relationship. *J. Am. Chem. Soc.* **2018**, *140* (28), 8652-8656.

197. Tiburcio, E.; Greco, R.; Mon, M.; Ballesteros-Soberanas, J.; Ferrando-Soria, J.; López-Haro, M.; Hernández-Garrido, J. C.; Oliver-Meseguer, J.; Marini, C.; Boronat, M.; Armentano, D.; Leyva-Pérez, A.; Pardo, E., Soluble/MOF-supported palladium single atoms catalyze the ligand-, additive-, and solvent-free aerobic oxidation of benzyl alcohols to benzoic acids. *J. Am. Chem. Soc.* **2021**, *143* (6), 2581-2592.

Chapter 2

Objectives

2 Objectives

The general aim of this *Thesis* is the synthesis and application of metal clusters (MCs) and single atoms catalysts (SACs) of Pd and Pt in homo- or cross-coupling reactions, in alcohol oxidation reactions, and in antitumoral treatments. In order to achieve these objectives this *Thesis* was developed as follows:

1. Search of the best applications of Pd and Pt.

2. Characterization of the species used in reactions, generated *in situ* or pre-synthesized.

3. Study of the synthesis of the clusters and single atoms, especially looking at different precursors and different synthetic strategies.

4. Study of the mechanism of formation of the catalytic species in the reaction and of the reaction itself, comparing the catalysts with more common catalytic systems.

5. Heterogenization of clusters and single atoms to stabilize the catalytic species.

This *Thesis* is part of the past and present work of our research group. Indeed, in previous works we observed the *in situ* formation of clusters and single atoms, which boosted the activity of the interested reactions. A common way to stabilize these species is to support them onto different solid with the proper functionalities. On the other hand, one of the best ways to use these small species should be in ligand-free conditions in order to have the highest availability of the metal atoms for the reaction substrate. Certainly, the use of these highly activated species is extremely relevant in the field of catalysis for organic reactions, such as C-C coupling and oxidation reactions.

Chapter 3

Materials and Methods

3 Materials and Methods

3.1 Materials

Unless stated otherwise, all chemicals were of reagent grade quality. They were purchased from commercial sources and used as received, without any further purification. In the case of synthesized precursors or reagents, it will be specified their experimental synthesis and their characterization.

3.2 Characterization Techniques

Here we present the techniques useful both to understand the nature of the catalysts applied in the reactions and to analyse the products obtained after these processes.

3.2.1 Qualitative and quantitative analysis of organic molecules

Gas Chromatography (GC)

It is one of the most used experimental way to identify and quantify reagents and products in a reaction. As in classical chromatography, the species in the mixture are distinguished by their molecular weight and their polarity, characteristics that provide different interaction with the column. In the GC, the capillary column can analyse gaseous samples that are moved through the column by a carrier gas (N_2 or He). Before entering the column, the sample passes in the injector, where all the species are able to go to the gaseous form. In this thesis it was used a GC Bruker 430-GC with a column HP-5MS (30 m

× 0.25 mm × 0.25 μm), whose stationary phase is made by 5% of phenylmethylsilicon. For the quantification of the compounds, it was used the internal standard method, in which the area of the compounds of interest was compared to the area of a standard. Knowing the amount of the latter, it is possible to calculate the amount of the species in our mixture, taking into account a specific response factor. The response was calculated with calibration curves made with commercial reagents or, when indicated, with species synthesised *in loco* and subsequently purified.

Gas Chromatography-Mass Spectrometry (GC-MS)

This chromatography coupled with mass spectrometry can identify compounds in a mixture thanks to their typical fragmentation into smaller ions or radicals. The MS is the responsible of the fragmentation and mass analysis of the molecule fragments and then, it is possible to know the species present in our solution, by comparison with libraries. In this thesis it was used a GC-MS Agilent 6890N with a column HP-5MS (30 m × 0.25 mm × 0.25 μm) with the stationary phase made by the 5% of phenylmethylsilicon and the detector 5973N.

Nuclear Magnetic Resonance (NMR)

In this technique the attempt of a magnetic field, B_0, to align the nuclear magnetic moment of the atoms in the molecules, μ, gives useful information about the structure of the species. The signals in the spectrum are correlated to the type of atoms and how they interact between them. Indeed, in a molecule the chemical environment changes the local magnetic field, B_{local}, generated by the electrons. Considering that B_{local} differs from B_0, the typical chemical shifts

will be given by the variation of the resonance frequency of each nucleus, due to the application of the external magnetic field B_0 [1]. The most common nuclei analyzed by NMR are ^1H, ^{13}C and ^{15}N. The ^1H NMR gives not only qualitative information, but also quantitative. The ^{13}C NMR is a very useful tool to understand how the carbons are bonded along the structure. In this thesis ^1H, ^{13}C, ^{19}F and ^{31}P NMR were performed on an instrument Bruker Avance of 300 MHz using as solvents $CDCl_3$, CD_3CN, D_2O or others as indicated.

Magic Angle Spinning Solid ^{13}C-NMR Spectroscopy

In the case of solid samples, this implemented NMR technique spins the sample at the magic angle to make the signals narrower. In fact, solid sample molecules have fixed orientation in B_0 and the strong dipole-dipole generated causes the formation of very broad signals, which can be narrowed only by the presence of a rotor and by the specific angle of impact of B_0 [1]. In this *Thesis* solid ^{13}C-NMR were performed on an instrument Varian of 400 MHz.

3.2.2 Spectroscopies

Ultraviolet-Visible (UV-Vis) and emission spectroscopy

The interaction of light with molecules in solution is widely applied in the characterization of species bearing chromophore groups, which absorb at specific wavelengths of UV-Vis radiation due to transitions of electrons to excited states. In some cases, the transition of the excited electrons to the lower energy states gives the phenomenon of fluorescence. The photons emitted in this way can be registered by emission spectroscopy and give information about the electronic structure of the interested molecule, together with the UV-Vis spectrum [2]. In this *Thesis*, these spectroscopies were mainly used for the

characterization of clusters and to verify the absence of nanoparticles. Indeed, small metallic clusters can behave as chromophores, due to discrete electronic energy levels, whereas nanoparticles present plasmon bands at higher wavelength, due to a collective movement of the conduction electrons after the interaction with light [3]. Moreover, considering that nanoparticles do not have discrete electronic energy levels, they do not show emission, in contrast to clusters. In fact, it was possible to theoretically calculate the number of atoms composing clusters by the relation $E_g = E_{Fermi}/N^{1/3}$, where E_g is the gap energy, i.e., the emission energy, E_{Fermi} is the Fermi energy of the bulk material and N is the number of atoms [4-6]. In this *Thesis*, UV-Vis and emission spectra were recorded at room temperature in quartz cuvette ($10 \times 10 \text{ mm}^2$) on a spectrophometer Varian UV0811M209 and on a fluorometer LP S- 220B (Photon Technology International) with a Xe lamp of 75 W, respectively.

Diffuse-reflectance (DR) UV-Vis spectroscopy

It refers to UV-Vis spectroscopy performed on solid samples. The diffuse reflectance is in fact a reflection of light, which can only happen on solid materials, where an incident ray of light is scattered at many angles instead of only one. In this thesis reflectance spectra in the region comprised between 190 and 1100 nm were recorded at room temperature on a spectrophotometer equipped with an integrating sphere. The mixture was contained in a quartz cell with 1 mm path length.

Inductively Coupled Plasma-Absorption Emission Spectroscopy (ICP-AES)

This spectroscopy allows to detect and quantify metals present in water solutions. The ICP makes possible the formation of excited atoms or ions, which lately interact with a specific radiation to give emission analyzed by the AES. The intensity of the emission is correlated to the concentration of each atom and this technique gives a quite sensitive quantification, detecting metals present in the order of ppm. For our purposes, in some cases it was necessary to digest solid samples with strong acids and then dissolve them in water. In this *Thesis* the instrument used was Varian 715-ES.

Infrared Spectroscopy (IR)

The interaction of the infrared radiation with the material allows to know the vibrational transitions, which are typical of each bond of the molecules. This gives us a fragmented "picture" of the species, in particular of the functional groups that are present on it. Fourier transform infrared (FT–IR) measurements of solid and liquid samples were recorded on a Thermo Nicolet iS10 spectrophotometer after impregnating the window with a dichloromethane solution of the analyte, and then leaving to evaporate, or by previous mixture of the solid with KBr.

X-Ray Photoelectron Spectroscopy (XPS)

When an X-ray beam interacts with a material, the electrons of the atoms are expelled with specific kinetic energies related to their energy level, consequently, giving information about the oxidation state and the chemical composition of the surface of the material. If an ion beam is used in

combination with the X-ray, the analysis can be performed at higher depths, in order to analyze the inner part of the material. In this *Thesis*, a spectrometer SPECS equipped with a multichannel analyzer Phoibos 150MCD with a MgKα radiation (1253.6 eV) was used for XPS analyses.

X-ray Absorption Spectroscopy

As the name suggests, also in this case the use of X-ray provides powerful information regarding the material. Indeed, this technique studies the relation between the absorption coefficient of a chemical specie and the energy of the radiation directed to the sample, giving information about the local structure of a particular atom. The radiation is commonly a synchrotron one, which generates very stable X-ray. The XAS spectrum is divided in two areas, the XANES (X-ray Absorption Near Edge Structure) and EXAFS (Extended X-ray Absorption Fine Structure) [7]. The XANES provides information about the geometries and the oxidation state of the sample, meanwhile with the EXAFS coordination number and distance between atoms can be known.

In this *Thesis*, X-ray absorption spectroscopy (XAS) measurements were carried out on CLAESS beamline at ALBA Synchrotron Light Source, Barcelona (Spain). The synchrotron light coming from the multipole wiggler was first vertically collimated, then monochromatized using two pairs of liquid nitrogen cooled Si(311) crystals and finally focused on the sample position down to *ca.* 500×500 μm^2. Rh stripe coating on the two optical mirrors guarantees the higher harmonics rejection.

3.2.3   Other techniques

X-Ray Diffraction (XRD)

XRD is one of the most used non-destructive techniques to characterize solid materials, in fact, it can give information about the crystallographic structure, but also about chemical composition and crystallites size.

For our purposes, different instruments were used, considering that different kinds of materials were examined with this technique.

Single-Crystal X-Ray Diffraction was performed using synchrotron radiation at the I19 beamline of the Diamond Light Source at $\lambda = 0.6889$ Å or with the Bruker-Nonius X8APEXII CCD area detector diffractometer using graphite-monochromated Mo Kα radiation ($\lambda = 0.71073$ Å).

Powder X-Ray Diffraction using the powder diffractometer Empyrean PANalytical, using Cu Kα radiation ($\lambda = 1,54056$ Å).

Microscopy

This technique allows to detect imagines of solid samples (thick around 100 nm) or suspensions of the latter. In the case of the Electron Microscopy, an electron beam passes through the material and then it is focused on an imaging device to form pictures of the samples. In this *Thesis*, different instruments were used.

High Resolution Transmission Electron Microscopy (HRTEM)

It was used to analyze the presence and the size of nanoparticles on MOFs, impregnating a copper or nickel grid with a suspension of the sample. The

instrument used was a JEOL 200 KeV.

<u>Scanning Electron Microscopy coupled with Energy Dispersive X–ray (SEM/EDX)</u>

It was carried out with a XL 30 ESEM (PHILIPS) microscope equipped with a home–made EDX energy dispersive X–ray detector. In other cases, morphology and element mapping of the single crystal samples, were analyzed with a Field Emission Scanning Electron Microscope (FESEM) model JEOL 7001F, equipped with a spectrometer of energy dispersion of X-ray (EDX) from Oxford Instruments.

<u>Aberration Corrected High-angle Annular Dark-field imaging Scanning Transmission Electron Microscopy (AC HAADF-STEM)</u>

The characteristics of this instrument make possible to imaging both very small samples and very diluted suspension. Electron microscopy studies were performed on a FEI Titan Themis 60–300 Double Aberration Corrected microscope working at 200kV.

Elemental (C, H, N, S) analysis

It can quantify the cited elements by the combustion of the sample in oxygen. In this *Thesis* a small amount of the sample (around 0.5 mg) was analysed with a Flash 200 elemental analyser.

3.3 Experimental procedures

3.3.1 Catalytic activity of palladium supramolecular complexes within metal-organic frameworks (MOFs)

Synthesis of 1,2-di(pyridin-4-yl)ethyne (L_1) and methyl 3,5-bis(pyridin-4-ylethynyl)benzoate (L_2)
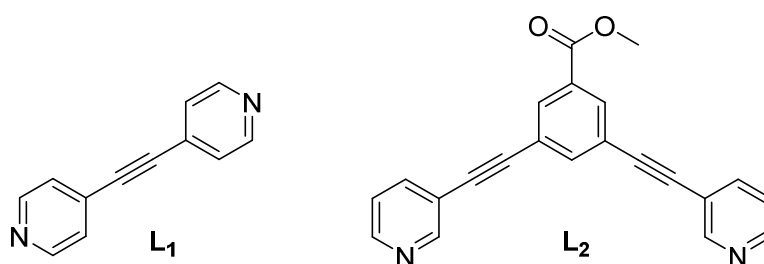
They were performed following reported procedures [8, 9].

Synthesis of 4,4'-((2-(2-(methylthio)ethoxy)-1,3-phenylene)bis(ethyne-2,1-diyl))dipyridine (L_3)
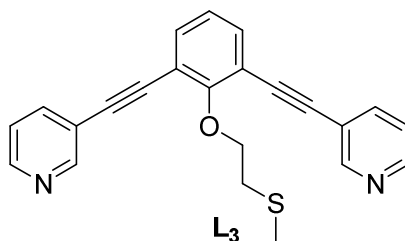
The synthesis involves the previous preparation of the precursor 1,3-dibromo-2-(2-methylsulfanylethoxy)benzene as follows. To a solution of 2,6-dibromophenol (4 mmol) in acetonitrile, K_2CO_3 (12 mmol) was added, and the reaction mixture was refluxed for 1 h. After cooling down to room temperature, 1-bromo-2-methylsulfonylethane (4 mmol) in acetonitrile was added and the reaction mixture was refluxed for 6 h. The mixture was cooled down, filtered and concentrated by rotatory evaporation. The solid, obtained after washing

with water and drying, was used without any further purification for the next synthetic step. Yield: 85 %. A mixture of 1,3-dibromo-2-(2-methylsulfanylethoxy)benzene (3.3 mmol), 4-ethynylpiridine hydrochloride (1.37 mmol), CuI (0.2 mmol) and bis(benzonitrile)palladium(II) dichloride (0.2 mmol) were added to a 100 mL round bottom flask. After several vacuum/argon cycles, degassed anhydrous 1,4-dioxane (50 mL), diisopropylamine (4.8 mmol) and tri(t-butyl)phosphine (2.47 mmol) were added and the suspension was stirred at 50 ºC for 20 h. After cooling to room temperature, the mixture was filtered, and the solvent was removed. The following purification was made by column chromatography using dichloromethane as first eluent and then a mixture of 1:1 dichloromethane:ethyl acetate, obtaining L_3 as pure product (80 %) [10].

Synthesis of $\{[Pd^{II}(en)(L_1)]_4(NO_3)_8\}$ $(Pd^{II}_4(L_1)_4)$

An aqueous solution (2 mM) of ethylenediaminepalladium(II) dinitrate (0.10 mmol) was added to a methanol solution (0.5 ml) of L_1 (0.10 mmol) at room temperature. After 5 min, the addition of an aqueous solution (2 ml) of $NaClO_4$ (0.40 mmol) precipitated a colourless powder, which was filtered and washed with a small amount of ethanol to give $Pd^{II}_4(L_1)_4$ (70 %) [11].

Synthesis of $[Pd^{II}_2(\mu–OH_2)_2(NH_3)_4)]_{0.5}[Pd^{II}_8(\mu–OH_2)_8(NH_3)_8(L_1)_4]_{0.125}\{Ni^{II}_4[Cu^{II}_2(Me_3mpba)_2]_3\} \cdot 43H_2O$ (**2**)

SCC@MOF **2** was obtained by soaking crystals of **1** [12] (0.010 mmol) in hot (50 ºC) acetonitrile/water (2:1 v/v) solution of L_1 (5 mL, 10 mM) for one week. Then, the supernatant solution was removed, and the crystals, after being washed with an acetonitrile solution (5 × 10 mL), were isolated by filtration

and dried. Synthesis performed in the ICMol by the Emilio Pardo´s group.

Synthesis of $[Pd^{II}_{16}(H_2O)_8(NH_3)_{24}(\mu–OH_2)_4(H_2O)_{24}(L_2)]_{0.125}\{Ni^{II}_4[Cu^{II}_2(Me_3mpba)_2]_3\} \cdot 30H_2O$ (**3**)

The synthesis was carried out as in the case of SCC@MOF **2**, but using a acetonitrile/water solution of L_2, to obtain SCC@MOF **3**. Synthesis performed in the ICMol by the Emilio Pardo´s group.

Synthesis of

$[Au^{III}_2(\mu-OH)_2(OH)_4)]_{0.5}[Au^{III}_2Cl_6Pd^{II}_2(NH_3)_6(L_3)_2]_{0.5}[Pd^{II}_2(\mu-OH_2)(NH_3)_6)]_{0.5}\{Ni^{II}_4[Cu^{II}_2(Me_3mpba)_2]_3\} \cdot 37H_2O$ (**4**)

After following the same procedure used for SCCs@MOF **2** and **3**, but using L_3, crystals of the precursor were washed with a solution of water/methanol (1:1 v/v) and then soaked in a solution of $AuCl_3$ in water/methanol (1:1 v/v) for 12 h. This process was repeated 5 times and at the end the crystals were washed with a solution of water/methanol (1:1 v/v), isolated by filtration and dried. Synthesis performed in the ICMol by the Emilio Pardo´s group.

Reaction procedure for the homocoupling of boronic acids catalyzed by **1–3** or $Pd(OAc)_2$/py or $Pd_4(L_1)_4$

5a R=H
5b R=B(OH)$_2$

Pd cat. (2 mol%)

p-benzoquinone (2 eq), KF (1 eq), EtOAc, 60°C, N$_2$, overnight

6a R=H
6b R=(thiophenyl)$_n$

7
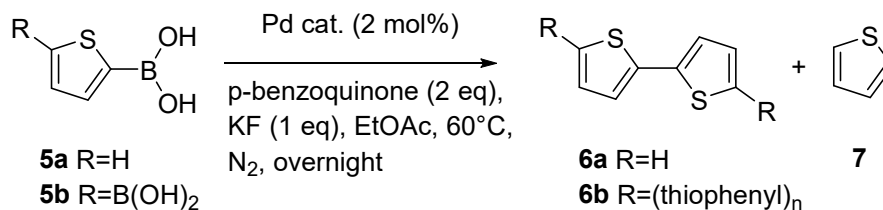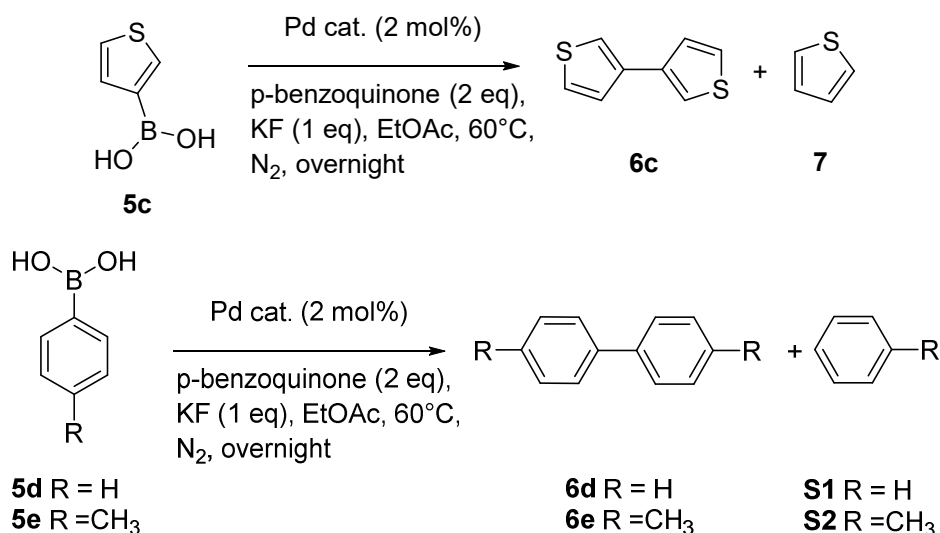
The boronic acid (0.1 mmol), KF (0.1 mmol), *p*-benzoquinone (0.2 mmol) and dodecane (10 μL), as an internal standard, were inserted with 2 mol% of the palladium catalyst in 1.5 ml of ethyl acetate or o-xylene under N_2 atmosphere, in a 10 ml glass vial equipped with a stirring bar. The vial was sealed, and the mixture was heated at 60 °C overnight. At the end, the possible excess of boronic acid was quenched with neopentyl glycol and the mixture was analyzed by GC and by GC-MS. The homocoupling products were isolated by preparative TLC using hexane as eluent.

General reaction procedure for the homocoupling of alkynes catalysed by **1–4** and $Pd(OAc)_2$/py or $Pd_4(L_1)_4$
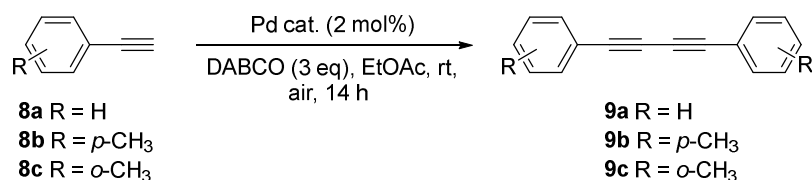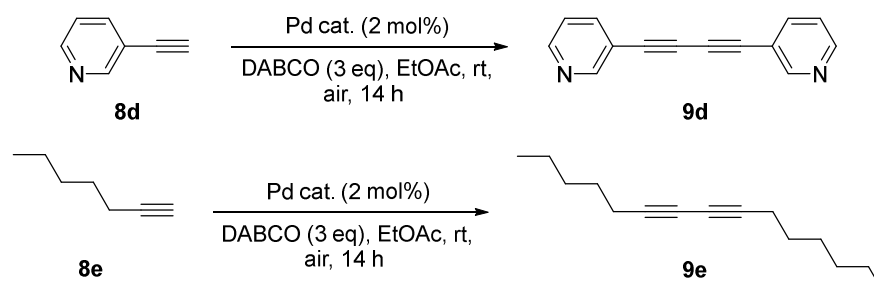
The alkyne (0.1 mmol), DABCO (0.3 mmol) and dodecane (10 µL), as an internal standard, were inserted with a 2 mol% of the corresponding palladium catalyst in 1.5 ml of ethyl acetate under air atmosphere, in a 10 ml glass vial equipped with a stirring bar. The vial was sealed, and the mixture stirred at room temperature for 14 h. Consequently, the mixture was analyzed by GC and by GC-MS. The homocoupling products were isolated by preparative TLC using mixtures of ethyl acetate/hexane as eluents. The in-flow reaction was performed using a similar reaction mixture for alkyne **8a**, which passed at 60 ºC at a flow of 0.01 ml·min^{-1} through **4** placed in a tubular fixed-bed reactor (4 mm diameter). Samples were collected every hour to be analyzed by GC and GC-MS.

General reaction procedure for the cross-coupling of phenylacetylene **8a** with alkynes **8f-h** catalysed by **4**
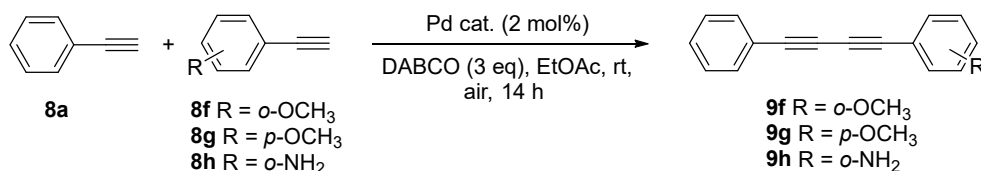
The alkyne **8f-h** (0.3 mmol), phenylacetylene **8a** (0.1 mmol), DABCO (0.3 mmol), and dodecane (10 µL), as an internal standard, were inserted in a 10 ml glass vial, equipped with a stirring bar, with a 2 mol% of **4** (4.2 mg) in 1.5 ml

90

of ethyl acetate under air atmosphere. The vial was sealed, and the mixture was stirred for 14 h at room temperature. After the reaction time, the mixture was analysed by GC and by GC-MS when necessary.

General reaction procedure for the cross-coupling of 2-thienylboronic acid **5a** with **8a** catalyzed by **1-4** and Pd(OAc)$_2$/Py or Pd$_4$(L$_1$)$_4$
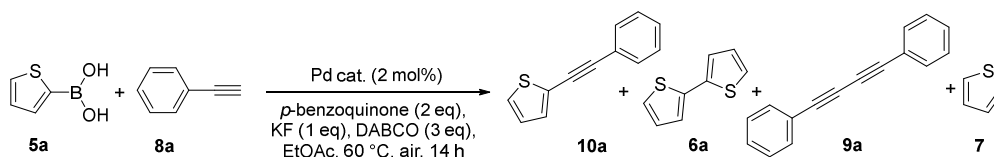
The alkyne **8a** (0.3 mmol), 2-thienylboronic acid **5a** (0.1 mmol), DABCO (0.9 mmol), KF (0.1 mmol), *p*-benzoquinone (0.1 mmol) and dodecane (10 µL), as an internal standard, were inserted together with a 2 mol% of the corresponding palladium catalyst in 1.5 ml of ethyl acetate under air atmosphere, in a 10 ml glass vial equipped with a stirring bar. The sealed vial was heated at 60 °C and stirred for 14 h. Finally, the mixture was analyzed by GC and by GC-MS.

Reuses of catalysts

The reaction procedures, described above, were followed for the corresponding SCCs@MOF in a ten-fold scale. At the end of the reaction, the solid catalyst was recovered by filtration and washed with ethyl acetate and water. Subsequently, the dried catalyst was weighted, and reagents and solvent were added in proportional amounts to the initial relative molar ratios.

Hot-filtration experiments

The reaction described above was stopped when the conversion of the starting material was *ca.* 20 % and the hot reaction mixture was filtered through a 0.25

μm Teflon filter into another vial equipped with a stirring bar. The reaction was heated for the remaining time and was periodically analyzed by GC for comparison with the reaction performed with the solid catalyst still in.

Synthesis of phenylacetylene-*d* (**8a-*d***) [13]

Phenylacetylene (10 mmol) and anhydrous THF (0.67 M) were inserted in a Schlenk flask, equipped with a stirring bar. The solution was cooled to -78 ºC and *n*-BuLi (2.5 M in hexanes, 1.5 eq) was added in a dropwise form over 5 min and stirred at -78 ºC for 20 min. Afterwards, the temperature was increased to room temperature and the reaction was stirred for additional 20 min. The solution was cooled to -78 ºC and D_2O (3 ml) was added. Then, the temperature was again increased to rt and stirred for 20 min. Finally, the reaction was quenched with HCl 3 M and extracted with diethyl ether (3 × 20 ml). The organic extracts were dried over $MgSO_4$, filtered, and the solvent was carefully removed with use of a rotary evaporator to give phenylacetylene-*d* (50 % yield).

3.3.2 Perfluorinated palladium catalysts for the direct catalytic oxidation of alkyl alcohols to carboxylic acids

General procedure for the calculation of k_f of complexes formed by Pd(OAc)$_2$/ligand

Pd(OAc)$_2$ was mixed with 4 different amount of the corresponding ligand and each sample was solubilized in CDCl$_3$. ^{1}H NMR and ^{19}F NMR allowed to reveal the signals related to the formation of the complexes and to quantify the amount of complex generated in each case. The calibration curve permitted to calculate k_f from the relation: $k_f = ([Pd] \cdot [L])/[PdL]$.

General reaction procedure for oxidation reaction of alkyl alcohols (**11a-e**)
catalyzed by **1, 2, 14-16** and Pd(OAc)$_2$/ligand
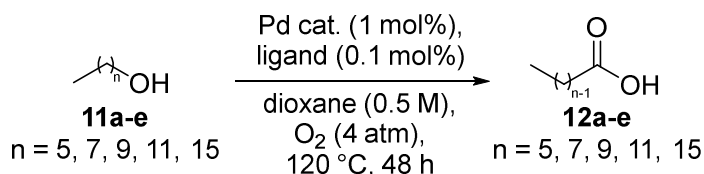
The alcohol (0.25 mmol), hexadecane (3 μL), as an internal standard, were
inserted with a 1 mol% of the corresponding palladium catalyst and 0.1 mol%
of ligand, when necessary, in 0.5 ml of dioxane, in a 10 ml glass vial equipped
with a stirring bar. The sealed vial was charged with O$_2$ and the mixture stirred
at 120 °C for 48 h. Consequently, the mixture was analyzed by GC and by GC-
MS.

General reaction procedure for oxidation reaction of hexanol (**11a**) catalyzed
by Pd(OAc)$_2$/^{2}F-py in presence of DABCO

The alcohol (0.25 mmol), DABCO (0.125 mmol), hexadecane (3 μL), as an
internal standard, were inserted with a 1 mol% of Pd(OAc)$_2$ and 0.1 mol% of
^{2}F-py in 0.5 ml of dioxane, in a 10 ml glass vial equipped with a stirring bar.
The sealed vial was charged with O$_2$ and the mixture stirred at 120 °C for 24 h.
At increasing amount of time, samples were taken and analyzed by GC. At each
point of the kinetic the vial was degassed and charged back with O$_2$.

Reuses of catalysts

After the reaction procedures described above, the solid catalyst was recovered
by filtration and washed with dioxane. Subsequently, the dried catalyst was
weighted, and reagents and solvent were added in proportional amounts to the

initial relative molar ratios.

3.3.3 Palladium single atoms for the direct catalytic oxidation of benzyl alcohols to carboxylic acids

General procedure for the oxidation reaction of benzyl alcohols catalyzed by Pd(OAc)$_2$, Pd/C and **21**-**22**

Pd(OAc)$_2$ was weighed (0.13−1.3 mg, which corresponds to 0.03 to 0.30 mol%, respectively) in a double-walled 10 mL reactor equipped with a needle connected to a manometer and a stirring bar. Then, the corresponding benzyl alcohol (1.96 mmol) was added, and after setting an atmosphere of 4 atm O$_2$, the reactor was heated at 150 °C at a stirring rate of 450 rpm for the required reaction time. The addition of mesitylene (3 μL) as an external standard allowed to follow the course of the reaction by GC and by GC-MS. Supported Pd nanoparticles of different loadings 10, 5, and 1 % in weight and MOF **22** (1 % in weight) were used as catalysts for the same purpose.

General procedure for trapping Pd species on active charcoal

The active catalytic species, formed *in situ*, were trapped in active charcoal after 60 min of the reaction described above, when catalyzed by Pd(OAc)$_2$. For this purpose, active charcoal and 2 ml of methanol were added after depressurization of the reaction, while the reaction mixture was being stirred at reaction temperature. After stirring for 10 min, the whole mixture was centrifuged and washed 3 times with 2 ml of fresh methanol each time. Afterwards, the samples were dried at 70 °C under vacuum overnight and then analyzed by HRTEM. The amount of charcoal was calculated in order to obtain a sample with *ca.* 2−3 wt% of Pd.

<u>General Procedure for Ultraviolet−Visible (UV−Vis) spectrophotometric titrations</u>

After the reaction procedure described above, the mixture was quenched at different reaction times with 4 mL of a 0.02 M triphenylphosphine solution in dichloromethane and analyzed by UV−Vis spectrophotometry in quartz cuvettes with an optical path of 10×10 mm^2.

<u>Synthesis of {Cu$_6$Sr[(S,S)-Mecysmox]$_3$(OH)$_2$(H$_2$O)}·15H$_2$O (**20**)</u>

(Me$_4$N)$_2${Cu$_2$[(S,S)-methox](OH)$_2$}·4H$_2$O (6.0 mmol) was dissolved in 50 ml of water. Then, Sr(NO$_3$)$_2$ (2.0 mmol) in water (10 ml) was added dropwise under stirring. The stirring was prolonged over 10 h, at room temperature, and at the end a green polycrystalline powder was obtained, filtrated and dried. Synthesis performed in the ICMol by the Emilio Pardo´s group.

<u>Synthesis of [Pd$_2$(H$_2$O)(NH$_3$)$_6$]$_{0.5}$Cl$_2$@{Sr^{II}Cu$^{II}_6$[(S,S)-Mecysmox]$_3$(OH)$_2$(CH$_3$OH)}·12H$_2$O (**21**)</u>

Crystals of **20** (0.015 mmol) were soaked in a water/methanol (1:1 v/v) solution of [Pd(NH$_3$)$_4$]Cl$_2$ (0.015 mmol) for 6 h. After the repetition of this process for five times, crystals of **21** were washed with a water/methanol (1:1 v/v) solution several times, filtrated on paper and dried. Synthesis performed in the ICMol by the Emilio Pardo´s group.

<u>Synthesis of (Pd^0)$_{0.5}$([Pd^{II}(H$_2$O)(NH$_3$)$_3$]Cl$_2$)$_{0.5}$@{Sr^{II}Cu$^{II}_6$[(S,S)-Mecysmox]$_3$(OH)$_2$(CH$_3$OH)}·13H$_2$O (**22**)</u>

A powder polycrystalline sample of **21** (*ca.* 2 g) was suspended in water/ethanol (1:1 v/v) solution to which NaBH$_4$ was added progressively over

72 h in 15 fractions (0.4 mmol of $NaBH_4$ per each). Each fraction was left to react for 1.5 h. Finally, the samples were washed with a water/methanol solution, filtered and dried. Synthesis performed in the ICMol by the Emilio Pardo´s group.

3.3.4   Subnanometric aqueous metal clusters as antitumoral agents

Preparation of metal clusters in solution

1.3 g of EVOH29 was dissolved in 10 ml of a 1-propanol/distilled water (1:1 v/v) solution and heated at 65 °C under reflux. Once the copolymer was completely dissolved, the mixture was left to cool down at room temperature. Then, the precursor of the clusters, i.e., K_2PtCl_4, $Rh(acac)_3$ or $IrCl_3 \cdot 3H_2O$, was added in order to obtain metal loading of 100 nM. The solution was stirred overnight. Finally, water (10 ml) was added, stirred for 30 minutes and centrifuged to separate the polymer from the solutions of metal clusters. The solution was kept at -18 °C.

Preparation of Pt clusters in EVOH films

13 g of EVOH29 was dissolved in 100 mL of a 1-propanol/distilled water solution (1:1 v/v), which was heated at 75 °C under reflux. Once the copolymer was completely dissolved, the mixture was left to cool down at room temperature, and after this, K_2PtCl_4 or H_2PtCl_4 was added in order to obtain a metal loading of 0.02 mmol $Pt \cdot g^{-1}$ dry polymer. The resultant suspension was spread on a Teflon–coated glass plate using a 200 μm spiral bar coater. A digital Mitutoyo micrometer was used to determine film thickness, with an average value of 0.012 ± 0.003 mm. The Pt clusters were released in water by soaking 150 mg of the films in 10 ml of water/ethanol (1:1 v/v) for 2 h under stirring

and then separating the polymeric matrix. The solution was then kept at -18 °C.

Metal cluster cell uptake

HeLa cells were seeded at a density of 1.5×10^4 cells/well in 24–well plates, whereas for A2870 and A2870cis cell lines the seeded were 6.0×10^4 cells/well. On the following day, the cultures were treated with 0.5 µM of metal clusters or cisplatin and incubated for 4 h. Then, the supernatants were collected, and the cells were washed once with PBS and then lysed using a 10% Triton-100 solution. All samples were stored at –18 ºC until its quantification by ICP–MS.

Cytotoxicity Assay

Cells were seeded in 96–well plates at a density of 2.5×10^3 cells/well for HeLa cell line and 1.0×10^4 for both A2870 and A2870cis cell lines. The cells were treated with different concentrations of metal clusters, ranging from 0.05 to 0.7 µM for Pt MCs, 0.05 to 5 µM for Rh MCs and Ir MCs, and 0.1 to 50 µM for Au MCs, whereas cisplatin was used as cytotoxic standard compound at concentrations from 0.1 to 50 µM. After 24 h, 3-[4,5-dimethylthiazole-2-yl]-2,5-diphenyltetrazolium bromide (MTT) was added at 0.5 mg/ml and incubated for 4 h at 37 ºC. Finally, the medium was removed and the purple MTT–formazan product was solubilized in 100 µl of DMSO. The plates were read at 540 nm using a Synergy H1 multi-mode microplate reader (Biotek). For each compound, dose-response curves were determined, allowing the calculation of IC50 values (concentration of compound causing the 50% reduction of the formazan product formation) with the Graph Pad 5.0 software. Experiments performed in The Hospital La Fe by the Inmaculada Andreu´s group.

Fluorescence microscopic analysis of cell death using Annexin–V/ propidium iodide staining

HeLa cells were seeded at a density of 1.5×10^4 cells/well in 24–well plates. The following day, the plates were treated with metal clusters at IC50 concentrations (previously determined by the MTT assay) for 24 h. Afterwards, the cells were then incubated with 5 μl annexin V–FITC and 50 μl propidium iodide for 30 min, avoiding the presence of light. Finally, the cell cultures were imaged with the Leica fluorescence microscope PAULA using contrast phase for cell morphology, green LED filter (λ_{exc} = 488 nm) for annexin–V staining and the red LED filter (λ_{exc} = 543 nm) for propidium iodide. Experiments performed in The Hospital La Fe by the Inmaculada Andreu´s group.

Caspase–3 activation assay

HeLa cells (1.0×10^4 cells/well seeded in 96–well black plates) were treated with metal clusters at IC50 concentrations for 24 h. The next day, 100 µl of caspase–3 substrate (bis–N–CBZ–L–aspartyl–L–glutamyl–L–valyl–L–aspartic acid amide; Z–DEVD–R110), diluted in Apo–ONE® Homogeneous Caspase–3/7 Buffer was added to each well. Fluorescent Rhodamine R110 release was continuously monitored using the Synergy H1 multi–mode microplate reader at 37ºC (λ_{exc} = 499 nm, λ_{em} = 521 nm). Experiments performed in The Hospital La Fe by the Inmaculada Andreu´s group.

Lactate dehydrogenase (LDH) release assay

Cells were plated in 96–well plates at a density of 1.0×10^4 cells/well. Afterward, the cells were treated with metal clusters at IC50 concentrations for 24 h. On the following day, the cell membrane integrity was evaluated using

the Cytotox–ONE Homogeneous Membrane Integrity Assay Kit (Promega) according to the manufacturer instructions. Fluorescence was recorded (λ_{exc} = 560 nm, λ_{em} = 590 nm) using the Synergy H1 multi–mode microplate reader. Experiments performed in The Hospital La Fe by the Inmaculada Andreu´s group.

3.4 Characterization of isolated compounds
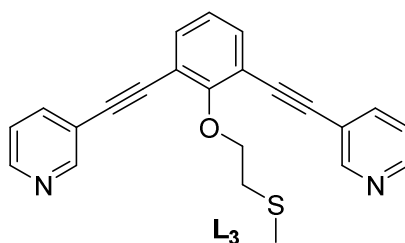
4,4'-((2-(2-(methylthio)ethoxy)-1,3-phenylene)bis(ethyne-2,1-diyl))dipyridine (L₃)

^{1}H-NMR (400 MHz, 293K, CDCl$_3$): δ = 7.56 (d, J= 8Hz, 2H), 6.82 (t, J= 8Hz, 1H), 4.23 (t, J= 6.8Hz, 2H), 2.91 (t, J= 6.8Hz, 2H), 2.16 (s, 3H).
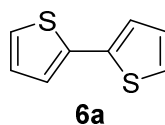
2,2'-bithiophene (**6a**) [14]

^{1}H NMR (300 MHz, CDCl$_3$) δ: 7.22 (dd, J = 5.1, 1.0 Hz, 2H), 7.19 (dd, J = 3.6, 1.0 Hz, 2H), 7.03 (dd, J = 5.1, 3.6 Hz, 2H). ^{13}C NMR (75 MHz, CDCl$_3$) δ: 137.56, 127.90, 124.49, 123.91. IR (υ, cm^{-1}): 698, 743, 912, 1050, 1250, 1770, 2990. GC-MS (m/z, M^{+}· 287), major peaks found: 166 (100%), 121 (32%), 93

(5%), 69 (9%), 45 (7%).

6c
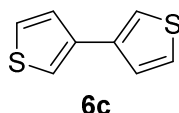
3,3'-bithiophene (**6c**) [15]

^{1}H NMR (300 MHz, CDCl$_3$) δ: 7.39 – 7.36 (m, 2H), 7.36 – 7.32 (m, 4H). IR (υ, cm^{-1}): 1089, 1468, 1410, 3411. GC-MS (m/z, M$^{+\cdot}$ 287), major peaks found: 166 (100%), 121 (33%), 95 (4%), 69 (7%), 45 (10%).

6d
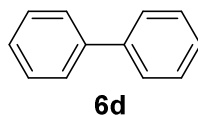
1,1'-biphenyl (**6d**) [16]

^{1}H NMR (300 MHz, CDCl$_3$) δ: 7.65 (d, J = 7.3 Hz, 4H), 7.49 (dd, J = 7.5, 7.5 Hz, 1H), 7.44 – 7.36 (m, 2H). ^{13}C NMR (75 MHz, CDCl$_3$) δ: 141.40, 128.89, 127.39, 127.31. IR (υ, cm^{-1}): 697, 728, 1250, 1770, 2990. GC-MS (m/z, M$^{+\cdot}$ 287), major peaks found: 154 (100%), 128 (5%), 102 (4%), 76 (11%), 51 (6%), 28 (4%).

6e
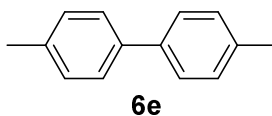
4,4'-dimethyl-1,1'-biphenyl (**6e**) [17]

^{1}H NMR (300 MHz, CDCl$_3$) δ: 7.55 (d, J = 8.1 Hz, 4H), 7.29 (t, J = 7.8 Hz, 4H), 2.46 (s, 6H). ^{13}C NMR (75 MHz, CDCl$_3$) δ: 138.44, 136.80, 129.57, 126.94, 21.19. IR (υ, cm^{-1}): 803, 1250, 1770, 2990. GC-MS (m/z, M$^{+\cdot}$ 287),

major peaks found: 182 (100%), 168 (44%), 152 (10%), 115 (8%), 90 (12%), 28 (8%).

9a
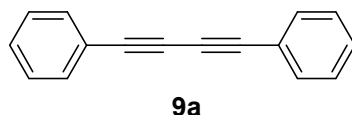
1,4-diphenylbuta-1,3-diyne (**9a**) [18]

^{1}H NMR (300 MHz, CDCl$_3$) δ: 7.60 – 7.49 (m, 4H), 7.43 – 7.30 (m, 6H). ^{13}C NMR (75 MHz, CDCl$_3$) δ: 132.65, 129.35, 128.58, 121.97, 81.71, 74.08. IR (υ, cm^{-1}): 687, 755, 915, 1440, 1480, 1590, 2150, 3050.

9b
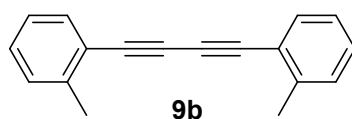
<u>1,4-di-*o*-tolylbuta-1,3-diyne (**9b**)</u> [19]

^{1}H NMR (300 MHz, CDCl$_3$) δ: 7.50 (d, *J* = 7.6 Hz, 2H), 7.32 – 7.10 (m, 6H), 2.50 (s, 6H). ^{13}C NMR (75 MHz, CDCl$_3$) δ: 141.78, 133.07, 129.72, 129.24, 125.80, 121.90, 81.30, 77.69, 20.86. IR (υ, cm^{-1}): 712, 754, 1040, 1110, 1460, 1480, 2140, 2920, 3060. GC-MS (m/z, M$^{+\cdot}$ 230), major peaks found: 230 (100%), 202 (20%), 115 (61%).

H$_3$CO   **9c**   OCH$_3$
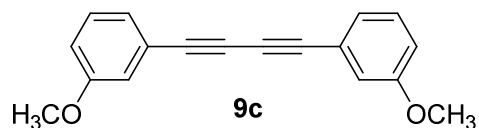
<u>1,4-bis(3-methoxyphenyl)buta-1,3-diyne (**9c**)</u> [18]

^{1}H NMR (300 MHz, CDCl$_3$) δ: 7.25 (dd, J = 7.9, 7.9 Hz, 1H), 7.13 (d, J = 7.5 Hz, 1H), 7.05 (s, 1H), 6.94 (d, J = 8.4 Hz, 1H), 3.81 (s, 6H). ^{13}C NMR (75

MHz, CDCl$_3$) δ: 159.48, 129.68, 125.23, 122.87, 117.27, 116.19, 81.67, 73.82, 55.45. IR (υ, cm^{-1}): 683, 779, 1050, 1150, 1220, 1290, 1460, 1490, 1590, 2150, 2830, 2940, 2960. GC-MS (m/z, M$^{+\cdot}$ 262), major peaks found: 262 (100%), 219 (20%), 176 (20%), 150 (9%).
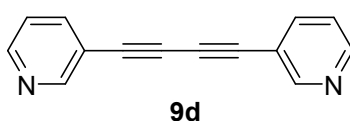
1,4-di(pyridin-3-yl)buta-1,3-diyne (**9d**) [18]

^{1}H NMR (300 MHz, CDCl$_3$) δ: 8.77 (d, J = 2.2 Hz, 1H), 8.60 (dd, J = 4.9, 1.7 Hz, 1H), 7.82 (ddd, J = 7.9, 2.0, 2.0 Hz, 1H), 7.30 (dd, J = 4.9, 7.9 Hz, 1H). ^{13}C NMR (75 MHz, CDCl$_3$) δ: 153.31, 149.65, 139.54, 123.24, 119.03, 79.32, 77.36. IR (υ, cm^{-1}): 696, 802, 1410, 2920. GCMS (m/z, M$^{+\cdot}$ 204), major peaks found: 204 (100%), 176 (9%), 151 (20%), 122 (8%), 98 (20%), 74 (9%).
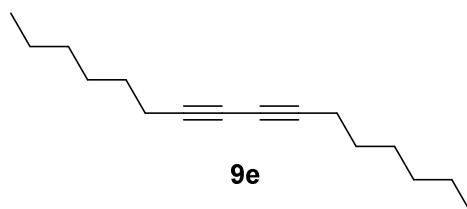
hexadeca-7,9-diyne (**9e**) [20]

^{1}H NMR (300 MHz, CDCl$_3$) δ: 2.24 (t, *J* = 6.9 Hz, 4H), 1.57 – 1.45 (m, 4H), 1.43 – 1.34 (m, 4H), 1.34 – 1.21 (m, 8H), 0.88 (t, *J* = 6.7 Hz, 3H). ^{13}C NMR (75 MHz, CDCl$_3$) δ: 77.67, 65.42, 31.45, 28.67, 28.48, 22.65, 19.36, 14.16. IR (υ, cm^{-1}): 748, 913, 2930. GC-MS (m/z, M$^{+\cdot}$ 218), major peaks found: 218 (0.1%), 189 (10%), 147 (10%), 119 (41%), 91 (100%), 67 (40%), 41 (36%).

10a
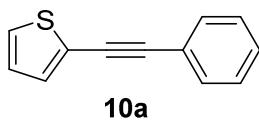
2-(phenylethynyl)thiophene (**10a**) [21]

^{1}H NMR (300 MHz, CD$_3$CN) δ: 7.58 – 7.50 (m, 1H), 7.44 – 7.37 (m, 5H), 7.32 (dd, J = 3.6, 1.1 Hz, 1H), 7.06 (dd, J = 5.2, 3.7 Hz, 1H).^{13}C NMR (75 MHz, CD$_3$CN) δ: 133.42, 132.22, 130.71, 129.68, 129.09, 128.55, 123.70, 123.57, 82.55. GC-MS (m/z, M[+.] 184), major peaks found: 184 (100%), 152 (13%), 139 (23%).

3.5 References

1. Günther, H., The physical basis of the nuclear magnetic resonance experiment, in *NMR spectroscopy: Basic principles, concepts and applications in chemistry, 3rd edition*, H. Günther, Editor. **2013**, Wiley-VCH.

2. Perkampus, H.-H., Principles, in *UV-Vis spectroscopy and its applications*, H.-H. Perkampus, Editor. **1992**, Springer-Verlag.

3. Moores, A.; Goettmann, F., The plasmon band in noble metal nanoparticles: An introduction to theory and applications. *New J. Chem.* **2006**, *30* (8), 1121-1132.

4. Vilar-Vidal, N.; Blanco, M. C.; López-Quintela, M. A.; Rivas, J.; Serra, C., Electrochemical synthesis of very stable photoluminescent copper clusters. *J. Phys. Chem. C* **2010**, *114* (38), 15924-15930.

5. de Heer, W. A., The physics of simple metal clusters: Experimental aspects and simple models. *Rev. Mod. Phys.* **1993**, *65* (3), 611-676.

6. Dye, D. H.; Ketterson, J. B.; Crabtree, G. W., The Fermi surface of platinum. *J. Low Temp. Phys.* **1978**, *30* (5), 813-838.

7. Bianconi, A., Surface X-ray absorption spectroscopy: Surface EXAFS and surface XANES. *Appl. Surf. Sci.* **1980**, *6* (3), 392-418.

8. Azcarate , I.; Huo, Z.; Farha , R.; Goldmann , M.; Xu, H.; Hasenknopf, B.; Lacôte , E.; Ruhlmann, L., Generation of photocurrent by visible-light irradiation of conjugated dawson polyoxophosphovanadotungstate-porphyrin copolymers. *Chem. Eur. J.* **2015**, *21* (22), 8271-8280.

9. Schmidt, B.; Berger, R.; Kelling, A.; Schilde, U., Pd-catalyzed [2+2+1] coupling of alkynes and arenes: Phenol diazonium salts as mechanistic trapdoors. *Chem. Eur. J.* **2011**, *17* (25), 7032-7040.

10. Adam, R.; Mon, M.; Greco, R.; Kalinke, L. H. G.; Vidal-Moya, A.; Fernandez, A.; Winpenny, R. E. P.; Doménech-Carbó, A.; Leyva-Pérez, A.; Armentano, D.; Pardo, E.; Ferrando-Soria, J., Self-assembly of catalytically active supramolecular coordination compounds within metal-organic frameworks. *J. Am. Chem. Soc.* **2019**, *141* (26), 10350-10360.

11. Fujita, M.; Sasaki, O.; Mitsuhashi, T.; Fujita, T.; Yazaki, J.; Yamaguchi, K.; Ogura, K., On the structure of transition-metal-linked molecular squares. *Chem. Commun.* **1996**, (13), 1535-1536.

12. Fortea-Pérez, F. R.; Mon, M.; Ferrando-Soria, J.; Boronat, M.; Leyva-Pérez, A.; Corma, A.; Herrera, J. M.; Osadchii, D.; Gascon, J.; Armentano, D.; Pardo, E., The MOF-driven synthesis of supported palladium clusters with catalytic activity for carbene-mediated chemistry. *Nat. Mater.* **2017**, *16* (7), 760-766.

13. Kohler, D. G.; Gockel, S. N.; Kennemur, J. L.; Waller, P. J.; Hull, K. L., Palladium-catalysed anti-Markovnikov selective oxidative amination. *Nat. Chem.* **2018**, *10* (3), 333-340.

14. Nising, C. F.; Schmid, U. K.; Nieger, M.; Bräse, S., A new protocol for the one-pot synthesis of symmetrical biaryls. *J. Org. Chem.* **2004**, *69* (20), 6830-3.

15. Billingsley, K.; Buchwald, S. L., Highly efficient monophosphine-based catalyst for the palladium-catalyzed Suzuki−Miyaura reaction of heteroaryl halides and heteroaryl boronic acids and esters. *J. Am. Chem. Soc.* **2007**, *129* (11), 3358-3366.

16. Bandari, R.; Höche, T.; Prager, A.; Dirnberger, K.; Buchmeiser, M. R., Ring-opening metathesis polymerization based pore-size-selective

functionalization of glycidyl methacrylate based monolithic media: Access to size-stable nanoparticles for ligand-free metal catalysis. *Chem.* **2010**, *16* (15), 4650-8.

17. Kuroboshi, M.; Waki, Y.; Tanaka, H., Palladium-catalyzed tetrakis(dimethylamino)ethylene-promoted reductive coupling of aryl halides. *J. Org. Chem.* **2003**, *68* (10), 3938-3942.

18. Park, J.; Park, E.; Kim, A.; Park, S. A.; Lee, Y.; Chi, K. W.; Jung, Y. H.; Kim, I. S., Pd-catalyzed decarboxylative coupling of propiolic acids: One-pot synthesis of 1,4-disubstituted 1,3-diynes via Sonogashira-homocoupling sequence. *J. Org. Chem.* **2011**, *76* (7), 2214-9.

19. Schmidt, R.; Thorwirth, R.; Szuppa, T.; Stolle, A.; Ondruschka, B.; Hopf, H., Fast, ligand- and solvent-free synthesis of 1,4-substituted buta-1,3-diynes by Cu-catalyzed homocoupling of terminal alkynes in a ball mill. *Chem. Eur. J.* **2011**, *17* (29), 8129-8138.

20. Zhang, S.; Liu, X.; Wang, T., An efficient copper-catalyzed homocoupling of terminal alkynes to give symmetrical 1,4-disubstituted 1,3-diynes. *Adv. Synth. Catal.* **2011**, *353* (9), 1463-1466.

21. Huang, H.; Jiang, H.; Chen, K.; Liu, H., Efficient iron/copper cocatalyzed alkynylation of aryl iodides with terminal alkynes. *J. Org. Chem.* **2008**, *73* (22), 9061-9064.

Chapter 4

Catalytic activity of palladium supramolecular complexes within Metal-Organic Frameworks (MOFs)

4 Catalytic activity of palladium supramolecular complexes within Metal-Organic Frameworks (MOFs)

4.1 Introduction

The possibility of tuning structural characteristics, such as shape, size, or porosity, provides to Metal-Organic Frameworks (MOFs) their remarkable host-guest chemical properties [1-4], consequently making them outstanding platforms for various applications. Moreover, the latest developments in single-crystal X-ray crystallography have given the possibility to structurally characterize these new materials, and then to fully understand what is happening within the channels [5-8]. This has had consequences on the quite enormous amount of MOFs applications in many different fields as adsorption and separation of gases [9-15] or small molecules [16-21], and catalysis [22-27]. However, there are still few examples in the direction of a potential ability of MOFs which has not yet been explored in depth: their capacity to work as chemical *nano*reactors [22, 28-33].

In this *Chapter*, the use of MOFs as vessels for the synthesis of Pd clusters [32] self-assembled in Supramolecular Coordination Complexes (SCCs) and their application in catalytic processes will be investigated.

As mentioned in *Chapter 1*, clusters are powerful catalysts, but they have a main drawback: their tendency to agglomerate even under gentle reaction conditions. Up to now, a solution to this problem has been the use of stabilizing ligands [34-37] and supporting on solids [38-40]. Even though the presence of ligands tolerates structural characterization of the clusters by single-crystal X-ray crystallography, ligand-stabilized clusters are hardly used in catalysis due to ligand/reactants exchange which can lead to decomposition of the clusters [37, 41-44]. On the other hand, the stability of supported clusters makes them novel and robust catalytic species, mainly due to the high reactivity of the uncoordinated atoms, as better explained in *Chapter 1*.

But what can happen if we combine the exceptional properties of supported clusters with supramolecular chemistry?

Over the last decades, SCCs have demonstrated their remarkable properties, e.g., catalysis within their distinctive confined environment [45-51]. Recently, a Co supramolecular complex has shown a quite elevated activity in the water splitting reaction carried out in photochemical or electrochemical conditions [52]. Despite the complex structures to be synthetised, Supramolecular Catalysis could be said not to have yet developed all its potential wide-ranging applications, possibly since the self-assembly of SCCs happens in solution, so in homogeneous phase. Consequently, this synthetic route causes a lack of control due also to the generation of very intricate complexes, often kept together by weak bonds [53-55]. Actually, this synthetic method brings to entirely-coordinated isolated metal atoms as structural nodes of the SCCs. Subsequently, the complete metal coordination

sphere obstructs any activation of the reagents on the metal site, not including the destruction of the complex, hence strictly limiting the use of SCCs in metal-based catalysis. This concept is proved by the few examples of catalytic reactions performed by the sensitive [56] spherical polyhedra with general formula Pd_nL_{2n} [57, 58]. However, the plethora of possible structures borne by the pivotal metal centres opens new paths in metal-based catalysis, encouraging to develop functional SCCs, otherwise not approachable.

In the following pages, we describe three original mechanically-bonded SCCs inside the distinctive confined space of MOF channels (SCCs@MOF) and their *in-situ* heterogeneous self-assembly, supported by a detailed structural characterization performed by single crystal X-ray diffraction (SCXRD). At the vertexes of these supramolecular complexes there are Pd_2 clusters, previously formed and stabilized by the MOF framework [32]. Using this MOF as reactor, a Pd_8 square metal-organic polygon, a Pd_{16} supramolecular cage and a heterobimetallic Au^{III}–Pd^{II} cage are formed.

The homocoupling of boronic acids, alkynes, and their cross-coupling, are heterogeneously catalysed by the SCCs describes above, reaching higher catalytic activity and selectivity than the ones obtained by using homogeneous Pd catalysts. The catalysis points out another important feature of these complexes: their ability to retain their structural integrity, in contrast to traditional cages assembled in solution and used in homogeneous catalysis. Indeed, the mechanical bonds between the cages and the MOF framework allow these materials to be quite stable under catalytic conditions, making them ones of a kind.

4.2 Synthesis and characterization of the SCCs@MOF catalysts

A collaborating group performed the synthesis of SCCs@MOF by a template-directed strategy, using Post-Synthetic Methodologies (PSMs) [59-63]. The selected chemical *nano*reactor was a highly crystalline MOF, with the following formula

$[Pd^{II}(NH_3)_4][Pd^{II}_2(\mu\text{-}O)(NH_3)_6)(NH_4)_2]_{0.5}\{Ni^{II}_4[Cu^{II}_2(Me_3mpba)_2]_3\}\cdot 52H_2O$ (**1**) [32].
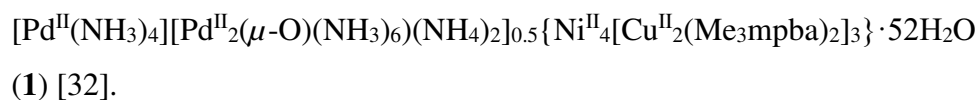
Crystals of MOF **1** were soaked with a solution of linear (L_1) and bended ($L_{2,3}$) ligands to produce the unique *in-situ* heterogeneous self-assembled SCCs within MOF channels, which act as templating agents, as shown in Figure 4.1. Not only did the environment offered by MOF channels contribute to the generation of these novel MOFs, but also the presence of dinuclear oxo-bridged palladium(II) entities in the MOFs pores helped to keep the Pd dimers as pivotal metal centers for the formation of the SCCs.
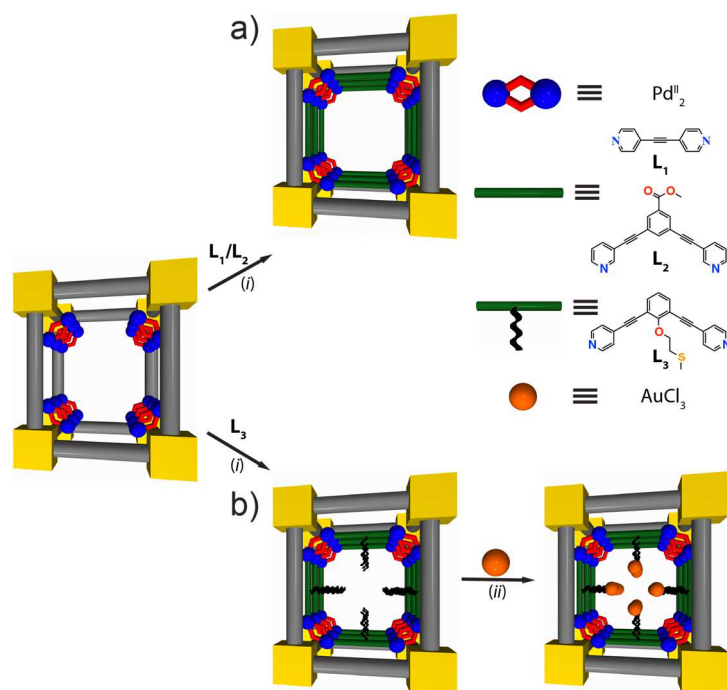
Figure 4.1 Post-synthetic methodologies for the sequential template-directed synthesis of original homo- (a) and heterobimetallic (b) mechanically-bonded catalytically-active SCCs within MOFs channels (SCCs@MOF). (i) Incorporation of desired organic ligand with suitable structures and their coordination and (ii) post-assembly Au metalation of SCCs@MOF, formed using L_3.

The large octagonal pores (virtual diameter of *ca*. 2.0 nm) of this MOF are hosting Pd^{II}_2 dimers, which occupy specific positions of the channels (Figure 4.2a center) and the use of several characterization techniques allowed to deeply understand these materials. First, SCXRD allowed to obtain the crystal structures of **2** and **3**, and nearly a full structural resolution of **4**. The crystallinity and robustness of these materials made possible to achieve these

original results and to use of X-ray crystallography techniques, which provided a novel route of visualization of SCCs within MOF channels (Figures 4.2 and 4.3).
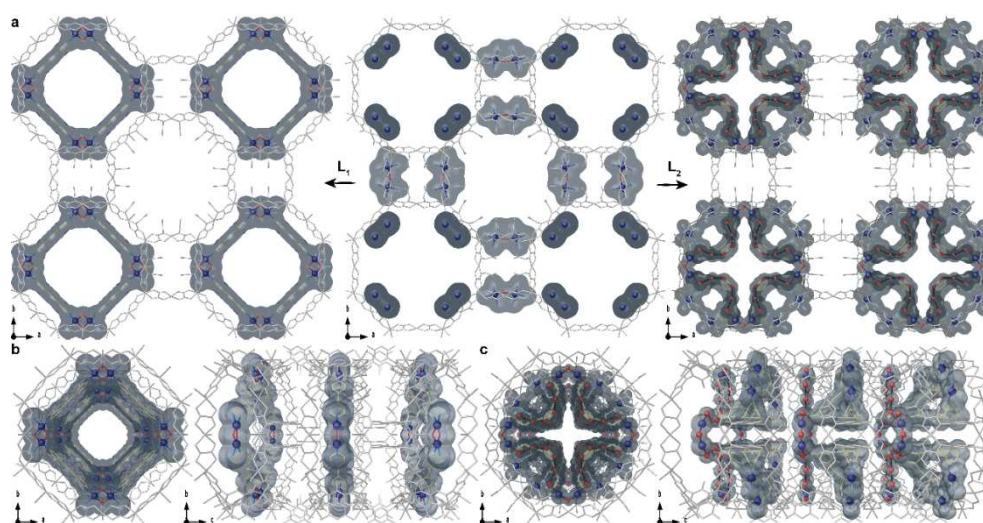
Figure 4.27 Structures along the channels, determined by synchrotron X-ray diffraction, of the Pd_8@MOF **2** (left) and the Pd_{16}@MOF **3** (right), synthesised from the *in-situ* reaction of the Pd^{II}_2-containing MOF **1** (center) with the dipyridine ligands L_1 and L_2, respectively [L_1 = 1,2-di(pyridn-4-yl)ethyne and L_2 = methyl 3,5-bis(pyridine-4-ylethynyl)benzoate] (a). Views of one single channel of **2** (b) and **3** (c) in the *ab* (left) and *bc* (right) crystallographic planes. Color scheme: the grey sticks represent the heterobimetallic CuNi 3D anionic network. The blue spheres and gold sticks are Pd^{II} cations in the pores of MOF **1**–**3** and ligands of the SCCs, respectively. The black dotted lines depict hydrogen-bonds that are resposible of the formation of the water-assisted Pd^{II}_{16} supramolecular assembly.

Thus, a novel Pd^{II}_8 square metal-organic polygon (**2**) was grown by soaking MOF **1** in a solution of the linear ligand L_1 and a water-assisted Pd^{II}_{16} supramolecular assembly (**3**) was prepared with the bended ligand L_2, respectively, with formulas

$[Pd^{II}_2(\mu–OH_2)_2(NH_3)_4)]_{0.5}[Pd^{II}_8(\mu–OH_2)_8(NH_3)_8(L_1)_4]_{0.125}$
$\{Ni^{II}_4[Cu^{II}_2(Me_3mpba)_2]_3\} \cdot 43H_2O$ (**2**) (Figures 4.2a left and 4.2b)

$[Pd^{II}_{16}(H_2O)_8(NH_3)_{24}(\mu\text{-}OH_2)_4(H_2O)_{24}(L_2)]_{0.125}\{Ni^{II}_4[Cu^{II}_2(Me_3mpba)_2]_3\} \cdot 30H_2O$ (**3**) (Figures 4.2a right and 4.2c).
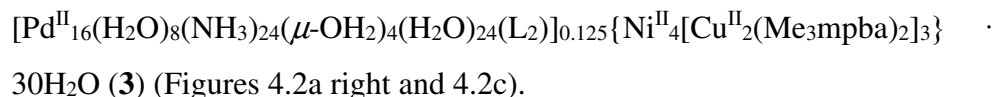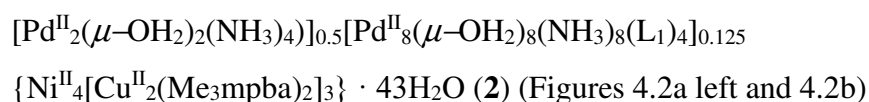
After the assembly of a SCC@MOF using L_3 as ligand, the thioether-functional group on the ligand behaved as a secondary point of anchoring for an additional metal, e.g., gold. Then, when the ligand was L_3, the synthesis of the supramolecular complex within MOF channels and the following metalation of the SCC@MOF resulted in the formation of a heterobimetallic assembly with formula

$[Au^{III}_2(\mu\text{-}OH)_2(OH)_4)]_{0.5}[Au^{III}_2Cl_6Pd^{II}_2(NH_3)_6(L_3)_2]_{0.5}[Pd^{II}_2(\mu\text{-}OH_2)(NH_3)_6)]_{0.5}\{Ni^{II}_4[Cu^{II}_2(Me_3mpba)_2]_3\} \cdot 37H_2O$ (**4**) (Figures 4.3).
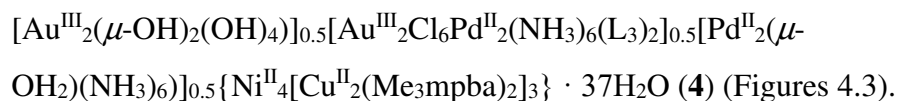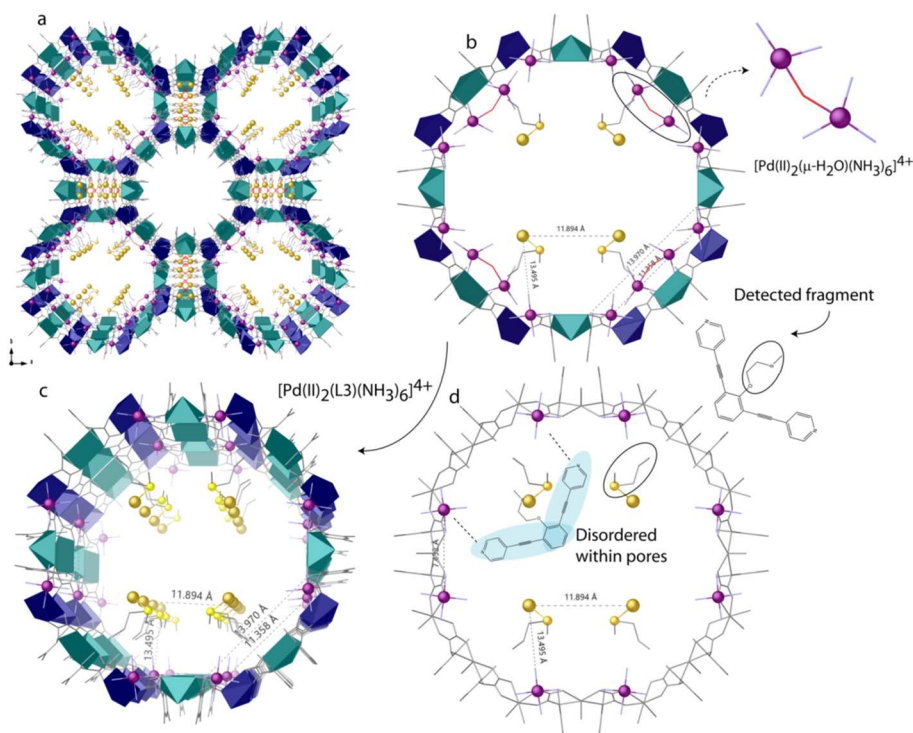
Figure 4.3 MOF **4** view along *c* crystallographic axis, illustrating the global distribution of metal ions within the MOF pores (a). View of a single pore of MOF **4**, highlighting the fragments of the $[Pd^{II}_2(\mu\text{-OH}_2)(NH_3)_6)]$ dimers and the $[Au^{III}_2Cl_6Pd^{II}_2(NH_3)_6(L_3)_2]$ heterobimetallic SCCs, detected by SCXRD (b). Views of a single pore along *c* axis only representative of $[Au^{III}_2Cl_6Pd^{II}_2(NH_3)_6(L_3)_2]$ fragments and showing parameters details associated to Pd···Pd and Pd···Au separations and ligand scheme (c-d).

Color scheme: Cu and Ni atoms of the framework are represented by cyan and blue polyhedral, respectively. The grey sticks represent the organic ligands. Palladium, gold, and sulfur are shown as purple, gold, and yellow spheres, respectively.

The crystal structures of **2**-**4** obtained by SCXRD highlight the stability of the 3D network crystallinity even during the MOF-templated self-assembled process. As shown in Figure 4.2, the known pillared square/octagonal layer architecture of **1** is preserved in **2**–**4** by the anionic $Ni^{II}_4Cu^{II}_6$ open-framework structure. From Figure 4.2, it is also clear that the largest hydrophobic octagonal channels and the smallest square pores hold Pd^{II} (**2**–**3**) and Pd^{II}/Au^{III} (**4**) complexes, resulting from the L_1-L_3 binding to the Pd species of **1**, i.e., mononuclear and dinuclear complexes $[Pd^{II}(NH_3)_4]^{2+}$ and $[Pd^{II}_2(\mu–O)(NH_3)_6]^{2+}$. The mechanical-bonds with the MOF network stabilize the SCCs of **2**–**4** in, which are strictly correlated to the nature of the applied ligands (L) in terms of shape, size, and symmetry.

In MOF **2**, half of the Pd^{2+} ions from **1** were coordinated by L_1 forming $[Pd^{II}_8(\mu–OH_2)_8(NH_3)_8(L_1)_4]^{16+}$ square polygons, with $[Pd^{II}_2(\mu-OH_2)_2(NH_3)_2]$ dimers at the vertexes of a quadrangular supramolecular metallacyclic complex (SMC) (Figures 4.2a left, 4.2b and 4.4). As shown in Figure 4.4, the regular square planar geometry had the following parameters: Pd-N [2.02(2) and 2.09(2) Å for Pd-N_{L1} and Pd-NH_3] and Pd-OH_2 [1.99(2) and 2.05(2) Å], distances similar to those present in the literature [56, 64], whereas the Pd^{II} distances *via* H_2O and L_1 bridges were 2.840(6) and 13.49(1) Å. The $Pd^{II}\cdots Pd^{II}$ separation among pillared adjacent polygons along *c* crystallographic axes is 15.15(1) Å and is stabilized by mechanical-bonds with the MOF net by terminal NH_3 molecules and oxamate residues [$H_3N\cdots O_{oxamate}$ 2.913(9) Å].
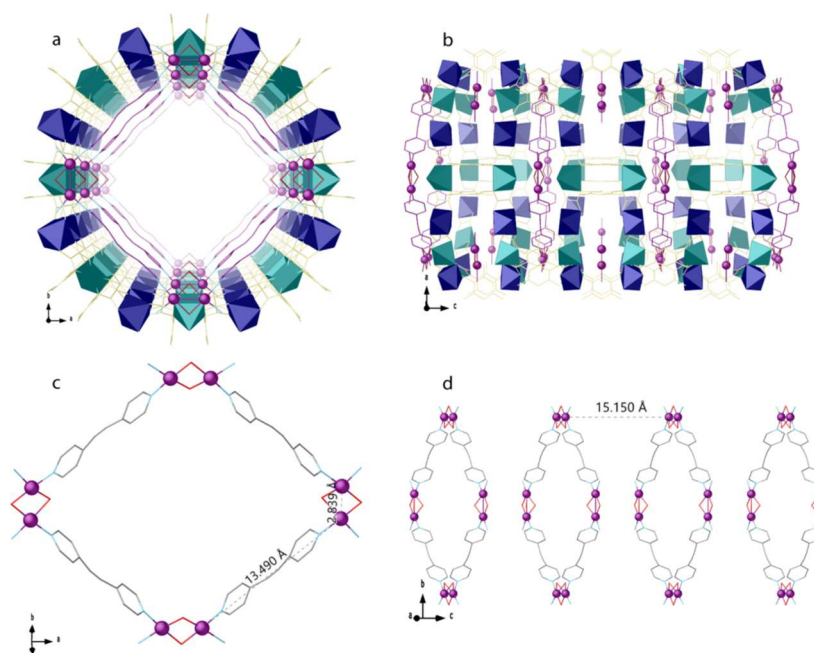
Figure 4.4 Perspective views of MOF **2** along c or b axes displaying the Pd^{II}_8 and Pd^{II}_2 complexes (a-b). Perspective view of a Pd^{II}_8 SMC (c) and of the propagation along the [101] direction of a single channel (d) highlighting the intra-assembly structural parameters associated to $Pd^{II}\cdots Pd^{II}$ separations. Color scheme: Cu and Ni atoms are represented by cyan and blue polyhedra, respectively. Ligands of the network are represented as yellow sticks, whereas L_1 is depicted as purple sticks. Pd^{2+} are purple spheres, meanwhile blue, red and grey sticks represent nitrogen, oxygen, and carbon atoms, respectively.

Considering the different structural parameters and symmetry, ligand L_2 enforces an entirely different assembly in MOF **3**, leading to a $[Pd^{II}_{16}(H_2O)_8(NH_3)_{24}(\mu\text{-}OH_2)_4(H_2O)_{24}(L_2)]$ supramolecular cage, where $[Pd^{II}_2(NH_3)_6(L_2)]$ dimers and $[Pd^{II}_2(\mu\text{-}OH_2)_4(H_2O)_6]$ dimers are connected by strong hydrogen bonds, between the carboxylate group of L_2 and H_2O

molecules [O···O of 2.31(1) for COO···O_{water} and 2.57(1) Å for O_{water}···O_{water}] (Figures 4.2a right, 4.2c and and 4.5).
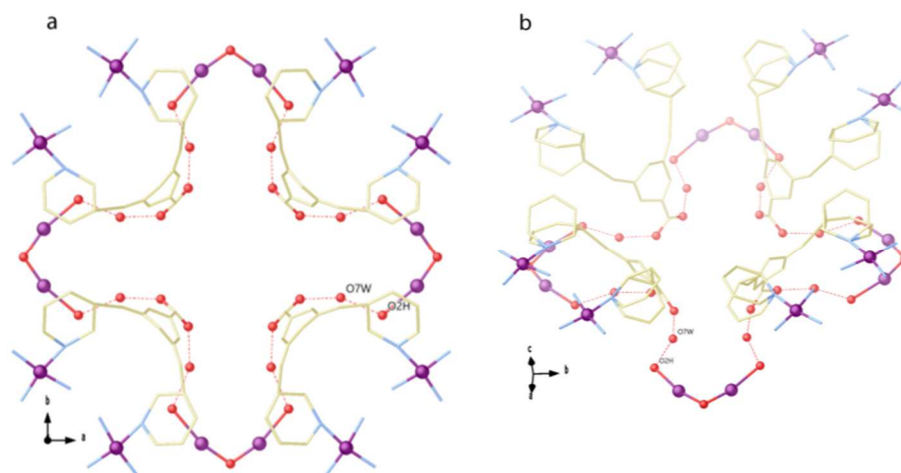
Figure 4.5 Structure of Pd^{II}_{16} cage in **3.** View along *c* crystallographic axis (a) and perspective view (b) of $[Pd^{II}_2(NH_3)_6(L_2)]$ and $[Pd^{II}_2(\mu\text{-}OH_2)_4(H_2O)_6]$ dimers. Color Scheme: Pd and O atoms are depicted as purple and red spheres. Carbon and nitrogen atoms of the ligands L_2 are depicted as yellow and blue sticks, respectively.

Pd^{II} ions were present in deformed square planar geometries with the following parameters: Pd-N in the $[Pd^{II}_2(NH_3)_6(L_2)]$ dimers of 1.99(1) and 2.00(1) Å for Pd-N_{L2} and Pd-NH_3, respectively, and Pd-OH_2 distances of the $[Pd^{II}_2(\mu\text{–}OH_2)_4(H_2O)_6]$ of 2.00(2) and 2.57(2) Å. In the $[Pd^{II}_2(NH_3)_6(L_2)]$ dimers the Pd^{II}···Pd^{II} separation was of 6.11(1) Å and of 9.00(1) Å in Pd_{16} assemblies. The latter were preserved, even during catalysis, by the strong H-

bonds and by the stable mechanical bonds with the net, demonstrating once more the relevance of interactions with a *nano*solvated confined space.

Regarding the crystal structure of **4**, a complete visualization of the SCC was not possible, due the lower precision of the data obtained by SCXRD. However, a proof of the SCC existence was given by the structure factor Fourier maps, that showed many local maxima ascribable to Pd^{2+} and Au^{3+} metal ions and few peaks associated to L_3 fragments. Moreover, it was quite possible that a self-assembly had happened in an analogous manner as detected in **2**, with the generation of $[Pd^{II}_2(NH_3)_6(L_3)_2]$ dimers residing in big hydrophobic pores with Pd(II) in square planar geometry with an average Pd-N distance of 2.10(2) Å, meanwhile Pd$\cdots$Pd and $N_{L3}\cdots N_{L3}$ separations between dimers were of 11.36 and 13.97(1) Å, as previously described in the literature for similar complexes [56, 64]. The high affinity of the thioether groups of L_3 for soft metal ions made possible the capture of $AuCl_3$ complexes by the $[Pd^{II}_2(NH_3)_6(L_3)_2]$ dimers, leading to self-assembled heterometallic SCCs of the type $[Au^{III}_2Cl_6Pd^{II}_2(NH_3)_6(L_3)_2]$ with Pd$\cdots$Au and Au$\cdots$Au distances of 13.50(1) and 11.89(1) Å, as shown in Figure 4.3. Additionally, the Au-S distance of 2.34(1) Å was unveiled by the resolved crystal structure, evidently showing thioether fragments. Attractively, the central position of Au^{III} ions in the big pores, dependent from L_3 symmetry, suggested an elevated accessibility for reactants and then a quite high applicability of this material in catalysis.

Moreover, the following methodologies were also employed for the characterization of these supramolecular entities: thermo-gravimetric and powder X-ray diffraction (powder XRD) analyses and N_2 adsorption isotherm

[65], elemental analysis, inductively coupled plasma-mass spectrometry, scanning electron microscopy (SEM), diffuse-reflectance (DR) UV-Vis, Raman, nuclear magnetic resonance (NMR), Fourier transform infrared (FT-IR) and X-ray photoelectron (XPS) spectroscopies (Table 4.1 and 4.2, Figures 4.6-4.9). Elemental analyses, ICP-AES and SEM/EDX allowed to know the atoms stoichiometry of the materials, as shown in Tables 4.1 and 4.2.

Table 4.10 Elemental analysis of compounds **1**, **2**, **3**, and **4**.

Compound	Element	% Calculated	% Found
1	C	25.65	25.68
	H	5.22	5.13
	N	7.67	7.33
2	C	28.65	28.75
	H	4.67	4.72
	N	6.36	6.31
3	C	29.50	29.39
	H	4.25	4.08
	N	6.50	6.23
4	C	28.39	28.85
	H	4.08	4.33
	S	0.75	0.90
	N	6.56	6.80

Table 4.2 ICP-MS and SEM/EDX analysis of compounds **1**, **2**, **3**, and **4**. The stoichiometry is given matching to formula unit.

Compound	Metal	ICP-MS		SEM/EDX	
		% mass	metal stoichiometry	*%* mass	metal stoichiometry
1	Cu	10.571	6.00	10.43	5.92
	Ni	6.518	4.01	6.47	3.98
	Pd	5.892	1.99	5.77	1.95
2	Cu	10.661	5.98	10.68	5.99
	Ni	6.584	4.00	6.63	4.03
	Pd	5.922	1.98	5.87	1.97
3	Cu	11.603	6.00	11.68	6.03
	Ni	7.134	3.99	7.23	4.05
	Pd	6.493	2.00	6.54	2.02
4	Cu	8.932	6.00	8.98	6.03
	Ni	5.573	4.05	5.56	4.04
	Pd	4.935	1.98	4.99	2.00
	Au	9.159	1.99	9.25	2.00

The comparison of the magic angle spinning solid ^{13}C nuclear magnetic resonance (MAS solid ^{13}C NMR) of MOF **1** with SCCs@MOF **2–4**, shown in Figure 4.6, underlined the appearance of new sharper signals at 165, 150 and 90 ppm, which agreed with the predicted values for the ligands. On the other hand, the signals at -40, 40, 130 and 230 ppm were associated to framework amides, being shifted and broadened by the paramagnetic action

of the Cu^{II} metal ions. Furthermore, the spectrum of **4** displayed a signal at 70 ppm corresponding to the expected chemical shift for ether moieties.
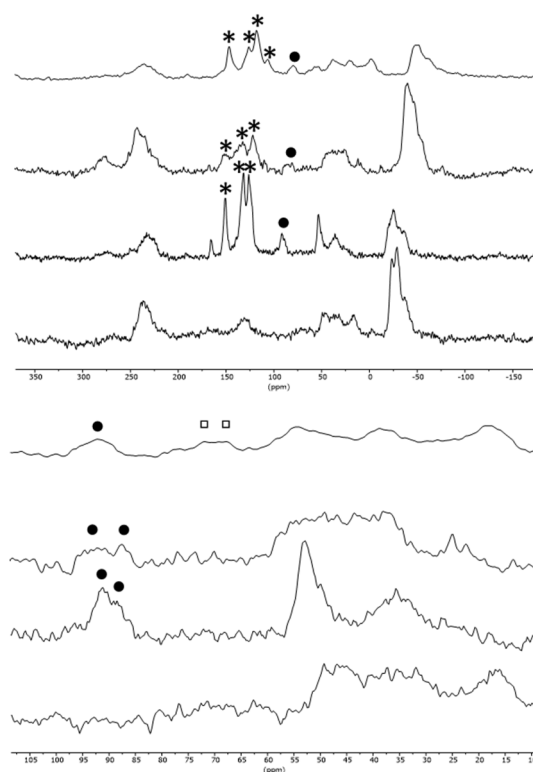
Figure 4.6 Magic-angle spinning solid ^{13}C NMR of MOF **1** (a) and SCCs@MOF **2** (b), **3** (c) and **4** (d) full spectra (top) and details of the 10-105 ppm region (bottom). Symbols scheme: * pyridine or benzene, • alkyne and ▫ ethoxy signals.

At the left side of Figure 4.7, DR UV-Vis measurements of **2-4** indicate the missing isolated palladium(II) adsorption band at λ_{max} = 320 nm, otherwise observed in **1**, and the presence of three new bands at λ_{max} = 270, 300 and 350

nm, which is linked to the creation of SCCs and corresponding to the observed bands of a previously reported $Pd^{II}_4(L_1)_4$ square SCC in solution [66]. Fourier-transformed infrared spectroscopy (FT-IR), at the right side of Figure 4.7, validates once again the integrity of the structural organic parts of the SCCs@MOF in **2**–**4** with the emergence of new signals corresponding to the ligand of the self-assembled entities.
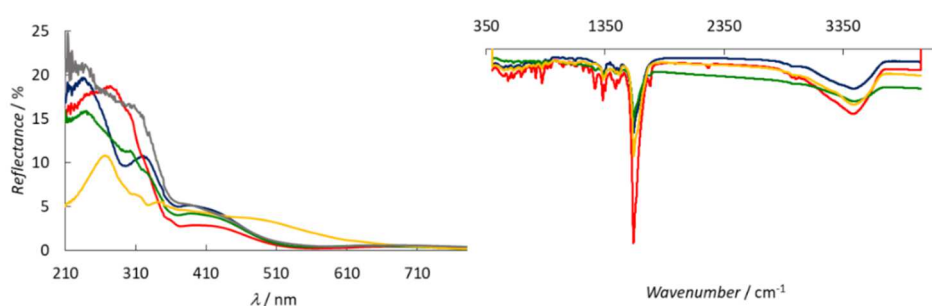
Figure 4.7 UV-Vis spectrum of $Pd_4(L_1)_4$ (yellow) and DR UV-Vis spectra of MOF **1** (blue), SCCs@MOF **2** (red), **3** (green), and **4** (grey) (left); FT-IR spectra of MOF **1** (blue), SCCs@MOF **2** (red), **3** (green), and **4** (yellow) (right).

As shown in Figure 4.8, XPS displays that the $Pd3d_{5/2}$ peak of the Pd^{II} atoms (338.6 eV) in **1** somewhat moves a little for **2-4** (338.3, 338.5 and 338.1 eV, respectively), as predictable by the presence of $L_{1–3}$ ligands [67]. Figure 4.9 presents the Raman spectra obtained by irradiating **4** with a laser light at 521 nm. The Raman measurements confirmed the presence of Au-S bonds by comparison with the compound before undergoing the process of auration.
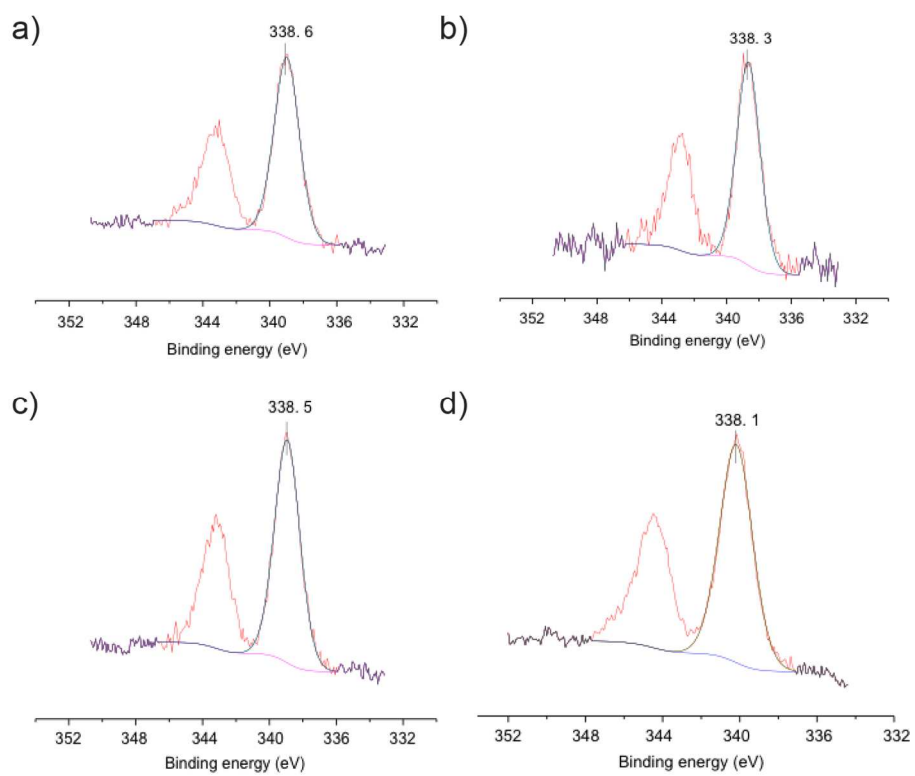
Figure 4.8 XPS spectra of MOF **1** (a), SCCs@MOF **2** (b), **3** (c) and **4** (d).
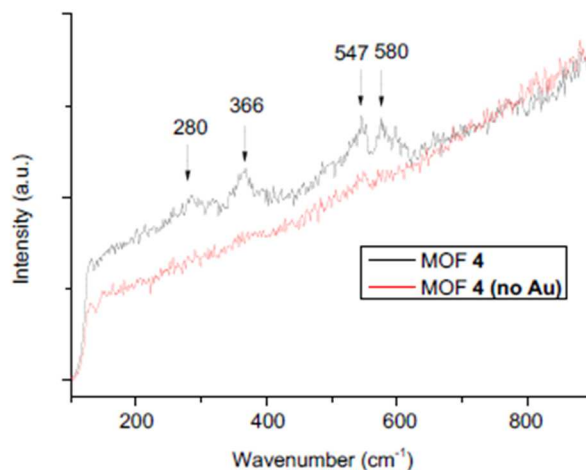
Figure 4.9 Raman spectra of MOF **4** before and after metalation with gold, irradiating with a laser light at 521 nm.

4.3 Catalysis with SCCs@MOF

4.3.1 Homocoupling of thienylboronic acids

4.3.1.1 Catalytic results

Oligo- and poly-thiophenes molecules are known to have high conductivity, which made them quite useful in applications like solar cells [68]. The synthesis of these compounds is usually performed by the homocoupling of thienylboronic acids catalysed by palladium. This reaction includes a challenging C-C bond-forming step that is typically carried out using oxidants and strong bases combined with a poisoning sulfur group too [69]. The results for the homocoupling of two thienylboronic acids, **5a** and **5b**, with a representative Pd^{II} complex catalyst are presented in Figure 4.10 [70].
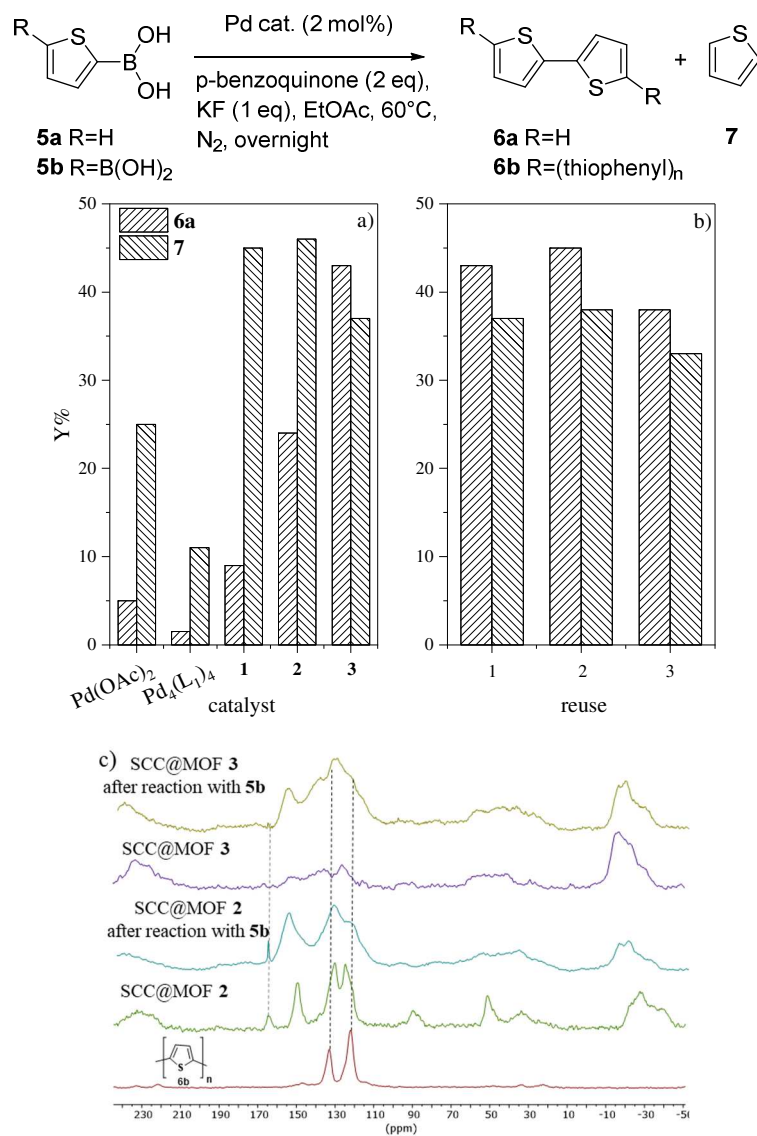
Figure 4.10 Scheme of the homocoupling reaction of thienyl boronic acids **5a** and **5b** using Pd catalysts (top) and its catalytic results (a). Reuses of the compound **2** used as catalyst in the homocoupling reaction of **5a** (b). MAS solid ^{13}C NMR of polythiophene, and the SCCs@MOF **2** and **3** before and after the reaction with **5b** (bottom to top) (c).

The soluble SMC $Pd^{II}_4(L_1)_4$ [66] and compounds **1-3** have also been used as catalysts, and SCCs@MOF **2** and **3** present higher activity and selectivity towards the product **6a** than those achieved by homogeneous Pd catalysts and MOF **1**. Furthermore, SCCs@MOF operate with good recyclability and the possibility to be used in the catalytic homocoupling of different boronic acids, as shown in Table 4.3. Moreover, the analyses performed on the catalysts after reaction showed unchanged spectra compared to the fresh sample, as shown by MAS solid ^{13}C NMR and UV-Vis measurements of **2** and **3** in Figures 4.10c and 4.11, respectively. The peaks associated to the polymer **6b**, obtained using the substrate **5b**, highlight the stability of the MOFs even after the polymerization reaction, as shown in Figure 4.10c. With these observations in mind, we were likely to conclude that the SCCs were stable within the MOF channels under catalytic reaction conditions.
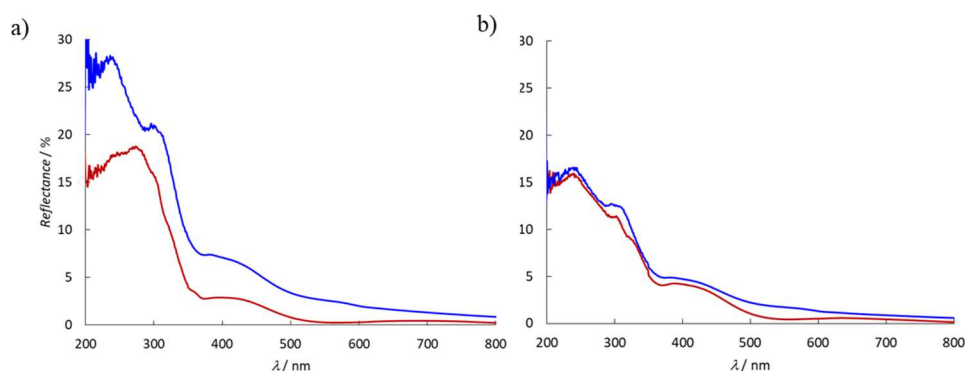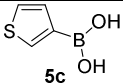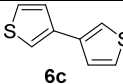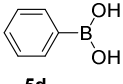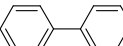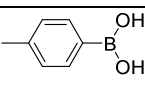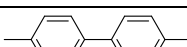
Figure 4.11 DR UV-Vis spectra of SCCs@MOF **2** (a) and **3** (b) before (red) and after reaction with thienylboronic acid **5a** (blue).

Table 4.3 Results for the homocoupling of different boronic acids with SCCs@MOF **2** and **3**. "S." indicates the selectivity towards the homocoupling product.

Entry	Catalyst	Conversion	Product yields		
		5c	6c	7	
1	**2**	39.0%	16.2% (S. 41.5%)	20.1%	
2	**3**	80.1%	43.8% (S. 54.7%)	33.2%	
		5d	6d	S1	
3	**2**	30.2%	22.3% (S. 73.8%)	5.5%	
4	**3**	22.5%	18.5% (S. 82.5%)	2.3%	
		5e	6e	S2	
5	**2**	30.4%	18.3% (S. 60.2%)	10.2%	
6	**3**	14.2%	8.3% (S. 58.5%)	5.6%	

4.3.1.2 Mechanistic studies

Mechanistic studies were performed to better understand the stability of SCCs@MOF compared to their soluble counterpart $Pd^{II}_4(L_1)_4$. The kinetic rate equation is shown in Table 4.4 and appeared to be first-order respect to all reagents for both **2** and **3**, but it is second-order for benzoquinone and half-order for Pd in the case of the soluble catalyst $Pd^{II}_4(L_1)_4$ [71].

Table 4.4 Rate equation of the homocoupling reaction of **5a** with SCCs@MOF **2** and **3** and $Pd^{II}_4(L_1)_4$.

$$r_0 = k_{app} \cdot [\textbf{5a}]^\alpha \cdot [Pd]^\beta \cdot [Benzoquinone]^\gamma \cdot [KF]^\delta$$

Entry	Catalyst	α	β	γ	δ
1	**2**	1	1	1	1
2	**3**	1	1	1	1
3	$Pd_4(L_1)_4$	1	1/2	2	1

To understand the different results obtained with $Pd^{II}_4(L_1)_4$, *in-situ* ^1H NMR analyses were performed with this complex, showing its fast degradation after the addition of **5a**, combined with the release of free L_1 to the solvent (Figure 4.12) [72]. As shown in Figure 4.13, the initial rate decreased with the addition of ligands, both L_1 and the more classical ethylenediamine, and showed the necessity of an oxidant, such as O_2, in contrast with the heterogeneous system (Table 4.5, Entries 4 and 9) [69, 71]. These finding confirmed the stability and activity of SCCs@MOF **2** and **3**, leaving $Pd^{II}_4(L_1)_4$ to play just the role of precursor for the Pd catalytic species in the homogeneous system.
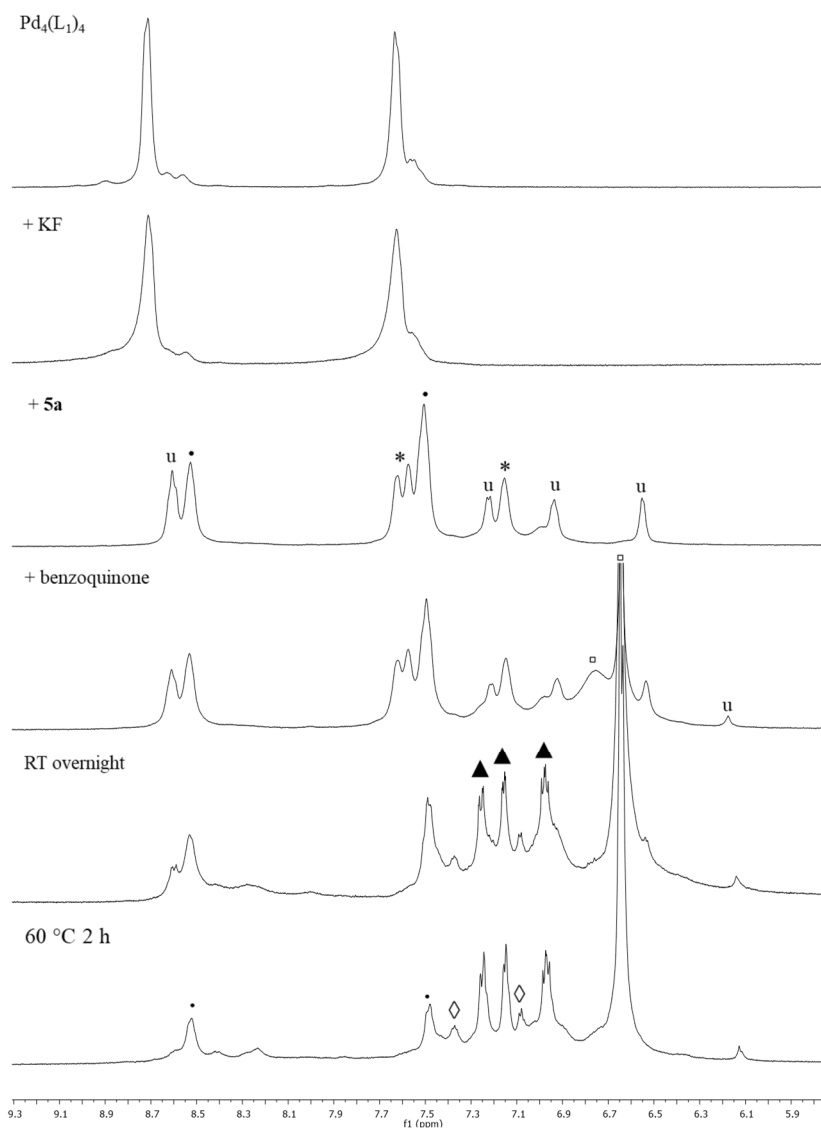
Figure 4.12 Aromatic area of the ^{1}H NMR spectra of Pd$_4$(L$_1$)$_4$ in CD$_3$CN after progressive addition of all the reagents used in the homocoupling of **5a**. Symbols scheme: • L1, * **5a**, □ benzoquinone, ▲ **6a**, ◊ **7**, u unidentified intermediates.
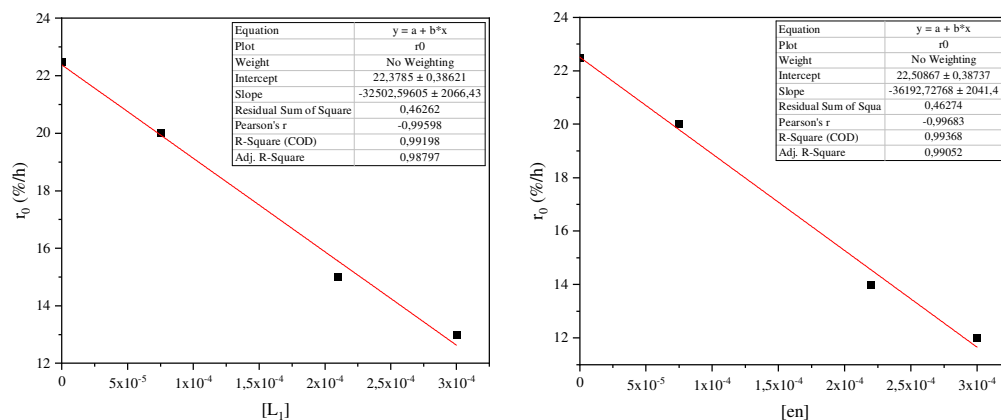
Figure 4.13 Initial rate vs. concentration of ligands L_1 (left) and ethylendiamine (right) for the homocoupling reaction of **5a** catalyzed by $Pd_4(L_1)_4$ in CH_3CN.

Table 4.11 Initial rates for the homocoupling of **5a** with different amounts of benzoquinone and under different atmospheres, catalyzed by SCC@MOF **2** or $Pd_4(L_1)_4$.

Entry	catalyst	benzoquinone (eq)	atmosphere	r_0 (%/h)
1		0	N_2	7.7
2		0	air	9.3
3	SCC@MOF **2**	0	O_2	11.7
4		0.25	N_2	20.4
5		0.25	O_2	7.4
6		0	N_2	7.4
7	$Pd_4(L_1)_4$	0	O_2	5.7
8		2	N_2	14.3
9		2	O_2	18.9
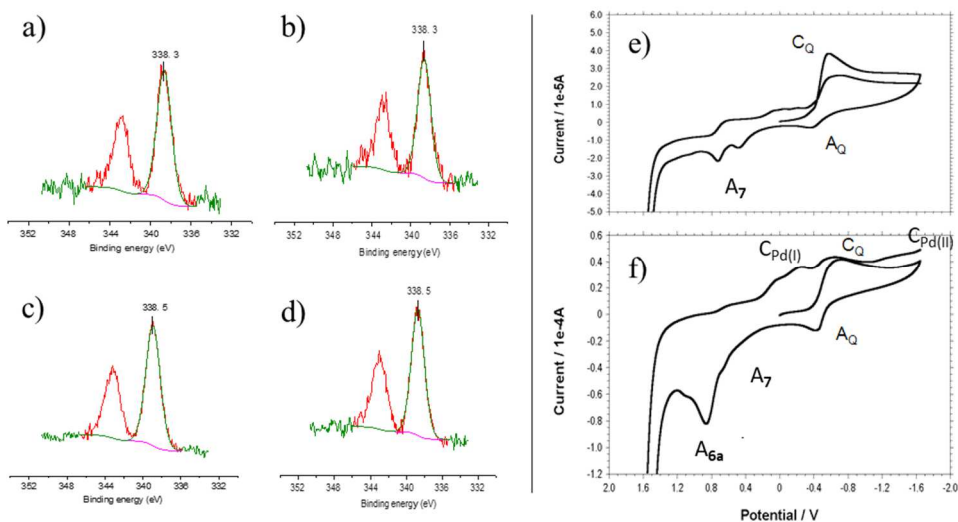
Figure 4.14 X-ray photoelectron spectroscopy of SCCs@MOF **2** (a-b) and **3** (c-d), before (a, c) and after (b, d) treatment with O_2 during 30 min. *In-situ* cyclic voltammograms of a solution of **5a** (1 mM), KF (1 mM), and benzoquinone (1 mM) in 0.10 M Bu_4NPF_6/MeCN before (e) and after (f) modifying glassy carbon electrodes with SCC@MOF **3**. "A" represents anodic signals and "C" cathodic signals; potential scan rate was 50 mV·s^{-1}.

As depicted in Figure 4.14 (a-d), the absence of oxidized Pd species, such as Pd^{IV}, was verified by XPS measurements, after treatments of **2** and **3** in O_2 atmosphere inside the analysis chamber of the XPS. In addition, Figures 4.14e and 4.14f show the cyclic voltammetry of **3** during the *in-situ* reaction of homocoupling reaction of **5a**. The cathodic signal ascribable to Pd^{II} atoms of SCC@MOF **3**, named $C_{Pd(II)}$ in Figure 4.14f, progressed to a new signal related to Pd^I ($C_{Pd(I)}$), which could not be confused with the signals of the

redox active benzoquinone (Q), the coupling product **6a** or the non-catalysed product **7**. This bimetallic Pd^I/Pd^{II} redox system, without the formation of Pd^0 or Pd^{IV} species, contributed to keep the structure integrity, avoiding distortions in the assemblies.

Finally, the combination of kinetics, spectroscopic and electrochemical results enabled us to establish a possible mechanism for the homocoupling reaction of boronic acids catalyzed by SCCs@MOF **2** and **3**, as presented in Figure 4.15. We confirmed that Pd^{II} dimers are responsible for the catalyzed reaction of homocoupling of **5a**, due to a redox mechanism where the Pd^{II} are reduced to Pd^I and **6** is released. Subsequently, Pd^I is re-oxidized by the benzoquinone and the catalyst goes back to the original form.
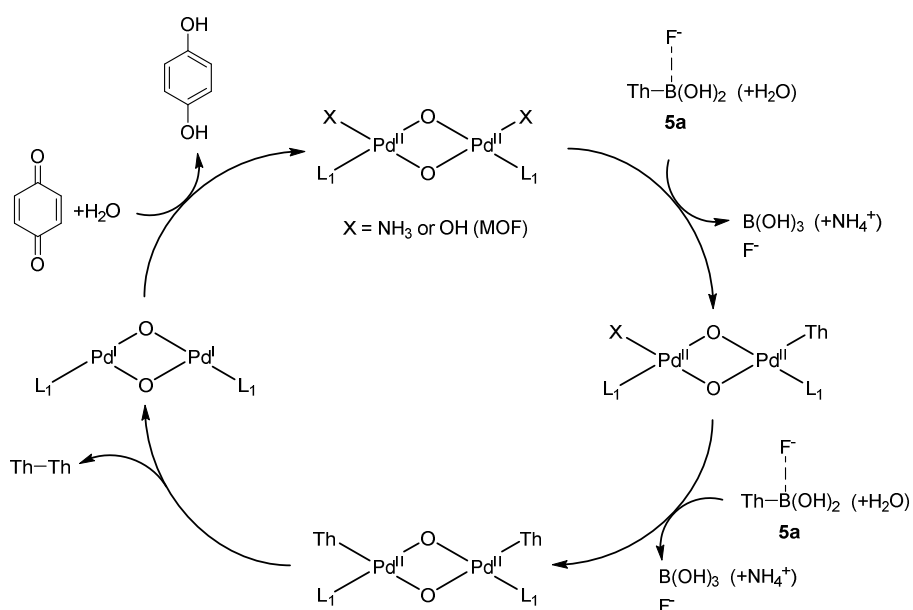
Figure 4.15 Proposed mechanism for the homocoupling of **5a** catalyzed by Pd dimers of the SCC@MOF **2**.

4.3.2   Homo- and cross-coupling of alkynes

4.3.2.1 Catalytic results

Taking into account the discoveries described until now, we considered to use SCCs@MOF **2** and **3** in addition to the heterobimetallic $Au^{III}Pd^{II}$ **4** in another catalytic process. Figure 4.16 shows the results for the coupling of alkynes catalyzed by the three SCCs@MOF, compared to those obtained with the homogeneous system formed by $Pd(OAc)_2$ and pyridine and with the corresponding homogeneous cage $Pd_4(L_1)_4$ [72]. As in the homocoupling of boronic acids, the activity was higher in the case of heterogenous catalysts than the homogenous ones. Moreover, a similar MOF composed by Au^{III} complexes supported by the thio-alkyl groups of the MOF network did not show any activity in the reaction mentioned above, underlining the relevance of the presence of Pd and slightly of Au [73]. Not only did SCC@MOF **4** showed the best selectivity towards **9a**, but also it was used in the homocoupling (**9b-e**) and in the cross-coupling (**9f-h**) of other alkynes (see Figure 4.17).
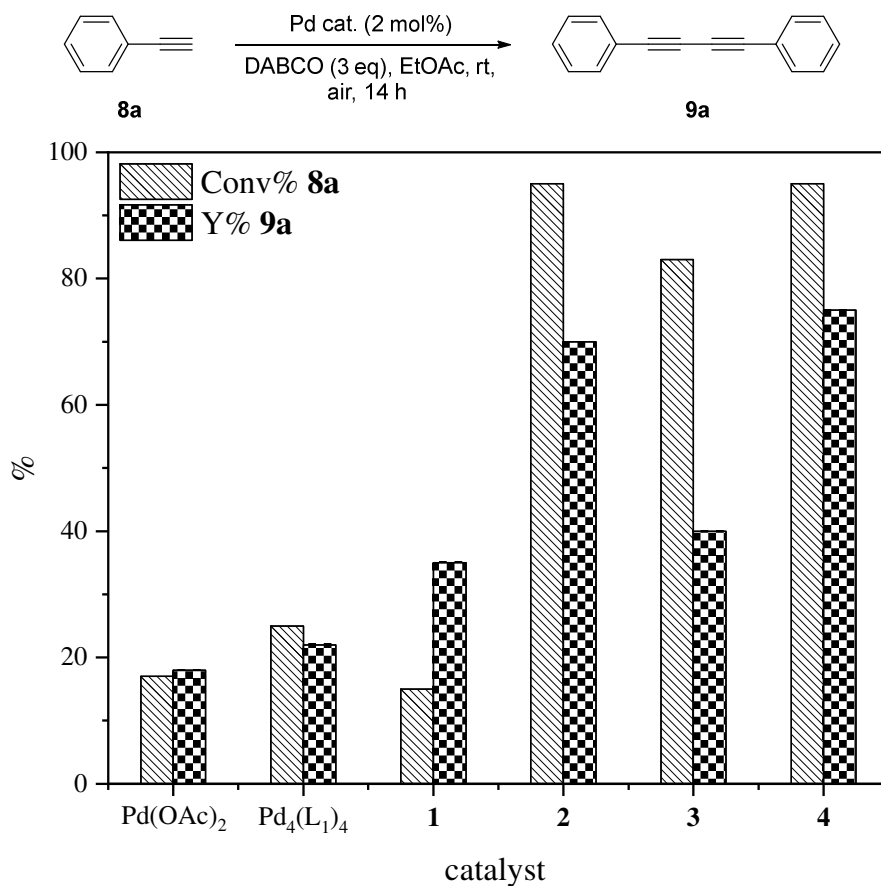
Figure 4.16 Catalytic results obtained with different Pd catalysts (bottom) in the reaction of homocoupling of phenylacetylene (top).

9b
Conv.% 100%
Y% 98%

9c
H3CO   OCH3
Conv.% 100%
Y% 72%

9d
Conv.% 90%
Y% 67%

9e
Conv.% 35%
Y% 33%

9f H3CO
Conv.% 100%
Y% 98%

9g OCH3
Conv.% 76%
Y% 71%

9h H2N
Conv.% 59%
Y% 53%
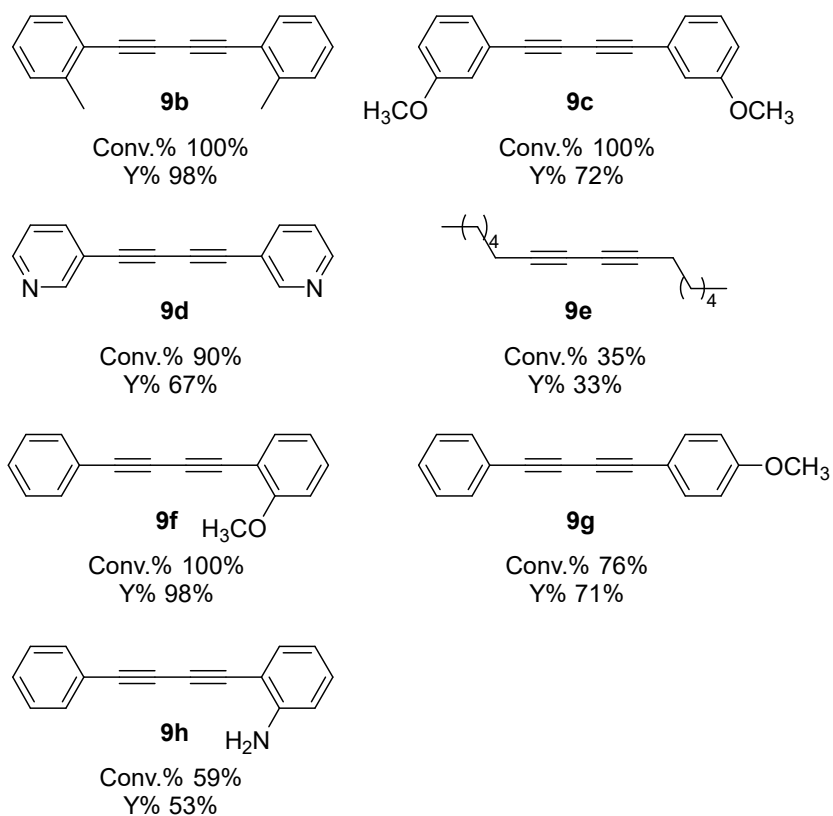
Figure 4.17 Reaction scope for the homocoupling and cross-coupling of alkynes **8b-h** catalyzed by SCC@MOF **4**.

Table 4.5 Equation rate for the homocoupling of **8a** with SCC@MOF **4** and $Pd^{II}_4(L_1)_4$.

$$r_0 = k_{app} \cdot [\textbf{8a}]^\alpha \cdot [Pd]^\beta \cdot [DABCO]^\gamma$$

Entry	Catalyst	α	β	γ
1	**4**	1	1	1
2	$Pd_4(L_1)_4$	0	1/2	1
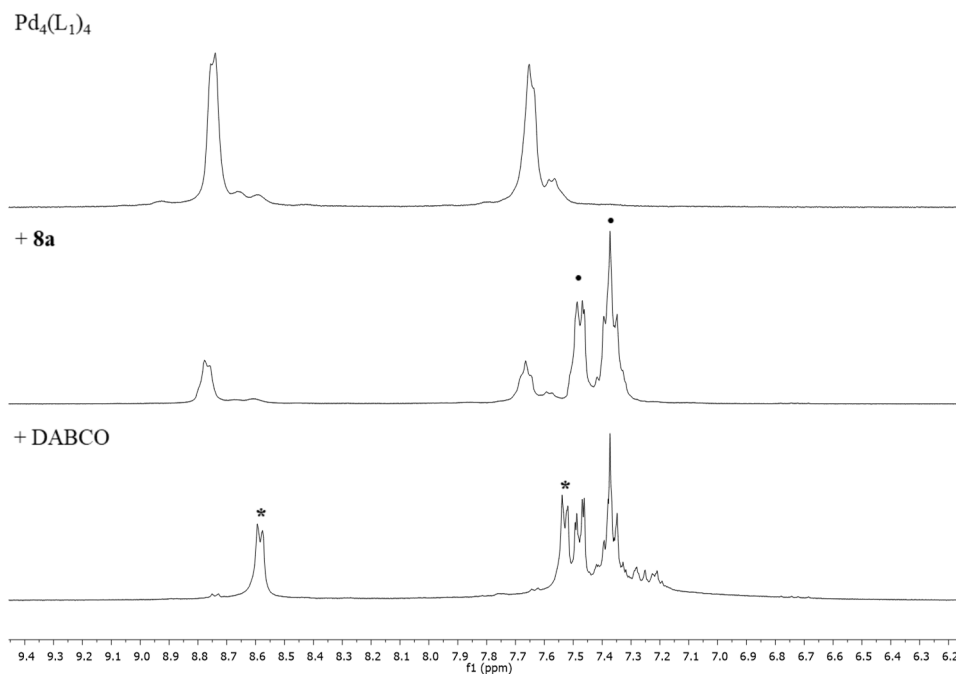
$Pd_4(L_1)_4$

Figure 4.18 Aromatic region of the ^1H NMR spectra of $Pd_4(L_1)_4$ in CD_3CN/D_2O after progressive addition of all the reagents used in the homocoupling of **8a**. Symbols scheme: • **8a**, * L_1.

4.3.2.2 Mechanistic studies

According to the results obtained for the homocoupling of boronic acids, kinetic experiments and ^1H NMR spectra were performed to better understand the mechanism of the homocoupling of **8a**. As shown in Table 4.6, the mentioned reaction followed a first-order respect to **8a** only when catalyzed by SCC@MOF **4**, whereas the substrate does not appear in the equation rate when the catalysis is performed by $Pd_4(L_1)_4$. The latter phenomenon fits the KIEs obtained in the two different situations: 3.4(7) for **4** and 0.9(1) for

$Pd_4(L_1)_4$ [74].

Taking into account the reaction orders respect to Pd, we obtained first-order for SCC@MOF **4**, but half-order for $Pd_4(L_1)_4$, which is explained by the fast decomposition of the cage after the addition of the reagents, as clarified by Figure 4.18. In addition, the use of different atmosphere conditions verified that the cage decomposition is more influenced by the presence of O_2 (see Table 4.7) [75].

Table 4.6 Initial rates obtained for the homocoupling of **8a** with different atmospheres and catalyzed by SCC@MOF **4** or $Pd_4(L_1)_4$.

Entry	Catalyst	atmosphere	r_0 (%/h)
1		N_2	3.7
2	SCC@MOF **4**	O_2	5.6
3		air	8.3
4		N_2	0.5
5	$Pd_4(L_1)_4$	O_2	3.1
6		air	1.7

Considering the positive results achieved with these catalysts, the latter were applied in the cross-coupling between **5a** and **8a** [76] and, despite the challenging reaction, moderate conversions and selectivity towards the product **10a** were obtained, in particular compared to the ones reached with the homogeneous counterparts (Figure 4.19).
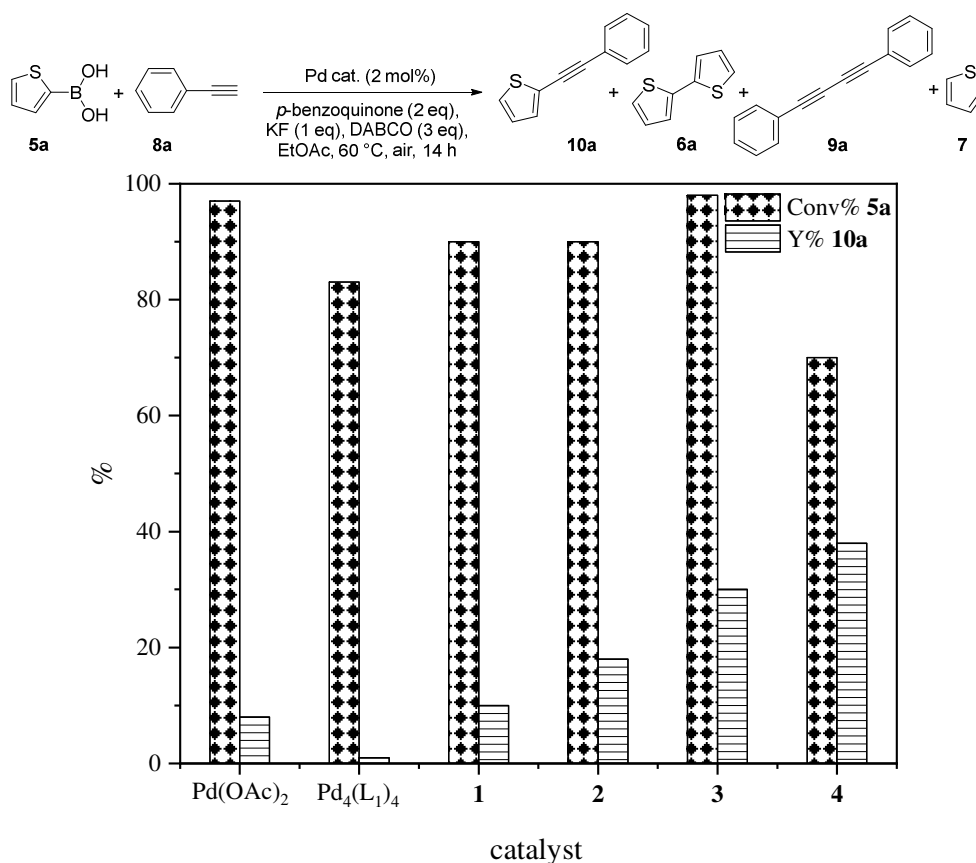
Figure 4.18 Conversions of **5a** and yields towards the product **10a** (bottom) in the cross-coupling of **5a** and **8a** (top) catalyzed by different palladium catalysts.

A more practical result of the reactions was given by the application of SCC@MOF **4** as catalyst in a flow process. Indeed, **4** catalyzed the homocoupling of **8a** in a fixed-bed tubular reactor. The results in Figure 4.20 show that we could achieve the otherwise hard production of **9a** [77, 78] and overcome the eventual difficulties due to the presence of the base by employing the solid catalyst in flow.
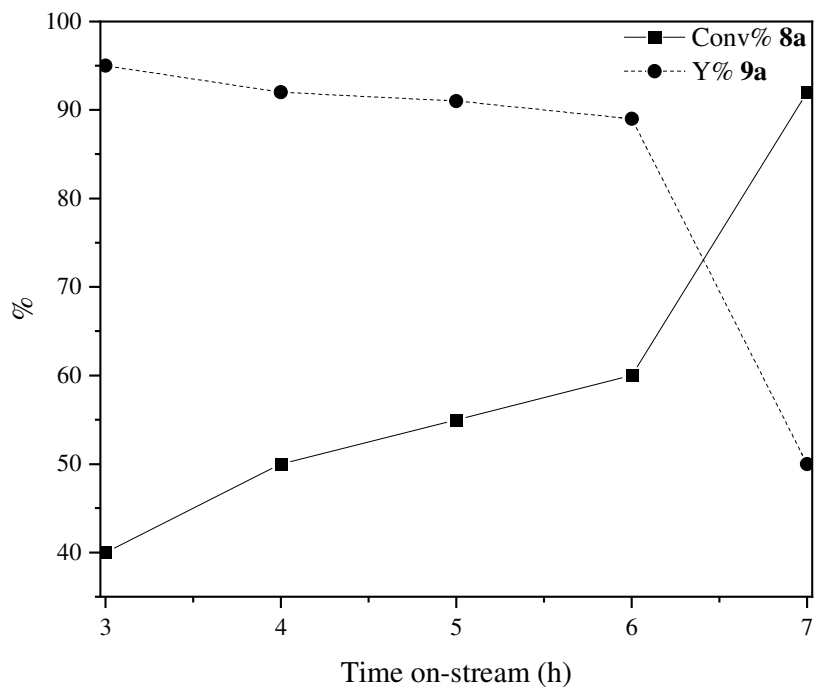
Figure 4.20 Homocoupling of **8a** carried out in flow conditions in a fixed-bed tubular reactor containing SCC@MOF **4**. Reaction conditions: 0.01 ml·min^{-1} of a mixture of **8a** and DABCO (3 eq) in EtOAc (0.05 M) over 50 mg of **4** at 60 ºC.

4.4 Conclusions

In this *Chapter*, the catalytic activity of supramolecular coordination complexes (SCCs) within MOF channels was described, highlighting their novel template-directed assembly synthesis. The latter made possible to achieve Pd^{II} dimers which represent pivotal entities to form the SCCs in the MOF channels and could not be prepared otherwise. The SCCs@MOF were fully characterized to prove the formation of three new complexes, a Pd_8 square metal-organic polygon, a Pd_{16} supramolecular cage and a Au^{III}-Pd^{II} cage.

The first two showed activity towards the homocoupling reaction of boronic acids and the mechanism of the reaction was deeply studied, comparing the SCCs@MOF to homogeneous counterparts. Moreover, the three complexes within MOF demonstrated a good activity for the reaction of homo- and cross-coupling of alkynes.

These results represent a novelty in the field of catalysis and supramolecular chemistry, due to the use of heterogeneous catalysts in processes which are usually catalyzed by homogeneous catalysts, and to the original supramolecular structures synthesized within MOF channels.

4.5 References

1. Deng, H.; Grunder, S.; Cordova, K. E.; Valente, C.; Furukawa, H.; Hmadeh, M.; Gándara, F.; Whalley, A. C.; Liu, Z.; Asahina, S.; Kazumori, H.; O'Keeffe, M.; Terasaki, O.; Stoddart, J. F.; Yaghi, O. M., Large-pore apertures in a series of metal-organic frameworks. *Science* **2012,** *336* (6084), 1018-1023.

2. Fracaroli, A. M.; Furukawa, H.; Suzuki, M.; Dodd, M.; Okajima, S.; Gándara, F.; Reimer, J. A.; Yaghi, O. M., Metal–organic frameworks with precisely designed interior for carbon dioxide capture in the presence of water. *J. Am. Chem. Soc.* **2014**, *136* (25), 8863-8866.

3. Guillerm, V.; Grancha, T.; Imaz, I.; Juanhuix, J.; Maspoch, D., Zigzag ligands for transversal design in reticular chemistry: unveiling new structural opportunities for metal–organic frameworks. *J. Am. Chem. Soc.* **2018,** *140* (32), 10153-10157.

4. Jiang, H.; Jia, J.; Shkurenko, A.; Chen, Z.; Adil, K.; Belmabkhout, Y.; Weselinski, L. J.; Assen, A. H.; Xue, D.-X.; O'Keeffe, M.; Eddaoudi, M., Enriching the reticular chemistry repertoire: merged nets approach for the rational design of intricate mixed-linker metal–organic framework platforms. *J. Am. Chem. Soc.* **2018**, *140* (28), 8858-8867.

5. Albalad, J.; Xu, H.; Gándara, F.; Haouas, M.; Martineau-Corcos, C.; Mas-Ballesté, R.; Barnett, S. A.; Juanhuix, J.; Imaz, I.; Maspoch, D., Single-crystal-to-single-crystal postsynthetic modification of a metal–organic framework via ozonolysis. *J. Am. Chem. Soc.* **2018**, *140* (6), 2028-2031.

6. Ferguson, A.; Liu, L.; Tapperwijn, S. J.; Perl, D.; Coudert, F.-X.; Van

Cleuvenbergen, S.; Verbiest, T.; van der Veen, M. A.; Telfer, S. G., Controlled partial interpenetration in metal–organic frameworks. *Nat. Chem.* **2016**, *8* (3), 250-257.

7. Lee, S.; Bürgi, H.-B.; Alshmimri, S. A.; Yaghi, O. M., Impact of disordered guest–framework interactions on the crystallography of metal–organic frameworks. *J. Am. Chem. Soc.* **2018**, *140* (28), 8958-8964.

8. Li, Y.; Yang, Z.; Wang, Y.; Bai, Z.; Zheng, T.; Dai, X.; Liu, S.; Gui, D.; Liu, W.; Chen, M.; Chen, L.; Diwu, J.; Zhu, L.; Zhou, R.; Chai, Z.; Albrecht-Schmitt, T. E.; Wang, S., A mesoporous cationic thorium-organic framework that rapidly traps anionic persistent organic pollutants. *Nat. Commun.* **2017**, *8* (1), 1354.

9. Kim, S.; Yoon, T.-U.; Oh, K. H.; Kwak, J.; Bae, Y.-S.; Kim, M., Positional installation of unsymmetrical fluorine functionalities onto metal-organic frameworks for efficient carbon dioxide separation under humid conditions. *Inorg. Chem.* **2020**, *59* (24), 18048-18054.

10. Shen, J.; He, X.; Ke, T.; Krishna, R.; van Baten, J. M.; Chen, R.; Bao, Z.; Xing, H.; Dinca, M.; Zhang, Z.; Yang, Q.; Ren, Q., Simultaneous interlayer and intralayer space control in two-dimensional metal-organic frameworks for acetylene/ethylene separation. *Nat. Commun.* **2020**, *11* (1), 6259.

11. Wu, Y.; Liu, Z.; Peng, J.; Wang, X.; Zhou, X.; Li, Z., Enhancing selective adsorption in a robust pillared-layer metal-organic framework via channel methylation for the recovery of C_2-C_3 from natural gas. *ACS Appl. Mater. Interfaces* **2020**, *12* (46), 51499-51505.

12. Zhao, X.; Wang, Y.; Li, D.-S.; Bu, X.; Feng, P., Metal–organic frameworks for separation. *Adv. Mater.* **2018**, *30* (37), 1705189.

13. Cadiau, A.; Adil, K.; Bhatt, P. M.; Belmabkhout, Y.; Eddaoudi, M., A metal-organic framework–based splitter for separating propylene from propane. *Science* **2016**, *353* (6295), 137-140.

14. Cadiau, A.; Belmabkhout, Y.; Adil, K.; Bhatt, P. M.; Pillai, R. S.; Shkurenko, A.; Martineau-Corcos, C.; Maurin, G.; Eddaoudi, M., Hydrolytically stable fluorinated metal-organic frameworks for energy-efficient dehydration. *Science* **2017**, *356* (6339), 731-735.

15. Rivero-Crespo, M. A.; Mon, M.; Ferrando-Soria, J.; Lopes, C. W.; Boronat, M.; Leyva-Pérez, A.; Corma, A.; Hernández-Garrido, J. C.; López-Haro, M.; Calvino, J. J.; Ramos-Fernandez, E. V.; Armentano, D.; Pardo, E., Confined Pt_1^{1+} water clusters in a MOF catalyze the low-temperature water–gas shift reaction with both CO_2 oxygen atoms coming from water. *Angew. Chem. Int. Ed.* **2018**, *57* (52), 17094-17099.

16. Chand, S.; Pal, A.; Pal, S. C.; Das, M. C., A trifunctional luminescent 3D microporous MOF with potential for CO_2 separation, selective sensing of a metal ion, and recognition of a small organic molecule. *Eur. J. Inorg. Chem.* **2018**, *2018* (24), 2785-2792.

17. Duan, X.; Shi, Z.; Wang, C.; Kong, Z., A new anionic metal-organic framework with suitable pore and PtS-type topology for selective adsorption and separation of cationic dyes. *Chem. Pap.* **2020**, *74* (11), 4003-4008.

18. Easun, T. L.; Moreau, F.; Yan, Y.; Yang, S.; Schroder, M., Structural and dynamic studies of substrate binding in porous metal-organic

frameworks. *Chem. Soc. Rev.* **2017**, *46* (1), 239-274.

19. Mon, M.; Lloret, F.; Ferrando-Soria, J.; Martí-Gastaldo, C.; Armentano, D.; Pardo, E., Selective and efficient removal of mercury from aqueous media with the highly flexible arms of a bioMOF. *Angew. Chem. Int. Ed.* **2016**, *55* (37), 11167-11172.

20. Navarro-Sánchez, J.; Argente-García, A. I.; Moliner-Martínez, Y.; Roca-Sanjuán, D.; Antypov, D.; Campíns-Falcó, P.; Rosseinsky, M. J.; Martí-Gastaldo, C., Peptide metal–organic frameworks for enantioselective separation of chiral drugs. *J. Am. Chem. Soc.* **2017**, *139* (12), 4294-4297.

21. Sun, F.-Z.; Yang, S.-Q.; Krishna, R.; Zhang, Y.-H.; Xia, Y.-P.; Hu, T.-L., Microporous metal-organic framework with a completely reversed adsorption relationship for C_2 hydrocarbons at room temperature. *ACS Appl. Mater. Interfaces* **2020**, *12* (5), 6105-6111.

22. Mon, M.; Rivero-Crespo, M. A.; Ferrando-Soria, J.; Vidal-Moya, A.; Boronat, M.; Leyva-Pérez, A.; Corma, A.; Hernández-Garrido, J. C.; López-Haro, M.; Calvino, J. J.; Ragazzon, G.; Credi, A.; Armentano, D.; Pardo, E., Synthesis of densely packaged, ultrasmall Pt^0_2 clusters within a thioether-functionalized MOF: catalytic activity in industrial reactions at low temperature. *Angew. Chem. Int. Ed.* **2018**, *57* (21), 6186-6191.

23. Rao, P. C.; Mandal, S., Potential utilization of metal-organic frameworks in heterogeneous catalysis: a case study of hydrogen-bond donating and single-site catalysis. *Chem. - Asian J.* **2019**, *14* (23), 4087-4102.

24. Syed, Z. H.; Sha, F.; Zhang, X.; Kaphan, D. M.; Delferro, M.; Farha, O. K., Metal-organic framework nodes as a supporting platform for tailoring the activity of metal catalysts. *ACS Catal.* **2020**, *10* (19), 11556-11566.

25. Ly, H. G. T.; Fu, G.; Kondinski, A.; Bueken, B.; De Vos, D.; Parac-Vogt, T. N., Superactivity of MOF-808 toward peptide bond hydrolysis. *J. Am. Chem. Soc.* **2018**, *140* (20), 6325-6335.

26. Zhang, T.; Manna, K.; Lin, W., Metal–organic frameworks stabilize solution-inaccessible cobalt catalysts for highly efficient broad-scope organic transformations. *J. Am. Chem. Soc.* **2016**, *138* (9), 3241-3249.

27. Zhang, X.; Huang, Z.; Ferrandon, M.; Yang, D.; Robison, L.; Li, P.; Wang, T. C.; Delferro, M.; Farha, O. K., Catalytic chemoselective functionalization of methane in a metal−organic framework. *Nat. Catal.* **2018**, *1* (5), 356-362.

28. Lian, X.; Huang, Y.; Zhu, Y.; Fang, Y.; Zhao, R.; Joseph, E.; Li, J.; Pellois, J.-P.; Zhou, H.-C., Enzyme-MOF nanoreactor activates nontoxic paracetamol for cancer therapy. *Angew. Chem. Int. Ed.* **2018**, *57* (20), 5725-5730.

29. Gao, P.; Shi, M.; Wei, R.; Pan, W.; Liu, X.; Li, N.; Tang, B., A biomimetic MOF nanoreactor enables synergistic suppression of intracellular defense systems for augmented tumor ablation. *Chem. Commun.* **2020**, *56* (6), 924-927.

30. Cui, H.; Liu, S.; Lv, Y.; Wu, S.; Wang, L.; Hao, F.; Liu, P.; Xiong, W.; Luo, H., Transfer hydrogenation of cinnamaldehyde to cinnamyl alcohol in hydrophobically modified core-shell MOFs nanoreactor: identification of the formed metal-N as the structure of an active site. *J. Catal.* **2020**, *381*, 468-481.

31. Kitao, T.; Zhang, Y.; Kitagawa, S.; Wang, B.; Uemura, T., Hybridization of MOFs and polymers. *Chem. Soc. Rev.* **2017**, *46* (11), 3108-3133.

32. Fortea-Pérez, F. R.; Mon, M.; Ferrando-Soria, J.; Boronat, M.; Leyva-Pérez, A.; Corma, A.; Herrera, J. M.; Osadchii, D.; Gascon, J.; Armentano, D.; Pardo, E., The MOF-driven synthesis of supported palladium clusters with catalytic activity for carbene-mediated chemistry. *Nat. Mater.* **2017**, *16* (7), 760-766.

33. Aguilera-Sigalat, J.; Bradshaw, D., Synthesis and applications of metal-organic framework–quantum dot (QD@MOF) composites. *Coord. Chem. Rev.* **2016**, *307*, 267-291.

34. Murahashi, T.; Fujimoto, M.; Oka, M.-a.; Hashimoto, Y.; Uemura, T.; Tatsumi, Y.; Nakao, Y.; Ikeda, A.; Sakaki, S.; Kurosawa, H., Discrete sandwich compounds of monolayer palladium sheets. *Science* **2006**, *313* (5790), 1104-1107.

35. Vuong, V. Q.; Madridejos, J. M. L.; Aradi, B.; Sumpter, B. G.; Metha, G. F.; Irle, S., Density-functional tight-binding for phosphine-stabilized nanoscale gold clusters. *Chem. Sci.* **2020**, *11* (48), 13113-13128.

36. Shichibu, Y.; Negishi, Y.; Tsukuda, T.; Teranishi, T., Large-scale synthesis of thiolated Au_{25} clusters via ligand exchange reactions of phosphine-stabilized Au_{11} clusters. *J. Am. Chem. Soc.* **2005**, *127* (39), 13464-13465.

37. Li, Y.; Xu, A.; Lum, Y.; Wang, X.; Hung, S.-F.; Chen, B.; Wang, Z.; Xu, Y.; Li, F.; Abed, J.; Huang, J. E.; Rasouli, A. S.; Wicks, J.; Sagar, L. K.; Peng, T.; Ip, A. H.; Sinton, D.; Jiang, H.; Li, C.; Sargent, E. H., Promoting CO_2 methanation via ligand-stabilized metal oxide clusters as hydrogen-donating motifs. *Nat. Commun.* **2020**, *11* (1), 6190.

38. Liu, L.; Díaz, U.; Arenal, R.; Agostini, G.; Concepción, P.; Corma, A.,

Generation of subnanometric platinum with high stability during transformation of a 2D zeolite into 3D. *Nat. Mater.* **2017**, *16* (1), 132-138.

39. Serna, P.; Gates, B. C., Molecular metal catalysts on supports: organometallic chemistry meets surface science. *Acc. Chem. Res.* **2014**, *47* (8), 2612-2620.

40. Du, Y.; Sheng, H.; Astruc, D.; Zhu, M., Atomically precise noble metal nanoclusters as efficient catalysts: a bridge between structure and properties. *Chem. Rev.* **2020**, *120* (2), 526-622.

41. Zhang, B.; Garcia, C.; Sels, A.; Salassa, G.; Rameshan, C.; Llorca, J.; Hradil, K.; Rupprechter, G.; Barrabes, N.; Burgi, T., Ligand and support effects on the reactivity and stability of $Au_{38}(SR)_{24}$ catalysts in oxidation reactions. *Catal. Commun.* **2019**, *130*, 105768.

42. Toshima, N.; Shiraishi, Y.; Teranishi, T.; Miyake, M.; Tominaga, T.; Watanabe, H.; Brijoux, W.; Bonnemann, H.; Schmid, G., Various ligand-stabilized metal nanoclusters as homogeneous and heterogeneous catalysts in the liquid phase. *Appl. Organomet. Chem.* **2001**, *15* (3), 178-196.

43. Shen, H.; Xiang, S.; Xu, Z.; Liu, C.; Li, X.; Sun, C.; Lin, S.; Teo, B. K.; Zheng, N., Superatomic Au_{13} clusters ligated by different N-heterocyclic carbenes and their ligand-dependent catalysis, photoluminescence, and proton sensitivity. *Nano Res.* **2020**, *13* (7), 1908-1911.

44. Reetz, M. T.; Lohmer, G., Propylene carbonate stabilized nanostructured palladium clusters as catalysts in Heck reactions. *Chem. Commun.* **1996**, *1996* (16), 1921-1922.

45. Cullen, W.; Misuraca, M. C.; Hunter, C. A.; Williams, N. H.; Ward, M. D., Highly efficient catalysis of the Kemp elimination in the cavity of a cubic coordination cage. *Nat. Chem.* **2016**, *8* (3), 231-236.

46. Hong, C. M.; Bergman, R. G.; Raymond, K. N.; Toste, F. D., Self-assembled tetrahedral hosts as supramolecular catalysts. *Acc. Chem. Res.* **2018**, *51* (10), 2447-2455.

47. Howlader, P.; Das, P.; Zangrando, E.; Mukherjee, P. S., Urea-functionalized self-assembled molecular prism for heterogeneous catalysis in water. *J. Am. Chem. Soc.* **2016**, *138* (5), 1668-1676.

48. Pilgrim, B. S.; Roberts, D. A.; Lohr, T. G.; Ronson, T. K.; Nitschke, J. R., Signal transduction in a covalent post-assembly modification cascade. *Nat. Chem.* **2017**, *9* (12), 1276-1281.

49. Ueda, Y.; Ito, H.; Fujita, D.; Fujita, M., Permeable self-assembled molecular containers for catalyst isolation enabling two-step cascade reactions. *J. Am. Chem. Soc.* **2017**, *139* (17), 6090-6093.

50. Lopez-Vidal, E. M.; Fernandez-Mato, A.; Garcia, M. D.; Perez-Lorenzo, M.; Peinador, C.; Quintela, J. M., Metallacycle-catalyzed S_NAr reaction in water: supramolecular inhibition by means of host-guest complexation. *J. Org. Chem.* **2014**, *79* (3), 1265-1270.

51. Ibanez, S.; Poyatos, M.; Peris, E., N-heterocyclic carbenes: a door open to supramolecular organometallic chemistry. *Acc. Chem. Res.* **2020**, *53* (7), 1401-1413.

52. Li, F.; Yang, H.; Zhuo, Q.; Zhou, D.; Wu, X.; Zhang, P.; Yao, Z.; Sun, L., A cobalt@cucurbit[5]uril complex as a highly efficient supramolecular catalyst for electrochemical and photoelectrochemical

water splitting. *Angew. Chem. Int. Ed.* **2021,** *60*, 1976-1985.

53. Chakrabarty, R.; Mukherjee, P. S.; Stang, P. J., Supramolecular coordination: self-assembly of finite two- and three-dimensional ensembles. *Chem. Rev.* **2011**, *111* (11), 6810-6918.

54. Chakraborty, S.; Newkome, G. R., Terpyridine-based metallosupramolecular constructs: tailored monomers to precise 2D-motifs and 3D-metallocages. *Chem. Soc. Rev.* **2018**, *47* (11), 3991-4016.

55. Ward, M. D.; Raithby, P. R., Functional behaviour from controlled self-assembly: challenges and prospects. *Chem. Soc. Rev.* **2013**, *42* (4), 1619-1636.

56. Sun, Q.-F.; Iwasa, J.; Ogawa, D.; Ishido, Y.; Sato, S.; Ozeki, T.; Sei, Y.; Yamaguchi, K.; Fujita, M., Self-assembled $M_{24}L_{48}$ polyhedra and their sharp structural switch upon subtle ligand variation. *Science* **2010**, *328* (5982), 1144-1147.

57. Pradhan, S.; Dutta, S.; John, R. P., A coordination driven self-assembled Pd6L8 nanoball catalyses copper and phosphine-free Sonogashira coupling reaction in both homogeneous and heterogeneous formats. *New J. Chem.* **2016**, *40* (8), 7140-7147.

58. Pradhan, S.; John, R. P., Self-assembled Pd_6L_4 cage and Pd_4L_4 square using hydrazide based ligands: synthesis, characterization and catalytic activity in Suzuki-Miyaura coupling reactions. *RSC Adv.* **2016**, *6* (15), 12453-12460.

59. Zhang, L.; Yuan, S.; Feng, L.; Guo, B.; Qin, J.-S.; Xu, B.; Lollar, C.; Sun, D.; Zhou, H.-C., Pore-environment engineering with multiple metal sites in rare-earth porphyrinic metal–organic frameworks. *Angew. Chem.*

Int. Ed. **2018**, *57* (18), 5095-5099.

60. Zhang, X.; Frey, B. L.; Chen, Y.-S.; Zhang, J., Topology-guided stepwise insertion of three secondary linkers in zirconium metal–organic frameworks. *J. Am. Chem. Soc.* **2018**, *140* (24), 7710-7715.

61. Islamoglu, T.; Goswami, S.; Li, Z.; Howarth, A. J.; Farha, O. K.; Hupp, J. T., Postsynthetic tuning of metal–organic frameworks for targeted applications. *Acc. Chem. Res.* **2017**, *50* (4), 805-813.

62. Cohen, S. M., The postsynthetic renaissance in porous solids. *J. Am. Chem. Soc.* **2017**, *139* (8), 2855-2863.

63. Yang, S.; Peng, L.; Sun, D. T.; Asgari, M.; Oveisi, E.; Trukhina, O.; Bulut, S.; Jamali, A.; Queen, W. L., A new post-synthetic polymerization strategy makes metal-organic frameworks more stable. *Chem. Sci.* **2019**, *10* (17), 4542-4549.

64. Fujita, D.; Ueda, Y.; Sato, S.; Mizuno, N.; Kumasaka, T.; Fujita, M., Self-assembly of tetravalent Goldberg polyhedra from 144 small components. *Nature* **2016**, *540* (7634), 563-566.

65. Adam, R.; Mon, M.; Greco, R.; Kalinke, L. H. G.; Vidal-Moya, A.; Fernandez, A.; Winpenny, R. E. P.; Doménech-Carbó, A.; Leyva-Pérez, A.; Armentano, D.; Pardo, E.; Ferrando-Soria, J., Self-assembly of catalytically active supramolecular coordination compounds within metal-organic frameworks. *J. Am. Chem. Soc.* **2019**, *141* (26), 10350-10360.

66. Fujita, M.; Sasaki, O.; Mitsuhashi, T.; Fujita, T.; Yazaki, J.; Yamaguchi, K.; Ogura, K., On the structure of transition-metal-linked molecular squares. *Chem. Commun.* **1996**, *1996* (13), 1535-1536.

67. Varnholt, B.; Oulevey, P.; Luber, S.; Kumara, C.; Dass, A.; Bürgi, T., Structural information on the Au–S interface of thiolate-protected gold clusters: a Raman spectroscopy study. *J. Phys. Chem. C* **2014**, *118* (18), 9604-9611.

68. Huynh, W. U.; Dittmer, J. J.; Alivisatos, A. P., Hybrid nanorod-polymer solar cells. *Science* **2002**, *295* (5564), 2425-2427.

69. Adamo, C.; Amatore, C.; Ciofini, I.; Jutand, A.; Lakmini, H., Mechanism of the palladium-catalyzed homocoupling of arylboronic acids: key involvement of a palladium peroxo complex. *J. Am. Chem. Soc.* **2006**, *128* (21), 6829-6836.

70. Steinhoff, B. A.; Guzei, I. A.; Stahl, S. S., Mechanistic characterization of aerobic alcohol oxidation catalyzed by Pd(OAc)$_2$/pyridine including identification of the catalyst resting state and the origin of nonlinear [catalyst] dependence. *J. Am. Chem. Soc.* **2004**, *126* (36), 11268-11278.

71. Hull, K. L.; Sanford, M. S., Mechanism of benzoquinone-promoted palladium-catalyzed oxidative cross-coupling reactions. *J. Am. Chem. Soc.* **2009**, *131* (28), 9651-9653.

72. Leyva-Pérez, A.; Doménech-Carbó, A.; Corma, A., Unique distal size selectivity with a digold catalyst during alkyne homocoupling. *Nat. Commun.* **2015**, *6* (1), 6703.

73. Mon, M.; Ferrando-Soria, J.; Grancha, T.; Fortea-Pérez, F. R.; Gascon, J.; Leyva-Pérez, A.; Armentano, D.; Pardo, E., Selective gold recovery and catalysis in a highly flexible methionine-decorated metal–organic framework. *J. Am. Chem. Soc.* **2016**, *138* (25), 7864-7867.

74. Toledo, A.; Funes-Ardoiz, I.; Maseras, F.; Albéniz, A. C., Palladium-

catalyzed aerobic homocoupling of alkynes: full mechanistic characterization of a more complex oxidase-type behavior. *ACS Catal.* **2018**, *8* (8), 7495-7506.

75. White, P. B.; Jaworski, J. N.; Zhu, G. H.; Stahl, S. S., Diazafluorenone-promoted oxidation catalysis: insights into the role of bidentate ligands in Pd-catalyzed aerobic aza-Wacker reactions. *ACS Catal.* **2016**, *6* (5), 3340-3348.

76. Natte, K.; Chen, J.; Neumann, H.; Beller, M.; Wu, X.-F., Palladium-catalyzed oxidative carbonylative coupling of arylboronic acids with terminal alkynes to alkynones. *Org. Biomol. Chem.* **2014**, *12* (30), 5590-5593.

77. Devarajan, N.; Karthik, M.; Suresh, P., Copper catalyzed oxidative homocoupling of terminal alkynes to 1,3-diynes: a $Cu_3(BTC)_2$ MOF as an efficient and ligand free catalyst for Glaser–Hay coupling. *Org. Biomol. Chem.* **2017**, *15* (43), 9191-9199.

78. Zhou, Z.; Liu, M.; Wu, X.; Yu, H.; Xu, G.; Xie, Y., Amine-bridged bis(phenol) ligands for efficient Pd-catalyzed aqueous C-C coupling reactions. *Appl. Organomet. Chem.* **2013**, *27* (10), 562-569.

Chapter 5

Perfluorinated palladium catalysts for the direct catalytic oxidation of alkyl alcohols to carboxylic acids

5 Perfluorinated palladium catalysts for the direct catalytic oxidation of alkyl alcohols to carboxylic acids

5.1 Introduction

Oxidation reactions are some of the most important processes in organic chemistry from a synthetic point of view, both on small laboratory scale and on industrial scale. Up to now, some of the most used oxidative catalytic systems are based on stoichiometric transition-metal-based salts and complexes, e.g., Mn salts, H_3BO_3, or Cr(VI) reagents [1-4], which form quite polluting and dangerous waste at the end of the reaction [5]. Indeed, during the last decades, a lot of effort has been put to search new catalytic and oxidant systems, which could be more ecofriendly and cheaper, such as Pt, Au, or Cu in catalytic amounts and O_2, H_2O_2, or TEMPO as oxidants [2, 6-10]. Despite the plethora of systems studied, there is still a lot to understand about the oxidation of the somehow inactivated species, like alkanes or primary alkyl alcohols. Indeed, the oxidation of the latter leads to the synthesis of carboxylic acids, extremely important in refinery and pharmaceutical companies [4, 9, 11].

The oxidation of primary alcohols to carboxylic acids is claimed to be composed by two steps: the dehydrogenation of alcohol to aldehyde, and the oxidation of the aldehyde to acid. In this scenery, the first step is usually the critical one. Indeed, it appears to be quite endergonic, whereas the second is exergonic, i.e., it is necessary to overcome the first energy barrier in order to obtain the acid, and subsequently, to avoid the formation of secondary products such as esters, generated by the Tishchenko-like process [4]. These secondary undesired reactions appear to be the main reason making the direct oxidation of primary alcohols to carboxylic acid quite ambitious.

Even though, during the last decades, many catalytic systems based on noble metals have been developed for the oxidation of primary alcohols to carboxylic acids [12-16], involving supported Pd catalysts or complexes with pyridine ligands [17-22], which could avoid secondary reactions and the unwanted formation of Pd black [23-27]. Most of examples work in presence of bases, which are the agents to start the dehydrogenation of the alcohol to aldehyde, by deprotonating the alcohol coordinated to the catalyst [16, 28].

From an electronic point of view, it is recognized that, in order to achieve higher activities and selectivity, the palladium has to keep his Lewis acidity, diminished by the presence of donor ligands, such as phosphines, which are well-known to form stable complexes with metals, e.g., palladium. Consequently, a compromise between Lewis acidity and ligand coordination is needed, which could be found in the use of ligands with electron withdrawing groups.

Following the last discoveries, in this *Chapter* we present electron poor palladium-based catalysts in homogeneous and heterogenous phase for the

direct oxidation of alkyl alcohols to the corresponding carboxylic acids, shown in Figure 5.1. Fluorinated pyridines were chosen as ligands, because of their wide commercially availability and the recognized activity of fluorinated-pyridines/Pd complexes in cross-coupling and oxidation reactions [29, 30].
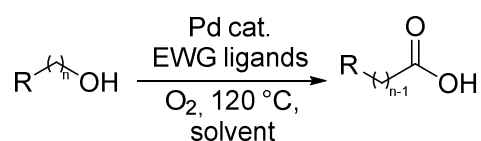
Figure 5.1 Direct oxidation of alkyl alcohols to the corresponding carboxylic acids with Pd-based catalysts.

Herein, we demonstrate the formation in homogenous phase of Pd complexes with fluorinated pyridines [29] and in heterogeneous phase with perfluorinated ones, with the helpful presence of a MOF network. The MOF network is the support for oxo-bridged Pd-dimers which are at the vertexes of square supramolecular complexes [31, 32], which will not be generated in homogenous conditions, because of the electronic nature of the ligands, shown in Figure 5.2.
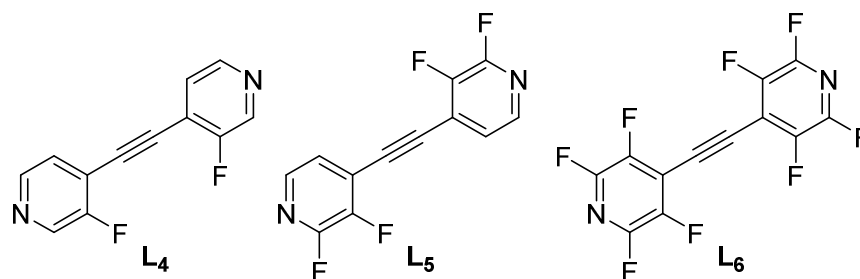
Figure 5.2 Synthetic ligands for the formation of square supramolecular Pd complexes in both homo- and heterogeneous phase.

5.2 Catalytic results

5.2.1 Homogeneous catalysts: Pd(OAc)$_2$ and substituted pyridines

The oxidation of 1-hexanol to hexanoic acid was studied as a benchmark reaction. The yields obtained using as a catalytic system Pd(OAc)$_2$ and different ligands showed the influence of the ligand nature on the selectivity towards hexanoic acid. Indeed, Figure 5.3 shows an increase of the amount of acid with the raise of the electron-withdrawing strength of the ligands, followed by a decrease of the yield when the ligand cannot form the complex with the palladium. Indeed, Figure 5.3 also shows the formation constants for each complex and compares the reactivity, reaching a maximum in ^{2}F-pyridine, which appears to have a good compromise between electron withdrawing strength and Pd coordination. The constant of formation (k$_f$) was calculated following the formation of the complex by ^{1}H NMR and ^{19}F NMR.
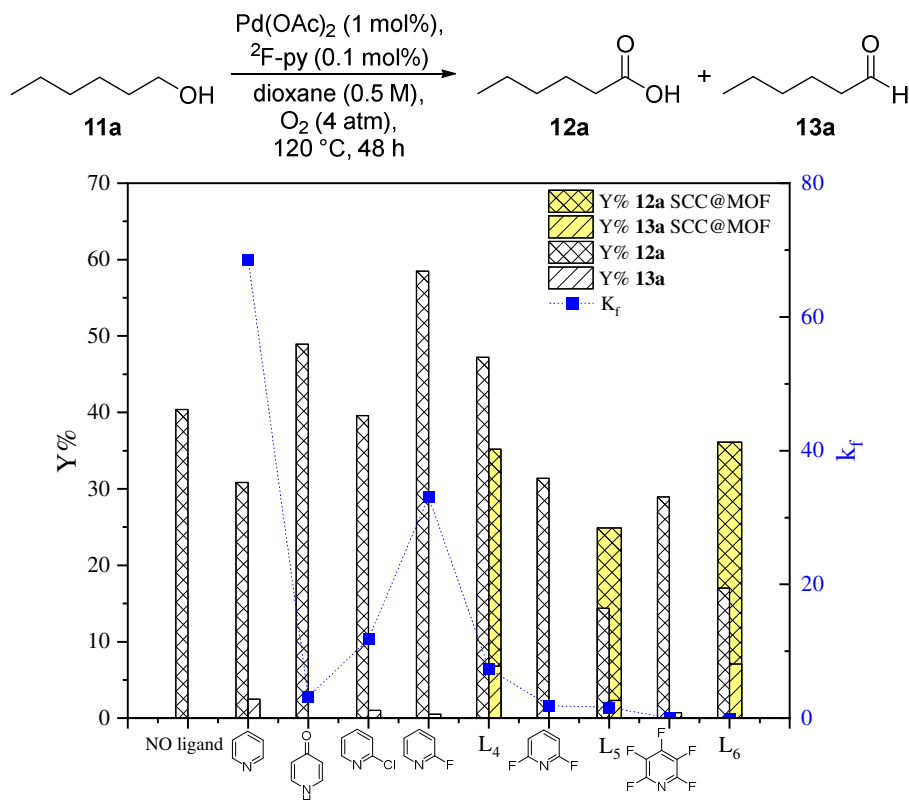
Figure 5.3 12a yields obtained by the direct oxidation of **11a** and their correlation with the constant of formation (k_f) for different Pd/pyridine complexes. Reaction conditions: **11a** 0.25 mmol; [Pd] 1 mol%; [L] 0.1 mol%; dioxane 0.5 M; 120 °C; 48 h; O_2 4 atm.

Interestingly, taking into account the TON, the more EWG ligands have the higher values, reaching a TON of $>10^7$ with the L_6 ligand, as shown in Figure 5.4.
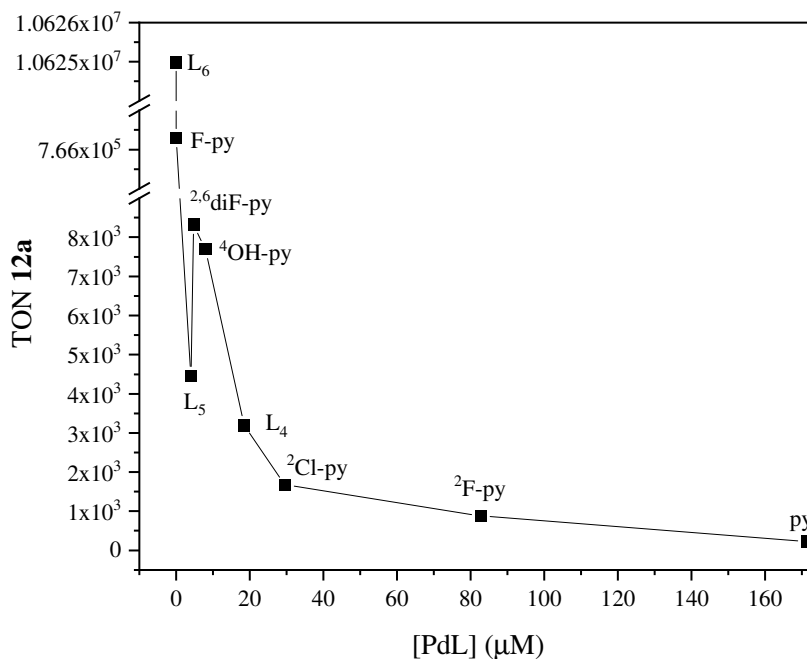
Figure 5.4 TON calculated as moles of **12a** formed per moles of Pd-complex (PdL) generated *in-situ* with the different ligands. Reaction conditions: **11a** 0.25 mmol; [Pd] 1 mol%; [L] 0.1 mol%; dioxane 0.5 M; 120 °C; 48 h; O_2 4 atm.

Moreover, we excluded the importance of water in the system and, surprisingly, we dismissed the relevance of any base, which usually is used in this reaction [28, 33], as shown in Table 5.1. By using *m*-chloroperbenzoic acid (MCPBA), we did not notice a change in the activity, confirming the absence of high valent palladium (see Table 5.1). Furthermore, taking into account that the reaction did not occur in the absence of O_2 (Table 5.1, entries 5, 9-11), a possible acceptor-less dehydrogenative mechanism could be discarded [34].

Table 5.12 Oxidation of **11a** to **12a** with various solvents and different additives. Reaction conditions: **11a** 0.25 mmol; [Pd(OAc)$_2$] 1 mol%; [^{2}F-py] 0.1 mol%; solvent 0.5 M; 120 °C; 48 h.

Entry	Solvent	Additive	Atmosphere	Y%	
				12a	**13a**
1	-*	-	O$_2$ (4atm)	0.2	0.2
2	toluene	-	O$_2$ (4atm)	8.6	n.d.
3	dodecane	-	O$_2$ (4atm)	5.6	0.4
4	THF	-	O$_2$ (4atm)	4.2	4.2
5	dioxane	-	O$_2$ (4atm)	48.9	0.8
6	butyric anhydride	-	O$_2$ (4atm)	n.d.	0.3
7	dioxane	NaOAc	O$_2$ (4atm)	57.0	2.2
8	dioxane	MCPBA	O$_2$ (4atm)	43.0	1.5
9	dioxane	H$_2$O	O$_2$ (4atm)	55.8	1.1
10	dioxane	-	N$_2$ (4atm)	2.1	3.3
11	dioxane	-	reflux	9.4	10.6
12	dioxane	-	air (4atm)	10.1	6.9

Figure 5.5 shows the kinetics of the reaction, with a strictly dependence between the disappearing of the aldehyde and the generation of the acid. The equation rate calculated for this reaction has demonstrated to be quite interesting: **r$_0$=[Pd][L]$^{-1}$**. Indeed, the rate is not dependent on the substrate nor the oxygen, but only on the palladium and the ligands, L$_4$ or ^{2}F-py.

In order to have a better understanding, we performed kinetic tests with lower concentrations of hexanol, demonstrating the oversaturation of the catalytic

species with the substrate under our reaction conditions. At lower concentrations of hexanol, the equation appears to be $r_0=[11a]^2[Pd][L]^{-1}$, making us suppose the *in-situ* generation of the complex shown in Figure 5.6. Moreover, a high concentration of ligand was unlikely to form the mentioned complex, bringing to a negative reaction order for each ligand tested in the kinetics.
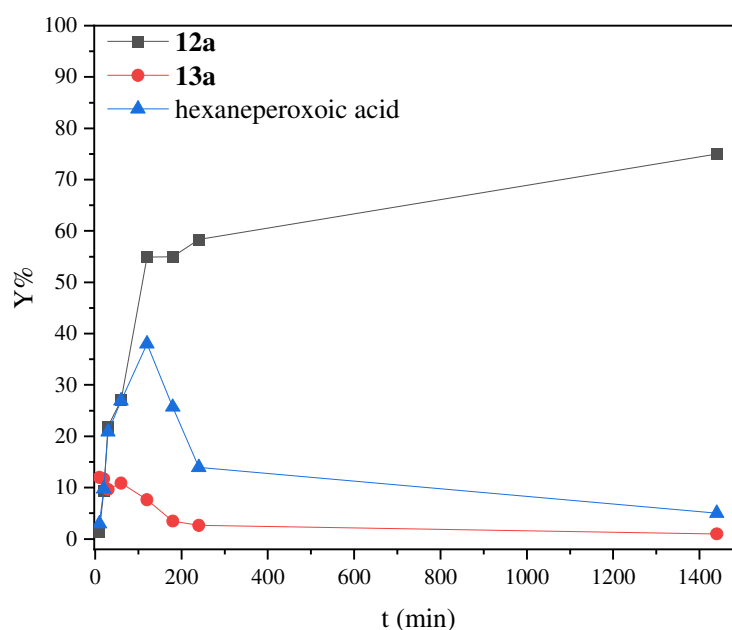
Figure 5.5 Time dependence of the formation of **12a** in the reaction of oxidation of **11a** (top) and **13a** (bottom). Reaction conditions: [Pd] 1 mol%; [L_4] 2 mol%; dioxane 0.5M; 120 °C; O_2 4 atm. The experiment was carried out releasing the oxygen for each point of the kinetic.
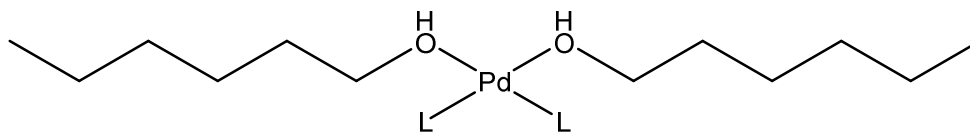
Figure 5.6 Possible complex formed in-situ during the reaction of oxidation of **11a**.

Considering that the aldehyde is the precursor of the acid, **13a** was studied as a starting material in the kinetics, showing an order 1 in oxidation reaction to **12a**. Despite the fact that the higher initial rates confirm that the rate determining step is the one bringing from **11a** to **13a**, the yield of aldehyde detected was always very low, due to its consumption in the reaction of formation of hexaneperoxoic acid, which showed the following equation rate: $r_0=[\textbf{11a}][\textbf{Pd}][\textbf{L}]^{-1}$. The use of radical inhibitor, DABCO, quenched both the oxidation of the aldehyde **13a** to **12a** and the dehydrogenation of alcohol **11a** to **13a**. These results strongly support that the formation of intermediate alkyl hydroperoxy acids is interrupted by the presence of the radical scavenger and the reaction cannot follow to the product (see Figure 5.7). The kinetic evidence and the experiments performed with the radical inhibitor, suggested the mechanism shown in Figure 5.8.
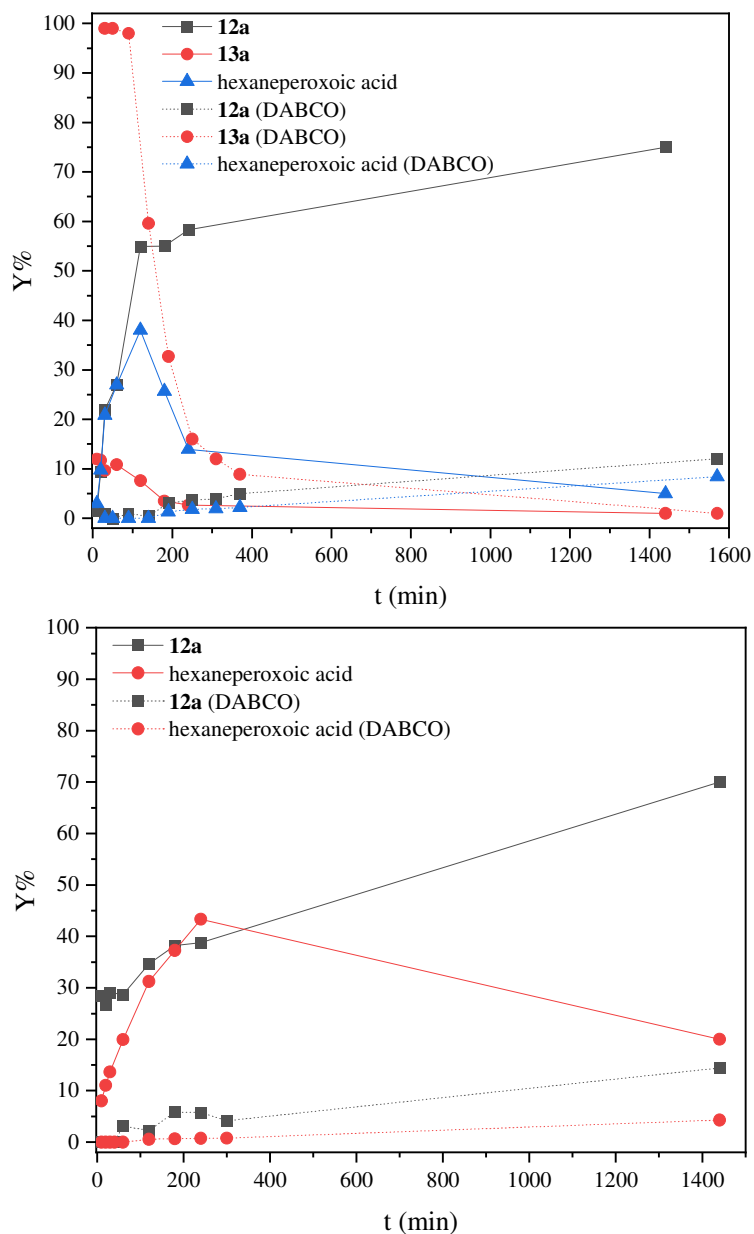
Figure 5.7 Radical inhibitors experiments, performed with DABCO, in the oxidation process of **11a** (top) and **13a** (bottom).
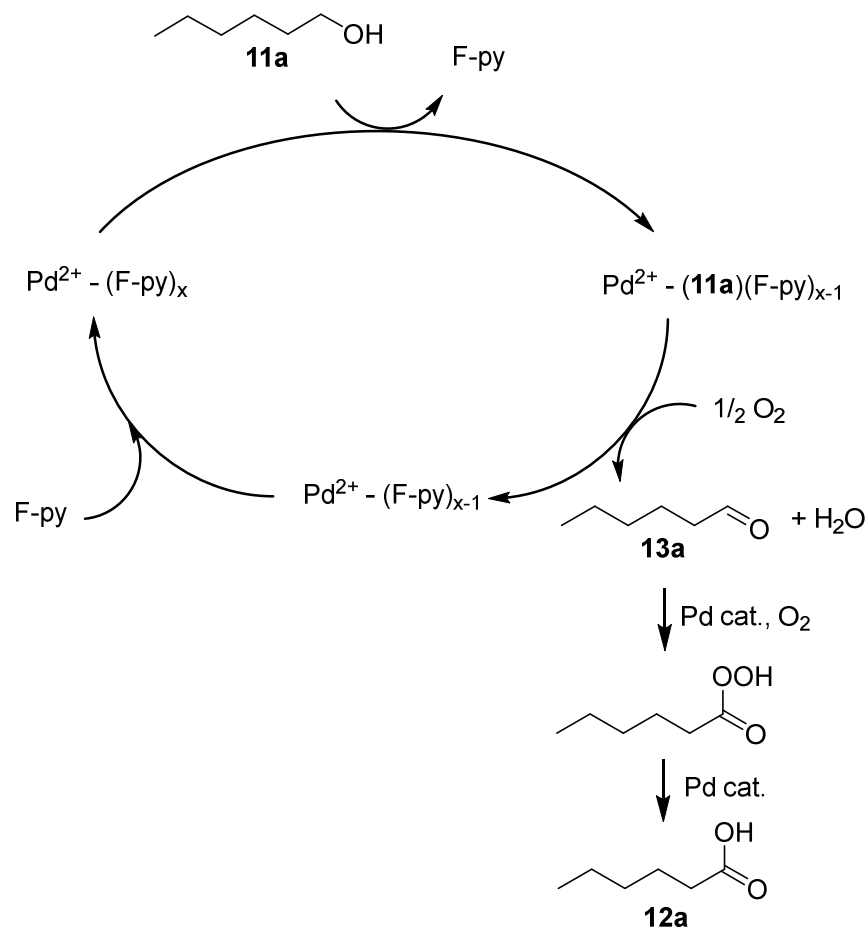
Figure 5.8 Possible mechanism for the reaction of oxidation of **11a** with a catalytic system formed by palladium and fluorinated pyridines.

5.2.2 Heterogeneous catalysts: SCCs@MOF

In order to confirm our hypothesis, we forced mechanically the formation of complexes which otherwise would not be generated in homogeneous phase, due to the quite low nucleophilicity of the ligand coordination sites, using

MOFs. As a matter of fact, we give birth to a family of fluorinated MOFs, starting from MOF **1**, described in *Chapter 4*. The use of three different ligands, shown in Figure 5.2, brought to the formation of three SCCs@MOF **14**-**16**, synthesized as in the case of SCC@MOF **2** (see *Chapters 3* and *4*). Figure 5.9 shows the results obtained with SCCs@MOF **14**-**16** compared with the pristine MOF **1** and SCC@MOF **2**, which was synthesized by soaking MOF **1** in a solution of L_1, shown in Figure 5.10. Certainly, the low catalytic results obtained with MOF **1** and SCC@MOF **2**, compared to SCCs@MOF **14-16**, underlined the importance of an electron-poor palladium for catalyzing the oxidation reaction.
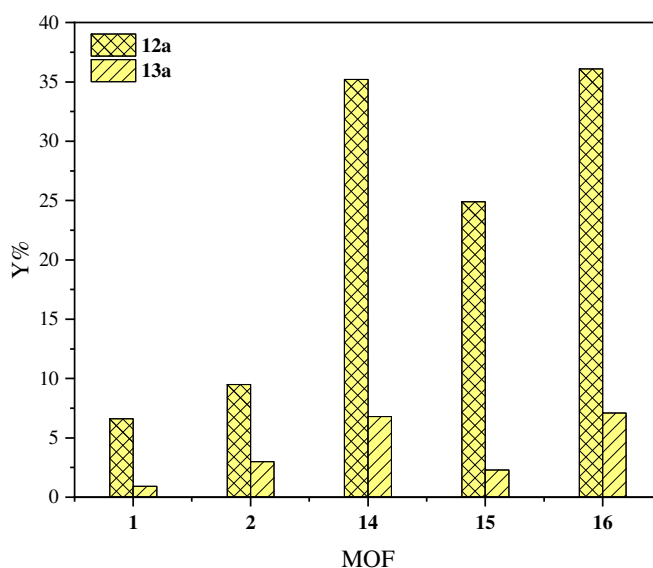
Figure 5.9 Hexanoic acid (**12a**) and hexanal (**13a**) yields obtained by the direct oxidation of hexanol with MOF **1** and SCCs@MOF **2** and **14-16**. Reaction conditions: **11a** 0.25 mmol; [Pd] 1 mol %; dioxane 0.5 M; 120 °C; 48 h; O_2 4 atm.
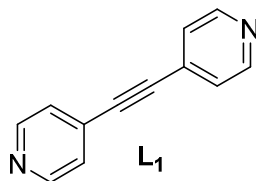
Figure 5.10 Structure of the ligand L$_1$ used for the synthesis of SCC@MOF **2**.

Table 5.2 Oxidation of **11a** with Pd(OAc)$_2$ or MOF **1** with different fluorinated ligands. Reaction conditions: **11a** 0.25 mmol; [Pd] 1 mol %; [L] 0.1 mol %; dioxane 0.5 M; 120 °C; 48 h; O$_2$ 4 atm.

Entry	Catalyst	Ligand	Y%	
			12a	13a
1	Pd(OAc)$_2$	-	40.4	0.0
2	**1**		6.6	0.9
3	Pd(OAc)$_2$	^{2}F-py	58.5	0.5
4	**1**		22.6	0.0
5	Pd(OAc)$_2$	L$_4$	47.2	0.0
6	**1**		15.4	1.3
7	Pd(OAc)$_2$	L$_5$	14.4	0.0
8	**1**		6.4	2.4
9	Pd(OAc)$_2$	L$_6$	17.0	0.0
10	**1**		25.1	0.0

In accordance with our hypothesis, the pre-synthesis of the SCCs@MOF is quite relevant. An experiment with the progenitor MOF **1** and L$_4$-L$_6$, used for

the synthesis of **14-16**, underlines the decrease in yields, as shown in Table 5.2. In contrast, Figure 5.3 shows that SCCs@MOF **15**-**16** present an increase in activity if compared with the equivalent homogeneous, formed by the combination of Pd(OAc)$_2$ and L$_4$-L$_6$, probably due to the improved formation of the complexes inside the MOF. On the other hand, SCC@MOF **14** and Pd(OAc)$_2$/L$_4$ bring to comparable results, because of the possible generation of the complex in homogeneous phase, confirmed by a higher k$_f$.

Figure 5.11 shows the results obtained with SCC@MOF **14** and Pd(OAc)$_2$/L$_4$ for alcohols with increased chain length. It is possible to say that the flattening in the yields curve, when using compound **14**, is probably due to the impossibility of longer chains to be guested in the MOF channels.

SCC@MOF **14** appeared to be reusable at least three times as depicted in Figure 5.12, and a hot filtration test confirmed the absence of leaching during the reaction (Figure 5.13).
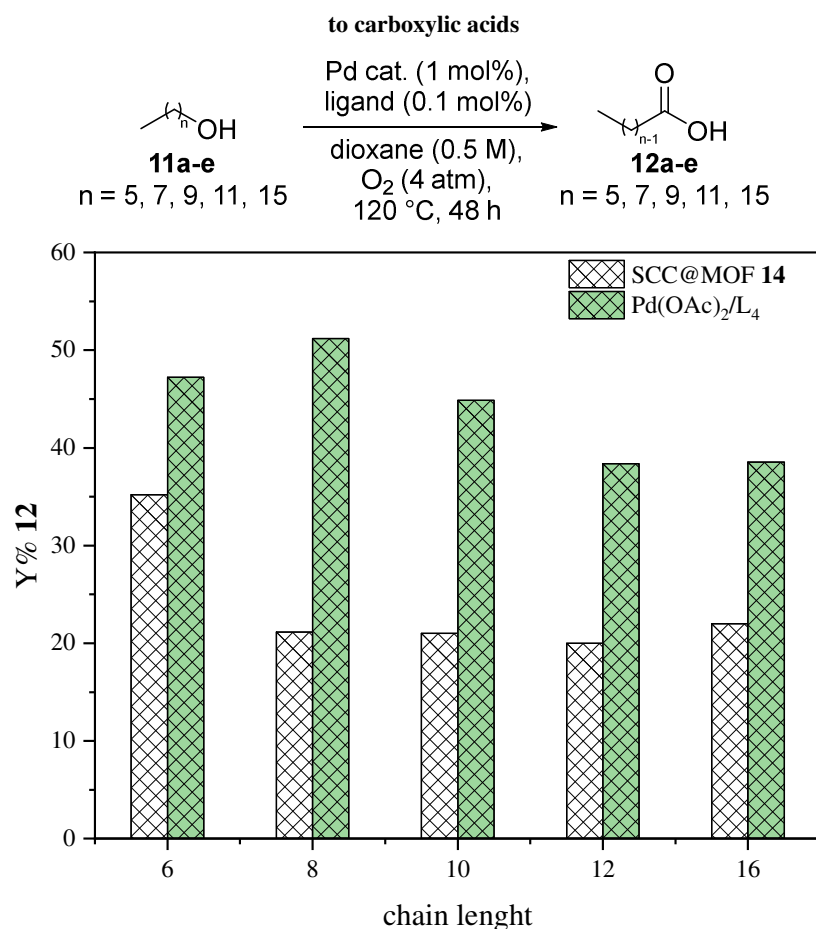
Figure 5.11 Acid yields obtained by the direct oxidation of alcohols with different chain lengths in presence of SCC@MOF **14** or Pd(OAc)$_2$/L$_4$. Reaction conditions: **11a-e** 0.25 mmol; [Pd] 1 mol%; [L$_4$] 0.1 mol%; dioxane 0.5 M; 120 °C; 48 h; O$_2$ 4 atm.
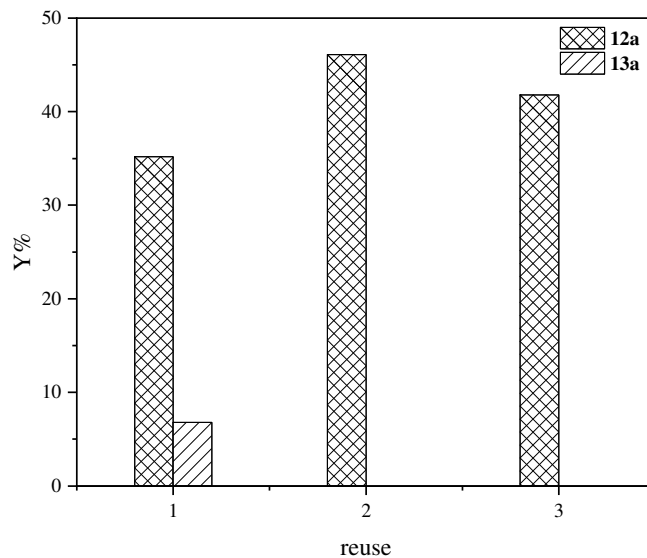
Figure 5.12 Reuses of SCC@MOF **14** in the oxidation reaction of **11a.**
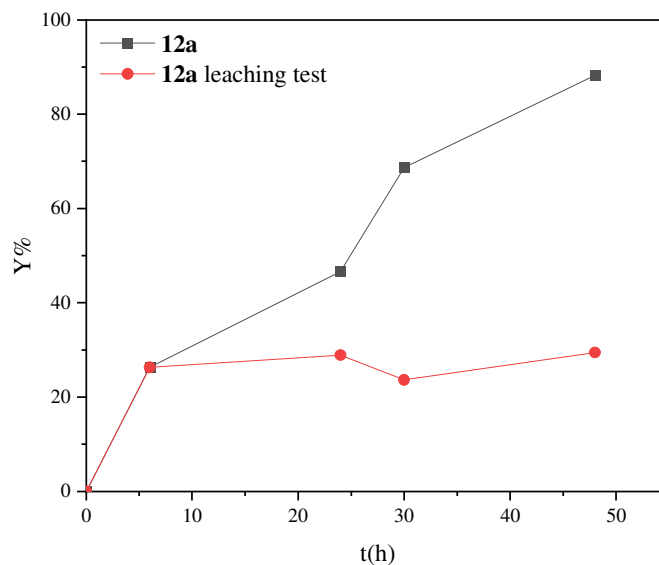
Figure 5.13 Leaching test of the SCC@MOF **14** in the oxidation reaction of **11a**.

5.3 Conclusions

In this *Chapter*, the oxidation of alkyl alcohols was described, using perfluorinated palladium catalysts. The catalysis was performed, both in homogeneous and heterogeneous phase. In the first case, a system formed by palladium and fluorinated pyridines and bipyridines showed high TON, especially in the case of perfluorinated ligands, which are known to be the cheapest ones.

The reaction could be performed also in heterogenous phase by using SCCs@MOF, formed employing fluorinated bipyridines as ligands. The SCCs@MOF were compared to non-fluorinated counterparts, which did not reveal activity towards the reaction of interest, showing the importance of an electron-poor palladium in the reaction of oxidation.

Finally, we were able to catalyze the one-pot base-free oxidation reaction of alkyl alcohols to alkyl acids, interesting products from an industrial point of view.

5.4 References

1. Sen, A.; Lin, M., Direct catalytic oxidative carbonylation of lower alkanes to acids. **1996**, U.S. 5,393,922.

2. Sheldon, R. A.; Arends, I. W. C. E.; Dijksman, A., New developments in catalytic alcohol oxidations for fine chemicals synthesis. *Catal. Today* **2000**, *57* (1), 157-166.

3. Catalano, V. J.; Heck, R. A.; Immoos, C. E.; Robinson, A.; Hill, M. G., Steric modulation of electrocatalytic benzyl alcohol oxidation by $[Ru(trpy)(R_2dppi)(O)]^{2+}$ complexes. *Inorg. Chem.* **1998**, *37* (9), 2150-2157.

4. Cherepakhin, V.; Williams, T. J., Direct Oxidation of Primary Alcohols to Carboxylic Acids. *Synthesis* **2021**, *53* (6), 1023-1034.

5. Sodhi, R. K.; Paul, S.; Clark, J. H., A comparative study of different metal acetylacetonates covalently anchored onto amine functionalized silica: a study of the oxidation of aldehydes and alcohols to corresponding acids in water. *Green Chem.* **2012**, *14* (6), 1649-1656.

6. Mallat, T.; Baiker, A., Oxidation of alcohols with molecular oxygen on platinum metal catalysts in aqueous solutions. *Catal. Today* **1994**, *19* (2), 247-283.

7. Mannam, S.; Sekar, G., Efficient CuCl-catalyzed selective and direct oxidation of β- and γ-substituted aliphatic primary alcohols to carboxylic acids. *Synth. Commun.* **2010**, *40* (19), 2822-2829.

8. Gu, Q.; Fang, W. H.; Wischert, R.; Zhou, W. J.; Michel, C.; Pera-Titus, M., $AuCu/CeO_2$ bimetallic catalysts for the selective oxidation of fatty alcohol ethoxylates to alkyl ether carboxylic acids. *J. Catal.* **2019**, *380*, 132-144.

9. Mahmoudi, B.; Rostami, A.; Kazemnejadi, M.; Hamah-Ameen, B. A., Catalytic oxidation of alcohols and alkyl benzenes to carbonyls using

Fe$_3$O$_4$@SiO$_2$@(TEMPO)-co-(Chlorophyll-Co^{III}) as a bi-functional, self-co-oxidant nanocatalyst. *Green Chem.* **2020**, *22* (19), 6600-6613.

10. Brink, G.-J. t.; Arends, I. W. C. E.; Sheldon, R. A., Green, catalytic oxidation of alcohols in water. *Science* **2000**, *287* (5458), 1636-1639.

11. Wang, F.; Wang, M.; Xu, J.; Ma, J.; Yu, M.; Zhang, X., Catalyst for preparing fatty acid by oxidizing fatty alcohol and application thereof. **2015**, CN 201410175020.2A.

12. Jiang, X.; Zhang, J.; Ma, S., Iron catalysis for room-temperature aerobic oxidation of alcohols to carboxylic acids. *J. Am. Chem. Soc.* **2016**, *138* (27), 8344-8347.

13. Zhao, M.; Zhang, X.-W.; Wu, C.-D., Structural transformation of porous polyoxometalate frameworks and highly efficient biomimetic aerobic oxidation of aliphatic alcohols. *ACS Catal.* **2017**, *7* (10), 6573-6580.

14. Možina, Š.; Iskra, J., Aerobic oxidation of secondary alcohols with nitric acid and iron(III) chloride as catalysts in fluorinated alcohol. *J. Org. Chem.* **2019**, *84* (22), 14579-14586.

15. Liu, H.-M.; Jian, L.; Li, C.; Zhang, C.-C.; Fu, H.-Y.; Zheng, X.-L.; Chen, H.; Li, R.-X., Dehydrogenation of alcohols to carboxylic acid catalyzed by in situ-generated facial ruthenium-CPP complex. *J. Org. Chem.* **2019**, *84* (14), 9151-9160.

16. Sha, J.; Zheng, E.-J.; Zhou, W.-J.; Liebens, A.; Pera-Titus, M., Selective oxidation of fatty alcohol ethoxylates with H$_2$O$_2$ over Au catalysts for the synthesis of alkyl ether carboxylic acids in alkaline solution. *J. Catal.* **2016**, *337*, 199-207.

17. Schultz, M. J.; Park, C. C.; Sigman, M. S., A convenient palladium-catalyzed aerobic oxidation of alcohols at room temperature. *Chem. Commun.* **2002**, (24), 3034-3035.

18. Jensen, D. R.; Schultz, M. J.; Mueller, J. A.; Sigman, M. S., A Well-

defined complex for palladium-catalyzed aerobic oxidation of alcohols: Design, synthesis, and mechanistic considerations. *Angew. Chem. Int. Ed.* **2003**, *42* (32), 3810-3813.

19. Yang, M.; Yip, K.-T.; Pan, J.-H.; Chen, Y.-C.; Zhu, N.-Y.; Yang, D., A sterically bulky cyclic thiourea as an efficient ligand for palladium-catalyzed aerobic oxidation of alcohols. *Synlett* **2006**, *2006* (18), 3057-3060.

20. Gowrisankar, S.; Neumann, H.; Gördes, D.; Thurow, K.; Jiao, H.; Beller, M., A convenient and selective palladium-catalyzed aerobic oxidation of alcohols. *Chem. Eur. J.* **2013**, *19* (47), 15979-15984.

21. Zhang, Y.-Y.; Li, J.-X.; Ding, L.-L.; Liu, L.; Wang, S.-M.; Han, Z.-B., Palladium nanoparticles encapsulated in the MIL-101-catalyzed one-pot reaction of alcohol oxidation and aldimine condensation. *Inorg. Chem.* **2018**, *57* (21), 13586-13593.

22. Hou, Z.; Theyssen, N.; Leitner, W., Palladium nanoparticles stabilized on PEG-modified silica as catalysts for the aerobic alcohol oxidation in supercritical carbon dioxide. *Green Chem.* **2007**, *9* (2), 127-132.

23. Abad, A.; Almela, C.; Corma, A.; Garcia, H., Efficient chemoselective alcohol oxidation using oxygen as oxidant. Superior performance of gold over palladium catalysts. *Tetrahedron* **2006**, *62* (28), 6666-6672.

24. Enache, D. I.; Edwards, J. K.; Landon, P.; Solsona-Espriu, B.; Carley, A. F.; Herzing, A. A.; Watanabe, M.; Kiely, C. J.; Knight, D. W.; Hutchings, G. J., Solvent-free oxidation of primary alcohols to aldehydes using Au-Pd/TiO$_2$ catalysts. *Science* **2006**, *311* (5759), 362-365.

25. Karimi, B.; Mansouri, F.; Vali, H., Minimizing the size of palladium nanoparticles immobilized within the channels of ionic liquid-derived magnetically separable heteroatom-doped mesoporous carbon for aerobic oxidation of alcohols. *ACS Appl. Nano Mater.* **2020**, *3* (11),

10612-10627.

26. Steinhoff, B. A.; Fix, S. R.; Stahl, S. S., Mechanistic study of alcohol oxidation by the Pd(OAc)$_2$/O$_2$/DMSO catalyst system and implications for the development of improved aerobic oxidation catalysts. *J. Am. Chem. Soc.* **2002**, *124* (5), 766-767.

27. Steinhoff, B. A.; Stahl, S. S., Mechanism of Pd(OAc)$_2$/DMSO-catalyzed aerobic alcohol oxidation: Mass-Transfer-Limitation effects and catalyst decomposition pathways. *J. Am. Chem. Soc.* **2006**, *128* (13), 4348-4355.

28. Sharma, G. V. M.; Chander, A. S.; Krishnudu, K.; Krishna, P. R., Pd(OAc)$_2$ mediated oxidative cyclization of γ,δ - olefinic alcohols: A new route to C-vinyl furanosides. *Tetrahedron Lett.* **1998**, *39* (38), 6957-6960.

29. Izawa, Y.; Stahl, S. S., Aerobic oxidative coupling of *o*-xylene: Discovery of 2-fluoropyridine as a ligand to support selective Pd-catalyzed C-H functionalization. *Adv. Synth. Catal.* **2010**, *352* (18), 3223-3229.

30. Korenaga, T.; Sasaki, R.; Shimada, K., Highly electron-poor Buchwald-type ligand: Application for Pd-catalysed direct arylation of thiophene derivatives and theoretical consideration of the secondary Pd[0]–arene interaction. *Dalton Trans.* **2015**, *44* (45), 19642-19650.

31. Fortea-Pérez, F. R.; Mon, M.; Ferrando-Soria, J.; Boronat, M.; Leyva-Pérez, A.; Corma, A.; Herrera, J. M.; Osadchii, D.; Gascon, J.; Armentano, D.; Pardo, E., The MOF-driven synthesis of supported palladium clusters with catalytic activity for carbene-mediated chemistry. *Nat. Mater.* **2017**, *16* (7), 760-766.

32. Adam, R.; Mon, M.; Greco, R.; Kalinke, L. H. G.; Vidal-Moya, A.; Fernandez, A.; Winpenny, R. E. P.; Doménech-Carbó, A.; Leyva-Pérez, A.; Armentano, D.; Pardo, E.; Ferrando-Soria, J., Self-assembly of

catalytically active supramolecular coordination compounds within metal–organic frameworks. *J. Am. Chem. Soc.* **2019**, *141* (26), 10350-10360.

33. Liu, S.-K.; Cui, X.-F.; Liu, X.-X.; Ma, H.-J.; Wei, D.-D.; Luo, X.-L.; Huang, G.-S., Cobalt(II)-catalyzed cross-dehydrogenative coupling reaction of benzamides with alcohols to build C-O bond. *ChemistrySelect* **2018**, *3* (14), 3989-3992.

34. Sutanuva, M., Acceptorless dehydrogenation of primary and secondary benzylic alcohols using a well defined phosphine free air stable mnII - catalyst. synthesis of imines via dehydrogenative coupling of alcohols and amines. *Int. J. Sci. Res. Rev.* **2019**, *8* (3), 34-48.

Chapter 6

Palladium single atoms for the direct catalytic oxidation of benzyl alcohols to carboxylic acids

6 Palladium single atoms for the direct catalytic oxidation of benzyl alcohols to carboxylic acids

6.1 Introduction

As mentioned in *Chapter 1*, Single Atom Catalysts (SACs) represent an appealing improvement in the field of catalysis, due to their very high catalytic activity compared to the corresponding bulk catalyst or even nanoparticles [1, 2]. Certainly, there are drawbacks to circumvent, such as the instability of these species in absence of ligands or supports or the difficulties with characterizing them [3, 4]. Consequently, the synthesis of naked Single Atoms (SAs) or even clusters is almost unexplored, due to their tendency to agglomerate and form nanoparticles and/or inactive bulk metal [5-7]. On the other hand, when the interested reaction involves molecules, able to stabilize the SACs, the situation can be advantageous for the formation of these small species, which will be eventually formed *in-situ* [8]. An example of stabilizing molecules might be benzyl alcohols, which are quite useful in organic synthesis in a plethora of processes, among them the oxidation process to benzaldehydes or benzoic acids [9-11]. As shown in Figure 6.1,

the oxidation of benzyl alcohols to benzoic acids happens through two steps: the dehydrogenation of the benzyl alcohol to benzaldehyde, which can spontaneously undergo a further radical oxidation to benzoic acid. The first step is well-known and widely studied in presence of different catalytic systems, including transition metal species as homo- or heterogeneous catalysts and oxidizing agents such as TEMPO or O_2 [9, 12-16]. The second step is spontaneous and happens *via* radicals [17], but it cannot occur in presence of benzyl alcohol, which acts as a radical scavenger even at very low concentrations [18]. According to this concept, it is not surprising that the direct oxidation of benzyl alcohols to benzoic acids needs harsh conditions, such as the use of strong bases or expensive organometallic catalysts [19-24].
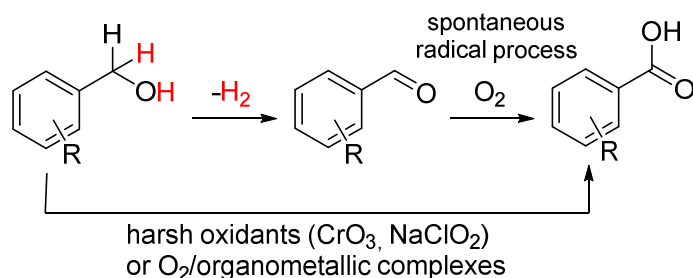
Figure 6.1 Standard catalysts and oxidizing agents for the oxidation of benzyl alcohols to benzaldehydes or benzoic acids.

Benzyl alcohol is a recognized reducing agent in the synthesis of noble metal nanoparticles, bringing as a consequence to the formation of oxidation products such as benzaldehyde [25, 26]. Following this rationale, we thought that the presence of very low amount of metal could generate SAs, reduced and stabilized by the presence of the benzyl alcohol. These species could then

act as a catalyst for the oxidation reaction of the same benzyl alcohol to benzoic acid. Indeed, the high reactivity of SAs, compared to classical catalysts, could give the necessary feature to the catalyst to perform the oxidation reaction.

6.2 Catalysis with Pd single atoms in solution

6.2.1 Catalytic results
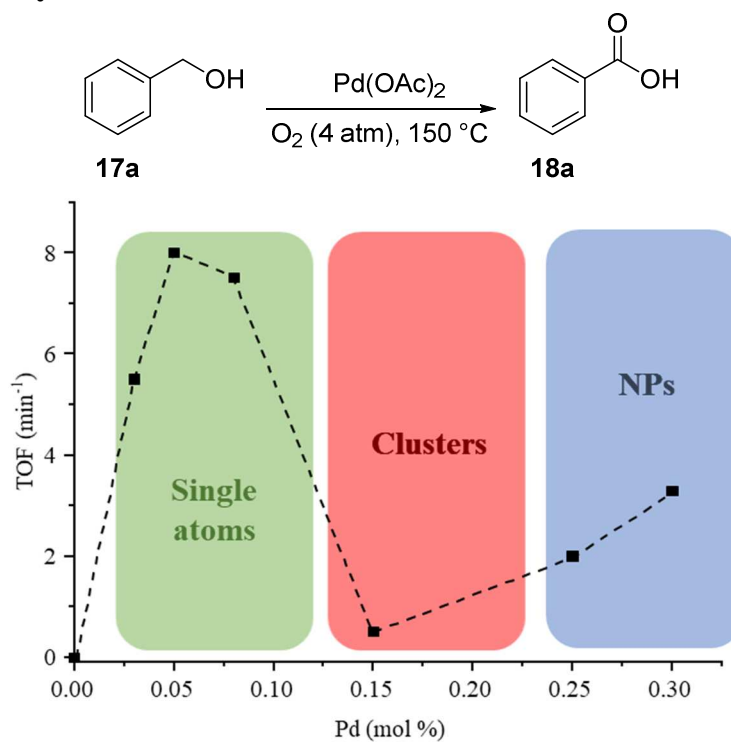
Figure 6.2 Initial turnover frequencies (TOF_0) expressed as initial rate of the oxidation reaction of **17a** to **18a** (shown at the top) divided by the moles of palladium.

As shown in Figure 6.2, the oxidation of benzyl alcohol with $Pd(OAc)_2$ in absence of solvent had its maximum TOF_0 with low amounts of palladium, less than 0.1 mol%, and, interestingly, started to slightly increase after 0.15 mol%. We supposed that the catalytic species at concentrations lower than 0.1 mol% were Pd SAs, whereas at higher amounts of palladium bigger species were formed, i.e., metal clusters and nanoparticles [27-29]. Table 6.1 shows the results obtained at 4 h with different precursors of palladium and underlines that the presence of stronger ligands, such as phosphines, did not lead to acceptable results (see Table 6.1, Entries 5 and 6).

Table 6.1 Yields obtained with palladium catalyst in the oxidation reaction of **17a**. Reaction conditions: **17a** 1.96 mmol, [Pd] 0.3 mol%, O_2 4 atm, 150 °C, 4 h (* 15 h).
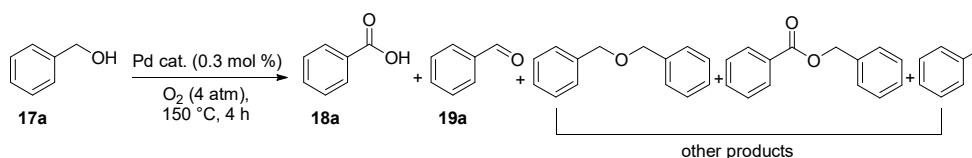
Entry	Catalyst	18a	19a	Other products
1	$Pd(OAc)_2$	75%	3.6%	6.9%
2	K_2PdCl_4	55.6%	15.5%	15.7%
3	$Pd_2(dba)_3$*	37.9%	18.2%	9.9%
4	$Pd(acac)_2$	51.4%	15.8%	9.6%
5	$Pd(PPh_3)_4$	7.2%	24.1%	8.8%
6	$Pd(PPh_3)_2Cl_2$	0.7%	4.5%	7.0%
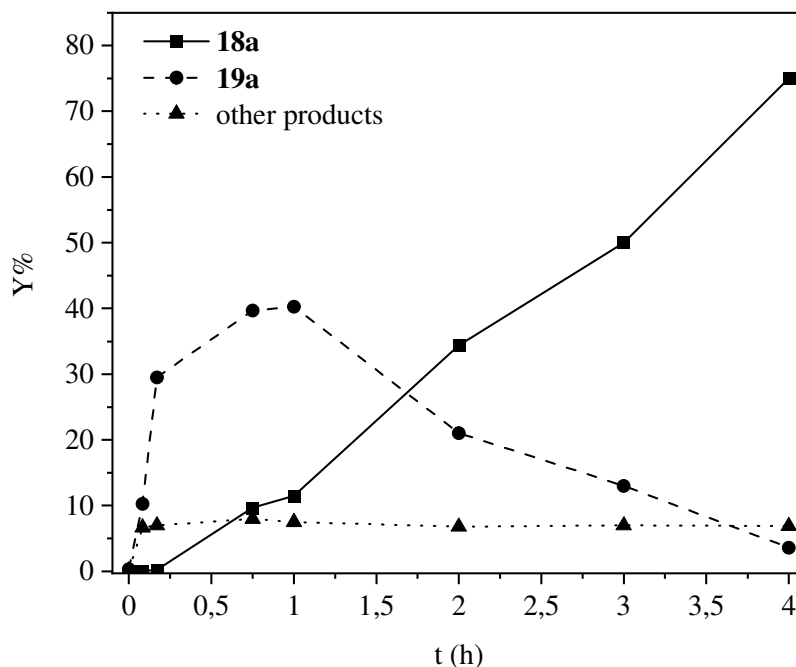
Figure 6.3 Kinetic plot for the oxidation of **17a** catalyzed by Pd(OAc)$_2$ (0.05 mol%).

Figure 6.3 gives another important insight of the reaction, showing that the formation of **18a** starts when the conversion of **17a** is not yet 50 %. This confirms that **17a** is not poisoning the catalyst and is not behaving as a quencher for the radical oxidation of **19a** to **18a** [18]. Moreover, an acceptor-less dehydrogenation route could be excluded due to the very low conversions obtained in a reaction performed in absence of oxygen, which consequently is needed to perform the direct oxidation [30, 31]. Moreover, PPh$_3$ was used to quench the possible monometallic active species in solution and the formation of **18a** could not proceed after the addition of the phosphine, as shown in Figure 6.4. The last finding confirmed that the concentration was

not crucial for the reaction to happen, but the species in solution were responsible for the oxidation, i.e., SAs were catalyzing the reaction.
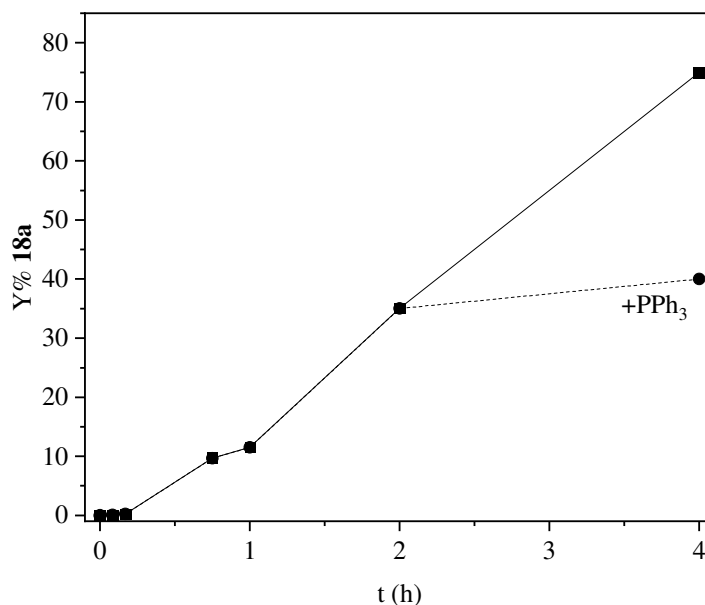
Figure 6.4 Quenching test with PPh3 in the oxidation reaction of **17a** catalyzed by Pd1 in solution.

6.2.2 Characterization of single atoms in solution

To confirm our hypothesis of the *in-situ* formation of SAs, the metal species, formed during the reaction at concentrations lower than 0.1 mol%, were trapped on active charcoal and analyzed by Aberration-corrected High-angle Annular Dark Field Scanning-transmission Electron Microscopy (AC HAADF- STEM), which confirmed the presence of Pd SAs, as shown in Figure 6.5. Considering that the AC HAADF- STEM imaging is proportional to Z^2, i.e., the squared atomic number, palladium species could be identified

as the brightest contrast in the image as illustrated by the orange circles in Figure 6.4. In the cases of concentrations higher than 0.1 mol%, clusters (MCs) and nanoparticles (NPs) were found in the images at concentrations of 0.15 mol% and 0.30 mol%, respectively (see Figure 6.6).

The formation of very small species was confirmed by *in-situ* X-ray Absorption Near Edge Structure (XANES) and Extended X-ray Absorption Fine Structure (EXAFS) measurements (Figure 6.7), which showed the partial reduction of palladium and allowed to calculate an average number of 6 Pd-Pd bonds at the concentration of 0.08 mol%. Moreover, the flattening in the XANES spectrum after 24500 eV is related to the quantum size effect generated by the presence of SAs and very small agglomerated. In addition, the disappearance of $Pd^{\delta+}$ was confirmed by adding PPh_3 and progressively analyzing the solution by Ultraviolet−Visible (UV−Vis) spectrophotometer (see Figure 6.8).

These techniques support the hypothesis of partially reduced Pd_1 species, which act as a catalyst in the aerobic one-pot oxidation of **17a**. However, we will further demonstrate this hypothesis by showing experiments performed using pre-synthetized or commercial Pd SACs, Pd clusters and Pd nanoparticles.
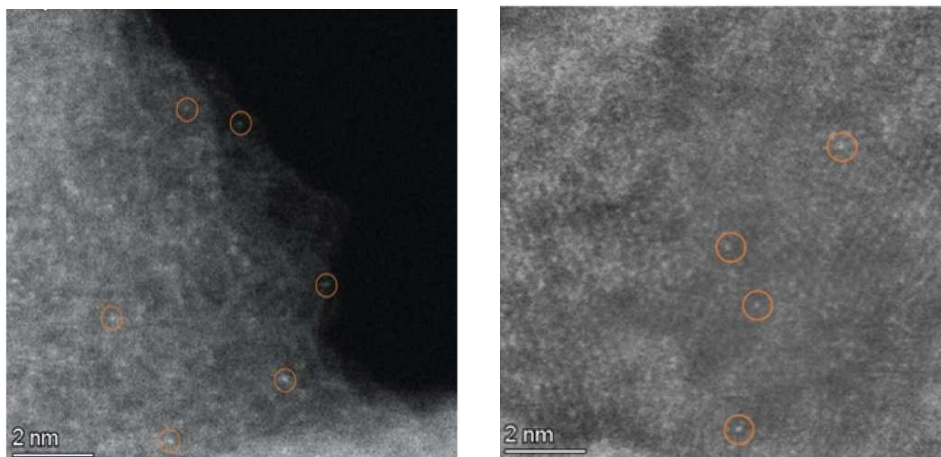
Figure 6.5 AC HAADF-STEM images of the Pd species formed in the reaction mixture at concentrations lower than 0.1 mol% and afterwards trapped in active charcoal. Pd single atoms are in the orange circles.
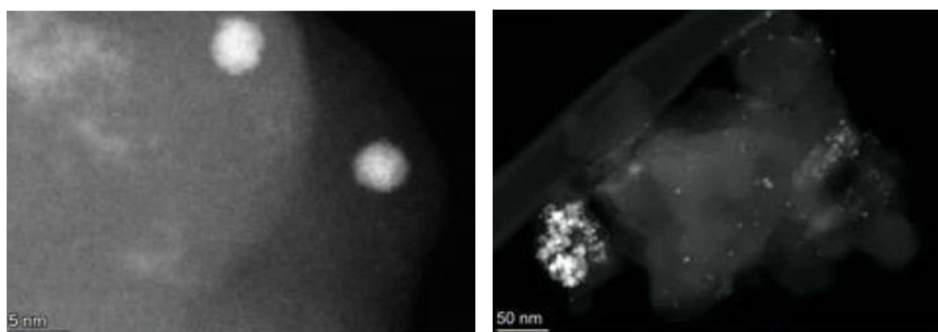
Figure 6.6 AC HAADF-STEM images of the Pd species in solution formed in the reaction mixture at concentrations of 0.15 mol% (left) and 0.30 mol% (right) and trapped in active charcoal.
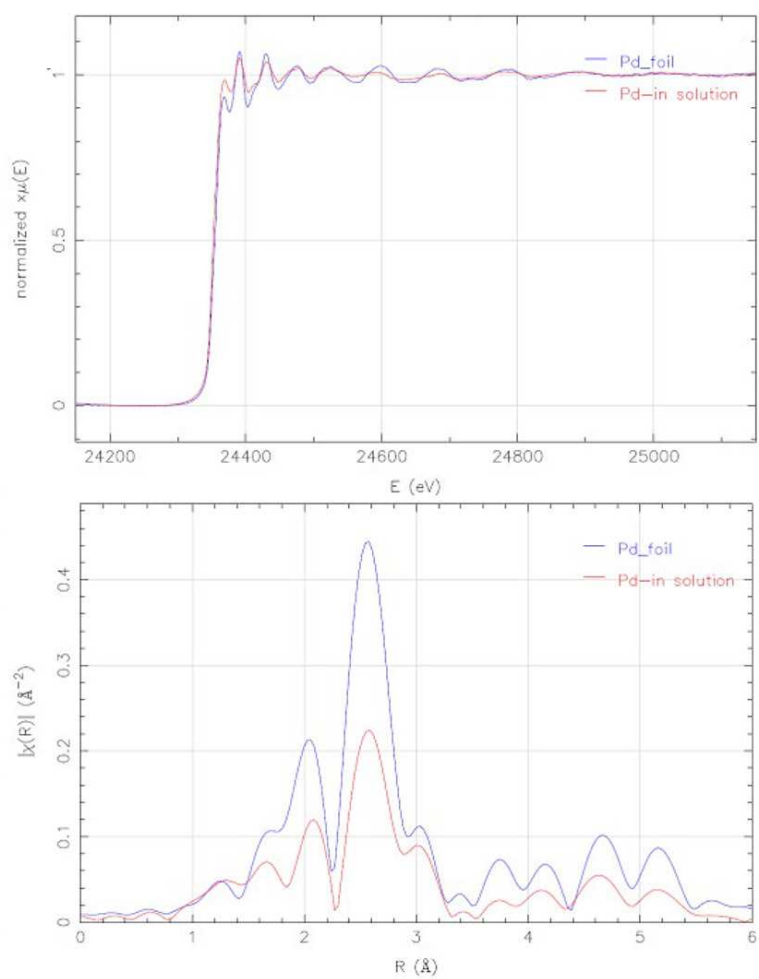
Figure 6.7 XANES (top) and EXAFS (bottom) measurements of palladium species in solution compared with Pd foil.
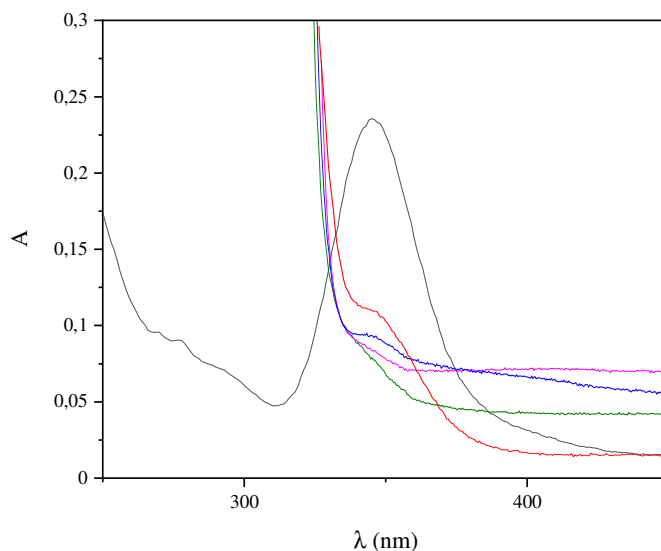
Figure 6.8 Ultraviolet-Visible spectrophotometric titrations of $Pd^{\delta+}$ in solution during the oxidation reaction of **17a**.

6.2.3 Mechanism of the oxidation reaction catalyzed by single atoms in solution

Kinetic experiments for the oxidation of **17a** allowed to obtain the following rate equation $\mathbf{r_0 = \textit{k}_{exp}\cdot[Pd]\cdot[O_2]\cdot[17a]^{-1}}$, which was similar when starting from benzaldehyde **19a** [32]. The reaction order for the substrate was obtained by dilution with *n*-hexadecane and the fact that it was negative agrees with the tendency of the benzyl alcohol **17a** to poison the catalyst. Moreover, the linearity respect to O_2 reveals the lack of diffusion problems in the neat reactant [33]. Furthermore, using **17a-d_2**, it was possible to calculate an experimental KIE of 2.6(7), revealing the dehydrogenation as the rate determining step. In order to understand the role of benzaldehyde **19a**, trapping experiments were performed with propylene glycol. The formation

of the acetal completely stopped the conversion to **18a**, as depicted in Figure 6.9. As a consequence, the benzaldehyde may be the intermediate in the oxidation of **17a** to **18a**, whereas other products (see Table 6.1) were ruled out as intermediates of **18a** by specific experiments, carried out using each of the secondary products as an independent substrate. In addition, DABCO was used as a radical scavenger and allowed to realize that, in its presence, only the formation of **18a** was stopped and not of **19a**. Indeed, the TOF_0 of **18a** dropped to 0.86 min^{-1} using 0.3 mol% of palladium, whereas in absence of DABCO it was almost 5 times higher (see Figure 6.1).

Having in hand all these findings, it was possible to establish a possible reaction mechanism, where the rate limiting step is the formation of benzaldehyde **19a** and the second step is represented by the radical oxidation of **19a** to **18a**, both steps catalyzed by palladium, as shown in Figure 6.10. Finally, we can say that Pd_1 have high performances in the first step, the dehydrogenation of **17a**, without the use of a base, which is common in the literature [34, 35]. To further confirm that the dehydrogenation is the rate limiting step, we performed kinetic experiments adding NaOAc in the reaction mixture, which boosted the yield of **19a**, as shown in Figure 6.11.
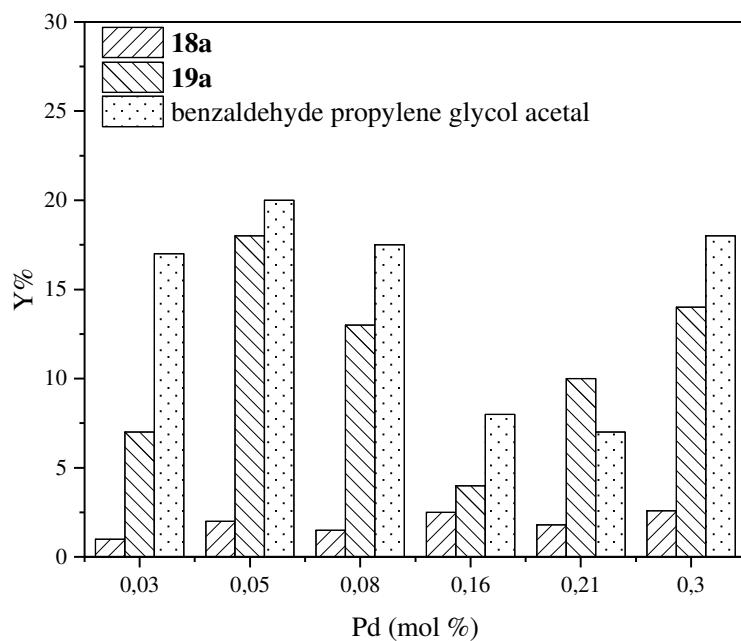
Figure 6.9 Trapping experiments of benzaldehyde **19a** with propylene glycol to form the acetal during the reaction of oxidation of **17a**.

one-pot oxidation, Pd$_1$ catalyzed
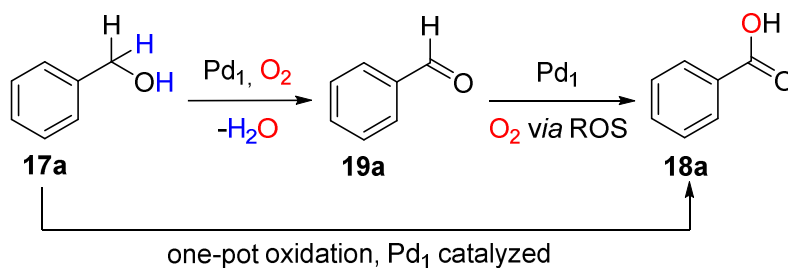
Figure 6.10 Proposed mechanism for the oxidation reaction of **17a** in presence of Pd$_1$ in solution as a catalyst and oxygen as the oxidizing agent.
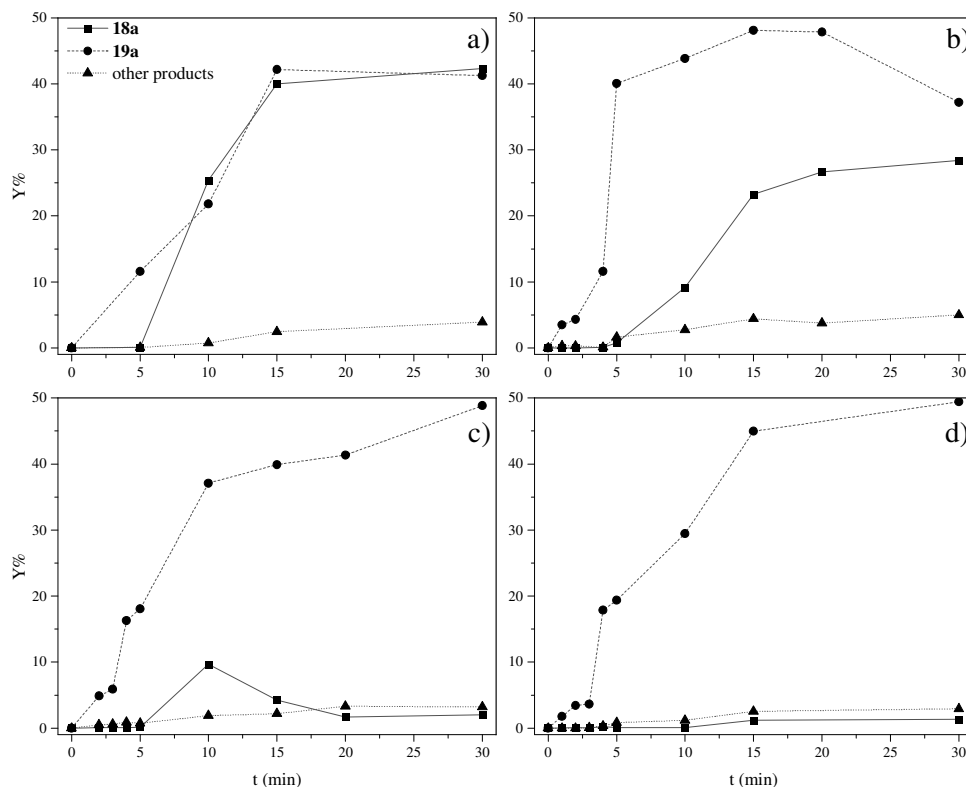
Figure 6.11 Kinetic plots of the oxidation of **17a** with 0.3 mol% of Pd(OAc)$_2$ as a catalyst, O$_2$ as an oxidant and NaOAc as a base, with increasing amounts of the latter: 0.15 mol% (a), 0.3 mol% (b), 0.6 mol% (c) and 1.0 mol% (d).

6.3 Catalysis with Pd clusters and nanoparticles

We speculated that concentrations of palladium between 0.1 and 0.25 mol% could lead to the formation Pd clusters (MCs), which in this case did not show any activity [6]. Consequently, Pd MCs were prepared following two previously reported methodologies, i.e., leaching from ethylene vinyl alcohol polymer (EVOH), where the clusters were previously embedded [8], and reduction in *N,N*-dimethylformamide (DMF)/water [6]. The MCs were used

as a catalyst in the oxidation reaction of **17a** with very low efficiency, thus confirming the very low yields obtained in the case of Pd(OAc)$_2$ at concentrations between 0.1 and 0.25 mol% (see Table 6.2). Not only could not MCs catalyze the redox reaction, but also they are unable to dislodge Pd$_1$ according to the Ostwald ripening mechanism [36]. In our system, SAs were probably stabilized and reduced by the very high amount of benzyl alcohol, which behaved as a "support", preferentially preserving SAs for sever agglomeration [1, 2, 4].

Table 6.2 Results for the oxidation of **17a** with Pd MCs.

Entry	Pd MCs	Y% 18a	Y% 19a
1	formed *in-situ*	10.0	50.2
2	in EVOH	0.0	5.1
3	in DMF	2.1	40.5

The formation of **18a** was again revealed at concentrations of palladium higher than 0.3 mol%, which is probably a good condition to form NPs. This is in good agreement with the facts that NPs are quite active in oxidation reactions [21-24, 37, 38] due to their ability of dissociate O$_2$, and are able to liberate single atoms in solutions, in contrast to MCs [36, 39]. Consequently, commercial Pd NPs supported on carbon (Pd/C) with palladium loadings between 1 and 10 wt% and different particle sizes (5-50 nm), were used as catalysts in the oxidation reaction of **17a**. The results, shown in Figure 6.12, confirmed that the biggest NPs were the more active in the reaction. Reasonably, our system is behaving in the same way, leading to a further

increase in the values of TOF_0 at concentrations where the NPs can be formed (see Figure 6.1).
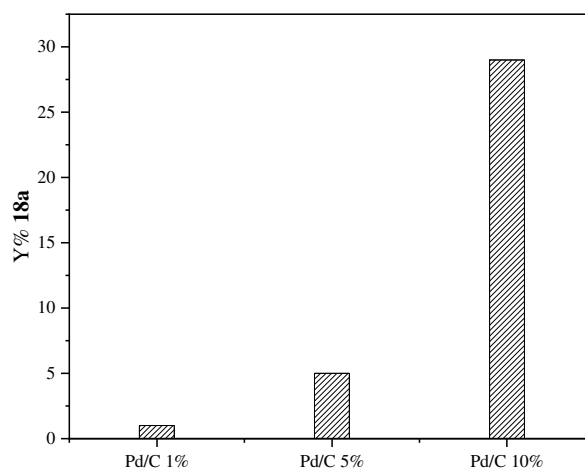
Figure 6.12 Yields of **18a** obtained by the oxidation of **17a** catalyzed by commercially available Pd/C catalysts, with different palladium amounts.

6.4 Catalysis with Pd SACs supported on a cysteine-based MOF

It is claimed that SACs are by definition supported SAs [1-4], consequently, having in mind the results shown up to now, it is interesting to see how supported Pd SAs behaves in the oxidation reaction. Indeed, as better explained in *Chapter 1*, the use of supports makes these tiny species more stable, preventing them from sintering, and allowing an easier characterization. We thought that an appropriate solid would be a MOF, which due to its microporosity and organic functionalities decorating the channels [40-42] could host and stabilize Pd SAs [43, 44] and could help in

the identification of these species using specific characterization techniques, such as SCXRD [45, 46].

6.4.1 Synthesis and characterization of Pd SACs supported on a cysteine-based MOF

For this purpose, a novel three-dimensional (3D) MOF, obtained using amino acid S-methyl-L-cysteine, with the following formula

$\{Cu_6Sr[(S,S)\text{-Mecysmox}]_3(OH)_2(H_2O)\} \cdot 15H_2O$ (**20**)
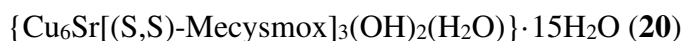
was prepared by a collaborating group. Mecysmox represents bis[S-methylcysteine]oxalyl diamide, shown in Figure 6.13a. The dimethyl thioether groups of the Mecysmox decorate the pores of the MOF allowing the formation and following stabilization of Pd SACs, as better explained in Figure 6.13. Indeed, starting from the pristine MOF **20**, MOF **21** and **22** were prepared by post synthetic methodologies [47, 48], with the following formulas
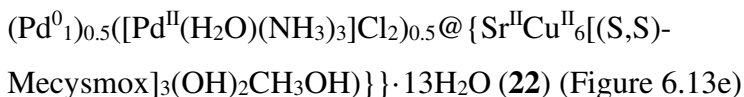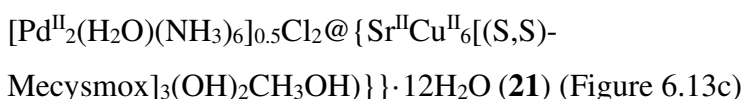
$[Pd^{II}_2(H_2O)(NH_3)_6]_{0.5}Cl_2@\{Sr^{II}Cu^{II}_6[(S,S)\text{-}$
$\text{Mecysmox}]_3(OH)_2CH_3OH)\}\} \cdot 12H_2O$ (**21**) (Figure 6.13c)

$(Pd^0_1)_{0.5}([Pd^{II}(H_2O)(NH_3)_3]Cl_2)_{0.5}@\{Sr^{II}Cu^{II}_6[(S,S)\text{-}$
$\text{Mecysmox}]_3(OH)_2CH_3OH)\}\} \cdot 13H_2O$ (**22**) (Figure 6.13e)
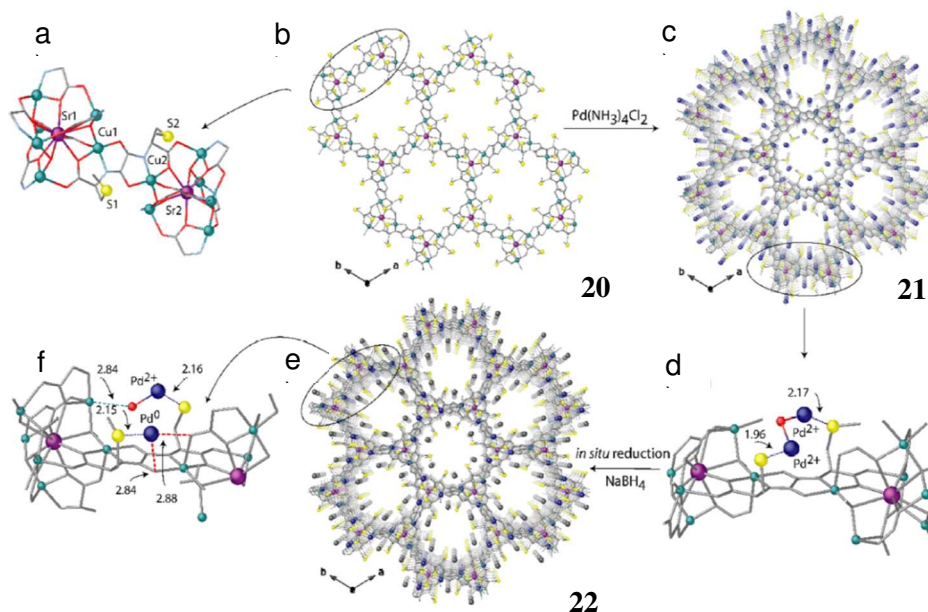
Figure 6.13 Insertion of $[Pd(NH_3)_4]^{2+}$ cations in the channels of the Mecysmox-based MOF **20** (a, b) to form **21** (c, d), followed by the reduction of Pd^{2+} to form Pd^0_1 and obtain **22** (e, f). All the structures were determined by SCXRD. Color scheme: copper and strontium atoms from the network are the cyan and purple spheres and organic ligands are represented as gray sticks. S and Pd atoms are depicted as yellow and blue spheres, whereas gray spheres are Pd^0 atoms. The dotted lines correspond to Pd···S interactions.

Firstly, Pd^{2+} were inserted in the structure of **20** using $[Pd(NH_3)_4]^{2+}$ and bringing to MOF **21**, where Pd^{2+} cations are hold in specific positions of the MOF pores by the thioether groups, and, subsequently, **21** underwent a reduction process to give Pd^0_1 in MOF **22**. In this process, the presence of the thioether groups was extremely relevant because they allowed a

homogeneous distribution of the palladium along the channels and avoid its agglomeration in the reduction step. The thioether arms can assume different conformations depending upon the type of hosts within the MOF pores, i.e., molecules of solvent in **20** (Figure 6.14a), Pd^{2+} in **21** (Figure 6.14b) and $Pd^0{}_1$ in **22** (Figure 6.14c). Even though, during the reduction not all the palladium could be reduced and only the reachable cations were converted to Pd^0, as confirmed by XPS (X-Ray Photoelectron Spectroscopy) analysis of MOF **22**. Indeed, Figure 6.15a shows the XPS spectra of **21** and **22**, where the Pd 3d line of **21** is only a doublet with a binding energy (BE) peak of 337.8 eV for the Pd $3d_{5/2}$, close to literature values [49]. On the other hand, in the spectrum of **22** (Figure 6.15b), the presence of two peaks is evident, one ascribed to the same Pd $3d_{5/2}$ doublet of **21** and a new peak at 335.8 eV related to reduced Pd SACs. The new peak allowed to calculate a 1:1 ratio between Pd^{2+} and Pd^0, confirming that only the more accessible palladium could be reduced, as already reported in previous works [50]. However, it is possible to assert that the sulfur of the thioether moieties did not change the electronic of the Pd sites.

Going further in the characterization of **22**, in Figure 6.16 it is highlighted that Pd^{2+} were stabilized by sulfur atoms in the interstitial voids, whereas $Pd_0{}^1$ were located in the larger hexagonal pores, anchored by Pd⋯S bonds too. As shown in Figure 6.17, the Pd⋯S distances calculated were of 1.96(4) and 2.17(2) Å for **21** and 2.16(2) for **22**, in line with previously reported values [51].
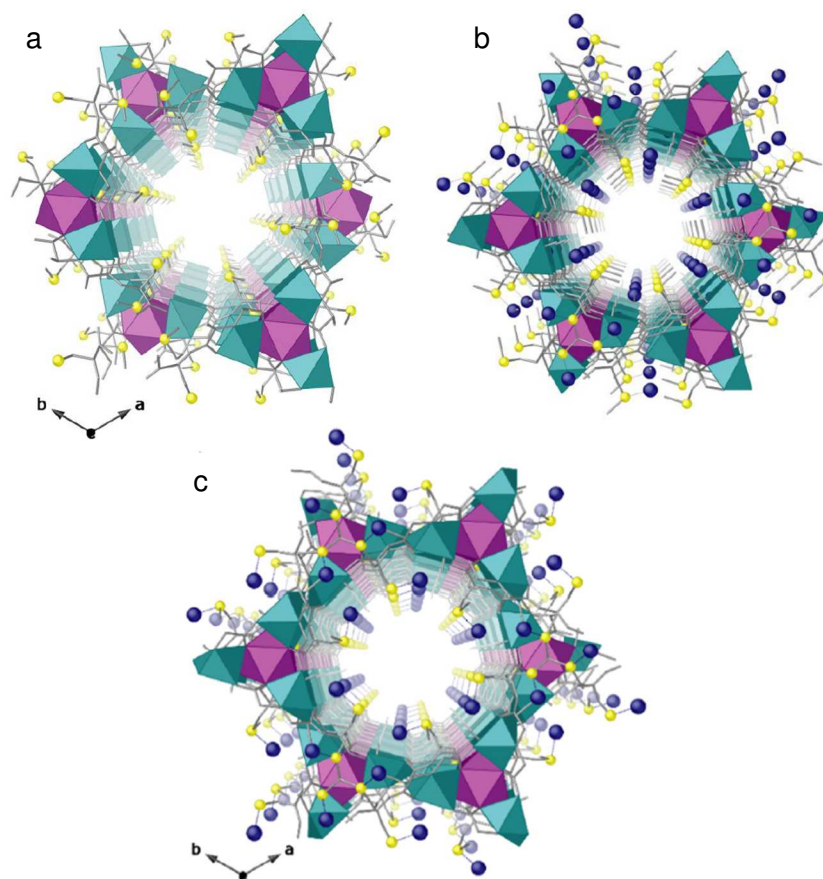
Figure 6.14 View along *c* axis of **20** (a), **21** (b) and **22** (c). Color scheme: copper and strontium atoms from the network are the cyan and purple spheres and organic ligands are represented as gray sticks. S and Pd atoms are depicted as yellow and blue spheres. The dotted lines correspond to Pd···S interactions.
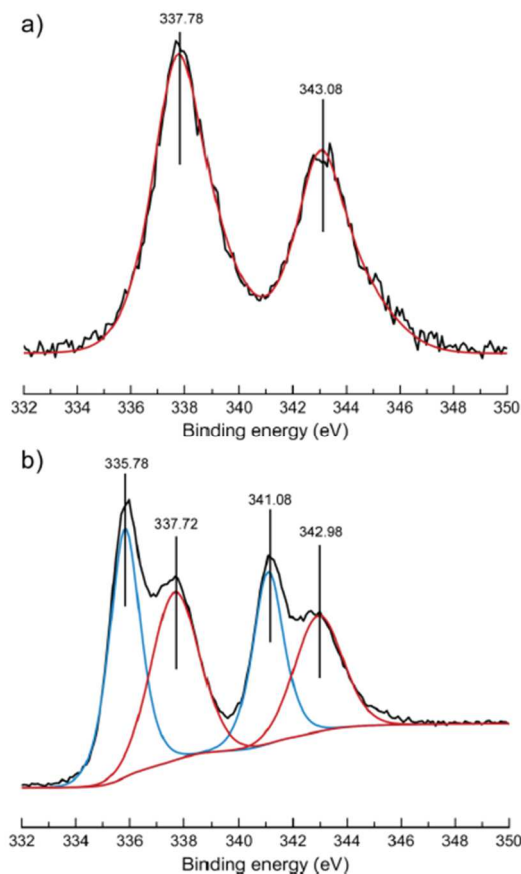
Figure 6.15 XPS spectra of MOF **21** (a) and MOF **22** (b).

Moreover, Pd SACs in **22** were weakly bonded to oxamate moieties with Pd···O distances of 2.84(1) and 2.88(1) Å (Figure 6.17b) and Pd^{2+} had a water molecule as a terminal ligand, which acted as bridge between two Pd^{2+} in the previous structure **21**. Pd···O_{water} distances were 2.00(6) and 3.03(7)Å in **21** and 1.99(2) Å in **22** (Figure 6.17).
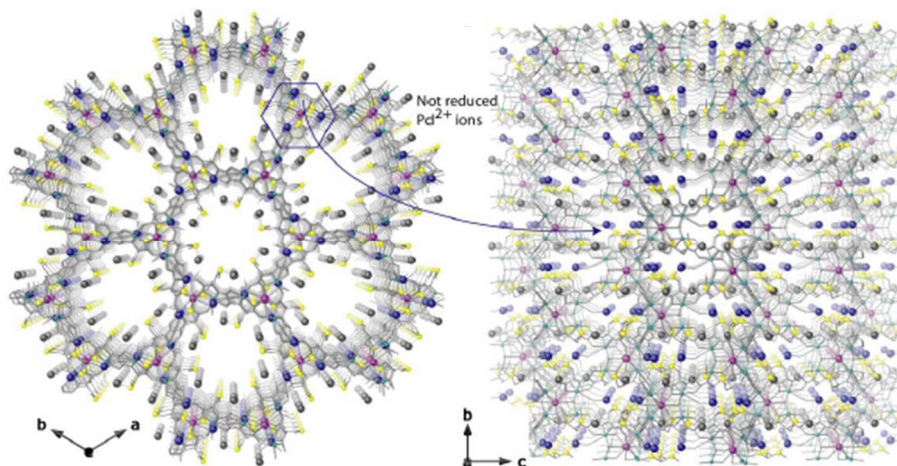
Figure 6.16 Detail of the crystal structure of **22** along *c* (left) and *a* (right) axes. Color scheme: copper and strontium atoms from the network are the cyan and purple spheres and organic ligands are represented as gray sticks. S and Pd atoms are depicted as yellow and blue spheres.
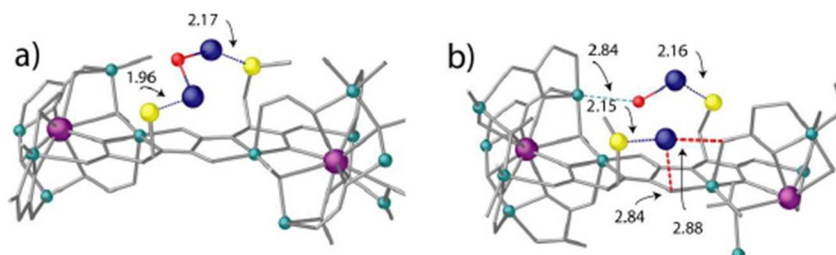
Figure 6.17 Interactions of Pd^{2+} or/and of Pd SACs with the atoms of the MOF network in **21** (a) and **22** (b). Color scheme: copper and strontium atoms from the network are the cyan and purple spheres and organic ligands are represented as gray sticks. S, Pd and O atoms are depicted as yellow, blue and red spheres, respectively.

The nature of the metallic species within the MOF **22** channels was also confirmed by XANES and EXAFS spectroscopic measurements, Fourier transform Infrared under CO (FTIR−CO) and computational calculations. The spectra obtained by XANES and EXAFS confirmed the findings reached with SCXRD.
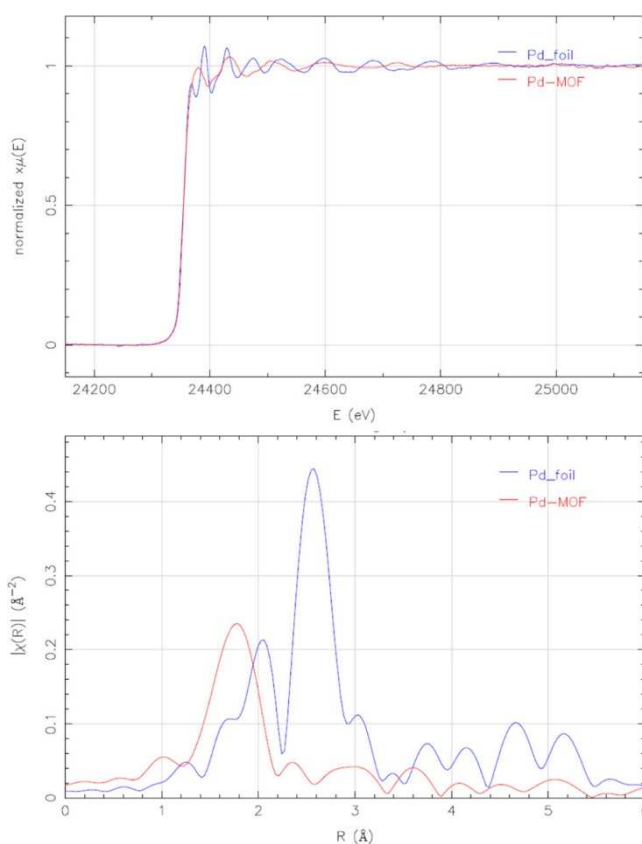

Figure 6.18 XANES (top) and EXAFS (bottom) measurements of MOF **22** in comparison with Pd foil.

Indeed, Figure 6.18 shows that, as in the case of Pd SAs in solution (Figure 6.6), there is a flattening respect to the foil in the XANES spectrum, caused

by the quantum size effect, which implies the presence of SAs and low coordination atoms. The EXAFS spectrum shows the absence of Pd-Pd bonds and confirms an average of 3 Pd-S bonds [52].

The use of low temperature FTIR-CO allows to differentiate between different oxidation states of palladium [53-55]. Indeed, Figure 6.19 shows the absence of signals above 2150 cm^{-1}, which would be related to an interaction of CO with Pd^{2+}, confirming the partial reduction of palladium. Consequently, the signals at 2114 and 2012 cm^{-1} can be ascribed to partially reduced palladium, i.e., Pd$^{\delta+}$ with $\delta = 0-1$ [56, 57]. Finally, the peak at 2137 cm^{-1} is related to free CO at high doses and the signal at 1820 cm^{-1} is due to the presence of Pd nanoparticles [58].
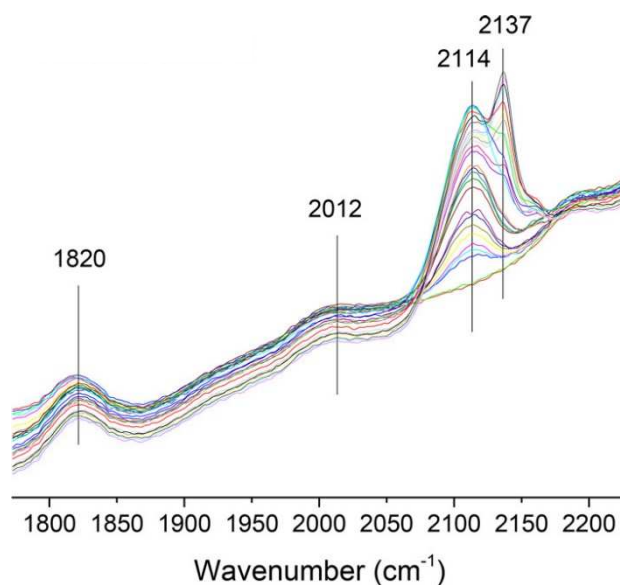

Figure 6.19 FT-IR-CO of MOF **22** performed at -196 °C.

DFT calculations agreed with all the experimental techniques displayed until now. In fact, Figure 6.20 depicts three different coordination environments of Pd^0 and $PdCl_2$ in MOF **22**. In agreement with crystallographic and XAS (X-ray Absorption Spectroscopy) data, Pd^0 is linearly coordinated to ligands containing O or S and Pd-O and Pd-S distances are 2.1-2.3 Å. Moreover, the calculated charge is 0.678 e in the case of $PdCl_2$, whereas in the case of Pd^0-A and B is only slightly positive (0.0405 and 0.1408 e, respectively) and slightly negative for Pd^0-C (-0.467 e). In addition, the DFT calculations agreed with the FTIR-CO measurements. CO interacts with Pd^0 in the three coordination environments, but it does not interact with $PdCl_2$. Interestingly, the interaction between Pd and CO in Pd^0-A is enough strong to break a Pd-O and brings to a calculated ν(CO) of 1997 cm^{-1}, which is similar to the value obtained by the experimental FTIR-CO (2012 cm^{-1}).

Other structural parameters of the MOFs were taken into account. For instance, the porosity of the MOFs did not change abruptly between **20**, **21** and **22**, since the diameter of the pores was ca. 0.9 nm in **20** and 0.7 nm in **21** and **22**. This was also confirmed by N_2 adsorption isotherms [32], which showed the preservation of the porosity after the post synthetic treatments, and by Brunauer−Emmett−Teller (BET) surface measurements, showing areas of 719, 548, and 572 m^2/g for **20**, **21** and **22**, respectively. Certainly, the presence of palladium species is responsible of a slight decrease in the pores size.
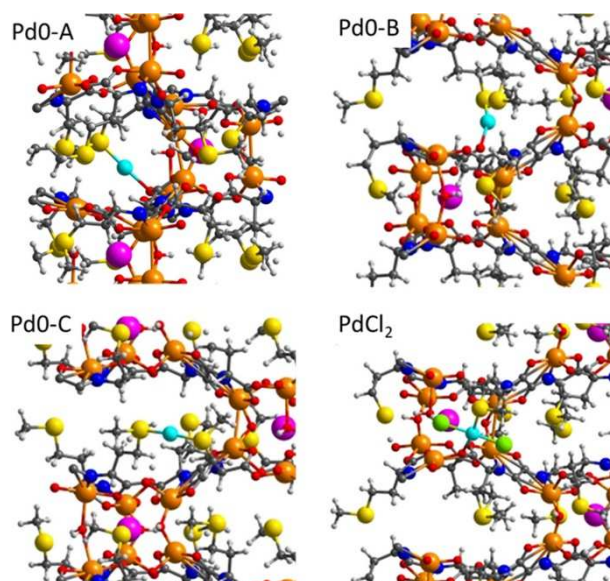
Figure 6.20 Structures obtained by DFT calculations, representing three different coordination environments of Pd^0 (A, B and C) and $PdCl_2$ within MOF **22**.

Furthermore, the chemical composition of **20**, **21** and **22** was determined by elemental analyses (C, H, S, and N), inductively coupled plasm-mass spectrometry (ICP-MS), powder X-ray diffraction (powder XRD), electronic microscopy, and thermogravimetric analyses (TGA) [32]. Table 6.3 and 6.4 show the stoichiometry of C, H, S, N and metals present in the materials, and in the case of the metals the calculations were made respect to the Cu.

Table 6.3 Elemental analysis of compounds **20**, **21** and **22**.

Compound	Element	% Calculated	% Found
20	C	20.56	20.51
	H	4.03	4.00
	S	10.98	10.99
	N	4.80	4.83
21	C	19.10	19.07
	H	3.93	3.89
	S	9.87	9.91
	N	6.47	6.45
22	C	19.53	19.48
	H	3.89	3.87
	S	10.01	10.03
	N	5.51	5.49

Table 6.4 ICP-MS and SEM/EDX analysis of compounds **21** and **22**.

		ICP-MS		SEM/EDX	
Compound	**Metal**	*%* mass	metal stoichiometry	*%* mass	metal stoichiometry
21	Cu	16.71	6.00	16.99	6.00
	Sr	1.77	1.01	1.58	0.88
	Pd	17.31	2.03	17.98	2.07
22	Cu	16.94	6.00	17.12	6.00
	Sr	1.78	0.99	1.43	0.79
	Pd	17.34	2.00	18.34	2.10

6.4.2 Catalysis with Pd SACs supported on a cysteine-based MOF

MOF **20**, **21** and **22** were used in the oxidation reaction of **17a** and only **22** showed activity towards the formation of **18a** (43%) and **19a** (28%), similar to those obtained with $Pd_2(dba)_3$ (see Table 6.1). The inactivity of **21** confirms the importance of Pd^0 species to catalyze the reaction and the necessity of stronger reducing agents to reduce the Pd^{2+} species to Pd^0 within the MOF, which evidently cannot be done by the benzyl alcohol **17a**, in contrast to the case of soluble palladium precursors. Remarkably, **22** can be reused up to three times without significant loss of activity, as shown in Figure 6.21.
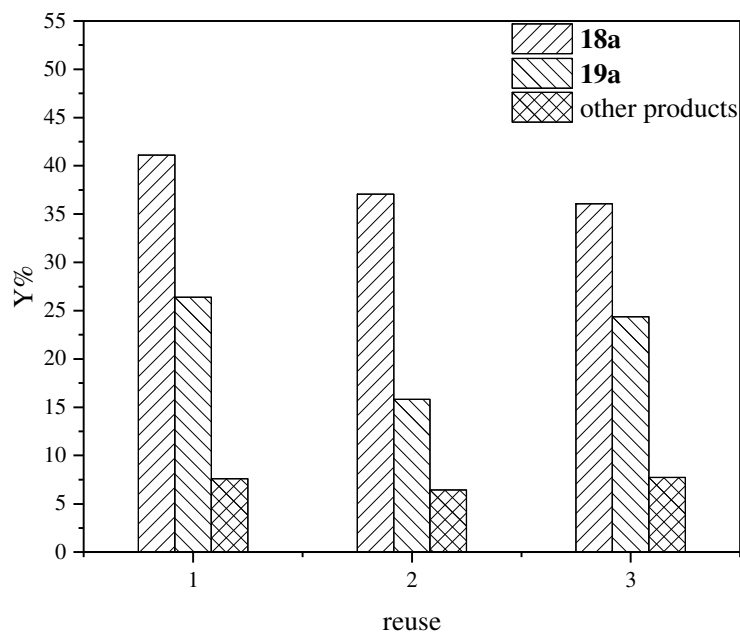
Figure 6.21 Reuses of MOF **22** in the oxidation reaction of **17a**.

The stability of the Pd SACs in MOF **22** was verified by AC HAADF-STEM images, powder XRD and XPS analysis after reaction. As shown in Figure 6.22, the Pd species present on the material were still very highly dispersed, with an average diameter of 0.135 nm, which is obviously related to monoatomic species. Only in some areas could be observed bigger agglomerates, though with a diameter lower than 0.5 nm. Subsequently, we could affirm that the Pd SACs on **22** did not sinter during the oxidative process.
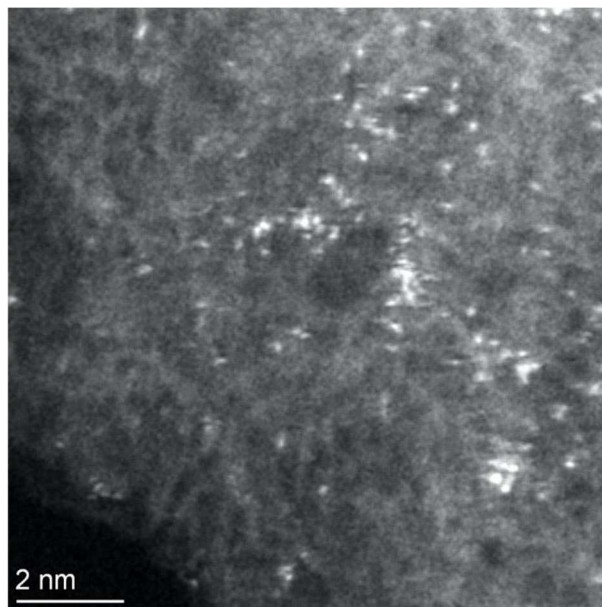
Figure 6.22 AC HAADF-STEM image of MOF **22** after oxidation reaction of **17a**.

Moreover, powder XRD analysis demonstrated the preservation of the crystallinity of **22** even after reaction, and the absence of Pd NPs and PdO_x [32]. In Figure 6.23, the XPS spectrum of MOF **22** after reaction is shown and underlines the conservation of the ratio 1:1 between Pd^{2+} and Pd^0, as in the fresh MOF.
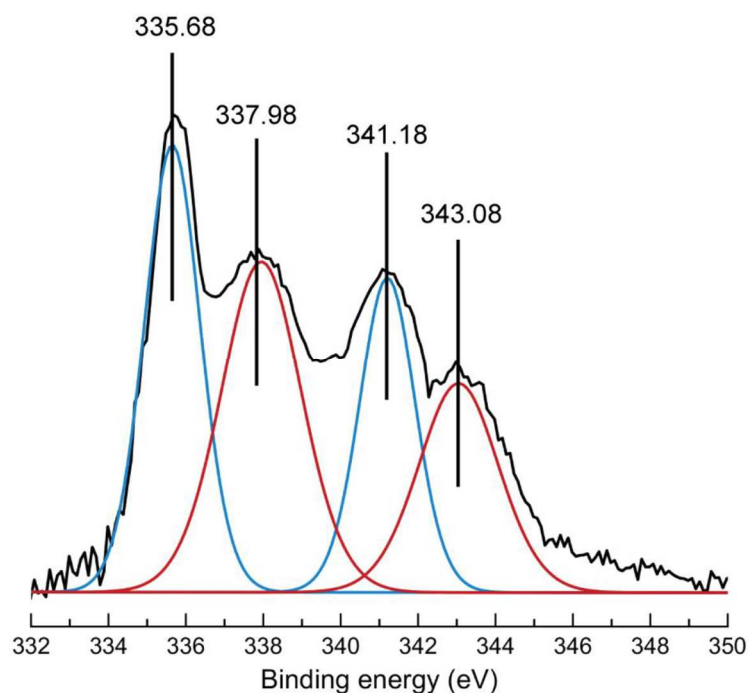
Figure 6.23 XPS spectrum of MOF **22** after the oxidation reaction of **17a**.

In order to further understand the behavior of MOF **22** in the reaction, leaching tests were performed. As shown in Figure 6.24, the hot filtration leaching tests uncovered that the reaction could not continue after filtration of the solid catalyst, revealing the absence of palladium species in solution after the removal of the MOF.

Taking into account the presence of Cu in the MOF structure, it was necessary to exclude its relevance in the catalysis. Consequently, experiments with $Cu(OAc)_2$ or with a Cu-MOF, i.e., without palladium but treated with $NaBH_4$ as MOF **22**, were performed, and it was evident that Cu did not catalyze the reaction of oxidation either in homogeneous phase or in heterogeneous phase (see Table 6.5).
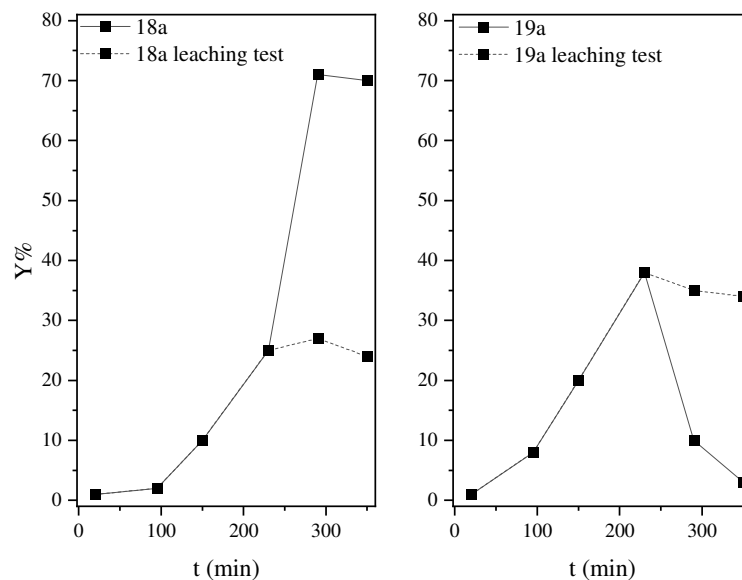
Figure 6.24 Yield of **18a** (left) and **19a** (right) in the leaching test of MOF **22**, during the oxidation reaction of **17a**.

Table 6.5 Comparison between catalytic systems with or without Cu, in homogeneous or in heterogeneous phase, in the oxidation reaction of **17a**.

Entry	Catalyst	Y% 18a	Y% 19a	Other products
1	Pd(OAc)$_2$	75%	3.6%	6.9%
2	Cu(OAc)$_2$	0.6%	2.8%	0.2%
3	Pd(OAc)$_2$/Cu(OAc)$_2$	38.7%	33.4%	11.4%
4	MOF **22**	41.1%	26.4%	7.6%
5	Cu-MOF	0.8%	5.0%	9.9%

All the experiments performed with MOF **22** confirmed the results obtained in solution, i.e., Pd SAs are responsible for the catalytic activity towards the oxidation reaction of **17a** in absence of solvents and additives.
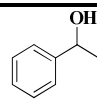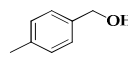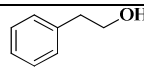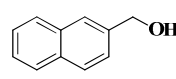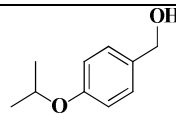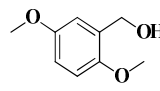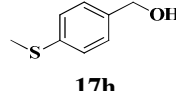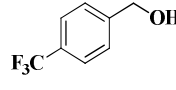
6.4.3 Mechanistic studies of the oxidation reaction catalyzed by Pd SACs supported on a cysteine-based MOF

As in the case of Pd SAs generated in solution, mechanistic studies were performed in order to better understand the oxidation process catalyzed by MOF **22**. After the experimental calculations of the initial rates for each species taking part to the reaction [32], the rate equation was found to be **$r_0 = k'_{exp}$·[Pd]·[17a]**, which differs from the one obtained for the Pd SAs in solution (see *Paragraph 6.2.3*). The absence of O_2 from the equation was related to diffusion limitations of the gas within the solid. Moreover, the difficulties of the substrate with reaching the catalytic sites were underlined by the experimental activation energy, which was 7.7 kcal·mol^{-1} in the case of Pd SAs in solution and 35.2 kcal·mol^{-1} when the reaction was catalyzed by MOF **22**.

6.5 Reaction scope

Furthermore, the reaction scope proposed in Table 6.6 shows a fairly number of benzyl alcohols (**17b-i**) oxidized by these catalytic systems to give yields of benzoic acids (**18b-i**), comparable to results previously reported in the literature [19-22, 24].

Table 6.6 Reaction scope for the oxidation of benzyl alcohols (**17b-i**) with Pd SAs in solution and MOF **22**[a] at a reaction time of 4 h or 15 h*. Numbers refer to GC yields.

Entry	17	Y% 18	Y% 19	Y% other products
1	17b	73.0%	x	10.5%
2	17c	58.3%* 16.6%[a]	16.1%* 40.2%[a]	23.5%* 42.8%[a]
3	17d	ND	6.6%	17.6%
4	17e	13.0%* 4.7%[a]	41.9%* 94.1%[a]	23.2%* 1.2%[a]
5	17f	53.7%* 20.3%[a]	19.1%* 35.2%[a]	27.2%* 40.3%[a]
6	17g	12.1%* 76.6%[a]	75.4%* 22.1%[a]	11.3%* 0.5%[a]
7	17h	16.5%	7.1%	65.1%
8	17i	ND	17.9%	86.5%

6.6 Conclusions

In summary, in this *Chapter*, we have shown the *in-situ* generation of ligand- and support-free Pd SAs, which catalyze the aerobic one-pot solvent-free oxidation reaction of benzyl alcohols. These catalytic species were characterized using different techniques. XAS techniques allowed to recognize their coordination environment and to confirm their totally reduced oxidation state. AC HAADF-STEM images supported the formation of subnanometric species, ascribable to Pd SAs. In contrast, Pd MCs and NPs were used as catalysts showing lower activity compared to that obtained with *in-situ* generated Pd SAs.

In order to stabilize Pd SAs, we used a cysteine-based MOF, which proved once again the high versatility of MOFs as support for metallic species. Indeed, the activity of the Pd SACs on the MOF was verified, showing a high stability of the Pd SAs even after reaction. Certainly, the MOF was fully characterized with SCXRD, XPS, XANES and EXAFS spectroscopies, which confirmed the presence of Pd SACs within the channels, also supported by DFT calculations.

In conclusion, we have shown a method to prepare ligand-free Pd SAs and Pd SACs on a cysteine-based MOF in multi-gram scale, both catalytically active in the aerobic oxidation of benzyl alcohol to benzoic acid.

6.7 References

1. Liu, L.; Corma, A., Metal catalysts for heterogeneous catalysis: from single atoms to nanoclusters and nanoparticles. *Chem. Rev.* **2018**, *118* (10), 4981-5079.

2. Yang, X. F.; Wang, A.; Qiao, B.; Li, J.; Liu, J.; Zhang, T., Single-atom catalysts: a new frontier in heterogeneous catalysis. *Acc. Chem. Res.* **2013**, *46* (8), 1740-8.

3. Chen, Z. W.; Chen, L. X.; Yang, C. C.; Jiang, Q., Atomic (single, double, and triple atoms) catalysis: frontiers, opportunities, and challenges. *J. Mater. Chem. A* **2019**, *7* (8), 3492-3515.

4. Flytzani-Stephanopoulos, M.; Gates, B. C., Atomically dispersed supported metal catalysts. *Annu. Rev. Chem. Biomol. Eng.* **2012**, *3*, 545-74.

5. Oliver-Meseguer, J.; Cabrero-Antonino, J. R.; Domínguez, I.; Leyva-Pérez, A.; Corma, A., Small gold clusters formed in solution give reaction turnover numbers of 10^7 at room temperature. *Science* **2012**, *338* (6113), 1452-5.

6. Leyva-Pérez, A.; Oliver-Meseguer, J.; Rubio-Marqués, P.; Corma, A., Water-stabilized three- and four-atom palladium clusters as highly active catalytic species in ligand-free C-C cross-coupling reactions. *Angew. Chem. Int. Ed.* **2013**, *52* (44), 11554-11559.

7. Oliver-Messeguer, J.; Liu, L.; García-García, S.; Canós-Giménez, C.; Domínguez, I.; Gavara, R.; Doménech-Carbó, A.; Concepción, P.; Leyva-Pérez, A.; Corma, A., Stabilized naked sub-nanometric Cu clusters within a polymeric film catalyze C–N, C–C, C–O, C–S, and C–

P bond-forming reactions. *J. Am. Chem. Soc.* **2015**, *137* (11), 3894-3900.

8. Fernández, E.; Rivero-Crespo, M. A.; Domínguez, I.; Rubio-Marqués, P.; Oliver-Meseguer, J.; Liu, L.; Cabrero-Antonino, M.; Gavara, R.; Hernández-Garrido, J. C.; Boronat, M.; Leyva-Pérez, A.; Corma, A., Base-controlled Heck, Suzuki, and sonogashira reactions catalyzed by ligand-free platinum or palladium single atom and sub-nanometer clusters. *J. Am. Chem. Soc.* **2019**, *141* (5), 1928-1940.

9. Enache, D. I.; Edwards, J. K.; Landon, P.; Solsona-Espriu, B.; Carley, A. F.; Herzing, A. A.; Watanabe, M.; Kiely, C. J.; Knight, D. W.; Hutchings, G. J., Solvent-free oxidation of primary alcohols to aldehydes using Au-Pd/TiO$_2$ catalysts. *Science* **2006**, *311* (5759), 362-365.

10. McCann, S. D.; Stahl, S. S., Copper-catalyzed aerobic oxidations of organic molecules: Pathways for two-electron oxidation with a four-electron oxidant and a one-electron redox-active catalyst. *Acc. Chem. Res.* **2015**, *48* (6), 1756-1766.

11. Parmeggiani, C.; Matassini, C.; Cardona, F., A step forward towards sustainable aerobic alcohol oxidation: New and revised catalysts based on transition metals on solid supports. *Green Chem.* **2017**, *19* (9), 2030-2050.

12. Dijksman, A.; Marino-González, A.; Mairata i Payeras, A.; Arends, I. W. C. E.; Sheldon, R. A., Efficient and selective aerobic oxidation of alcohols into aldehydes and ketones using ruthenium/TEMPO as the catalytic system. *J. Am. Chem. Soc.* **2001**, *123* (28), 6826-6833.

13. Partenheimer, W., The high yield synthesis of benzaldehydes from benzylic alcohols using homogeneously catalyzed aerobic oxidation in

acetic acid. *Adv. Synth. Catal.* **2006**, *348* (4-5), 559-568.

14. Jiang, B.; Feng, Y.; Ison, E. A., Mechanistic investigations of the iridium(III)-catalyzed aerobic oxidation of primary and secondary alcohols. *J. Am. Chem. Soc.* **2008**, *130* (44), 14462-14464.

15. Hoover, J. M.; Ryland, B. L.; Stahl, S. S., Copper/TEMPO-catalyzed aerobic alcohol oxidation: Mechanistic assessment of different catalyst systems. *ACS Catal.* **2013**, *3* (11), 2599-2605.

16. Huang, K.; Fu, H.; Shi, W.; Wang, H.; Cao, Y.; Yang, G.; Peng, F.; Wang, Q.; Liu, Z.; Zhang, B.; Yu, H., Competitive adsorption on single-atom catalysts: Mechanistic insights into the aerobic oxidation of alcohols over CoNC. *J. Catal.* **2019**, *377*, 283-292.

17. McNesby, J. R.; Heller, C. A., Jr., Oxidation of liquid aldehydes by molecular oxygen. *Chem. Rev.* **1954**, *54*, 325-46.

18. Sankar, M.; Nowicka, E.; Carter, E.; Murphy, D. M.; Knight, D. W.; Bethell, D.; Hutchings, G. J., The benzaldehyde oxidation paradox explained by the interception of peroxy radical by benzyl alcohol. *Nat. Commun.* **2014**, *5* (1), 3332.

19. Buffin, B. P.; Belitz, N. L.; Verbeke, S. L., Electronic, steric, and temperature effects in the Pd(II)-biquinoline catalyzed aerobic oxidation of benzylic alcohols in water. *J. Mol. Catal. A Chem.* **2008**, *284* (1), 149-154.

20. Liu, C.; Fang, Z.; Yang, Z.; Li, Q.; Guo, S.; Guo, K., Highly practical sodium(I)/azobenzene catalyst system for aerobic oxidation of benzylic alcohols. *RSC Adv.* **2015**, *5* (97), 79699-79702.

21. Abad, A.; Concepción, P.; Corma, A.; García, H., A collaborative effect

between gold and a support induces the selective oxidation of alcohols. *Angew. Chem. Int. Ed.* **2005**, *44* (26), 4066-4069.

22. Tsunoyama, H.; Sakurai, H.; Negishi, Y.; Tsukuda, T., Size-specific catalytic activity of polymer-stabilized gold nanoclusters for aerobic alcohol oxidation in water. *J. Am. Chem. Soc.* **2005**, *127* (26), 9374-9375.

23. Savara, A.; Chan-Thaw, C. E.; Rossetti, I.; Villa, A.; Prati, L., Benzyl alcohol oxidation on carbon-supported Pd nanoparticles: Elucidating the reaction mechanism. *ChemCatChem* **2014**, *6* (12), 3464-3473.

24. Karimi, B.; Khorasani, M.; Vali, H.; Vargas, C.; Luque, R., Palladium nanoparticles supported in the nanospaces of imidazolium-based bifunctional PMOs: The role of plugs in selectivity changeover in aerobic oxidation of alcohols. *ACS Catal.* **2015**, *5* (7), 4189-4200.

25. Bilecka, I.; Elser, P.; Niederberger, M., Kinetic and thermodynamic aspects in the microwave-assisted synthesis of ZnO nanoparticles in benzyl alcohol. *ACS Nano* **2009**, *3* (2), 467-477.

26. Juárez, R.; Concepción, P.; Corma, A.; Fornés, V.; García, H., Gold-catalyzed phosgene-free synthesis of polyurethane precursors. *Angew. Chem. Int. Ed.* **2010**, *49* (7), 1286-1290.

27. Ananikov, V. P.; Beletskaya, I. P., Toward the ideal catalyst: From atomic centers to a "cocktail" of catalysts. *Organometallics* **2012**, *31* (5), 1595-1604.

28. Eremin, D. B.; Ananikov, V. P., Understanding active species in catalytic transformations: From molecular catalysis to nanoparticles, leaching, "cocktails" of catalysts and dynamic systems. *Coord. Chem. Rev.* **2017**, *346*, 2-19.

29. Polynski, M. V.; Ananikov, V. P., Modeling key pathways proposed for the formation and evolution of "cocktail"-type systems in Pd-catalyzed reactions involving ArX reagents. *ACS Catal.* **2019**, *9* (5), 3991-4005.

30. Sutanuva, M., Acceptorless dehydrogenation of primary and secondary benzylic alcohols using a well defined phosphine free air stable Mn^{II} - catalyst. Synthesis of imines via dehydrogenative coupling of alcohols and amines. *Int. J. Sci. Res. Rev.* **2019**, *8* (3), 34-48.

31. Musa, S.; Shaposhnikov, I.; Cohen, S.; Gelman, D., Ligand–metal cooperation in PCP pincer complexes: rational design and catalytic activity in acceptorless dehydrogenation of alcohols. *Angew. Chem. Int. Ed.* **2011**, *50* (15), 3533-3537.

32. Tiburcio, E.; Greco, R.; Mon, M.; Ballesteros-Soberanas, J.; Ferrando-Soria, J.; López-Haro, M.; Hernández-Garrido, J. C.; Oliver-Meseguer, J.; Marini, C.; Boronat, M.; Armentano, D.; Leyva-Pérez, A.; Pardo, E., Soluble/MOF-supported palladium single atoms catalyze the ligand-, additive-, and solvent-free aerobic oxidation of benzyl alcohols to benzoic acids. *J. Am. Chem. Soc.* **2021**, *143* (6), 2581-2592.

33. Sato, T.; Hamada, Y.; Sumikawa, M.; Araki, S.; Yamamoto, H., Solubility of oxygen in organic solvents and calculation of the Hansen solubility parameters of oxygen. *Ind. Eng. Chem. Res.* **2014**, *53* (49), 19331-19337.

34. Sharma, G. V. M.; Chander, A. S.; Krishnudu, K.; Krishna, P. R., Pd(OAc)$_2$ mediated oxidative cyclization of γ,δ - olefinic alcohols: a new route to C-vinyl furanosides. *Tetrahedron Lett.* **1998**, *39* (38), 6957-6960.

35. Sha, J.; Zheng, E.-J.; Zhou, W.-J.; Liebens, A.; Pera-Titus, M., Selective oxidation of fatty alcohol ethoxylates with H_2O_2 over Au catalysts for the synthesis of alkyl ether carboxylic acids in alkaline solution. *J. Catal.* **2016**, *337*, 199-207.

36. Hansen, T. W.; DeLaRiva, A. T.; Challa, S. R.; Datye, A. K., Sintering of catalytic nanoparticles: particle migration or Ostwald ripening? *Acc. Chem. Res.* **2013**, *46* (8), 1720-1730.

37. García-Suárez, E. J.; Tristany, M.; García, A. B.; Collière, V.; Philippot, K., Carbon-supported Ru and Pd nanoparticles: Efficient and recyclable catalysts for the aerobic oxidation of benzyl alcohol in water. *Microporous Mesoporous Mater.* **2012**, *153*, 155-162.

38. Abad, A.; Corma, A.; García, H., Catalyst parameters determining activity and selectivity of supported gold nanoparticles for the aerobic oxidation of alcohols: The Molecular reaction mechanism. *Chem. Eur. J.* **2008**, *14* (1), 212-222.

39. Boronat, M.; Leyva-Pérez, A.; Corma, A., Theoretical and experimental insights into the origin of the catalytic activity of subnanometric gold clusters: Attempts to predict reactivity with clusters and nanoparticles of gold. *Acc. Chem. Res.* **2014**, *47* (3), 834-844.

40. Ferey, G., Hybrid porous solids: Past, present, future. *Chem. Soc. Rev.* **2008**, *37* (1), 191-214.

41. Furukawa, H.; Cordova, K. E.; O'Keeffe, M.; Yaghi, O. M., The chemistry and applications of metal-organic frameworks. *Science* **2013**, *341* (6149).

42. Wang, C.; Liu, D.; Lin, W., Metal-organic frameworks as a tunable

platform for designing functional molecular materials. *J. Am. Chem. Soc.* **2013**, *135* (36), 13222-13234.

43. Otake, K.-I.; Cui, Y.; Buru, C. T.; Li, Z.; Hupp, J. T.; Farha, O. K.; Farha, O. K., Single-atom-based vanadium oxide catalysts supported on metal-organic frameworks: Selective alcohol oxidation and structure-activity relationship. *J. Am. Chem. Soc.* **2018**, *140* (28), 8652-8656.

44. Abdel-Mageed, A. M.; Behm, R. J.; Rungtaweevoranit, B.; Pei, X.; Yaghi, O. M.; Rungtaweevoranit, B.; Pei, X.; Yaghi, O. M.; Parlinska-Wojtan, M., Highly active and stable single-atom Cu catalysts supported by a metal-organic framework. *J. Am. Chem. Soc.* **2019**, *141* (13), 5201-5210.

45. Burgun, A.; Coghlan, C. J.; Huang, D. M.; Chen, W.; Horike, S.; Kitagawa, S.; Alvino, J. F.; Metha, G. F.; Sumby, C. J.; Doonan, C. J., Mapping-out catalytic processes in a metal-organic framework with single-crystal x-ray crystallography. *Angew. Chem. Int. Ed.* **2017**, *56* (29), 8412-8416.

46. Mon, M.; Bruno, R.; Elliani, R.; Tagarelli, A.; Qu, X.; Chen, S.; Ferrando-Soria, J.; Armentano, D.; Pardo, E., Lanthanide discrimination with hydroxyl-decorated flexible metal–organic frameworks. *Inorg. Chem.* **2018**, *57* (21), 13895-13900.

47. Viciano-Chumillas, M.; Mon, M.; Ferrando-Soria, J.; Corma, A.; Leyva-Pérez, A.; Armentano, D.; Pardo, E., Metal-organic frameworks as chemical nanoreactors: Synthesis and stabilization of catalytically active metal species in confined spaces. *Acc. Chem. Res.* **2020**, *53* (2), 520-531.

48. Adam, R.; Mon, M.; Greco, R.; Kalinke, L. H. G.; Vidal-Moya, A.;

Fernandez, A.; Winpenny, R. E. P.; Doménech-Carbó, A.; Leyva-Pérez, A.; Armentano, D.; Pardo, E.; Ferrando-Soria, J., Self-assembly of catalytically active supramolecular coordination compounds within metal–organic frameworks. *J. Am. Chem. Soc.* **2019**, *141* (26), 10350-10360.

49. Fortea-Pérez, F. R.; Mon, M.; Ferrando-Soria, J.; Boronat, M.; Leyva-Pérez, A.; Corma, A.; Herrera, J. M.; Osadchii, D.; Gascon, J.; Armentano, D.; Pardo, E., The MOF-driven synthesis of supported palladium clusters with catalytic activity for carbene-mediated chemistry. *Nat. Mater.* **2017**, *16* (7), 760-766.

50. Mon, M.; Rivero-Crespo, M. A.; Ferrando-Soria, J.; Vidal-Moya, A.; Boronat, M.; Leyva-Pérez, A.; Corma, A.; Hernández-Garrido, J. C.; López-Haro, M.; Calvino, J. J.; Ragazzon, G.; Credi, A.; Armentano, D.; Pardo, E., Synthesis of densely packaged, ultrasmall Pt^0_2 clusters within a thioether-functionalized MOF: Catalytic activity in industrial reactions at low temperature. *Angew. Chem. Int. Ed.* **2018**, *57* (21), 6186-6191.

51. Colbon, P.; Ruan, J.; Purdie, M.; Xiao, J., Direct acylation of aryl chlorides with aldehydes by palladium–pyrrolidine co-catalysis. *Org. Lett.* **2010**, *12* (16), 3670-3673.

52. Gronvold, F.; Rost, E., The crystal structure of $PdSe_2$ and PdS_2. *Acta Crystallogr.* **1957**, *10* (4), 329-331.

53. Liang, B.; Zhou, M.; Andrews, L., Reactions of laser-ablated Ni, Pd, and Pt atoms with carbon monoxide: Matrix infrared spectra and density functional calculations on $M(CO)_n$ (n = 1-4), $M(CO)_n^-$ (n = 1-3), and $M(CO)_n^+$ (n = 1-2), (M = Ni, Pd, Pt). *J. Phys. Chem. A* **2000**, *104* (17),

3905-3914.

54. Willner, H.; Bodenbinder, M.; Bröchler, R.; Hwang, G.; Rettig, S. J.; Trotter, J.; von Ahsen, B.; Westphal, U.; Jonas, V.; Thiel, W.; Aubke, F., Superelectrophilic tetrakis(carbonyl)palladium(II)- and -platinum(II) undecafluorodiantimonate(V), $[Pd(CO)_4][Sb_2F_{11}]_2$ and $[Pt(CO)_4][Sb_2F_{11}]_2$: Syntheses, physical and spectroscopic properties, their crystal, molecular, and extended structures, and density functional calculations: An experimental, computational, and comparative study. *J. Am. Chem. Soc.* **2001**, *123* (4), 588-602.

55. Fernández-García, M.; Iglesias-Juez, A.; Martínez-Arias, A.; Hungría, A. B.; Anderson, J. A.; Conesa, J. C.; Soria, J., Role of the state of the metal component on the light-off performance of Pd-based three-way catalysts. *J. Catal.* **2004**, *221* (2), 594-600.

56. Chakarova, K.; Ivanova, E.; Hadjiivanov, K.; Klissurski, D.; Knözinger, H., Co-ordination chemistry of palladium cations in Pd-H-ZSM-5 as revealed by FTIR spectra of adsorbed and co-adsorbed probe molecules (CO and NO). *Phys. Chem. Chem. Phys.* **2004**, *006* (13), 3702-3709.

57. Szanyi, J.; Kwak, J. H., Dissecting the steps of CO_2 reduction: 2. The interaction of CO and CO_2 with Pd/γ-Al_2O_3: An in situ FTIR study. *Phys. Chem. Chem. Phys.* **2014**, *16* (29), 15126-15138.

58. Dani, A.; Crocellà, V.; Maddalena, L.; Barolo, C.; Bordiga, S.; Groppo, E., Spectroscopic study on the surface properties and catalytic performances of palladium nanoparticles in poly(ionic liquid)s. *J. Phys. Chem. C* **2016**, *120* (3), 1683-1692.

Chapter 7

Subnanometric aqueous metal clusters as antitumoral agents

7 Subnanometric aqueous metal clusters as antitumoral agents

7.1 Introduction

In the previous *Chapters*, the use of metal single atoms and clusters (MCs) was explored in the field of catalysis, but, during the last years, their use has been boosted in the field of biology and medicine, e.g., in cellular imaging techniques [1, 2] and for DNA and proteins sensors [3]. Nevertheless, there is a field which has been less studied, i.e., the employment of these metallic species in cancer treatments.

Nowadays, cancer constitutes the second cause of death worldwide. The most common cancer therapies involve surgery, chemotherapy and/or radiotherapy, which are quite invasive and, consequently, have many side effects [4]. The well-known cisplatin, $[PtCl_2(NH_3)_2]$, represents the most typical treatment for different cancer lines [5, 6] and appears in the essential medicine World Health Organization's List. The main drawbacks of cisplatin are connected to the Pt-cell resistance produced during prolonged treatments and to the acute side-effects, which are directly related to its physiological mechanism of action. Indeed, the latter involves an unselective cell internalization by either passive or active diffusion, due to its low molecular size, followed by fast hydrolysis and DNA damage within the cells, both tumoral and non-tumoral [6-8]. In addition, cisplatin represents an elevated expense for the public health system and for patients, due to its costs >200 €

per gram. Therefore, over the last decades, the chase for alternative drugs has been continuously active [9-15], aiming to find a Pt drug able to overcome cisplatin resistance. Especially, this *Chapter* will be focused on ovarian cancer lines, which are recognized to be some of the Pt-resistant tumours mentioned above.

Initially, the improvements in the field of nanoscience brought to use nanoparticles (NPs) as antitumoral agents, but, because of the nanometer size, the internalization process of the NPs has been discovered to be a much slower endocytosis process, opposite to the typical direct diffusion across the lipid bilayer, as in the case of cisplatin and analogues, bringing to a severe drop of the cytotoxic activity [16-18]. Certainly, different strategies were used to overcome this drawback, such as functionalizing the NPs with polymers, like polyethylene glycols (PEGs) or polyamidoamine (PAMAM). Consequently, this strategy helped with the transport of the NPs throughout the human body and with an easier detection and degradation of the species by the cells [19-21]. Even though the functionalization of NPs may be of support for their antitumoral activity, many studies have revealed that the size of the metallic species is extremely relevant, i.e., the smaller the NP the higher the activity [20], not only due to a better internalization of smaller NPs, but also to an easier disaggregation within the cell medium to give the ligand-free ions, which are responsible for the cytotoxicity [22]. Moreover, some studies unveiled the presence of less side effects of smaller NPs, because of their easier release from the body by renal clearance [23]. Considering all together the findings mentioned up to now, subnanometric ligand-free MCs may be the appropriate entities to overcome the main disadvantages of NPs, because of a simpler internalization by direct diffusion [24, 25] and a faster generation

of aqueous ions within the cell media. Indeed, Figure 7.1 exemplifies the main differences between different Pt species and their biomedical characteristics, such as water solubility, internalization, and cytotoxicity. Having properties between NPs and organometallic complexes, MCs appears to have the perfect balance between size and atom density in order to enter into the cell and to be disaggregated to highly cytotoxic ions. As NPs, MCs have a high atom density [26, 27], because of the exclusive presence of metal-metal bonds, bringing to a faster ions formation, and as organometallic complexes, they have the right size to enter effortlessly within the cells.

To the best of our knowledge, there are not examples of antitumoral activity of ligand-free Pt MCs, probably because a biocompatible synthesis of these species has not yet been achieved. In fact, MCs tend to agglomerate to NPs with simple modifications of their synthetic or storage conditions, e.g., concentration, temperature, or solvent [28]. As a consequence, only with few techniques the synthesis of ligand-free MCs has been possible, for instance, by soft-landing [29] and electrochemical synthesis [30]. In the case of Pt, the synthetic constraints are enhanced by the tendency of "heavy" atoms to aggregate, because of the relativistic effect [31, 32], and to the impossibility of the use of electrochemical synthesis, which commonly operates with Pt electrodes. Consequently, if we do not consider the few examples using mass-selected synchrotron techniques [33] and solid supporting [34-36], only the use of dendrimer encapsulation has brought to the synthesis of biocompatible Pt MCs [35, 37], associated in this case with a more difficult internalization process, such as endocytosis.

All the difficulties with the synthesis and stabilization of Pt MCs would make one think that these species might have severe limitations in biomedical

application but, because of their interesting properties between NPs and organometallic complexes, it is relevant to study their use in antitumoral treatments.
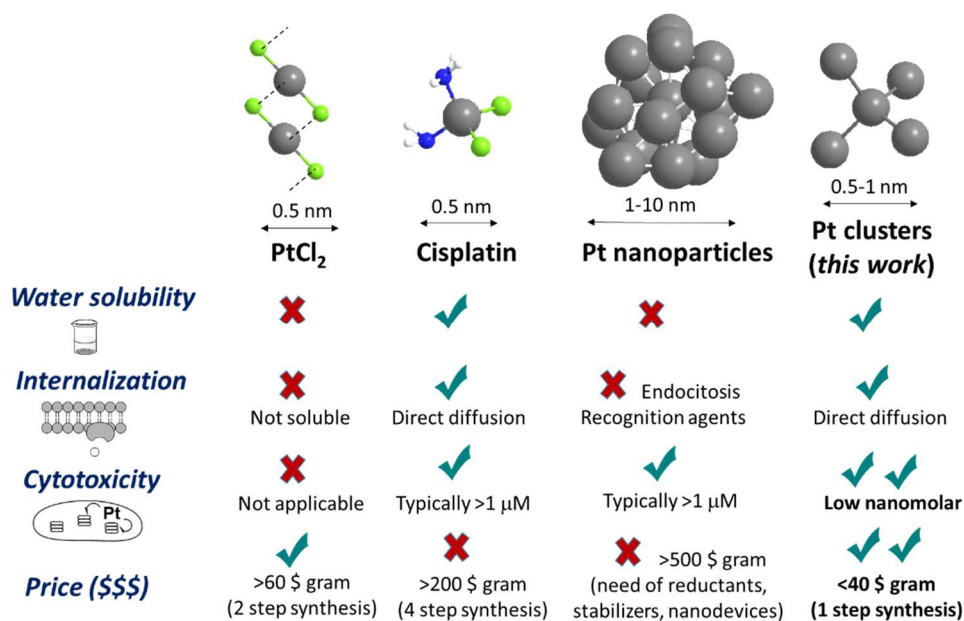

Figure 7.1 Comparison of biomedical characteristics and 2020 prices of PtCl$_2$, cisplatin, Pt NPs, and MCs.

A well-known method for the synthesis of MCs is the endogenous reduction of precursors of the metal, in the form of salts, using amide solvents, such as *N,N'*-dimethyl formamide (DMF) or *N*-methyl pyrrolidone. Some examples are the synthesis of Cu [38, 39], Pd [40], Ag [41, 42] and Au [43] MCs, where in some cases the polymer polyvinylpyrrolidone (PVP) acts as a support for generating very small aggregates [41, 44]. We slightly modified this procedure, exchanging the amide group for an alcohol, which represents the reducing agent. The alcohol is borne by a biocompatible polymer, ethylene

vinyl alcohol (EVOH), which not only can behave as a reductant, but also as a support [45]. We thought that Pt MCs could be generated in water in presence of EVOH and a following filtration of the polymer could bring to neat MCs in aqueous solution. This method represents a cheap and scalable way to obtain ligand-free aqueous MCs, which may be defined biocompatible, due to the absence of classical non-biocompatible reducing agents, like amides or $NaBH_4$.

Finally, considering that Cu, Au and Ag MCs prepared by other methods had shown biological activity in previous reports [42], we synthesized different MCs to be used in antitumoral treatments of different cell lines. In this *Chapter*, the preparation of ligand-free aqueous Pt, Ir, Rh, and Au MCs will be described together with their characterization and their use as antitumoral agents in ovarian cancer cell lines, among them a cisplatin-resistant one.

7.2 Synthesis and characterization of aqueous metal clusters

7.2.1 Synthesis of metal clusters

As shown in Figure 7.2, the experimental procedure for the synthesis of MCs was very simple and even scalable up to one liter of solution. It consisted in a previous dissolution of the polymer EVOH in a mixture of water/^{i}PrOH at 65 °C for 2 hours. Consequently, the addition of the precursor of the metal was performed at room temperature, in order to avoid the formation of undesired NPs. The solution was kept under stirring overnight and then the filtration of the polymer brought to a solution of the neat ligand-free MCs (0.1 µM), ready to be characterized and stable for months when kept in the fridge. Moreover, this procedure was scalable, and it was possible to obtain 1 liter of solution of Pt MCs.
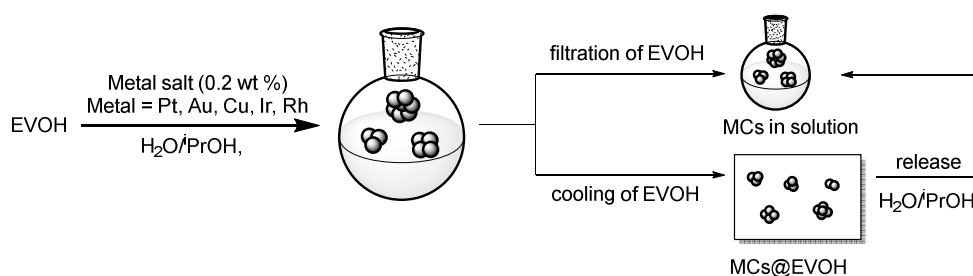
Figure 7.2 Synthetic procedure for the preparation of MCs in solution or embedded within the polymer matrix of EVOH (MCs@EVOH).

This method was also applied for the preparation of MCs embedded in EVOH (MCs@EVOH), which after the stirring with a metal precursor was cooled down and extruded into foils [45]. The latter could be kept at room temperature even for two years and could release MCs in water/^{i}PrOH at room temperature. The species prepared in this way could be used as a comparison in the characterization of MCs prepared with the first methodology and as a MCs storage.

7.2.2 Characterization of metal clusters

Figure 7.3 shows the emission spectra of Pt MCs in solution, prepared by filtration of EVOH, and Pt@EVOH, prepared by extruding a mixture of EVOH and Pt precursor into foils. Using the jellium model [40], the emission spectra allowed to calculate an average dimension of Pt clusters of 9 atoms, from the equation $E_g = E_{Fermi}/N^{1/3}$, where E_g is the gap energy, i.e., the emission energy, E_{Fermi} is the Fermi energy of the bulk material and N is the number of atoms composing the cluster [46-48]. Moreover, the comparison with UV-Vis (Ultraviolet-Visible) spectra of the precursor K_2PtCl_4 and the

MCs generated in solution confirmed the absence of the precursor, meaning the total reduction of the salt, and the absence of plasmonic bands related to NPs (see Figure 7.4).
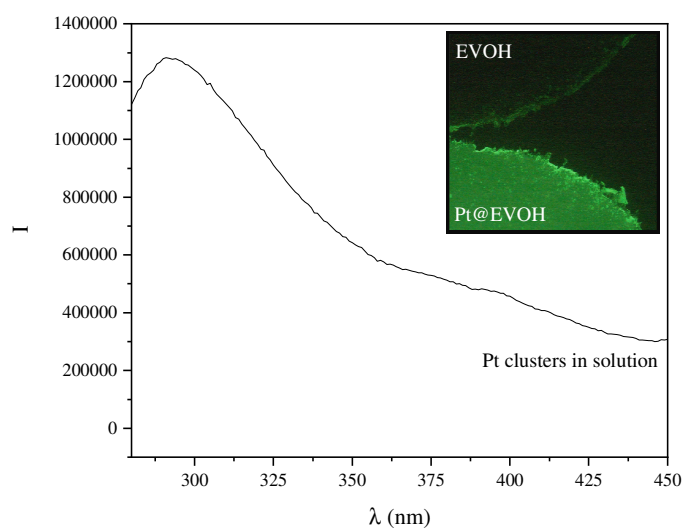

Figure 7.3 Emission spectrum of Pt MCs in solution, irradiating at 225 nm, and fluorescence microscopy of Pt@EVOH (inset).

Looking at the UV-Vis and emission spectra, we could assert that clusters were formed, considering the incapability of single atoms and NPs to emit.
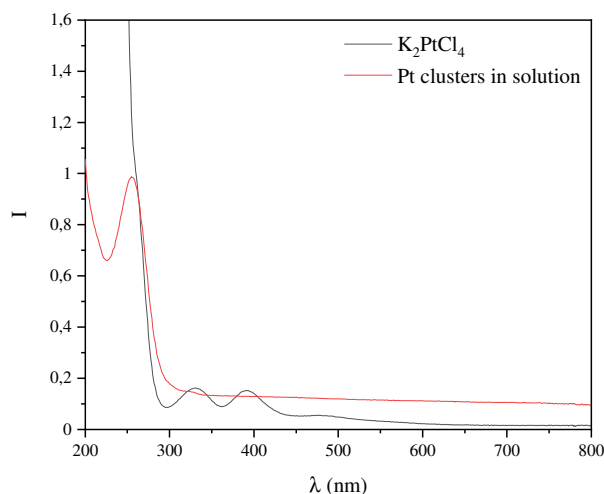
Figure 7.4 Comparison of the UV-Vis spectra of K_2PtCl_4, precursor of the Pt MCs, and of the Pt MCs generated in solution.

Taking into account the very low concentrations of Pt MCs, it soon appeared quite difficult a further characterization with a MALDI-TOF (Matrix-Assisted Laser Desorption/Ionization-Time of Flight) mass spectrometer. Consequently, we bypassed this problem using an Orbitrap mass analyser (HPLC-Orbitrap MS) with flow injection-high resolution mass spectrometry (HMRS). In full scan mode, the Orbitrap analyser is known to reach a very high sensitivity, apt to obtain accurate mass information even at very low concentrations of analytes. Indeed, it has been previously applied in the analysis of trace levels of organic contaminants [49], but its ability in the analysis of small metallic aggregates has not yet been explored. Figure 7.5 shows the mass analysis of Pt MCs in solution with the use of an Orbitrap analysis. The chromatogram makes clear once again the absence of the precursor K_2PtCl_4 and the presence of Pt hydroxide, chloride, and oxide

clusters, which is related to the *m/z* values, the isotopic distribution of Pt and the loss of oxygen atoms (16 a.u.).
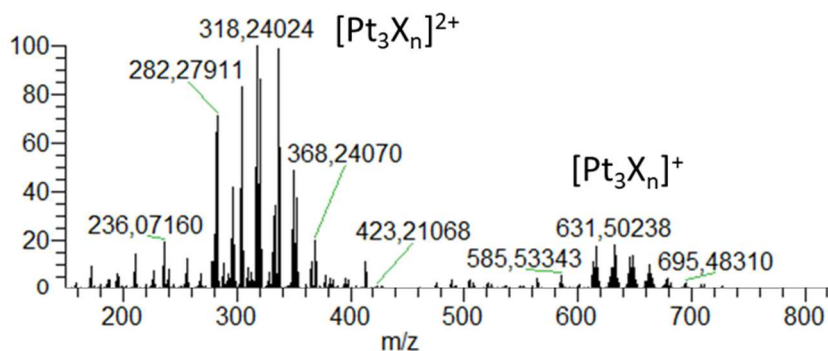

Figure 7.5 Mass fragmentation analyzed by an Orbitrap analyzer of Pt MCs in solution.

The MCs were also characterized by Aberration–corrected High Angle Annular Dark Field–scanning Transmission Electron Microscopy (AC HAADF-STEM), which allowed to visualize the MCs as main species in solution, as shown in Figure 7.6a. The denoised HAADF–STEM images in Figures 7.6b and 7.6c, with the corresponding *k*–means clustering analysis [50], allowed to differentiate Pt in orange and the background in blue. The binarized images made possible the estimation of the Pt MCs size calculating the equivalent diameter of the orange areas, considered as circles, and resulting in a histogram of the MCs size distribution. The 90% of the Pt aggregates are subnanometric, with a Pt atomicity between 3 and 10, in agreement with the fluorescence measurements and with the following theoretical calculations of the MCs size.
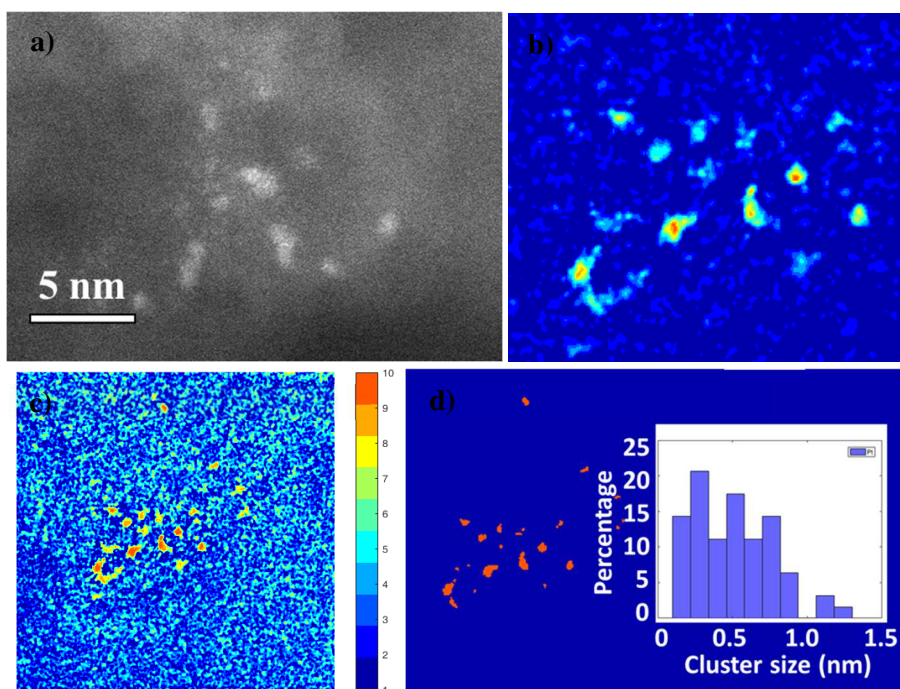
Figure 7.6 AC HAADF-STEM image of the aqueous solution of Pt MCs (a). RGB (Red Green Blue) image of the Pt MCs after processing the image, by denoising and removal of the background (b) *k*–means clustering method results after the processing of the experimental image (c) identification of the Pt species using segmentation by *k*–means clustering and the corresponding MCs size distribution histogram (d).

In addition, to further understand the oxidation state and the chemical environment of the Pt species, XAS techniques were used. Due the low concentration of MCs in solution, these species could not be analyzed by XAS spectroscopies, which were more suitable for the analysis of Pt@EVOH foil. Indeed, Figure 7.7 shows EXAFS and XANES analysis, confirming the presence of oxidized species, as already evidenced by Orbitrap mass analysis.

The comparison of Pt@EVOH to Pt NPs brought to calculate an oxidation state of +0.66 in the case of Pt@EVOH, whereas a non-active sample showed an oxidation state of +0.88. In addition, EXAFS underlined the presence of Pt-Pt and Pt-O-Pt bonds. The oxidation state of Pt was also analyzed by XPS analysis, which confirms the presence of partially oxidated species.

The characterization mentioned up to now did not exclude the presence of single atoms, in fact, AC HAADF-STEM detected particles with a diameter smaller than 0.4 nm and the XAS spectroscopies detected always O or other Pt in the coordination sphere of the Pt. Hence, the solution of aqueous Pt MCs was treated with activated charcoal, because the adsorption of single atoms on this material should happen preferentially, due to the smaller size and to the higher charge/radius ratio compared to MCs, bringing to a better interaction with the negative charged charcoal. Indeed, the images in Figure 7.8 shows the preferential adsorption of Pt_1 and Pt_2, which represent *ca.* 10% of the species in solution, remarkably fitting the amount of Pt not found by AC HAADF-STEM of MCs in solution.

Finally, we could say that the main species in solution were MCs, representing the 90% of the total Pt, K_2PtCl_4 quantitatively reacted, and Pt NPs were not formed. This methodology was applied for the synthesis of MCs of Rh, Ir, and Au, which were characterized by spectrophotometry, chromatography, and microscopy, as shown in Figures 7.9-7.11.
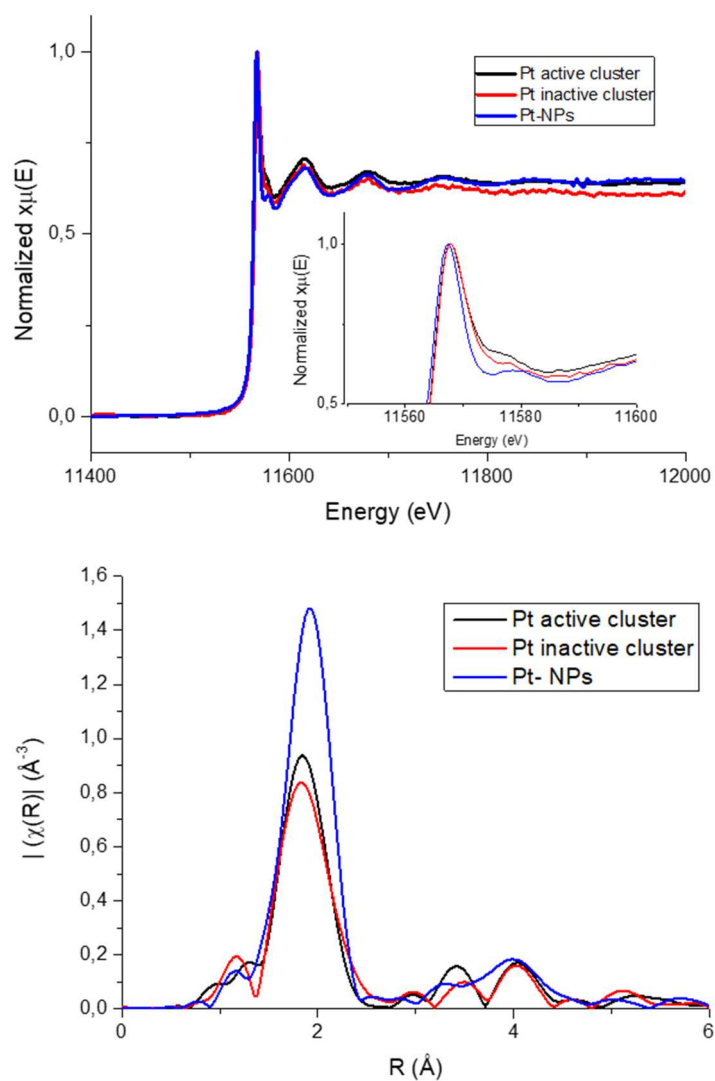
Figure 7.7 XANES (top) and EXAFS (bottom) spectra of Pt@EVOH and Pt NPs.
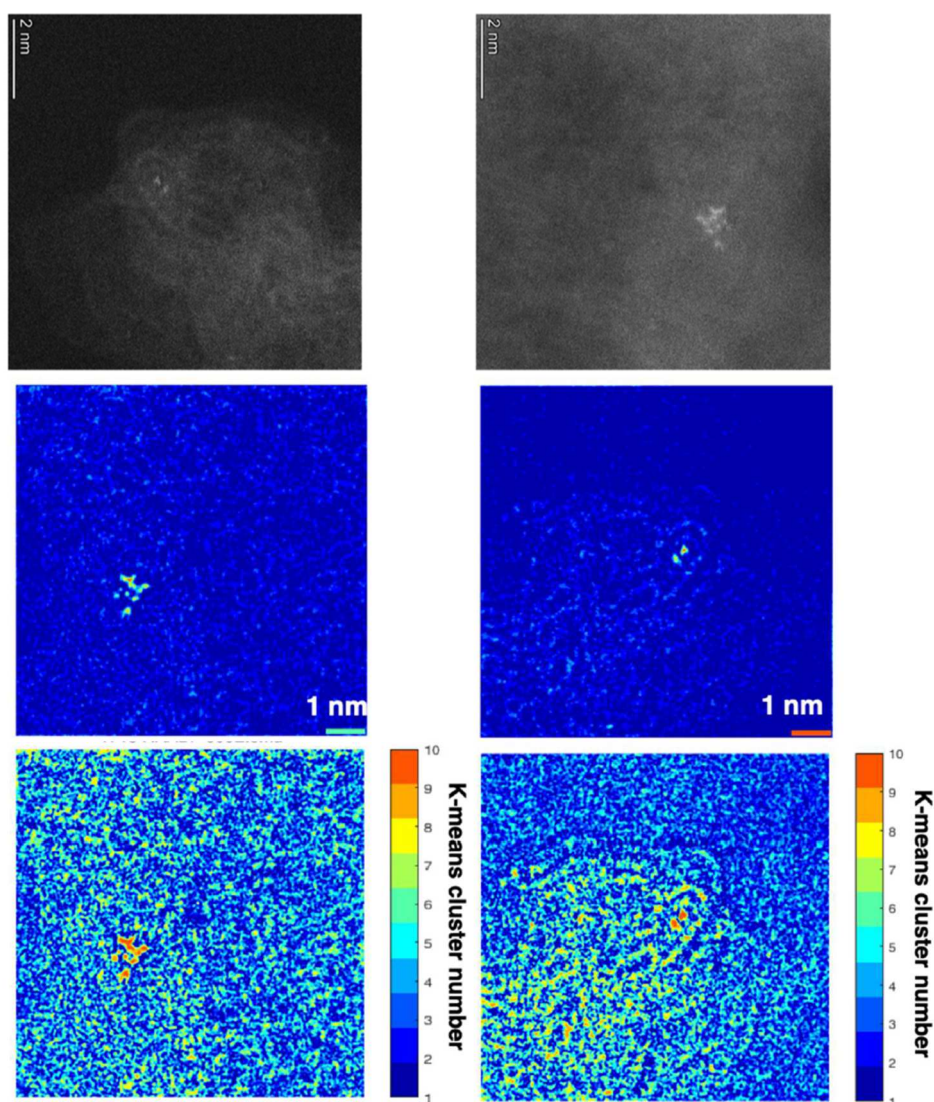
Figure 7.8 AC HAADF-STEM images of activated charcoal, previously mixed with Pt MCs in aqueous solution. The original images have been processed with the *k*-means clustering method, after denoising and background subtraction.
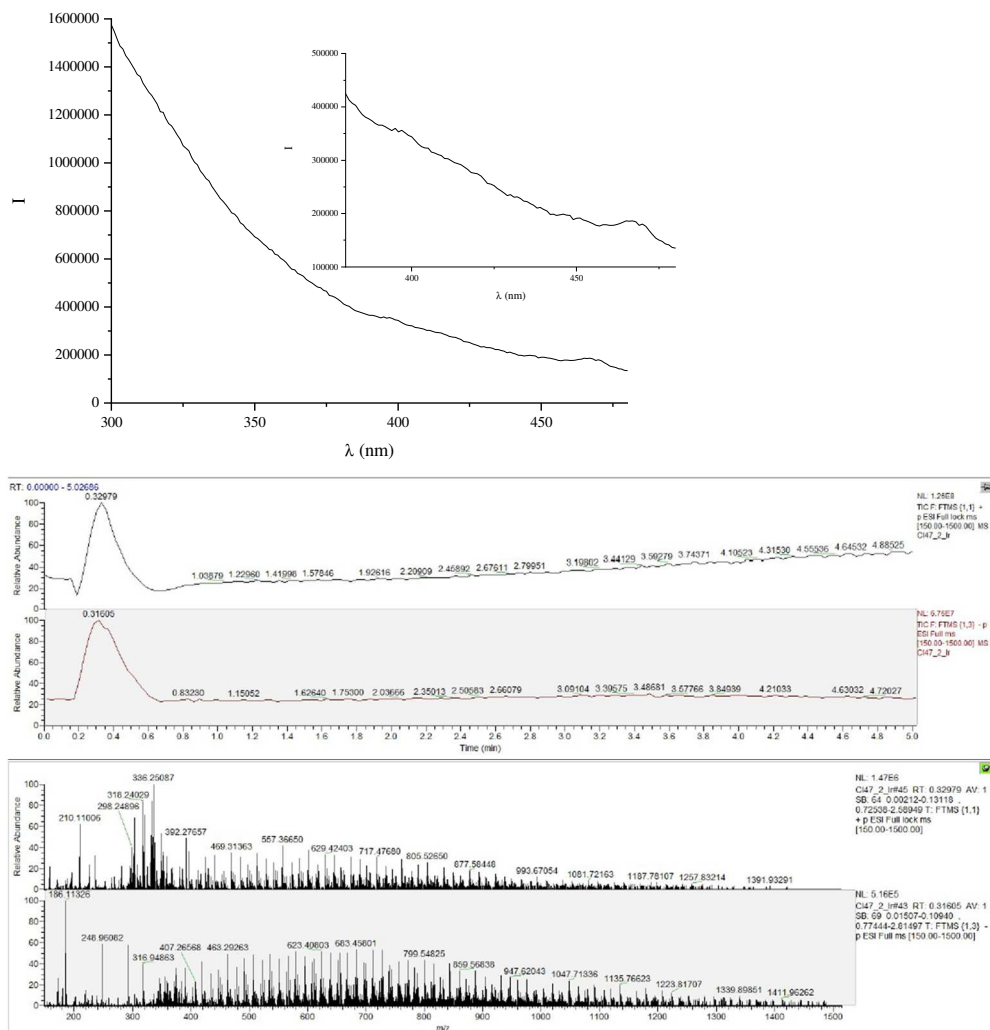
Figure 7.9 Emission spectra irradiating at 300 nm (top) and Orbitrap mass analysis (bottom) of Ir MCs prepared in solution using EVOH.
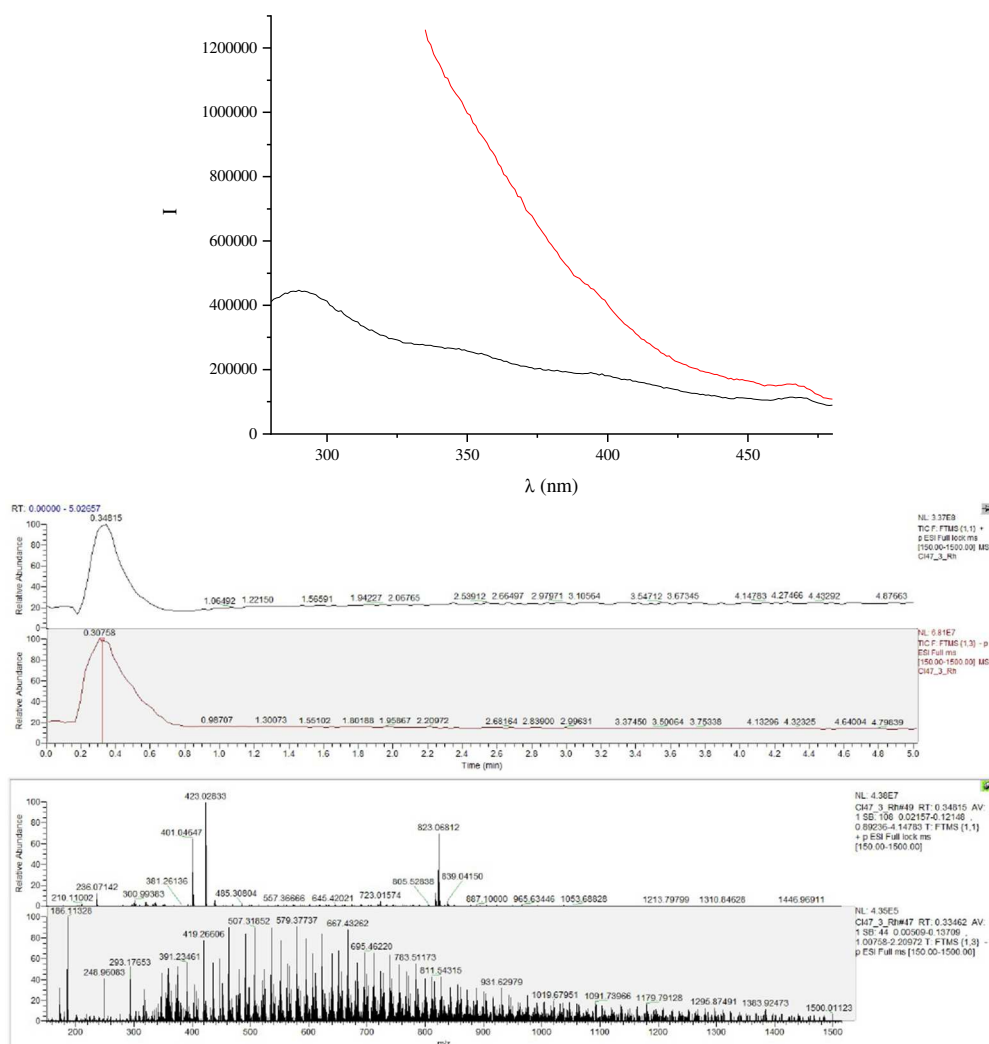
Figure 7.10 Emission spectra irradiating at 280 and 330 nm (top) and Orbitrap mass analysis (bottom) of Rh MCs prepared in solution using EVOH.
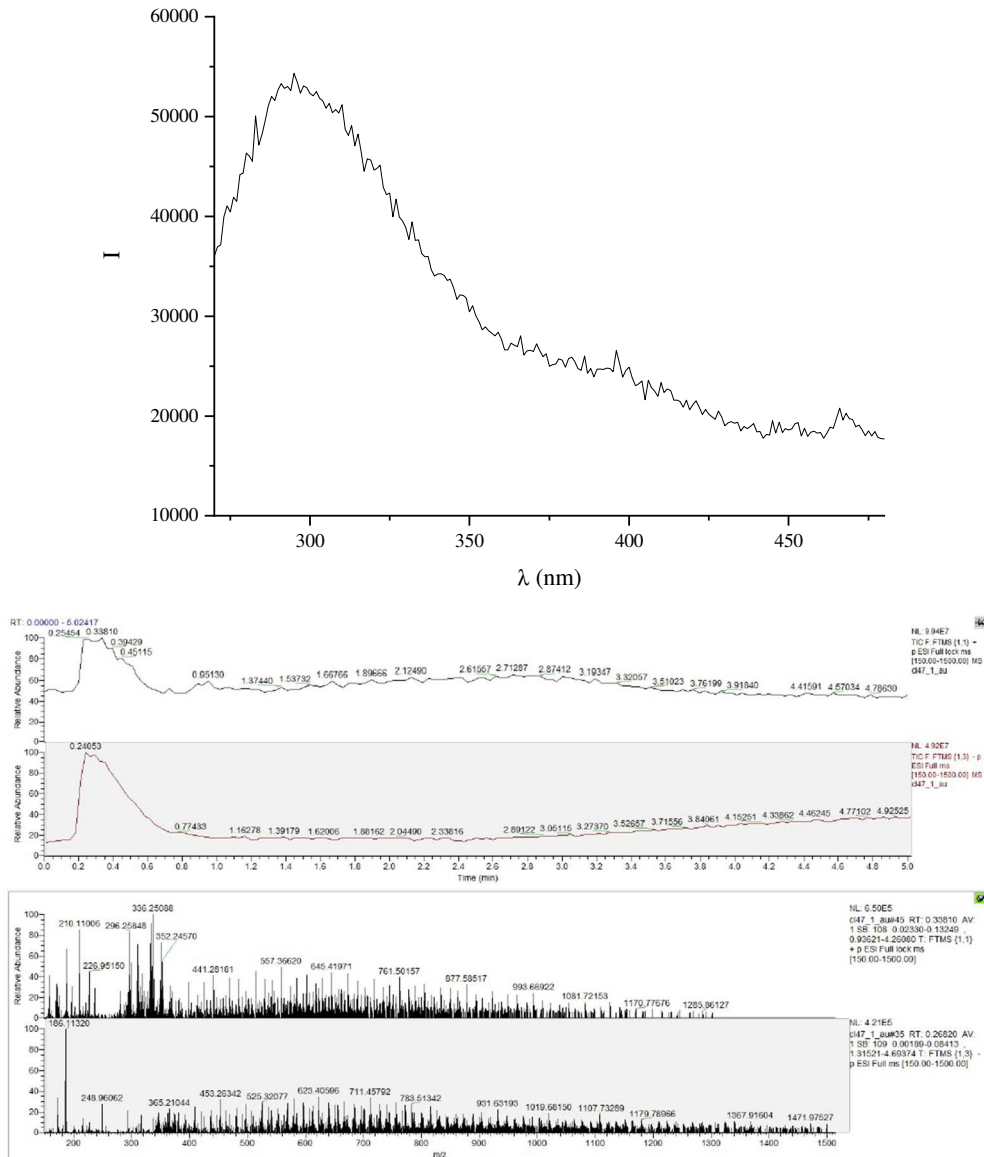
Figure 7.11 Emission spectra irradiating at 280 nm (top) and Orbitrap mass analysis (bottom) of Au MCs prepared in solution using EVOH.
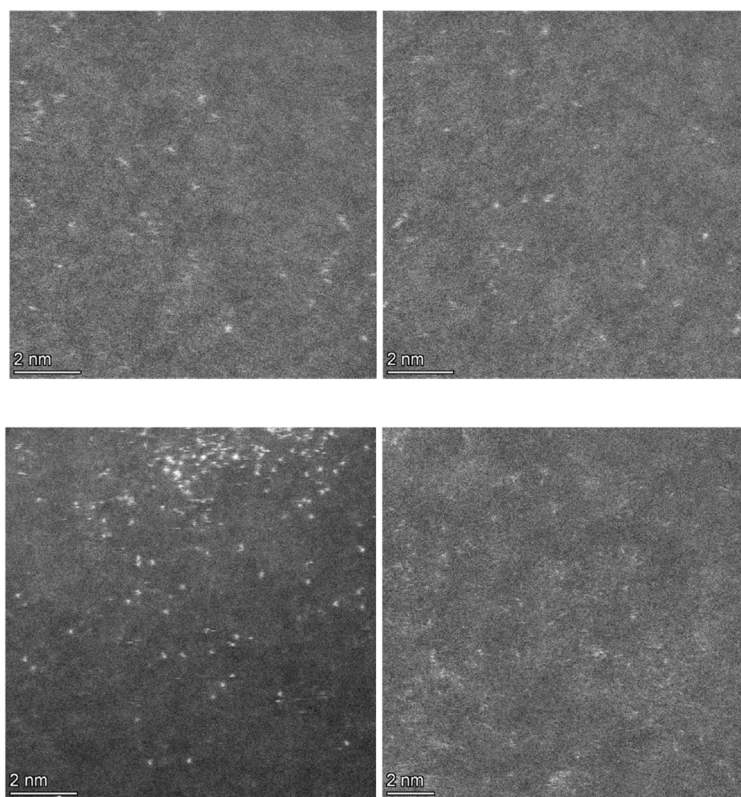
Figure 7.12 HAADF- STEM images of Ir (top) and Rh (bottom) MCs in solution, supported on Cu-carbon grids.

To compare different synthetic approaches, Pt and Au clusters were also prepared using a template-mediated technique, using the dendrimer PAMAM as a ligand. Fifth-generation dendrimer encapsulated PAMAM-OH5 Pt_{3-7} clusters, where the core, formed by the MC, is surrounded by the bulky ligand leading to 2-3 nm of size, were synthesized [53, 54] and characterized by spectrophotometry (see Figure 7.13). Besides, Au clusters were prepared using PAMAM-OH2 as a ligand and they were characterized as shown in

Figure 7.14, where a plasmonic band in the UV-Vis spectra can be observed at higher concentrations (red curve) and the emission spectra allowed to calculate the size of the MCs, i.e., Au_8 (60%), Au_{13} (30%) and Au_{21} (10%).
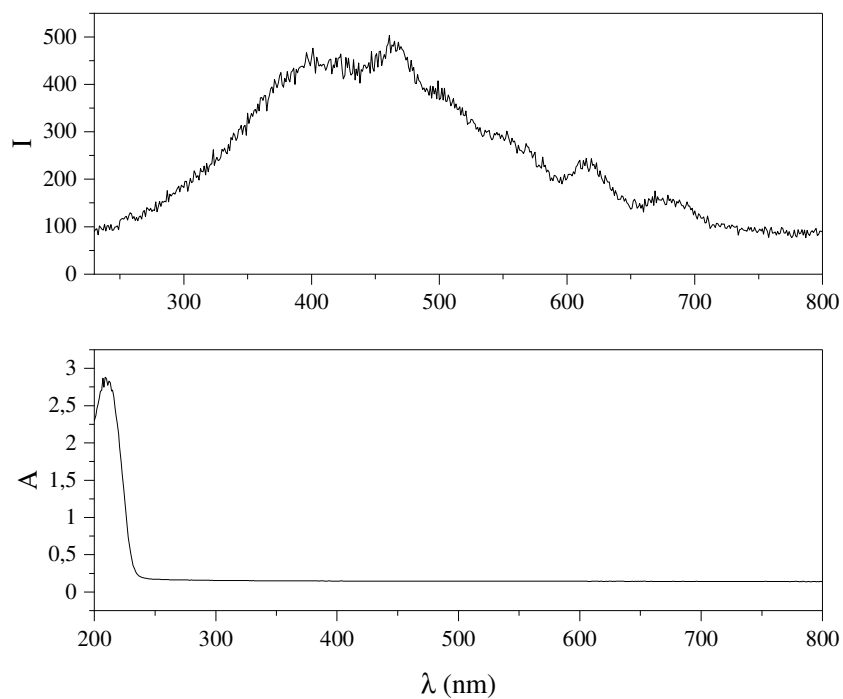

Figure 7.13 Emission spectrum irradiating at 220 nm (top) and UV-Vis spectrum (bottom) of dendrimer encapsulated PAMAM Pt MCs.
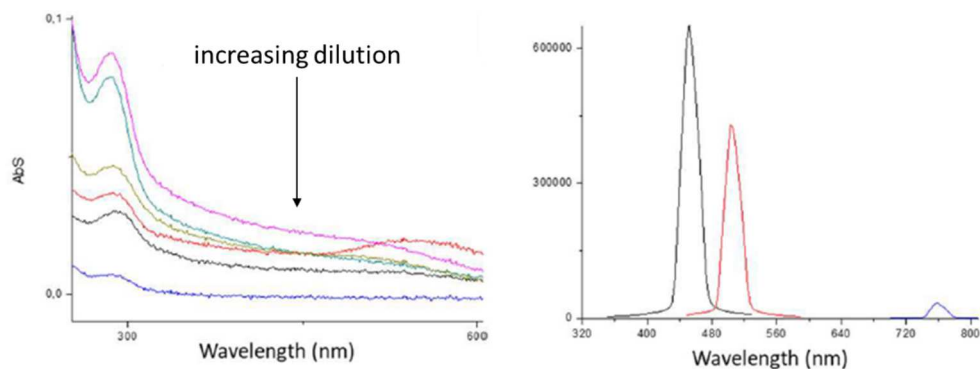
Figure 7.14 Absorption UV-Vis spectra (left) and emission spectra (right) for Au$_{8-13}$ MCs stabilized by PAMAM-OH2 in EtOH, at increasing dilutions.

7.3 Antitumoral activity of aqueous metal clusters

The MCs described above where successively used for treatments of the human cervix carcinoma (HeLa). Certainly, the identification of the MCs within the cells was not easy, because of the low concentration and the small size of the aggregates, which could not be revealed by fluorescence microscopy, common technique for the visualization of the inner environment of cells [51, 52]. Thus, the internalization of the MCs was followed by ICP-AES after treatment of the cells with the solution of MCs and the following cell lysis with a 10% Triton-100 solution. Table 7.1 confirms the presence of the metals inside the cells, showing higher concentrations in the case of MCs compared to the more classical cisplatin. These results strongly suggested the possible internalization of the MCs, but what about their antitumoral activity? Certainly, it depends upon the metal, due to the absence of any additive and/or ligands.

Table 7.1 Concentration of metal after treatment of the cells with MCs solutions, followed by the cell lysis using a Triton-100 solution, and corresponding IC50 values of HeLa cell line. The concentrations refer to ICP-AES measurements and the IC50 are obtained from the MTT assay after 24 h treatment with MCs.

Entry	MCs	[ ] internalized (μmol)[a]	IC50 (μM)[b]
1	Pt	305	0.48 ± 0.02
2	Rh	150	4.5 ± 0.5
3	Ir	162	2.4 ± 0.2
4	Au	900	> 40
5	Cisplatin	120	11 ± 1

Moreover, Table 7.1 shows the IC50 values for HeLa cells after 24 h treatments with aqueous MCs and cisplatin and calculated by the colorimetric MTT (3–[4,5–dimethylthiazole–2–yl]–2,5–diphenyltetrazolium bromide) assay, where the formation of the insoluble blue formazan dye after the reduction of the soluble MTT is related to viable cells. As also shown in Figure 7.15, the IC50 values obtained were higher in the case of Pt MCs (0.48 μM) when compared to cisplatin (11 μM).
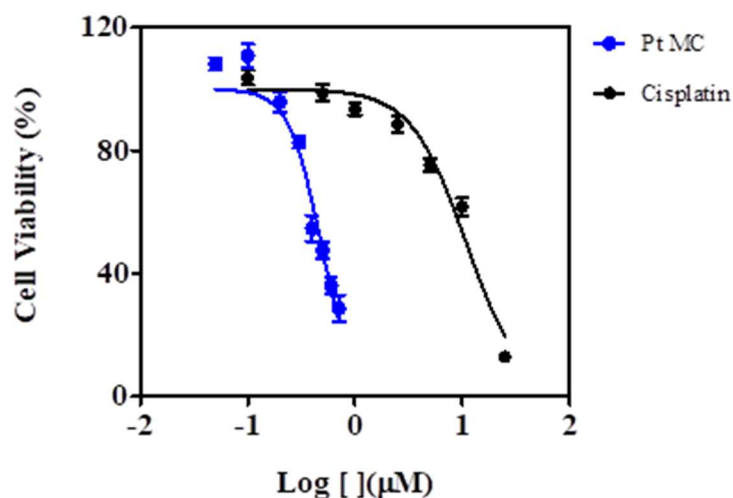
Figure 7.15 Effect of Pt MCs on cell proliferation of HeLa cells determined by the colorimetric MTT assay. Cells were incubated with concentrations of Pt MCs from 0.05 to 0.7 µM for 24 h, whereas cisplatin, used as standard compound, was used in concentration from 0.1 to 50 µM. Data correspond to the mean ± SD of three independent dose-response experiments.

Furthermore, the dendrimer encapsulated PAMAM-OH5 Pt_{3-7} MCs were used in cell proliferation experiments of HeLa cells, as shown in Figure 7.16. The latter illustrates that Pt MCs lost completely the antitumoral activity when are synthesized using the PAMAM ligand, reaching IC50 comparable to the neat PAMAM.
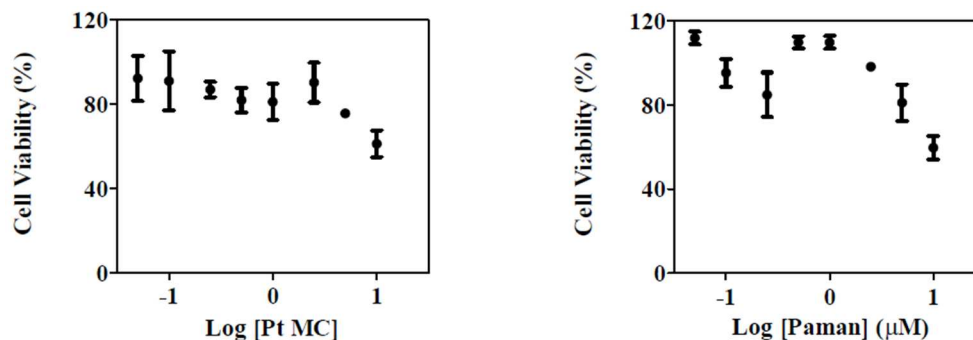
Figure 7.16 Cell proliferative analyses of HeLa cells with Pt_5-PAMAM-OH5 (left) and pure PAMAM-OH5 (right), determined by MTT assays.

As shown in Table 7.1 and Figure 7.17, Ir and Rh MCs described above represent a positive advance, presenting an IC50 of 2.4 and 6.0 µM, respectively, in the treatment of HeLa cells, in agreement with recent values obtained with Ir and Rh organometallic complexes [53-56].
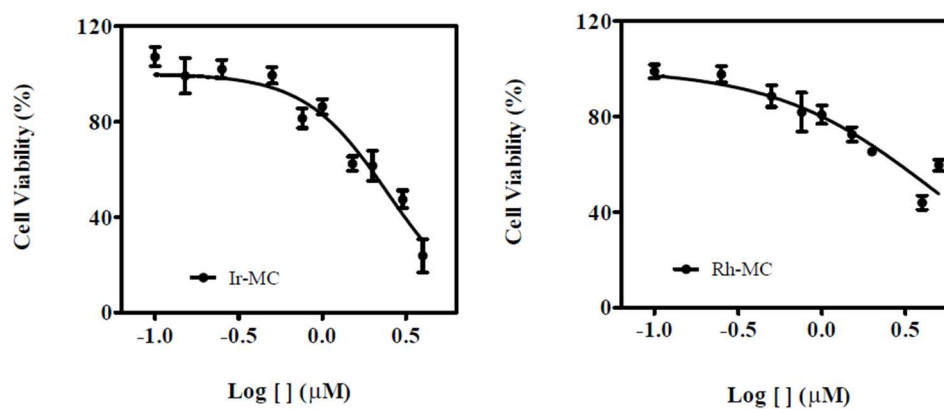

Figure 7.17 Cell proliferative analyses of HeLa cells, determined by MTT assays, with Ir MCs (left) and Rh MCs (right) prepared in solution.

Meanwhile, Au MCs showed a very low cytotoxicity compared to Pt, Ir and Rh (see Table 7.1), despite being highly internalized by the cells. In order to test the antitumoral activity of Au prepared following a different synthetic procedure, the Au clusters stabilized by PAMAM-OH2 were tested in cell proliferative analyses of HeLa cells, showing similar IC50 to those obtained using Au MCs prepared in solution and to the neat PAMAM, as presented in Figure 7.18. Finally, it is possible to say that the size or the synthetic method of the Au MCs does not change the intrinsically low antitumoral activity of Au, but also that the internalization as MCs of active metals, like Pt, Ir and Rh, can boost their antitumoral activity.
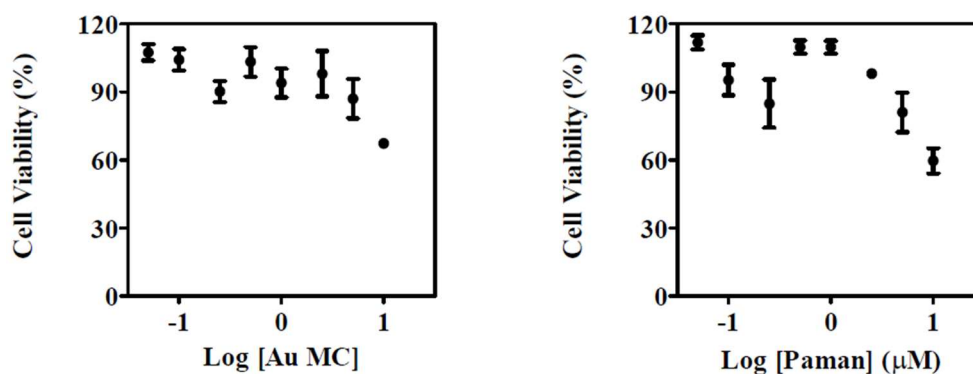
Figure 7.18 Cell proliferative analyses of HeLa cells with Au_{8-13}-PAMAM-OH2 (left) and pure PAMAM-OH2 (right), determined by MTT assays.

7.3.1 Cell death mechanism

Certainly, the antitumoral activity of MCs has been demonstrated up to now, but it is interesting to go deeper into the mechanism of the death cell, which can happen following a necrotic or apoptotic pathway, where the former represents an accidental death, due to external uncontrolled factors and

including the total damage of the membrane of the cells, and the latter is a programmed process, related to specific external stimuli and to a cascade process starting from the inner part of the cell [57]. For this purpose, HeLa cells were stained with annexin V/propidium iodide (AnnV/PI) and treated with MCs. Successively, the samples were analyzed by fluorescence microscopy to distinguish between apoptotic and necrotic cells. Indeed, AnnV, conjugated with the green-fluorescent dye FITC, can detect the phosphatidylserine externalization related to apoptosis, whereas PI stains the already dead cells giving a red fluorescence [58]. As shown in Figure 7.19, Pt and Rh showed the higher cell deaths and all the cells appeared to be dead following an apoptotic process. To further confirm this hypothesis, caspase-3 activity [59] and LDH release [60] experiments were performed to reveal an apoptotic or necrotic process, respectively. Figure 7.20 validates that the death of the cells happened, for both Pt and Rh MCs, following an apoptotic route, with high differences compared to the control sample, i.e., untreated cells.
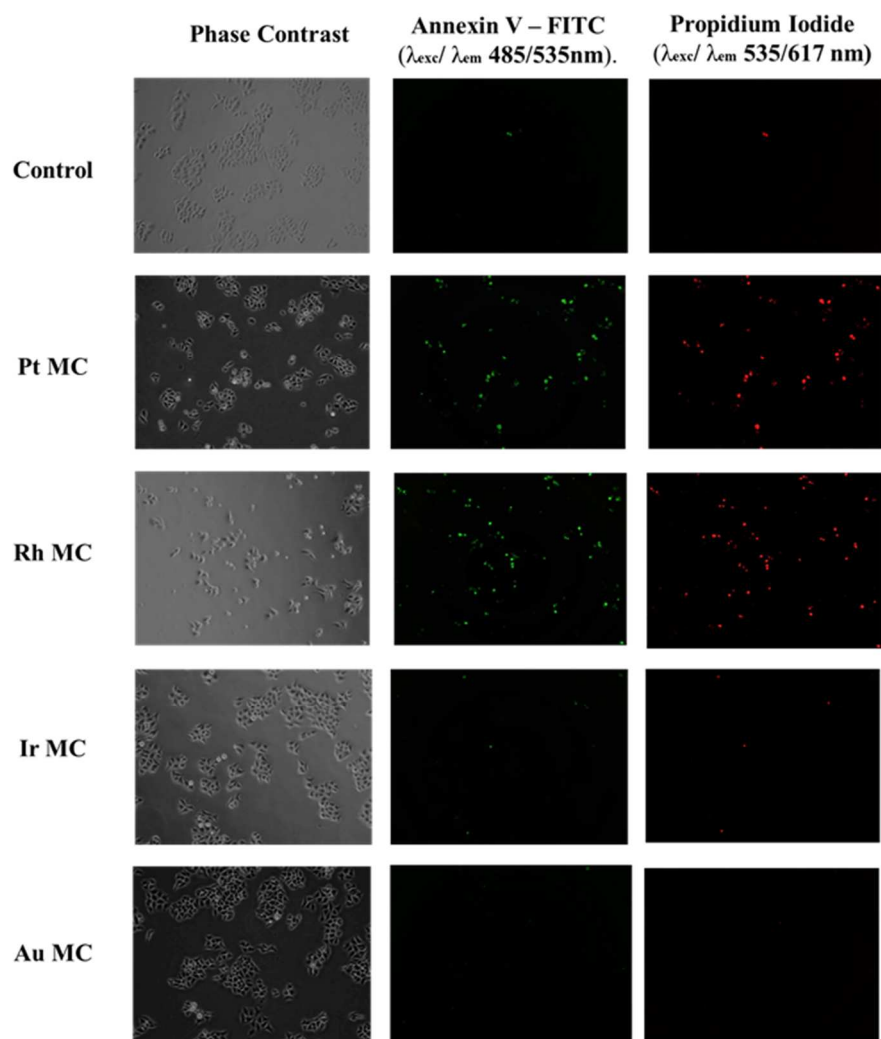
Figure 7.19 Cell morphology and fluorescent microscopy images of AnnV/PI double-staining of HeLa cells after treatment with MCs. Cells were labelled with AnnV-FITC ($\lambda_{exc}/\lambda_{em}$ 485 nm/535 nm; green fluorescence) and PI ($\lambda_{exc}/\lambda_{em}$ 535 nm/617 nm; red fluorescence) and visualized with the Leica fluorescence microscope PAULA.
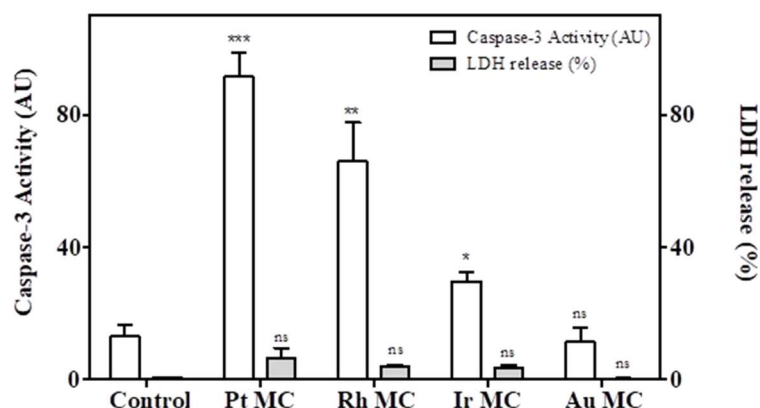
Figure 7.20 Caspase-3 activation assay and LDH release by HeLa cells after treatment with MCs. Data represent the means ± SD of three independent dose-response experiments. Asterisks indicate significant differences comparing them with untreated cells using the t-Student test (***$p<0.001$, **$p<0.01$, *$p<0.05$; ns: non-significant).

7.3.2 Mechanism of action of metal clusters

To relate the antitumoral activity to the presence of MCs and to confirm their preservation during the cell treatments, their characteristics were analyzed by spectrophotometry using the same conditions applied in the treatments, but omitting the presence of the cells, which will compromise the analysis. Figures 7.21-7.23 show that MCs were stable in acetonitrile (ACN) and at pH equal to 7.4 in presence of phosphate-saline-buffer (PBS).

Figure 7.21 UV-Vis spectra (top) and emission spectra (bottom) of Pt MCs in water (black), in water/ACN (red) and adding PBS (blue). In all the emission spectra the sample was irradiated at 250 nm.

Figure 7.22 UV-Vis spectra (top) and emission spectra (bottom) of Rh MCs in water (black), in water/ACN (red) and adding PBS (blue). In all the emission spectra the sample was irradiated at 250 nm.
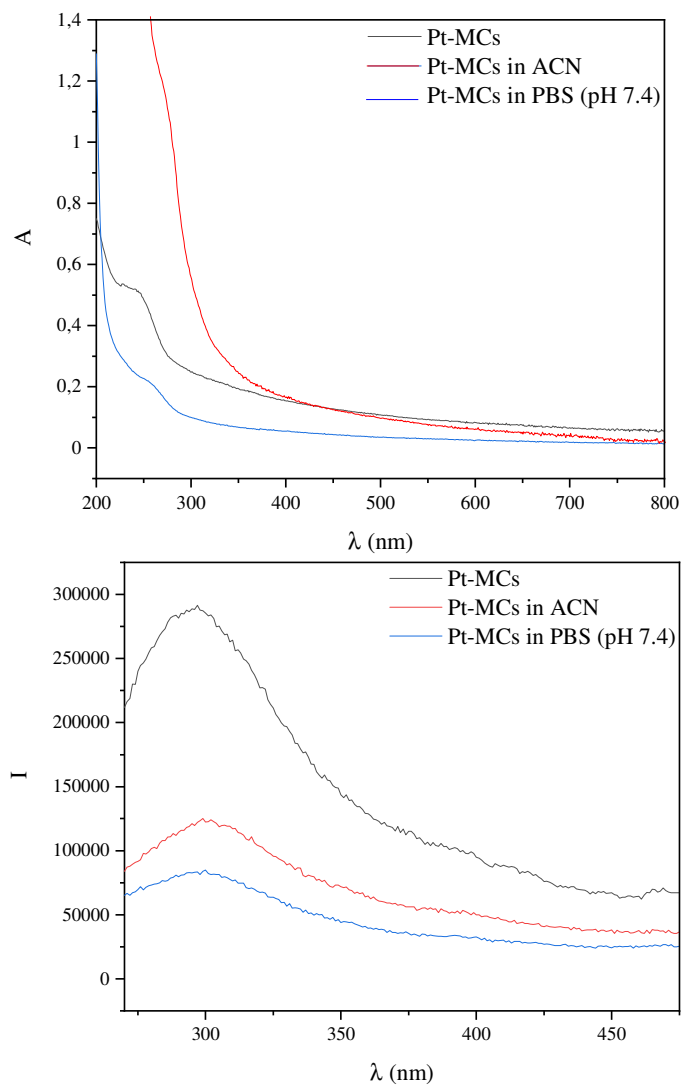
Figure 7.23 UV-Vis spectra (top) and emission spectra (bottom) of Ir MCs in water (black), in water/ACN (red) and adding PBS (blue). In all the emission spectra the sample was irradiated at 250 nm.
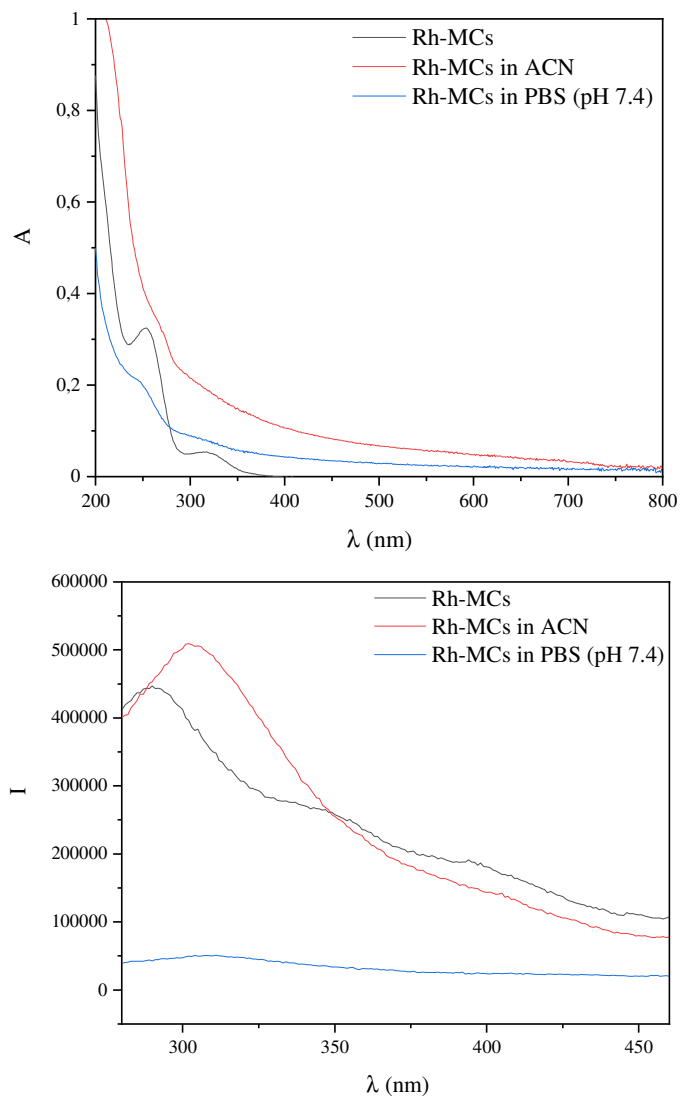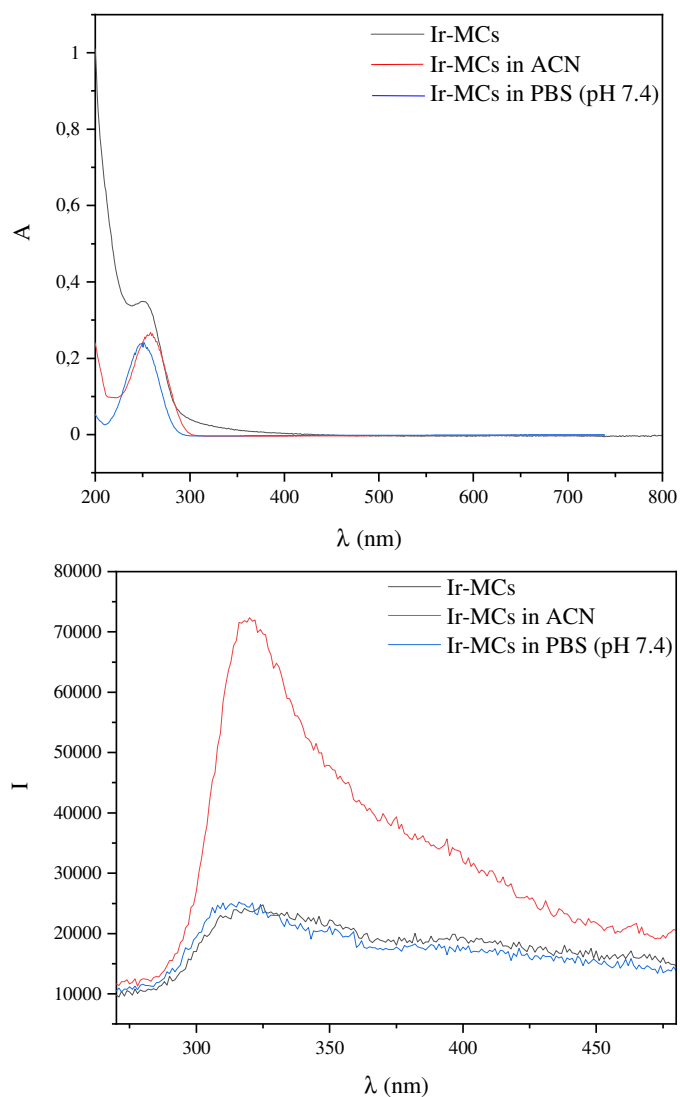
In order to support the experimental data, computational calculations helped with understanding how Pt species attacked the cell. Figure 7.24 shows that Pt_3-Pt_{11} are able to form a complex with the guanine of the DNA, reaching minima of complexation energies between -38 and -59 kcal·mol^{-1}, even in the case of partially oxidized Pt clusters with the same atomicity of the pure-Pt parent cluster, Pt_xO_{x-1}, with $2 \leq x \leq 6$. Actually, Pt_2O and Pt_3O_2, which represent the smallest oxidized species, can form adduct as in the case of their pure-Pt counterparts, i.e., Pt_3 and Pt_5, whereas the biggest species, Pt_4O_3, Pt_5O_4 and Pt_6O_5, form more stable complexes if compared with those formed with the pure-Pt clusters with the same atomicity. Consequently, the number of atoms composing the MCs assumes a central relevance, because MCs composed by 5 to 8 atoms appear to have the strongest interactions with DNA.
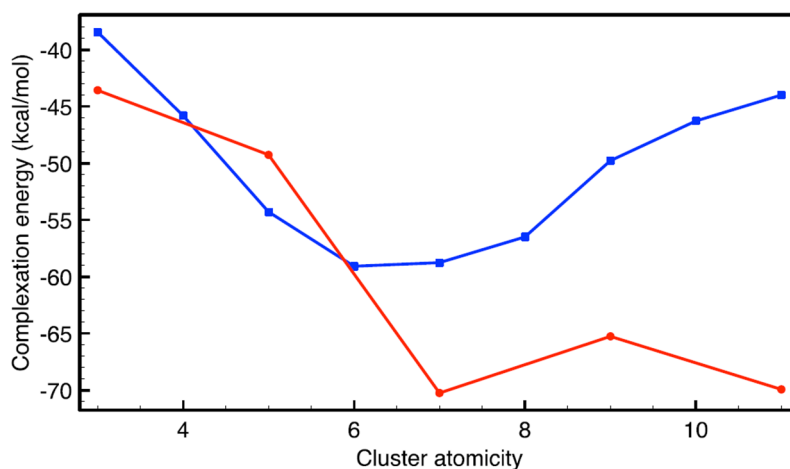

Figure 7.24 DFT calculated complexation energies (in kcal/mol) as a function of the MC atomicity (total number of atoms), of pure Pt metal MCs (blue) and their oxidized counterparts (red).
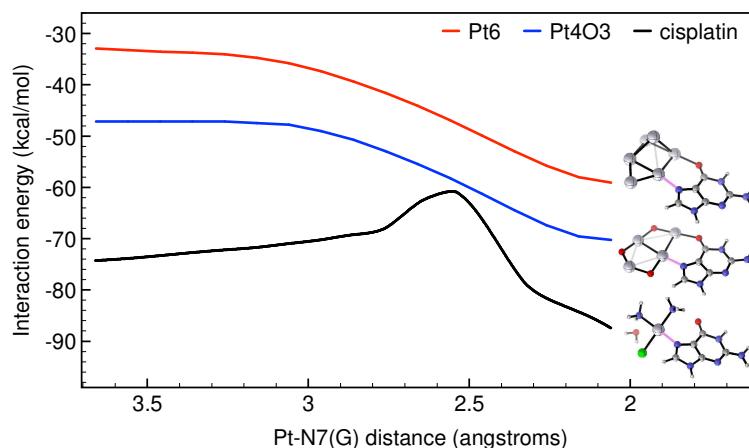
Figure 7.25 Interaction energy profile (kcal/mol) along the reaction of Pt clusters or cisplatin with DNA guanine base. The geometries are optimized by monitoring the distance between the reactive Pt centre and the N7 site. Colour scheme: gray, C atoms; blue, N atoms; red, O atoms; green, Cl atom; white, H atoms. Pt atoms are displayed as larger gray balls.

The computational studies were deepened towards the understanding of the interaction between the Pt species and the N7 guanine atom, which is the most available site for accepting Pt [12]. In Figure 7.25, Pt_6 and Pt_4O_3, the most reactive species in the formation of the complex, are compared to cisplatin. The latter forms a more stable adduct with guanine, with an interaction energy of -87 kcal·mol^{-1}, probably due to its formal 2+ charge corresponding to a higher interaction energy, but the presence of a maximum is related to an activation energy related to the hydrolysis of one of the chlorines, leading to an energy barrier of 16 kcal·mol^{-1}. On the other hand, MCs do not need any activation and can bind the DNA with a barrierless profile.

Of course, we tried to visualize experimentally what happened to the MCs internalized within the cells. Figure 7.26 illustrates HRTEM and AC HAADF-STEM images of osmium- and uranyl-stained HeLa cells after the treatment with Pt MCs. It is evident the formation of amorphous Pt oxides, which probably derives from small Pt oxide particles and not from preformed NPs, which were not previously detected. Actually, the addition of osmium and uranyl, necessary to visualize the cells, had effects on the imaging of the metallic entities, which resulted to be composed mainly by osmium from the energy-dispersive X-ray (EDX) spectra.
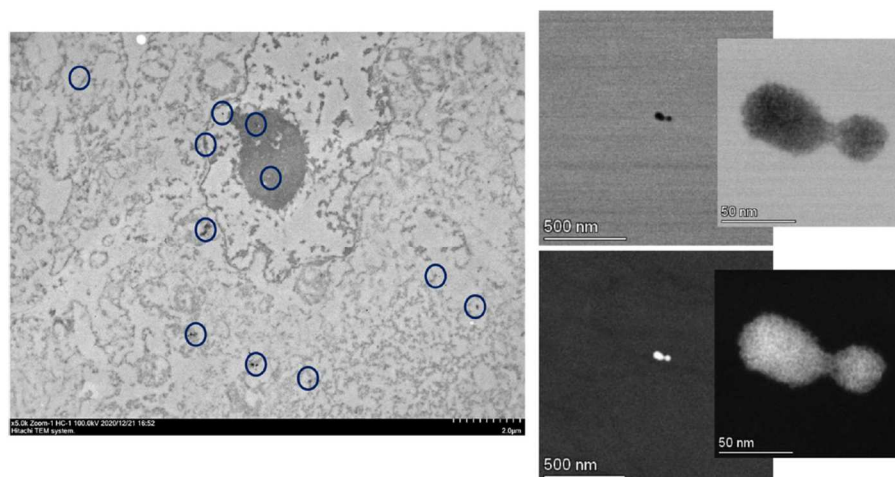
Figure 7.26 Bright–field (BF) HR–TEM (left, amorphous aggregations of Pt MCs circled in blue) and AC HAADF–STEM (right) images of HeLa cells treated with Pt MCs.

7.4 Antitumoral activity of aqueous metal clusters towards cisplatin-resistant cells

As mentioned above, some types of cancers are still resistant towards cisplatin, due probably to a poor internalization of the drug by active diffusion though the Cr1 Cu channels of the cells [61]. In the case of MCs, the internalization might be passive, avoiding the drawback generated by the lack of "communication" between Cr1 Cu channels and cisplatin. Envisioning this, we applied Pt MCs in cell proliferative assays of human ovarian cancer A2780 cell line and its cisplatin-resistant variant A2780cis.
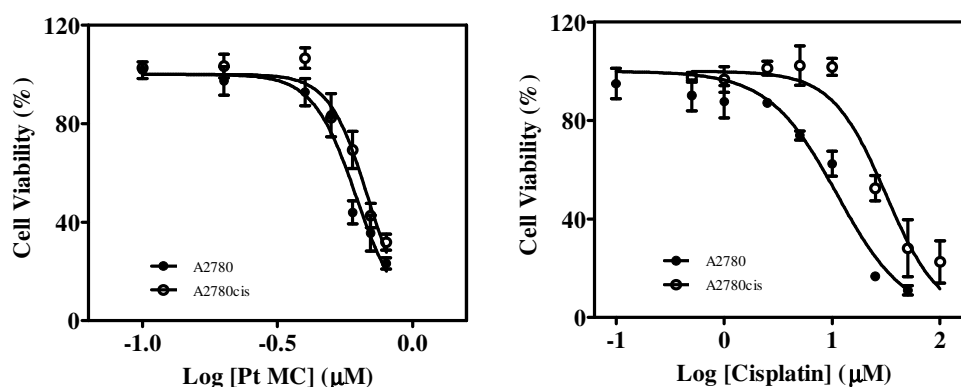
Figure 7.27 Cytotoxicity profiles of Pt MCs (left) and cisplatin (right) of ovarian cancer cells A2780 and cisplatin–resistant A2780cis. Cells were incubated with Pt MCs or cisplatin for 24 h. Data are the mean ± SD of three independent dose–response experiments.

Remarkably, Pt MCs presented an antitumoral activity higher than in the case of cisplatin and similar for the A2780cis and A2780 cells, leading to IC50 of 0.68 μM and 0.48 μM, respectively, as shown in Figure 7.27. Even though

these results are just preliminary, they can represent a starting point for new strategies in the treatment of cisplatin-resistance cancers.

7.5 Conclusions

Despite being the cheapest and most used antitumoral drug, cisplatin is synthesized with a four-step approach starting from K_2PtCl_4 and bringing to an expense of 200 € per gram. In this *Chapter*, the synthesis of much cheaper and highly antitumoral active Pt MCs was presented. The synthesis of these species involves the use of K_2PtCl_4, but only one synthetic step is needed. In addition, the synthesis could be easily scaled up and, on the other hand, the clusters could be embedded in a polymeric matrix and preserved up to two years at room temperature. Computational calculations gave the possibility to better understand the mechanism of interaction of these tiny entities and the DNA of the tumoral cells. Moreover, Ir, Rh and Au MCs were synthetized in the same way and the first two showed high antitumoral activity.

All the clusters were used in HeLa cells, with activity remarkably comparable to cisplatin, and Pt clusters were also tested in a cisplatin-resistant cell line, showing surprisingly a better activity than cisplatin.

The species described in this *Chapter* can easily represent good candidates as anticancer drugs or clear the way for new applications of subnanometric metallic species in biomedical applications.

7.6 References

1. Choi, S.; Dickson, R. M.; Yu, J., Developing luminescent silver nanodots for biological applications. *Chem. Soc. Rev.* **2012**, *41* (5), 1867-1891.

2. Xavier, P. L.; Chaudhari, K.; Baksi, A.; Pradeep, T., Protein-protected luminescent noble metal quantum clusters: an emerging trend in atomic cluster nanoscience. *Nano Rev.* **2012**, *3* (1), 14767.

3. Shiang, Y.-C.; Huang, C.-C.; Chen, W.-Y.; Chen, P.-C.; Chang, H.-T., Fluorescent gold and silver nanoclusters for the analysis of biopolymers and cell imaging. *J. Mater. Chem.* **2012**, *22* (26), 12972-12982.

4. Lheureux, S.; Gourley, C.; Vergote, I.; Oza, A. M., Epithelial ovarian cancer. *The Lancet* **2019**, *393* (10177), 1240-1253.

5. Ghosh, S., Cisplatin: The first metal based anticancer drug. *Bioorg. Chem.* **2019**, *88*, 102925.

6. Siddik, Z. H., Cisplatin: Mode of cytotoxic action and molecular basis of resistance. *Oncogene* **2003**, *22* (47), 7265-7279.

7. Qi, L.; Luo, Q.; Zhang, Y.; Jia, F.; Zhao, Y.; Wang, F., Advances in toxicological research of the anticancer drug cisplatin. *Chem. Res. Toxicol.* **2019**, *32* (8), 1469-1486.

8. Huang, J.; Li, J.; Lyu, Y.; Miao, Q.; Pu, K., Molecular optical imaging probes for early diagnosis of drug-induced acute kidney injury. *Nat. Mater.* **2019**, *18* (10), 1133-1143.

9. Eskandari, A.; Kundu, A.; Ghosh, S.; Suntharalingam, K., A triangular platinum(II) multinuclear complex with cytotoxicity towards breast cancer stem cells. *Angew. Chem. Int. Ed.* **2019**, *58* (35), 12059-12064.

10. Deng, Z.; Wang, N.; Liu, Y.; Xu, Z.; Wang, Z.; Lau, T.-C.; Zhu, G., A

photocaged, water-oxidizing, and nucleolus-targeted Pt(IV) complex with a distinct anticancer mechanism. *J. Am. Chem. Soc.* **2020**, *142* (17), 7803-7812.

11. Wang, Z.; Deng, Z.; Zhu, G., Emerging platinum(iv) prodrugs to combat cisplatin resistance: from isolated cancer cells to tumor microenvironment. *Dalton Trans.* **2019**, *48* (8), 2536-2544.

12. Veclani, D.; Melchior, A.; Tolazzi, M.; Cerón-Carrasco, J. P., Using theory to reinterpret the kinetics of monofunctional platinum anticancer drugs: Stacking matters. *J. Am. Chem. Soc.* **2018**, *140* (43), 14024-14027.

13. Xue, X.; Hall, M. D.; Zhang, Q.; Wang, P. C.; Gottesman, M. M.; Liang, X.-J., Nanoscale drug delivery platforms overcome platinum-based resistance in cancer cells due to abnormal membrane protein trafficking. *ACS Nano* **2013**, *7* (12), 10452-10464.

14. Segovia, C.; San José-Enériz, E.; Munera-Maravilla, E.; Martínez-Fernández, M.; Garate, L.; Miranda, E.; Vilas-Zornoza, A.; Lodewijk, I.; Rubio, C.; Segrelles, C.; Valcárcel, L. V.; Rabal, O.; Casares, N.; Bernardini, A.; Suarez-Cabrera, C.; López-Calderón, F. F.; Fortes, P.; Casado, J. A.; Dueñas, M.; Villacampa, F.; Lasarte, J. J.; Guerrero-Ramos, F.; de Velasco, G.; Oyarzabal, J.; Castellano, D.; Agirre, X.; Prósper, F.; Paramio, J. M., Inhibition of a G9a/DNMT network triggers immune-mediated bladder cancer regression. *Nat. Med.* **2019**, *25* (7), 1073-1081.

15. Liu, P.; Zhao, L.; Pol, J.; Levesque, S.; Petrazzuolo, A.; Pfirschke, C.; Engblom, C.; Rickelt, S.; Yamazaki, T.; Iribarren, K.; Senovilla, L.; Bezu, L.; Vacchelli, E.; Sica, V.; Melis, A.; Martin, T.; Xia, L.; Yang,

H.; Li, Q.; Chen, J.; Durand, S.; Aprahamian, F.; Lefevre, D.; Broutin, S.; Paci, A.; Bongers, A.; Minard-Colin, V.; Tartour, E.; Zitvogel, L.; Apetoh, L.; Ma, Y.; Pittet, M. J.; Kepp, O.; Kroemer, G., Crizotinib-induced immunogenic cell death in non-small cell lung cancer. *Nat. Commun.* **2019**, *10* (1), 1486.

16. Ashraf, S.; Hassan Said, A.; Hartmann, R.; Assmann, M.-A.; Feliu, N.; Lenz, P.; Parak, W. J., Quantitative particle uptake by cells as analyzed by different methods. *Angew. Chem. Int. Ed.* **2020**, *59* (14), 5438-5453.

17. Sindhwani, S.; Syed, A. M.; Ngai, J.; Kingston, B. R.; Maiorino, L.; Rothschild, J.; MacMillan, P.; Zhang, Y.; Rajesh, N. U.; Hoang, T.; Wu, J. L. Y.; Wilhelm, S.; Zilman, A.; Gadde, S.; Sulaiman, A.; Ouyang, B.; Lin, Z.; Wang, L.; Egeblad, M.; Chan, W. C. W., The entry of nanoparticles into solid tumours. *Nat. Mater.* **2020**, *19* (5), 566-575.

18. Zhang, C.; Yan, L.; Gu, Z.; Zhao, Y., Strategies based on metal-based nanoparticles for hypoxic-tumor radiotherapy. *Chem. Sci.* **2019**, *10* (29), 6932-6943.

19. Kim, D.; Shin, K.; Kwon, S. G.; Hyeon, T., Synthesis and biomedical applications of multifunctional nanoparticles. *Adv. Mater.* **2018**, *30* (49), 1802309.

20. Xia, H.; Li, F.; Hu, X.; Park, W.; Wang, S.; Jang, Y.; Du, Y.; Baik, S.; Cho, S.; Kang, T.; Kim, D.-H.; Ling, D.; Hui, K. M.; Hyeon, T., pH-Sensitive Pt nanocluster assembly overcomes cisplatin resistance and heterogeneous stemness of hepatocellular carcinoma. *ACS Cent. Sci.* **2016**, *2* (11), 802-811.

21. Li, H.-J.; Du, J.-Z.; Du, X.-J.; Xu, C.-F.; Sun, C.-Y.; Wang, H.-X.; Cao,

Z.-T.; Yang, X.-Z.; Zhu, Y.-H.; Nie, S.; Wang, J., Stimuli-responsive clustered nanoparticles for improved tumor penetration and therapeutic efficacy. *Proc. Natl. Acad. Sci. U. S. A.* **2016**, *113* (15), 4164-4169.

22. Asharani, P.; Xinyi, N.; Hande, M. P.; Valiyaveettil, S., DNA damage and p53-mediated growth arrest in human cells treated with platinum nanoparticles. *Nanomedicine* **2010**, *5* (1), 51-64.

23. Loynachan, C. N.; Soleimany, A. P.; Dudani, J. S.; Lin, Y.; Najer, A.; Bekdemir, A.; Chen, Q.; Bhatia, S. N.; Stevens, M. M., Renal clearable catalytic gold nanoclusters for in vivo disease monitoring. *Nat. Nanotechnol.* **2019**, *14* (9), 883-890.

24. Chen, D.; Gao, S.; Ge, W.; Li, Q.; Jiang, H.; Wang, X., One-step rapid synthesis of fluorescent platinum nanoclusters for cellular imaging and photothermal treatment. *RSC Adv.* **2014**, *4* (76), 40141-40145.

25. Yamagishi, Y.; Watari, A.; Hayata, Y.; Li, X.; Kondoh, M.; Yoshioka, Y.; Tsutsumi, Y.; Yagi, K., Acute and chronic nephrotoxicity of platinum nanoparticles in mice. *Nanoscale Res. Lett.* **2013**, *8* (1), 395.

26. Boronat, M.; Leyva-Pérez, A.; Corma, A., Theoretical and experimental insights into the origin of the catalytic activity of subnanometric gold clusters: Attempts to predict reactivity with clusters and nanoparticles of gold. *Acc. Chem. Res.* **2014**, *47* (3), 834-844.

27. Oliver-Meseguer, J.; Cabrero-Antonino, J. R.; Domínguez, I.; Leyva-Pérez, A.; Corma, A., Small gold clusters formed in solution give reaction turnover numbers of 10^7 at room temperature. *Science* **2012**, *338* (6113), 1452-1455.

28. Corma, A.; Concepción, P.; Boronat, M.; Sabater, M. J.; Navas, J.;

Yacaman, M. J.; Larios, E.; Posadas, A.; López-Quintela, M. A.; Buceta, D.; Mendoza, E.; Guilera, G.; Mayoral, A., Exceptional oxidation activity with size-controlled supported gold clusters of low atomicity. *Nat. Chem.* **2013**, *5* (9), 775-781.

29. Tyo, E. C.; Vajda, S., Catalysis by clusters with precise numbers of atoms. *Nat. Nanotechnol.* **2015**, *10* (7), 577-588.

30. Buceta, D.; Busto, N.; Barone, G.; Leal, J. M.; Domínguez, F.; Giovanetti, L. J.; Requejo, F. G.; García, B.; López-Quintela, M. A., Ag_2 and Ag_3 clusters: Synthesis, characterization, and interaction with DNA. *Angew. Chem. Int. Ed.* **2015**, *54* (26), 7612-7616.

31. Lee, J.; Yang, J.; Kwon, S. G.; Hyeon, T., Nonclassical nucleation and growth of inorganic nanoparticles. *Nat. Rev. Mater.* **2016**, *1*, 16034.

32. Leyva-Pérez, A.; Corma, A., Similarities and differences between the "relativistic" triad gold, platinum, and mercury in catalysis. *Angew. Chem. Int. Ed.* **2012**, *51* (3), 614-635.

33. Vajda, S.; Pellin, M. J.; Greeley, J. P.; Marshall, C. L.; Curtiss, L. A.; Ballentine, G. A.; Elam, J. W.; Catillon-Mucherie, S.; Redfern, P. C.; Mehmood, F.; Zapol, P., Subnanometre platinum clusters as highly active and selective catalysts for the oxidative dehydrogenation of propane. *Nat. Mater.* **2009**, *8* (3), 213-6.

34. Mon, M.; Rivero-Crespo, M. A.; Ferrando-Soria, J.; Vidal-Moya, A.; Boronat, M.; Leyva-Pérez, A.; Corma, A.; Hernández-Garrido, J. C.; López-Haro, M.; Calvino, J. J.; Ragazzon, G.; Credi, A.; Armentano, D.; Pardo, E., Synthesis of densely packaged, ultrasmall Pt^0_2 clusters within a thioether-functionalized MOF: Catalytic activity in industrial reactions

at low temperature. *Angew. Chem. Int. Ed.* **2018**, *57* (21), 6186-6191.

35. Imaoka, T.; Akanuma, Y.; Haruta, N.; Tsuchiya, S.; Ishihara, K.; Okayasu, T.; Chun, W.-J.; Takahashi, M.; Yamamoto, K., Platinum clusters with precise numbers of atoms for preparative-scale catalysis. *Nat. Commun.* **2017**, *8* (1), 688-688.

36. Guillén-Villafuerte, O.; García, G.; Anula, B.; Pastor, E.; Blanco, M. C.; López-Quintela, M. A.; Hernández-Creus, A.; Planes, G. A., Assembly of subnanometric 2D Pt nanoislands in parallel rows onto Au(111) by self-organization of Pt clusters. *Angew. Chem. Int. Ed.* **2006**, *45* (26), 4266-9.

37. Li, Y.; Liu, J. H.-C.; Witham, C. A.; Huang, W.; Marcus, M. A.; Fakra, S. C.; Alayoglu, P.; Zhu, Z.; Thompson, C. M.; Arjun, A.; Lee, K.; Gross, E.; Toste, F. D.; Somorjai, G. A., A Pt-cluster-based heterogeneous catalyst for homogeneous catalytic reactions: X-ray absorption spectroscopy and reaction kinetic studies of their activity and stability against leaching. *J. Am. Chem. Soc.* **2011**, *133* (34), 13527-13533.

38. Oliver-Messeguer, J.; Liu, L.; García-García, S.; Canós-Giménez, C.; Domínguez, I.; Gavara, R.; Doménech-Carbó, A.; Concepción, P.; Leyva-Pérez, A.; Corma, A., Stabilized naked sub-nanometric Cu clusters within a polymeric film catalyze C–N, C–C, C–O, C–S, and C–P bond-forming reactions. *J. Am. Chem. Soc.* **2015**, *137* (11), 3894-3900.

39. Maity, P.; Yamazoe, S.; Tsukuda, T., Dendrimer-encapsulated copper cluster as a chemoselective and regenerable hydrogenation catalyst. *ACS Catal.* **2013**, *3* (2), 182-185.

40. Leyva-Pérez, A.; Oliver-Meseguer, J.; Rubio-Marqués, P.; Corma, A.,

Water-stabilized three- and four-atom palladium clusters as highly active catalytic species in ligand-free C-C cross-coupling reactions. *Angew. Chem. Int. Ed.* **2013**, *52* (44), 11554-11559.

41. Pastoriza-Santos, I.; Liz-Marzán, L. M., Formation of PVP-protected metal nanoparticles in DMF. *Langmuir* **2002**, *18* (7), 2888-2894.

42. Santiago-Gonzalez, B.; Monguzzi, A.; Caputo, M.; Villa, C.; Prato, M.; Santambrogio, C.; Torrente, Y.; Meinardi, F.; Brovelli, S., Metal nanoclusters with synergistically engineered optical and buffering activity of intracellular reactive oxygen species by compositional and supramolecular design. *Sci. Rep.* **2017**, *7* (1), 5976.

43. Kawasaki, H.; Yamamoto, H.; Fujimori, H.; Arakawa, R.; Iwasaki, Y.; Inada, M., Stability of the DMF-protected Au nanoclusters: Photochemical, dispersion, and thermal properties. *Langmuir* **2010**, *26* (8), 5926-5933.

44. Maity, P.; Takano, S.; Yamazoe, S.; Wakabayashi, T.; Tsukuda, T., Binding motif of terminal alkynes on gold clusters. *J. Am. Chem. Soc.* **2013**, *135* (25), 9450-9457.

45. Fernández, E.; Rivero-Crespo, M. A.; Domínguez, I.; Rubio-Marqués, P.; Oliver-Meseguer, J.; Liu, L.; Cabrero-Antonino, M.; Gavara, R.; Hernández-Garrido, J. C.; Boronat, M.; Leyva-Pérez, A.; Corma, A., Base-controlled Heck, Suzuki, and Sonogashira reactions catalyzed by ligand-free platinum or palladium single atom and sub-nanometer clusters. *J. Am. Chem. Soc.* **2019**, *141* (5), 1928-1940.

46. Vilar-Vidal, N.; Blanco, M. C.; López-Quintela, M. A.; Rivas, J.; Serra, C., Electrochemical synthesis of very stable photoluminescent copper

clusters. *J. Phys. Chem. C* **2010**, *114* (38), 15924-15930.

47. de Heer, W. A., The physics of simple metal clusters: experimental aspects and simple models. *Rev. Mod. Phys.* **1993**, *65* (3), 611-676.

48. Dye, D. H.; Ketterson, J. B.; Crabtree, G. W., The Fermi surface of platinum. *J. Low Temp. Phys.* **1978**, *30* (5), 813-838.

49. Domínguez, I.; Arrebola, F. J.; Martínez Vidal, J. L.; Garrido Frenich, A., Assessment of wastewater pollution by gas chromatography and high resolution Orbitrap mass spectrometry. *J. Chromatogr. A* **2020**, *1619*, 460964.

50. Liu, L.; Lopez-Haro, M.; Lopes, C. W.; Li, C.; Concepcion, P.; Simonelli, L.; Calvino, J. J.; Corma, A., Regioselective generation and reactivity control of subnanometric platinum clusters in zeolites for high-temperature catalysis. *Nat. Mater.* **2019**, *18* (8), 866-873.

51. Mattheyses, A. L.; Simon, S. M.; Rappoport, J. Z., Imaging with total internal reflection fluorescence microscopy for the cell biologist. *J. Cell Sci.* **2010**, *123* (21), 3621-3628.

52. Axelrod, D., Total internal reflection fluorescence microscopy in cell biology. *Traffic* **2001**, *2* (11), 764-774.

53. Bailis, J. M.; Weidmann, A. G.; Mariano, N. F.; Barton, J. K., Rhodium metalloinsertor binding generates a lesion with selective cytotoxicity for mismatch repair-deficient cells. *Proc. Natl. Acad. Sci. U. S. A.* **2017**, *114* (27), 6948-6953.

54. Conesa, J. J.; Carrasco, A. C.; Rodríguez-Fanjul, V.; Yang, Y.; Carrascosa, J. L.; Cloetens, P.; Pereiro, E.; Pizarro, A. M., Unambiguous intracellular localization and quantification of a potent iridium anticancer

compound by correlative 3D cryo X-ray imaging. *Angew. Chem. Int. Ed.* **2020**, *59* (3), 1270-1278.

55. Okrut, A.; Runnebaum, R. C.; Ouyang, X.; Lu, J.; Aydin, C.; Hwang, S.-J.; Zhang, S.; Olatunji-Ojo, O. A.; Durkin, K. A.; Dixon, D. A.; Gates, B. C.; Katz, A., Selective molecular recognition by nanoscale environments in a supported iridium cluster catalyst. *Nat. Nanotechnol.* **2014**, *9*, 459.

56. Ma, D. L.; Chan, D. S.; Leung, C. H., Group 9 organometallic compounds for therapeutic and bioanalytical applications. *Acc. Chem. Res.* **2014**, *47* (12), 3614-31.

57. Fink, S. L.; Cookson, B. T., Apoptosis, pyroptosis, and necrosis: Mechanistic description of dead and dying eukaryotic cells. *Infect. Immun.* **2005**, *73* (4), 1907-1916.

58. Crowley, L. C.; Marfell, B. J.; Scott, A. P.; Waterhouse, N. J., Quantitation of apoptosis and necrosis by annexin v binding, propidium iodide uptake, and flow cytometry. *Cold Spring Harb. Protoc.* **2016**, *2016* (11).

59. Mazumder, S.; Plesca, D.; Almasan, A., Caspase-3 activation is a critical determinant of genotoxic stress-induced apoptosis, in *Apoptosis and cancer: Methods and protocols*, Mor, G.; Alvero, A. B. Editors. **2008**, Humana Press.

60. Chan, F. K.-M.; Moriwaki, K.; De Rosa, M. J., Detection of necrosis by release of lactate dehydrogenase activity, in *Immune homeostasis: Methods and protocols*, Snow, A. L.; Lenardo, M. J. Editors. **2013**, Humana Press.

61. Ishida, S.; Lee, J.; Thiele, D. J.; Herskowitz, I., Uptake of the anticancer drug cisplatin mediated by the copper transporter Ctr1 in yeast and mammals. *Proc. Natl. Acad. Sci. U. S. A.* **2002**, *99* (22), 14298-302.

Chapter 8

General conclusions

8 General conclusions

This *Thesis* describes the synthesis and different applications of Pd clusters (MCs) and single atoms (SAs) and Pt MCs.

Indeed, different synthetic procedure were presented.

- Template-mediated synthesis of Pd dimers and Pd SAs within MOFs channels.
- Template-mediated synthesis of Pt MCs on a polymeric matrix (EVOH).
- Synthesis in solution of Pd SAs and Pt MCs.

All the approaches mentioned were supported by the use of characterization techniques to confirm the presence of the interested species.

- X-ray diffraction to visualize Pd dimers and Pd SAs within the MOFs channels, followed by quantification of the metal in the network with Induced Coupled Plasma-Absorption Emission Spectroscopy (ICP-AES) and Scanning Electron Microscopy-Energy Dispersive X-ray (SEM/EDX).
- Spectrophotometric techniques for the detection of Pt MCs in solution and Field Emission Scanning Electron Microscopy (FESEM) to visualize Pt MCs embedded in the EVOH matrix, followed by the use of mass analysis of the species, performed with an Orbitrap mass analyzer.

- X-ray Absorption (XAS) and X-ray Photoelectron (XPS) Spectroscopies to verify the oxidation state and the chemical coordination sphere of the metals.

- Aberration Corrected High-angle Annular Dark-field Scanning Transmission Electron Microscopy (AC HAADF-STEM) for analyzing the size distribution of Pt MCs and to verify the presence of Pd SAs in solution.

Consequently, MCs and SAs were used in different catalytic processes.

- Pd dimers within MOF channels were used as pivotal centers for the formation of Supramolecular Coordination Complexes (SCCs) within the MOF channels (SCCs@MOF), active as catalysts in homo- and cross-coupling reactions of boronic acids and alkynes and in the oxidation reaction of alkyl alcohols.

- Ligand-free Pd SAs generated *in situ* were able to catalyze the oxidation reaction of benzyl alcohols.

- Pt MCs in solution were tested in antitumoral treatments. The activity of the MCs was compared to cisplatin, presenting quite remarkable results, even in cisplatin-resistant cell lines.

Finally, we can say that different synthesis of stable ligand-free MCs and SAs were presented. All the species represented advances in systems, which usually include the use of more pollutant reactants. In general, MCs and SAs represent an improvement in the field of catalysis due to their higher activity, compared to NPs or bulk metals, even at low concentrations, consequently,

bringing to a decrease in the cost of the necessary catalytic specie. Moreover, it is possible to express the same concept for the case of antitumoral Pt MCs, which showed antitumoral activity at lower concentrations than cisplatin and were synthetized following a cheaper approach.

Overall, the results showed in this *Thesis* can be helpful for the design of novel catalytic systems, looking especially in downsizing the catalysts, and for the improvement of MCs application in biomedical fields.

Publications

Publications

Publications related to this *Thesis*

- Adam, R.; Mon, M.; <u>Greco, R.</u>; Kalinke, L. H. G.; Vidal-Moya, A.; Fernandez, A.; Winpenny, R. E. P.; Doménech-Carbó, A.; Leyva-Pérez, A.; Armentano, D.; Pardo, E.; Ferrando-Soria, J., Self-assembly of catalytically active supramolecular coordination compounds within metal-organic frameworks. *J. Am. Chem. Soc.* **2019**, *141* (26), 10350-10360.

- Tiburcio, E.; <u>Greco, R.</u>; Mon, M.; Ballesteros-Soberanas, J.; Ferrando-Soria, J.; López-Haro, M.; Hernández-Garrido, J. C.; Oliver-Meseguer, J.; Marini, C.; Boronat, M.; Armentano, D.; Leyva-Pérez, A.; Pardo, E., Soluble/MOF-supported palladium single atoms catalyze the ligand-, additive-, and solvent-free aerobic oxidation of benzyl alcohols to benzoic acids. *J. Am. Chem. Soc.* **2021**, *143* (6), 2581-2592.

Other publications

- Garnes-Portolés, F.; <u>Greco, R.</u>; Oliver- Meseguer, J.; Castellanos-Soriano, J.; Jiménez, M. C.; López-Haro, M.; Hernández-Garrido, J. C.; Boronat, M.; Pérez-Ruiz, R.; Leyva-Pérez, A., Regioirregular and catalytic Mizoroki-heck reactions. *Nat. Catal.* **2021**, https://doi.org/10.1038/s41929-021-00592-3.

- <u>Greco, R.</u>; Lloret, V.; Rivero-Crespo, M. A.; Hirsch, A.; Doménech-Carbó, A.; Abellán, G.; Leyva-Pérez, A., Acid catalysis with alkane/water microdroplets in ionnic liquids. *J. Am. Chem. Soc. Au*, **2021**.